High-Energy-Density Physics Experiments Relevant to Astrophysical Systems

by

Channing Moore Huntington

A dissertation submitted in partial fulfillment
of the requirements for the degree of
Doctor of Philosophy
(Applied Physics)
in The University of Michigan
2012

Doctoral Committee:

Professor R. Paul Drake, Chair
Professor James P. Holloway
Professor Karl M. Krushelnick
Assistant Professor Alexander George Roy Thomas
Associate Research Scientist Eric S. Myra

TABLE OF CONTENTS

LIST OF FIGURES

Figure

LIST OF TABLES

Table

LIST OF APPENDICES

Appendix

ABSTRACT

High-Energy-Density Physics Experiments Relevant to Astrophysical Systems

by

Channing M. Huntington

Chair: R. Paul Drake

This thesis details a trio of distinct high-energy-density experiments, each related to a specific astrophysical phenomenon. The greatest attention is paid to the application of novel diagnostic techniques to a radiative shock system in xenon gas. The radiative shock was created using the OMEGA Laser to launch a beryllium pusher into a xenon-filled shock tube. Significant radiative cooling of the xenon leads to a layer of dense gas that facilitates x-ray radiography and, in a novel application of the technique, x-ray Thomson scattering. Previously limited to low-Z, solid density materials, the investigation of the fast, high-Z, weakly coupled Xe shock with scattered x-rays required concurrent developments in experimental design, theory, and diagnostic capabilities. Similar structures abound in astrophysics; examples include the interaction of shocks with molecular clouds, blast waves generated by gamma-ray bursts, and the evolution of late-stage supernova remnants.

Other aspects of gamma-ray bursts and supernovae physics were explored with an experiment on the ultrafast HERCULES Laser, and simulations of an experiment designed for the National Ignition Facility, respectively. At the HERCULES Laser, a relativistic electron beam was imaged after propagation through increasing lengths

of background plasma. The beam was observed to evolve and break apart as a result of filamentation instabilities, the same forces that act on the charged particle fluxes from gamma-ray bursts.

Finally, the radiative shock was revisited by performing 1D simulations of a 200 MBar, x-ray driven pressure pulse that is only achievable at the National Ignition Facility. The HYDRA code was used to model shock propagation though a Rayleigh-Taylor unstable interface in a low-density foam target. Using models of radiative Rayleigh-Taylor growth from literature, the plasma conditions were extracted from the simulations and used to predict the instability growth in the upcoming experiment. Although they study vastly different regimes, each of the these experiments relates the physics of astrophysical objects to laboratory-based laser plasma science, and in doing so advances understanding of both fields.

CHAPTER I

Introduction

Few topics have inspired the wonder–and sustained scientific research–as the cosmos. Studies of early civilizations reveal the detailed knowledge these people had of the movement of solar and extra-solar bodies, as evidence by the alignment of marvels like Stonehenge and the Great Pyramids of Giza to the locations of celestial bodies. Centuries later, armed with only a notebook and a keen eye, diligent astronomers recorded the motions of the stars with such precision that they were able to identify new points of light; objects now known to have been supernovae explosions [1]

With the development of magnifying optics and the telescope in the 17^{th} century, observational astronomy entered a new age. In the modern era, visible light observations of the stars are complemented by radiation measurements across a wide range of wavelengths, made possible by radio telescopes and observation stations which rival in scale and sophistication any of man's scientific endeavors. Now, the technological innovations of the past several decades once again have the potential to revolutionize the way we understand astrophysical objects.

[1] The most famous such example occurred in November, 1572, when the Danish astronomer Tycho Brahe recorded the appearance of what is formally known as SN 1572 "B Cassiopeiae," but is often referred to as "Tycho's Supernova." The discovery contradicted the widely held view of the time that the nighttime sky was unchanging, and the importance was not lost on Brahe, whose manuscript on the subject is titled *Concerning the New Star, never before seen in the life or memory of anyone...* (translated from the Latin *De nova et nullius aevi memoria prius visa stella, iam pridem anno nato...*)

To study astrophysical objects terrestrially, connection must be rigorously developed between the experiment and the astrophysical system one intends to investigate. While their size cannot be matched, supernovae (SN), gamma ray bursts, and astrophysical shock-cloud interactions are all examples of systems characterized by high Mach-number flows, ionized gas, and significant radiation transport effects – physical processes that can be studied in the laboratory. To do this, facilities have been constructed to direct large amounts of energy into small volumes, in some cases with astounding quickness. The ability to create high energy density systems allows the rigorous matching of laboratory experiments to astrophysical systems through *dimensionless parameter scalings*. In the following sections I describe the nascent field of Laboratory Astrophysics and provide give several examples of experiments related to astrophysical objects. This is followed by a brief description the capabilities of the laboratories that have been used to perform this work, as well as other high-energy-density physics (HEDP) facilities where "lab astro" experiments are conducted.

1.1 Laboratory Astrophysics

The number of physical processes involved in the dynamics of astrophysical objects is daunting. In a Type II supernova, for example, all four of the fundamental (gravitation, electromagnetic, strong nuclear, and weak nuclear) forces are evident: the gravitational collapse of a star compresses the burning gas until the strong-force-mediated neutron-neutron repulsion (as well as the increasing neutron degeneracy pressure) slows the implosion. At this stage neutrinos, possibly 10^{57} per second and interacting via the weak force, carry away tremendous amounts of energy [13]. The rebounding matter is highly ionized and relativistic, setting up intense electric and magnetic fields as the remnants stream out into the interstellar media. Correctly modeling such an event is a challenge on a computer, and matching it in the lab is an impossibility.

Given the scope of the task, to make progress one must simplify the system and focus on a small segment of the dynamics. In the example of a Type II supernova, an experiment may be dedicated to understanding the nuclear forces of strongly coupled plasma. Or, relevant to the explosion phase, one can investigate the hydrodynamics of the outflowing material. Still later in the explosion, an experiment may be designed to observe the dynamics of the relativistic electrons that escape from the supernovae remnants (SNR). In each case a comparison of the parameters of the experiment and astrophysical object must be made, with attention paid to the scalings of dimensionless parameter that match rigorously, and those that are yet unachieved in the lab. In the following sections I describe three astrophysical phenomena: astrophysical radiative shocks, gamma ray bursts, and Rayleigh-Taylor instabilities in supernovae. For each case, a laboratory experiment has been designed, the outline of which is presented here. The detailed results of these are presented in the subsequent, respective chapters.

1.1.1 Astrophysical Radiative Shocks

There are myriad examples of astrophysical objects whose dynamics are strongly influenced by the production and transport of radiation. Examples include the interaction of radiative shocks with molecular clouds [75], blast waves generated by gamma-ray bursts [142], and the evolution of late-stage supernova remnants. In the case of a spherically expanding shock from a supernova, one observable difference between the radiative and non-radiative (adiabatic) case is the rate of expansion. The well-known adiabatic solution for the expansion of a blast wave is given by $R \propto t^{2/5}$. This was independently shown by von Neumann, Sedov in 1946, and Taylor in 1950 in their investigations of nuclear explosions, and is now called the *Sedov-Taylor blast wave* in honor of the historically significantly work [191, 204, 205] [2]. In the radiative

[2]The second of Geoffrey Taylor's 1950 papers incorporated experimental data, in the form of photographs of the 1945 Trinity nuclear test. The photographs were taken at regular intervals after

case relevant to supernova remnants, a similar power-law dependence has been derived by Edison and Keity [142] where $R \propto (at)^n$, and a and n depend on the upstream and downstream adiabatic indices, the energy loss fraction, and the initial conditions of the system. Indeed, experimental evidence has shown that radiation lowers the effective adiabatic index, leading to deviations from the Sedov-Taylor scaling [98].

Experiments to explore radiative shocks have been performed by many groups [51, 20, 119, 193, 181, 180, 179, 197]. The present work follows efforts of Reighard *et al.*, and later Doss *et al.*, whose experiments investigating the structure and dynamics of a radiative shock in xenon gas made possible the scattering experiments described in §V. The threshold for determining the radiative effects of the shock is found by equating the radiation energy flux and the kinetic energy flux at the shock front. The former is given by the Stephan-Boltzmann law,$\Phi = \sigma T^4$, where Φ is the radiation energy flux, σ is the Stefan-Boltzmann constant and T is the immediate post-shock temperature. The kinetic energy flux is a function of the shock velocity u_s and the upstream material density ρ_o, and is given by $\rho u_s^3/2$. A shock is said to be radiative when R_{rad} approaches or exceeds unity, where R_{rad} is given by

$$R_{rad} \approx \frac{2\sigma T^4}{\rho_o u_s^3} \propto \frac{u_s^5}{\rho_o}. \tag{1.1}$$

Clearly the effects of radiation are most pronounced in a fast shock passing through a low-density material. The proportionality of Eqn. 1.1 is developed further in the later discussion of the xenon radiative shock system.

When R_{rad} nears one, strong radiative cooling of the electrons is taking place. In the experiments described here a cooling layer is formed, and is accompanied by a region of xenon which is compressed to higher density than predicted by strong shock relations with $\gamma \approx 4/3$. However, the details of this process are dependent on the

the detonation, allowing Taylor to compare the scaling to the data with close agreement. He further calculated the total energy released by the atomic blast, reporting 16.8 kilotons TNT-equivalent. This also agreed well with the 18.6 kiloton equivalent later reported [46]

specifics of radiation transport through the system. A useful metric for quantifying this transport is the optical depth, defined in terms of the total opacity χ_ν as

$$\tau_\nu = \int_s^{s_0} \chi_\nu(s')ds'. \tag{1.2}$$

We leave the details of xenon opacity to the description of the experiment in §3.3. Qualitatively, however, the optical depth characterizes the occlusion of radiation at frequency ν between point s and s_0. A large optical depth implies that radiation is readily absorbed and/or scattered–a regime termed *optically thick*. In the *optically thin* regime, where τ is small, radiation of frequency ν flows essentially unimpeded through the system. The optical depth may be different in pre- and post-shocked materials. In the frame of reference of the shock, the pre-shocked region is termed *upstream*, while the post-shock region is *downstream*. Given this nomenclature, radiative shocks can be classified by the upstream and downstream optical depth. Several examples of radiative shocks in the lab and in nature are given in Tbl. 1.1.1.

A strong shock launched into a gas or low-density solid with a moderate to high number of loosely bound electrons will, in many cases, develop into a thick–thin radiative shock. Such a system is thus readily accessible in the lab, and numerous experiments have addressed this case. A particularly robust thick-thin shock experimental platform has been established at the University of Michigan by Reighard and Doss using atmospheric Xe gas as the shock medium. The above descriptions are elaborated upon for the specific case of the xenon thick-thin system Chap. III.

For the xenon system at the University of Michigan, x-ray radiography has been the primary diagnostic for diagnosing the plasma conditions. The resulting 2D images were used to infer shock compression, velocity, and to perform stability analysis. However, the electron temperature T_e, which plays a central role in determining the radiative properties (Eqn. 1.1) cannot be measured through imaging. In Chap. IV

Down	Up	Astrophysical examples	Laboratory examples
Thick	Thick	· Shocks in stellar interiors [224] · Blast waves in supernova, prior to breakout	· Difficult to produce
Thick	Thin	· Supernova blast wave emerging from stars [65] · Accretion shocks in young stellar nebula [41, 30, 107]	· High-Z gas (Xe) at low pressure [20, 127] · Low-density SiO_2 aerogel [119] · High-Z gas (Xe) at atmospheric pressure [179]
Thin	Thin	· Phases of type II SN [36] · Shock-cloud interactions [75] · Shock in jet outflows from young stars [103]	· Low density gas experiments [98]
Thin	Thick	· Possible in some phases of supernova remnant interaction with molecular clouds [19]	· May exist in a transient sense, likely to transition to thin-thin

Table 1.1: A partial summary of radiative shocks in astrophysics and in the laboratory. They are classified based on the optical depth of the upstream and downstream material.

a complementary diagnostic – non-collective x-ray Thomson scattering (XRTS) – is described in detail. This technique has the potential to directly measure the electron temperature, and also to infer the average ionization of the system. The details of recent experiments and results from XRTS measurements, and their implications for future radiative shock experimental diagnosis, are the subject of Chap. V.

1.1.2 Gamma Ray Bursts and Current Filamentation instabilities

The first data from gamma ray bursts (GRBs) was collected in 1969 by the *Vela* satellite project. Developed by the U.S. Air Force and managed by the Advanced Research Projects Agency and the U.S. Atomic Energy Commission, the first *Vela* satellites were launched in October 1963 to monitor compliance (primarily of the Soviet Union) with the atmospheric nuclear test ban treaty signed the same year. Because of the precession of the satellites, several times each day the diagnostic packages–including numerous x-ray, gamma-ray, and neutron detectors– pointed away from the Earth and swept out an arc through the sky [42]. Though early designs of the *Vela* probes likely observed GRB signal, later versions with improved instrumentation enabled scientists to conclusively determine that over a dozen of the gamma ray signals that had been detected were of cosmic origin [123].

For nearly two decades mysterious gamma-ray signals were detected. It was not until the launch of the Compton Gamma-Ray Observatory (CGRO) in 1991 that the next step in GRB research could be taken. In particular, a set of time-resolved detectors spanning six decades of the electromagnetic spectrum (30 keV - 30 GeV) aboard the CGRO showed that GRBs are isotropically distributed through the sky [81, 68]. Further progress in understanding the nature of GRBs was made by the Italian-Dutch Beppo-SAX satellite project, which observed in GRB970228 the longer-duration "afterglow" which had been predicted to follow a GRB event [167, 118, 157, 43].

Gamma ray bursts have been observed at distances greater than 13 billion light years from Earth [174, 44]. This fact highlights the tremendous energy release associated with these events. However, research into the mechanisms by which that energy is converted to the observed light curves (which vary drastically from one GRB to the next [150]) is an active field. It has been proposed that a portion of the observed spectra may be the result of relativistic electrons interacting with tiny, tangled magnetic fields. If the fields are strong enough to appreciably deflect the electrons, they will radiate in a process dubbed "jitter radiation," [154, 183][3] The proposed origin of these fields is the Weibel instability, which tends to form current filaments from relativistic electron populations (see §6.1). However, the details of the instability scale lengths and radiation spectrum produced by Weibel-mediated electron beam filamentation have not been studied in the laboratory, suggesting the utility of a lab-astro experiment to understand the nature of GRB light curve.

In collaboration with scientists at the HERCULES Laser at the University of Michigan Center for Ultrafast Optical Science (CUOS) and several other groups, an experiment to create and measure electron filamentation and the resulting radiation was designed in 2007. In 2008 we conducted several weeks of experiments aimed at seeding and controlling Weibel filamentation in relativistic electron beams. The results of these measurements are given in Ref. [111]. Although these experiments are not decisive with regard to the open questions of GRB light curve generation, they have been important to understanding the dynamics of electron beams and may prove a useful test bed for further laboratory GRB research.

[3]More generally, Fleishman has pointed out that the movement of an electron interacting with random EM fields is akin to a diffusion process, and refers to the radiation from this process "diffusive synchrotron radiation." [69]. This work extends the work of Ref [154] by applying a non-perturbative approach to the calculation of the spectra which remains valid as the coherence length of the magnetic field increases.

1.1.3 Supernova-Relevant Radiative Rayleigh-Taylor Instability

The Rayleigh-Taylor (RT) instability is a fluid instability which results from opposing pressure and density gradients. Numerous terrestrial examples exist, including the rate of rise of salt domes [223], and the familiar inversion of a jar of oil and vinegar salad dressing. Rayleigh Taylor instability plays a role in astrophysical objects as well, and the Type II supernovae described previously has been an area of active research in the laboratory astrophysics community.

The opposing pressure and density gradients necessary for RT instability are set up in an exploding star as follows: while the massive ($> 8M_{\odot}$) progenitor star burns, lighter elements like hydrogen and helium are fused into heavier ones. This occurs at the core, with each successive fusion cycle generating the pressure needed to halt core collapse. This cycle repeats until iron is produced (as a decay product of nickel), at which point further fusion cycles are no longer energetically favorable. Iron continues to be produced until the core reaches the *Chandrasekhar limit* of $\approx 1.4M_{\odot}$ [31]. Next, the core begins to gravitationally contract and heat, initiating electron capture and photo-disintegration of the iron and producing the neutrino flux discussed previously.

The inrushing core material moves at such high speed that the outer layers of the star are not immediately affected. When these less dense materials begin collapsing, they encounter the outflow of the rebounding core material and a shock is formed, traveling radially outward. As the shock propagates it is overtaken by a rarefaction and evolves into a blast wave that passes through the progressively less dense layers. After the blast wave has crossed the interfaces between layers (He to H, for example), the density gradient is directed inwards, (from H to He, for example), but the pressure gradient established by the blast wave is directed along its propagation vector. In this way opposing pressure and density gradients are established, producing a Rayleigh-Taylor unstable configuration in the Type II supernova.

Both theoretical and experimental studies of the hydrodynamic RT unstable sys-

tem described above have been conducted [5, 117, 187, 186, 136, 135]. However, as established earlier, a shock which is cooling via radiation will evolve differently than a hydrodynamic one. In the case of supernovae surrounded by a dense outflow, as arises from red supergiant stars, it has been shown that the ejecta from the star will create a radiative forward shock in the direction of propagation as well as a radiative reverse shock that travels back into the ejecta [166]. A qualitatively similar system exists in the deceleration phase of imploding ICF capsules, further motivating experiments addressing this method of RT stabilization. To directly measure the effect of a radiative shock on an embedded, RT unstable interface, we designed an experiment based on previous, non-radiative RT work by Kuranz et al. [136, 135]. Design work has been performed in one-and two-dimensional simulations, and details of this work are presented in Chapter VII.

The capability to drive a shock radiative shock through an RT-unstable system which is diagnostically viable has only recently been made possible by the completion of the National Ignition Facility (NIF) [133, 109]. While the NIF is a unique laboratory, it is one of many HED facilities in the United States and throughout the world.

1.2 Facilities

Laboratory astrophysics is a young field, largely because the tools needed to create high-energy-density conditions in the lab did not exist until recently. Each of the experiments alluded to previously use a different laser to deliver energy to the physics target. While study of these "laser driven" experiments represents one of the most active areas of HED science, using a laser to drive the experiment is not the only method of creating high energy density conditions. An overview of the facilities used for the work presented here is given in the following sections, as well as a brief description of other facilities around the world.

1.2.1 OMEGA Laser Facility

Located at the Laboratory for Laser Energetics (LLE) at the University of Rochester in Rochester, NY, OMEGA (sometimes referred to as OMEGA 60, to differentiate it from OMEGA EP, described in section 1.2.4) has been a workhorse facility for laser-driven HED experiments since it began operation in 1979. The current configuration includes 60 beams that can be individually pointed, each delivering up to 500 J at 3ω (351 nm). Owing to the mechanism of producing and amplifying the seed pulse, the sixty beams are grouped into three sets of 20, which share pulse shape and some timing characteristics, but are themselves uniformly distributed around the spherical target chamber. The target chamber is seen on the left in Fig. 1.1, separated by the laser bay on the right by a shielding wall, and all sitting above several rooms housing the capacitors that power the laser amplifiers. The neodymium:glass laser system can fire slightly more than once per hour, allowing up to a dozen or more shots in a single day. Each shot is analyzed with a set of fixed and user-specified diagnostics. By taking advantage of the flexibility in laser setup and the large suite of diagnostics, a tremendous range of physics experiments have been performed at OMEGA.

1.2.2 HERCULES Laser

Construction of the HERCULES laser at the University of Michigan began in 1990, when the Center for Ultrafast Optical Science (CUOS) was established by the National Science Foundation. The single-beam facility uses Ti:sapphire crystals and chirped pulse amplification (CPA) to achieve record-setting focused intensities, greater than 10^{22} W/cm^2 [221]. These intensities are reached by compressing a modest amount of energy, $\approx$15J, into an exceptionally short pulse length of 30 fs. When focused to single-micron spot sizes relativistic plasma conditions are reached, as quantified by a normalized vector potential $a_0 = \frac{eE}{m_e c \omega_0} > 1$ [4]. In this form E is the electric

[4]Guassian cgs units are used throughout, unless otherwise noted.

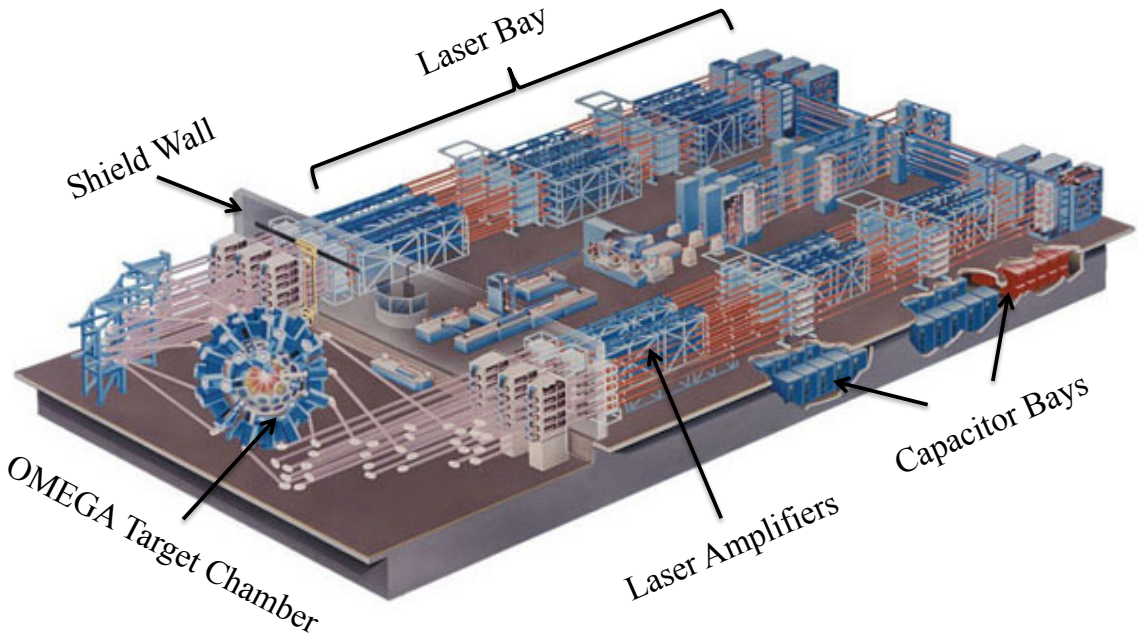

Figure 1.1: Diagram of the OMEGA Laser Facility. Adapted from LLE Facility Documents

field strength, ω_0 is the laser frequency, c is the speed of light, and e and m_e are the electron charge and momentum, respectively. For $a_0 > 1$ the kinetic energy imparted to the electron by the laser electric field is greater than the electron rest energy and relativistic effects begin to play an important role the plasma dynamics. By focusing this ultrarelativistic pulse into a region of low-density gas an electric field structure can be setup that is able to accelerate electrons to near the speed of light. This process is called *Laser Wakefield Acceleration (LWFA)*, and has been used by researchers at HERCULES to produce electrons with energies of many hundreds of MeV. At somewhat lower energies, similar electron beams were created and used to study the GRB dynamics introduced in §1.1.2. Details of the LWFA mechanism are given in Chapter VI, as well as results of the GRB-motivated electron beam filamentation experiment.

1.2.3 National Ignition Facility

By a significant margin, the largest laser facility in the world is the National Ignition Facility (NIF) at Lawrence Livermore National Laboratory (LLNL), in Livermore, CA. With the expressed goal of achieving nuclear fusion, the NIF uses 192 beams to deliver a total 1.8 MJ energy (at the time of writing) to the center of a 30-foot diameter spherical target chamber. The beams are not uniformly distributed like the 60 beams of OMEGA, but instead are arranged in two nearly-circular rings around each pole. This configuration was motivated by an x-ray driven approach to inertial confinement fusion (ICF) design. The choice of diagnostics at the NIF also reflects the ICF mission, with neutron and gamma ray detectors in place to record the flux and energy of the fusion products. Numerous x-ray diagnostics, many of which leverage well-tested designs from OMEGA, have also been commissioned. Chapter VII further describes the ramifications of the beam arrangement and diagnostic suite on indirect drive platform development with respect to laboratory astrophysics ex-

periments on the NIF.

1.2.4 Other facilities: Lasers, Pinches, and Accelerators

Beyond the laser facilities described above, there are many additional laboratories both in the United States and abroad performing HED experiments. Noting three in particular, the addition of the four-beam OMEGA EP laser at LLE adds short-pulse capabilities to the OMEGA 60 chamber, or can be used for independent experiments. The Nike Laser at the Naval Research Lab achieves an exceptionally uniform laser spot from a krypton-fluorine gas amplifier, and has been used to perform numerous experiments on Rayleigh-Taylor instability issues relevant to ICF. At Sandia National Laboratories, the Z-machine is able to release 26 million Amps of current through tiny wire arrays, compressing them on axis and creating HED plasmas and intense x-ray sources. With careful experimental design, each of the facilities described here are capable of creating astrophysically-relevant conditions in the laboratory and helping expand our knowledge of the basic physics mechanisms at work in the cosmos.

CHAPTER II

X-ray production for experimental diagnostics

Many of the methods used to probe high-energy-density systems rely on an external source of x-rays. This is the case for x-ray Thomson scattering, the subject of Chapter V, as well as for x-ray radiography, used to image the radiative Rayleigh-Taylor experiment in Chapter VII. In both cases, the success of the diagnostic relies in part on the properties of the x-ray source. For a given experiment, one must prioritize the brightness, energy, and degree of energy spread of the x-ray probe. Understanding the processes by which x-rays are produced in laser-matter interaction is essential to designing appropriate sources, and is the topic of this chapter.

In discussing the emission spectrum from a laser-produced x-ray source, the contributions of continuum and line emission may be considered separately. Continuum emission is an important diagnostic for magnetically confined plasmas [137], but is not commonly used as a diagnostic in laser-produced plasma experiments. As such, it is discussed only briefly here. Line emission is the primary source of x-rays for HED experiments, and has been employed for decades as a diagnostic probe for radiography, scattering, and spectroscopy experiments [3, 4, 9, 10, 12, 15, 21, 26, 35, 40, 53, 71, 72, 73, 74, 82, 83, 89, 87, 94, 108, 112, 115, 121, 129, 130, 131, 134, 139, 140, 138, 141, 147, 168, 169, 176, 192, 207, 213, 216, 217]. Following our mention of continuum emission, we describe the basic mechanisms of generating line emission,

explain briefly the suite of computational tools used to model x-ray spectra, review the physics of laser-solid interaction frequently used to generate x-rays, and provide an illustrative example of a recent x-ray source experiment.

2.1 Continuum radiation

Continuum emission in the systems of interest here is dominated by the radiation of accelerating free electrons, called *Bremsstrahlung* radiation. Bremsstrahlung is produced when an electron interacts with an ion, decelerating and changing direction, without being captured by the ion[1]. The power emitted into the spectral region around the energy $\hbar\omega$ per unit volume is reported as reported in Ref. [97] is:

$$P_{ff}(\hbar\omega) = \frac{32}{3}\sqrt{\frac{\pi}{3}} r_0^2 c \sqrt{\frac{E_H}{T_e}} Z^2 n_i n_e exp\left(-\frac{\hbar\omega}{T_e}\right) d(\hbar\omega). \tag{2.1}$$

In this equation $r_0 = e^2/mc^2 = 2.818 \times 10^{-13}$ cm is the classical electron radius, c is the speed of light, and $E_H = 13.6$ eV is the binding energy of the ground state hydrogen electron. Equation 2.1 is valid in the classical limit, with quantum corrections being incorporated in the form of the multiplicative Gaunt factor. However, this factor is near unity over a wide range of parameter space [188] and can often be neglected. The subscript on P indicates the *free-free* nature of the electron before and after the interaction. This is contrasted with bound-free and bound-bound processes in the discussion of photon scattering of Chapter V.

Radiative losses from bremsstrahlung can be the main cooling mechanism in low-Z plasmas [188], and the measurement of bremsstrahlung can be a useful diagnostic for understanding plasma conditions [120]. Continuum radiation has been used as a

[1]If the electron is captured by the ion, this is categorized as *radiative recombination*. The power spectrum of radiative recombination is continuum, but is also dependent on the binding energy of the level into which the electron was captured. Radiative recombination is a small effect which is dominated by bremsstrahlung in the systems described here.

diagnostic source for HED experiments [76, 220], and development of brighter continuum sources continues. One example is the work on *dynamic hohlraums*, which consist of a thin plastic shell filled with a high-Z gas. The shell is imploded via direct laser irradiation, and the spherically converging shock produces a plasma which strongly emits continuum radiation up to several keV [100]. Such a source is useful for absorption spectrometry or gated spectrometer measurements. However, for the purpose of creating higher energy x-ray sources for imaging or scattering measurements, the exponentially decreasing nature of Eqn. 2.1 with photon energy means that the continuum emission is often only a low background under the line-emission spectrum.

2.2 Line emission

Line emission is produced by the transitions of electrons between energy levels of an atom. The energy of the photon emitted is a function of the electronic structure of the atom, and to a lesser extent the properties of the plasma surrounding the emitting atom. Because the exact quantized energy of the transitions depends on the electronic structure of the element, line radiation from each element is slightly different, motivating the term "characteristic" x-ray radiation.

Characteristic line emission is produced in two related processes, namely inner-shell transitions and ionic resonance line transitions. In the former, an electron from the inner shell of a neutral or weakly ionized atom absorbs energy and is liberated from the atom. An electron from a higher shell then falls to repl3ace it, and in doing so radiates energy equal to the potential difference between its initial and final state. Transitions from the L to K shell produce K_α radiation, which is the most commonly used inner-shell transition in HED experiments. K_β radiation is generated by transitions from the M shell to K shell, and the ratio of K_β / K_α can be used as a diagnostic for the x-ray source material bulk temperature [161, 159, 162, 207, 95].

However, the ratio is necessarily small ($\leq$0.14), and K_β radiation is rarely generated specifically for use as a diagnostic probe.

Unlike the inner shell transitions, resonance transitions occur in highly ionized atoms retaining only one, two, or a few electrons (called H-like, He-like, etc, owing to their similarity in electronic structure to these low atomic number elements). The energy of the line transition is again equal to the difference between initial and final states of the decaying electron, but the distribution of possible electron levels resembles that of the neutral atom with the same number of electrons. The increased Coulombic potential from the remaining nuclear charge increases the energy of the transitions. For hydrogen-like atoms, the energy of the transitions was measured empirically before the advent of quantum mechanics (at which time the numerical coefficient in Eqn. 2.2, taking $Z = 1$, became known as the *Rydberg energy*), and was later explained by the Bohr model,

$$\hbar\omega_{i,f} = \frac{Z^2 e^2}{2a_0}\left(\frac{1}{n_f^2} - \frac{1}{n_i^2}\right). \tag{2.2}$$

Here, the subscripts i, and f indicate the initial and final principle quantum level n, a_0 is the Bohr radius, Z is the nuclear charge, and $\hbar\omega$ is the energy of the photon emitted. Thus, the energy emitted in the $n_i = 2 \rightarrow n_f = 1$ transition in a H-like Al atom ($Z = 13$) is $\sim 13^2\times$ more than the same Ly_α transition in hydrogen. Although the Bohr model serves to illustrate the basic scalings of the line transitions, the electronic structure of a real plasma is tremendously more complicated than this. Calculation of the emission spectra for experimental design and analysis requires computer models capable of solving the coupled equations–or some simplified subset of the equations–that describe the system.

2.3 Calculation and modeling of emission spectra

For simple, single-atom systems the calculation of emission energy can proceed by Eqn. 2.2, suitably modified to account for shifts in the energy levels. For a real system, however, the level structure of the atom can be tremendously complicated, and transitions may occur between potentially millions of level pairs. The rate at which these transitions occur depend on the relative occupations of the level pairs, and for a plasma with gradients in temperature and density, these occupations are *not* well described by a simple Boltzmann model. A calculation of the level occupations must include (at least) the dominant processes that move electrons between the levels, including:

- Collisional excitation (*bound-bound* collisional processes)
- Collisional ionization (*bound-free* collisional processes)
- Collisional de-excitation
- Spontaneous radiative decay
- Photoexcitation
- Radiative recombination
- others, depending on the system.

Each of these transitions has associated rates, either measured or calculated for every atom, and a complete description of the level populations can be found by solving the set of equations which couples all of the levels though these processes. For a single level i, the population rate of change of is given by

$$\frac{\mathrm{d}n_i}{\mathrm{d}t} = \sum_{i \neq j}^{N_L} n_j W_{ji} + n_i \sum_{i \neq j}^{N_L} W_{ij}, \tag{2.3}$$

where W_{ji} and W_{ij} are the populating and depopulating rates between levels i and j, and N_L is the total number of energy levels in the system. In practice this requires an

unrealistically large collection of cross section data (note that W_{ji} and W_{ij} each have numerous contributions) and produces a computationally overwhelming set of coupled equations. Progress can only be made by applying several simplifying assumptions.

A tractable solution to the atomic level population calculation has been developed in the form of the *collisional-radiative model* (CR model) [122, 39]. The CR model assumes that collisions are the primary mechanism for excitation, and thus neglects transitions from interaction of the atoms with the radiation field. Additionally, not every possible level is modeled explicitly. Instead, a group of transitions between levels with nearly-equal energy differences (specifically, when the spacing between neighboring lines is comparable to or greater than the line width), are treated as a single, broad distribution of transition energies. These are called *unresolved transition arrays*, and are important for reducing the number or transitions in moderate- and high-Z atoms. These features, along with many other technical aspects beyond the scope of this document, have been incorporated into the set of CR codes that are readily available for analysis of plasma population and x-ray emission properties.

2.4 Laser-produced x-ray sources

Laser irradiation of transition metals is commonly employed to produce characteristic x-rays for use in high-energy-density experiments. At its simplest, this technique requires only a moderate amount of laser energy (with respect to the scale of facilities described previously) to be focused on a metal foil. To investigate how the specific regions of a laser-irradiated x-ray source produce radiation, it is useful to describe here the basics of laser-solid interaction. The description below assumes a "high-intensity" laser pulse on the order $10^{13} < I_L < 10^{17}$, with laser intensity I_L in units of W/cm^2. Below this intensity the high energy fluxes described here are not delivered, while above this intensity relativistic electron motion driven by the strong electric field begins to play a role in the dynamics.

The thickness of the target foil is determined by the experimental geometry. The foil is thin (order of several μm) if the x-rays are intended to be used on the side opposite the laser, or can be arbitrarily thick when the intended target of the x-rays is on the laser-irradiated side. Near-instantaneously, relative to a 100 *ps* or longer pulse, a laser impinging on a solid target heats it, and the heated material expands into the vacuum. This expanding plasma is known as the *corona region*, and is necessarily lower density than the solid material. Laser light cannot penetrate beyond a certain electron density, known as the critical density and given by:

$$n_c = \frac{\pi m_e c^2}{e^2 \lambda_L^2} \tag{2.4a}$$

$$n_c = \frac{1.1 \times 10^{21}}{\lambda_\mu^2} \mathrm{cm}^{-3}. \tag{2.4b}$$

The critical density depends only on the the laser wavelength λ_L and the physical constants of electron mass m_e, speed of light c, and electron charge e, and as such can be expressed in the convenient engineering form of Eqn. 2.4b, where λ_μ is in units of microns. The laser heats the *underdense* region, where $n_e < n_c$, but is strongly absorbed near n_c. The other interface of note is the ablation front, the point from which mass flows away from the solid material [63]. These are indicated in the schematic shown in Fig. 2.1.

The laser energy deposited near n_c is transported into the plasma by x-rays, which can penetrate to higher densities, and by electron heat conduction. For this reason, it is called the *conduction* or *transport* layer. The electron distribution is largely Maxwellian, and the lateral propagation of electrons through the target serves to smooth hot spots that may be present in the laser. This has little role in x-ray generation, but is relevant to the hydrodynamic instabilities described in Chap. VII, where laser-imprinted perturbations of the ablation front can be unstable to Rayleigh-

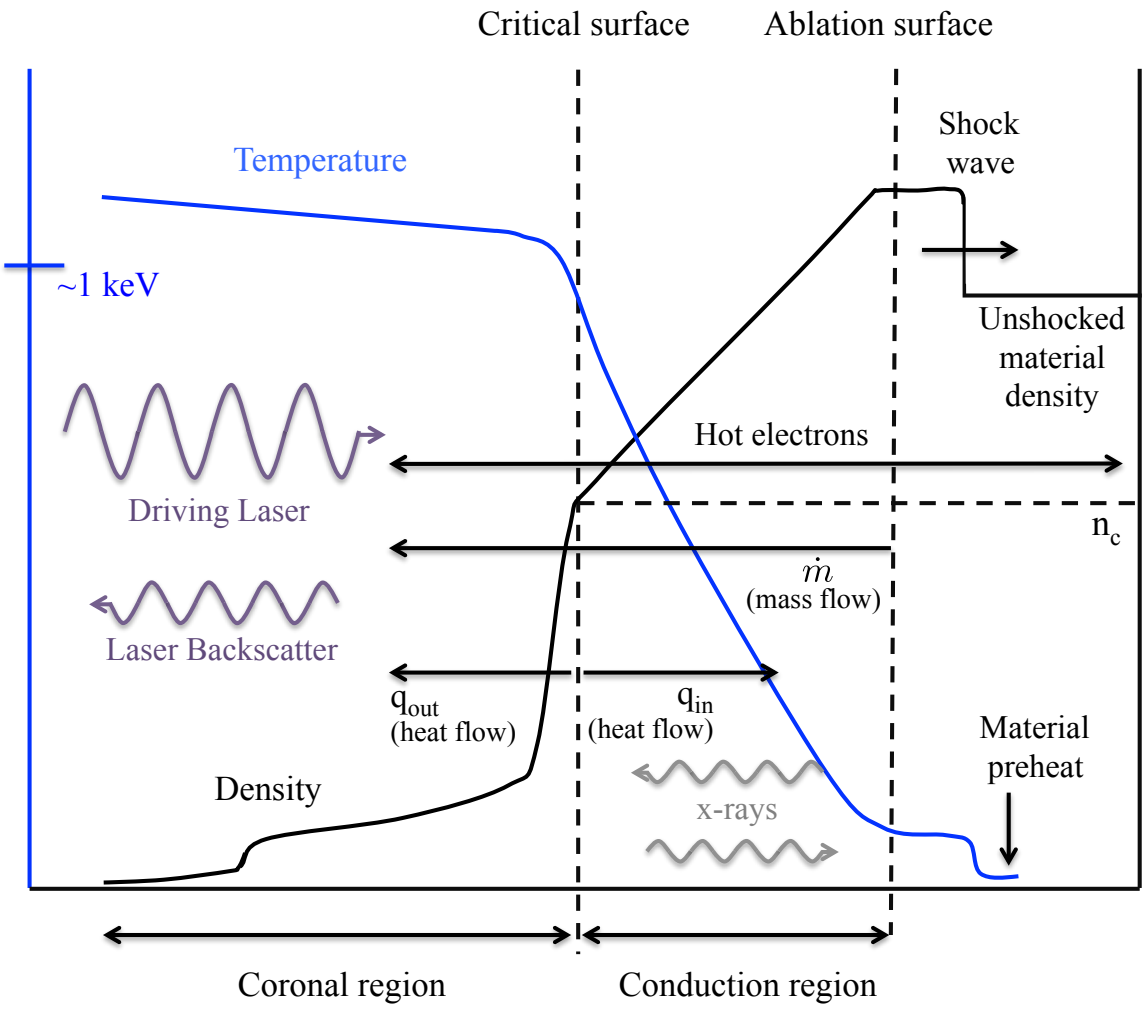

Figure 2.1: Diagram of the temperature and density profiles established in a laser-produced plasma (not drawn to scale). The flow directions of several energy-transport mechanisms are indicated by the arrows, in relation to the plasma corona and conduction regions.

Taylor growth. In addition to the Maxwellian population, for laser intensity greater that 10^{15} W/cm^2 the generation of supra-thermal electrons with energies of tens of keV to MeV is well documented [27, 33, 62, 73, 104, 160, 207, 215, 222, 169]. This "hot electron" population is the result of electrons interacting with waves in the plasma, particularly those generated by stimulated Raman scattering (SRS) in the plasma corona [66, 58]. This process is related to the acceleration of electrons via laser wakefield acceleration, which is the topic of Chap. VI. Hot electrons play an important role in x-ray generation, and are discussed further in §2.5.

Although it is not usually an important feature for x-ray production experiments, the establishment of an ablation surface leads to recoil motion of the upstream material in the opposite direction. We diverge briefly to explore this, as it is an important feature in experiments subsequently discussed. At the critical surface, the conservation equations for mass, momentum, and energy can be written:

$$\rho_c u_c = \rho u \equiv \dot{m}, \tag{2.5a}$$

$$\rho_c u_c^2 + P_c = \rho u^2 + P, \tag{2.5b}$$

$$\dot{m}\left(\frac{\gamma}{\gamma-1}\frac{P_c}{\rho_c}+\frac{1}{2}u_c^2\right)+q_{out}=\dot{m}\left(\frac{\gamma}{\gamma-1}\frac{P}{\rho}+\frac{1}{2}u^2\right)+q_{in}+I. \tag{2.5c}$$

In these equations ρ is material density, u is the plasma flow velocity, P is pressure, q is the electron heat flux, I is the absorbed laser energy flux, $\dot{m}$ is the areal mass rate of change, and γ is the polytropic index. The subscript of c indicates the quantity is evaluted on the laser-irradiated side of the critical surface, where quantities without subscripts are on the conduction zone side of n_c. At the ablation surface the equations

are somewhat different:

$$\rho u = \dot{m} = \text{constant} \tag{2.6a}$$

$$P_a = \rho u^2 + P, \tag{2.6b}$$

$$\dot{m}\left(\frac{\gamma}{\gamma - 1}\frac{P}{\rho} + \frac{1}{2}u^2\right) + q_{in} = 0. \tag{2.6c}$$

Here P_a denotes the ablation pressure. Note that Eqn. 2.6a indicates that the ablation surface is a "source" of plasma in the laboratory frame, which relates to the definition of the ablation surface. The density profile in the corona region is that of an isothermal rarefaction, implying a flow velocity given by the isothermal sound speed

$$u_c = c_T = \sqrt{\frac{P}{\rho}}. \tag{2.7}$$

With Eqns. 2.5a and 2.5b we find the ablation pressure to be

$$P_a = 2\dot{m}c_T. \tag{2.8}$$

After a brief period as the shock passes though the material (*shock transit time*), the ablation pressure serves to accelerate an initial mass m_0 to a velocity v at time t given by

$$P_a = m(t)\frac{\mathrm{d}v(t)}{\mathrm{d}t} \tag{2.9}$$

where, assuming a constant mass flow rate we have

$$m(t) = m_0 - \int_0^t \left(\frac{\mathrm{d}m}{\mathrm{d}t}\right)\mathrm{d}t = m_0 - \dot{m}t. \tag{2.10}$$

Using our value for ablation pressure from Eqn. 2.8 in Eqns. 2.9 & 2.10 and inte-

grating yields the *rocket equation*:

$$v(t) = 2c_T \ln\left(\frac{m_0}{m(t)}\right) \tag{2.11}$$

At cessation of a constant power laser pulse, the final mass $m_f = m_0 - \delta m$ is accelerated in response to the outgoing mass δm traveling at exhaust velocity $v_{ex} \approx 2c_T$. This is a result of the absorbed energy flux I. Taking $\gamma = 5/3$ in Eqns. 2.5c & 2.6c, I can be solved for,

$$I = 4\dot{m}c_T^2, \tag{2.12}$$

where we have taken $q_{out} = \rho u_c^3 = \dot{m}u_c^2$, which represents the energy that must be added at the critical surface to keep the rarefaction isothermal [6].

To a good approximation for low-Z materials, the important quantities given here are expressed by Atzeni and Meyer-ter-Vehn [6] as

$$T_c = 13.7(I_{15}\lambda_\mu^2)^{2/3} \text{ keV}, \tag{2.13a}$$

$$c_T = 8.75 \times 10^7 (I_{15}\lambda_\mu^2)^{1/3} \text{ cm/s}, \tag{2.13b}$$

$$p_a = 57(I_{15}/\lambda_\mu)^{2/3} \text{ Mbar}, \tag{2.13c}$$

$$\dot{m}_a = 3.26 \times 10^5 (I_{15}/\lambda_\mu^4)^{1/3} \text{ g/cm}^2 \text{ s}, \tag{2.13d}$$

where I_{15} is laser irradiation is I / 10^{15} W/cm^2 and λ_μ is the laser wavelength in microns. Note that the numerical coefficients may vary across references [54, 143], depending on assumptions of the plasma outflow speed (taken here to be c_T, but elsewhere $\sqrt{2}$ larger than this), the electron flux model used to evaluate q, and the degree of ionization (this enters in the form of the gas constant in calculation of Eqn. 2.13a). While the quantitative values of these parameters are rarely important in designing x-ray sources, understanding the profiles and fluxes depicted in Fig. 2.1 is

crucial for analysis of laser-irradiated foil experiments.

2.5 Illustrative x-ray source experimental analysis

Laser-irradiated foils provide a simple method of x-ray generation but suffer from low conversion efficiency from laser energy to multi-keV x-rays. Experiments using underdense gas targets have shown significantly higher conversion efficiency, but gaseous targets are available in only limited energy ranges and are more difficult to field experimentally [12, 11]. It has been suggested that low density solid "foam" targets may behave more like gaseous targets, yielding increased conversion efficiency while remaining simple to field [56]. To investigate this, we performed an experiment using a 10% solid density copper (foam) target, and compared this with a solid copper (foil) target, under near-identical laser irradiation at the Omega EP Laser Facility.

As is often the case for laser-irradiated metallic foils, the data from this experiment (Fig. 2.2) shows peaks from inner-shell x-ray emission as ionic resonance transitions. The K-shell ionization of cold material is attributed to electron impact ionization, and the observation of the K_α radiation from this process has been used as a means of inferring the properties of the hot electron population [14]. It has been shown that the temperature of this non-Maxwellian population, denoted as T_{hot}, scales roughly as $(I\lambda^2)^{1/3}$. These electrons are sufficiently energetic to ionize K-shell electrons from the solid density region of the x-ray source foil, generating the K_α radiation. X-rays generated by hot electron refluxing can be the dominant signal in high-intensity, short pulse (order *ps* or less) x-ray sources. In such experiments the laser pulse ceases before significant hydrodynamic expansion of the target occurs (*isochoric* heating), limiting the He_α production [161, 159, 162, 207, 95].

For the experiment presented here, however, approximately 930 J of 1.053 μm wavelength laser light was delivered in 74 *ps* into a 200 μm spot size, producing an intensity of 4 $\times 10^{16}$ W/cm^2. The hydrodynamic expansion depicted in Fig. 2.1 *does*

occur on this time scale, and as a result He_α peaks are evident in both the foam and foil targets. The solid-density copper target was a 250 μm diameter, 10 μm-thick copper disk, while the foam target consisted of a short cylinder of elemental Cu at $\rho = 0.89$ g/cm^3, affixed to a CH substrate. The cylinder was 1865 μm in diameter and 706 μm high; making it significantly more massive ($\approx 360\times$) than the foil. For both targets, a single short pulse beam from OMEGA EP was used at near-normal incidence.

The primary diagnostic for this experiment was the Dual Channel HOPG Spectrometer (DCHOPG), which uses a pair of highly-ordered pyrolytic graphite (HOPG) crystals, one optimized for copper K_α (8 keV) and the other in second order diffraction for silver K_α (22 keV) [4]. Both take advantage of mosaic focusing of the HOPG crystal, which has a mosaic spread of 0.4 degrees. Only the low-energy channel was employed for the copper targets, having an approximate energy range 7500 - 10500 eV. The detector was a BAS-MS 2040 image plate (IP), which was digitized with a Fuji FLA7000 scanner.

As seen in Fig. 2.2 (a), clear peaks mark the transitions in the neutral or weakly ionized atom (K_α and K_β lines). Line emission from highly ionized atom is produced mainly from the He-like state, with Li-like and H-like lines also evident. Figure 2.3 shows the occupation fractions of the higher charge states for a range of electron temperatures, with density held constant at $n_e = n_c = 1\times10^{21}$ cm^{-3}. For temperatures > 2 keV, the distribution is strongly peaked at He-like ions, consistent with the observed spectra. This is a result of the increased ionization energy required to remove the first electron from any closed atomic shell, which leads to peaks in the charge state distribution at noble gas-like ion states.

The K_α peaks from the foam and foil targets are seen to have nearly equal intensity and shape. The foam target produced significantly more K_β, though this feature *is* resolved on both shots. Both measurements record the resonance lines though they

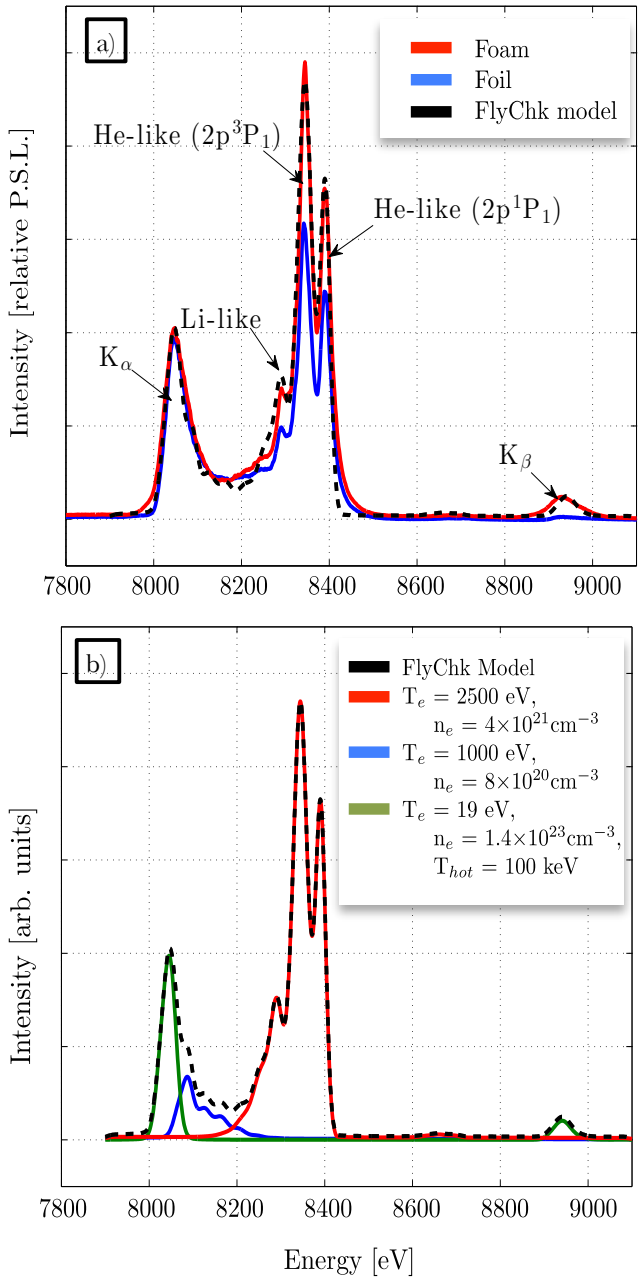

Figure 2.2: Experimental and synthetic spectra. a) Data from copper foil and 10% solid density copper foam are shown with the composite synthetic spectrum from FLYCHK. b) Details of the components of the synthetic spectrum. Note that the dashed curve is identical in both plots.

differ in intensity, with the foam target producing 50% more integrated emission in the range 8.2 - 8.8 keV. While it is known that the absolute yield of x-rays will fluctuate between nominally identical shots [217, 12], this result encourages further investigation of low-density metallic foams as efficient x-ray radiation sources.

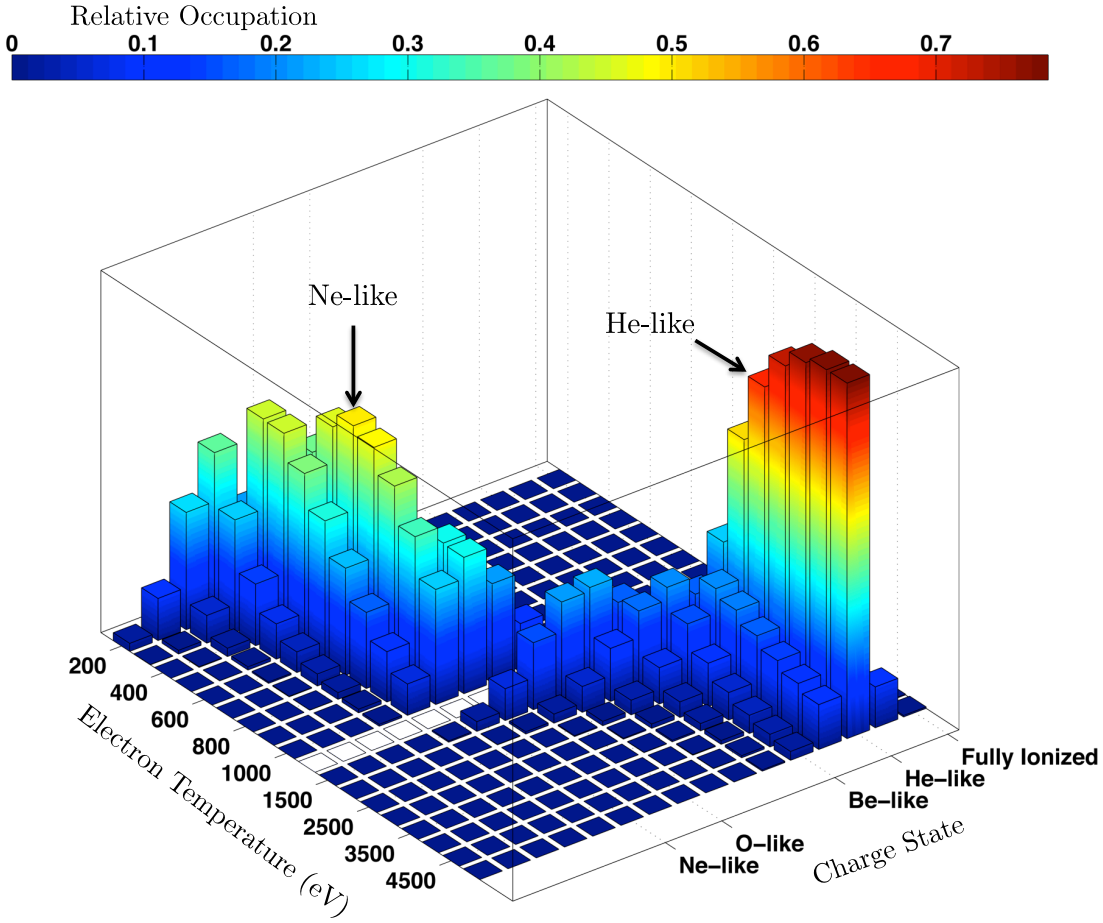

Figure 2.3: Distribution of charge states for Cu plasma, as calculated by the FLYCHK steady-state collisional-radiative model. The density is fixed at $n_e = 10^{21}$ cm^{-3} for temperatures between 200 - 5000 eV (note the break at 1 keV). The increased ionization potential of the closed shell configurations (Ne, and more so He) mean these states have higher occupation fractions over a wider range of parameter space.

To model the x-ray emission, synthetic spectra were generated from the radiative-collisional code FLYCHK [39]. However, because the DCHOPG spectrometer is spatially and temporally integrating, the data shown in Fig. 2.2 (a) is the total emission

from a system with a range of plasma conditions. To account for distinct plasma conditions, the model curve shown is a combination of synthetic spectra from three plasma regions, which are shown separately in Fig. 2.2 (b). The contributions of the individual components were adjusted to match the spectrum, which correspond to the volume of emitting plasma in the physical system. Each plasma at a specific temperature and density represents itself a complex average over a range of plasma states, as described in detail below.

Considering first the ionized resonance lines in the region 8.2 - 8.6 keV, least-squares comparison of normalized FLYCHK spectra to the data yields a best fit for plasma condition with temperature T_e = 2500 eV and electron density n_e = $4\times10^{21}/cm^3$. This is approximately four times the critical density n_c, and corresponds to the most dense region where temperatures are high enough to reach the ionized states [9]. Note that the FLYCHK output has been convolved with a Gaussian instrument response function with FWHM = 25 eV, which is in addition to the natural broadening mechanisms accounted for by the FLYSPEC code. This is in addition to the resolution limiting effects accounted for by the FLYSPEC code, namely the calculation of Doppler and Stark broadening, and represents the instrument resolution which is dominated by depth broadening [4] in the HOPG crystal. The same FLYCHK spectrum is also a good fit to the foil resonance lines (not shown).

To model the K-shell lines a hot electron population was added to the Maxwellian electron distribution function in FLYCHK simulations of greater-than-solid density Cu. Extrapolation of Beg scaling [$T_{hot} = 215(I_{18}\lambda^2)^{1/3}$ keV] to the intensity of this experiment suggests a suprathermal electron population of 71 keV [32], though the computed spectra are not a strong function of the specific value used [207]. For low thermal electron temperatures (< 50 eV), both K_α and K_β lines are predicted. As shown in Fig. 2.2 (b), the best fit to the K-shell emission from the foam target is T_e = 19 eV and electron density $n_e = 1.4\times10^{23}/cm^3$.

The region between the K_α and Li-like line is spanned by numerous transitions in lesser-ionized atoms (Be-like, B-like, C-like, etc. See Fig. 2.3). In the experiment these conditions correspond to the plasma which expands laterally during the laser pulse, and to the cooling, expanding plasma after the laser has turned off. Empirically this region is well modeled by a plasma with conditions T_e = 1000 eV and electron density $n_e = 8{\times}10^{20}/\text{cm}^3$. This is the third component of the synthetic spectra shown in Fig. 2.2 (b). Together, the FLYCHK spectra from the hot coronal plasma, K-shell lines, and cooler coronal plasma yield a spectra nearly equalling the measured foam x-ray emission.

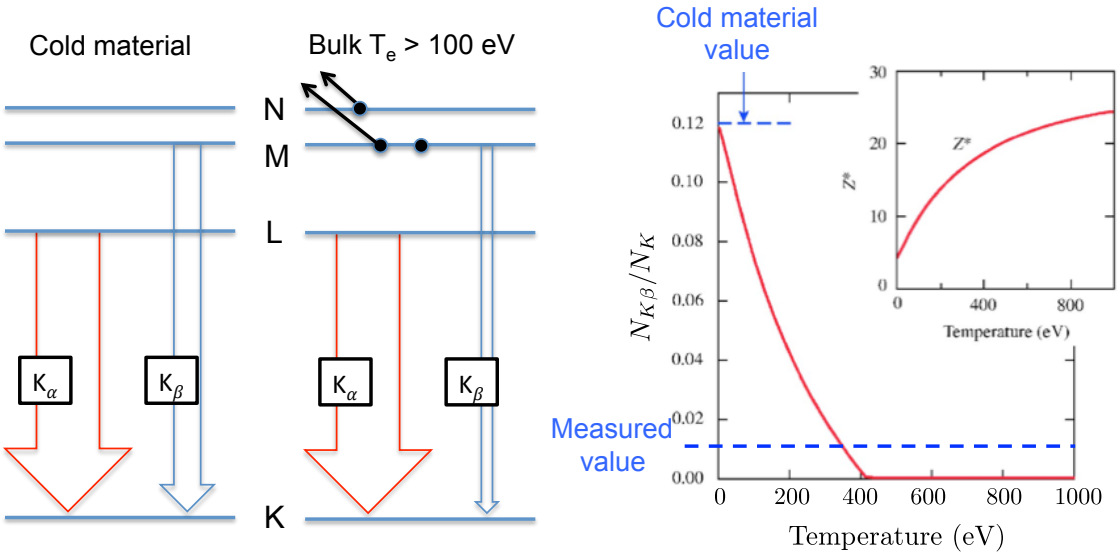

Figure 2.4: a) Depletion of the M shell by bulk heating decreases the K_β emission (*Image adapted from P. Nilson et al., Ref.* [162]) b) The cold K_β / K_α value is a maximum, and the ratio decreases as the M shell is depleted at higher T_e. (*Image from J. Myatt et al., Ref.* [159])

Predictive estimates of absolute K_α and K_β emission requires Monte-Carlo simulation beyond the scope of this work. However, the ratio of K_β/K_α has been calculated as a function of bulk temperature in low mass targets similar to the foil used here in several references [159, 162], one of which is reproduced in Fig. 2.4 b). From our data, the measured K_β/K_α for the foam target is 0.117, and is decreased to 0.013 in

the foil target. On comparison with the studies in References [159] and [162], this implies K-shell emission from nearly-cold copper in the case of the massive foam, and a bulk temperature of >300 eV in the low mass foil target.

Research into the mechanisms described here is ongoing, with the goal of producing brighter, more efficient x-ray sources. For use as a diagnostic probe, the details of a given experiment dictate whether K-shell or resonance line x-rays are the preferred option. For the purpose of radiography the He_α and K_α peaks represent nearly-equivalent energies, assuming that the target to be imaged does not have absorption lines that fall between the peaks (elements with Z_i-1, where Z_i is the x-ray source material atomic number, can have this effect. Nickel, for example has a K-edge near 8.3 keV, falling between the K_α and He_α peaks of Zn). For x-ray Thomson scattering experiments, however, monoenergetic sources are preferred. In particular, K_α emission provides an excellent incident source because of the paucity of red-wing satellites in the region where down-scattered signal is expected. Thomson scattering is the topic of the Chapters IV and V, where the stringent requirements on the x-ray source are presented in full details.

CHAPTER III

Radiative shock experiments

3.1 Introduction to the xenon radiative shock

The astrophysical motivation for studying radiative shocks was described in the Introduction. Additionally, radiative hydrodynamic systems are shaped by a complex interaction of physics processes, including radiation transport and fluid motion, but also the atomic physics of ionization, line emission, significant departures from LTE conditions, and the boundary effects inherent in finite-sized experiments. This complexity makes radiative shock experiments compelling from a simulation benchmarking perspective as well[1].

Before quantifying important physical parameters of the system, it is useful to introduce the experiment and its lineage. Early measurements of the xenon radiative shock were taken by Reighard *et al.* [181, 179, 180], and continued by Doss *et al.* [50, 53, 52, 51]. Fundamentally, the radiative xenon shock system consists of a 660 μm diameter polyimide tube capped with a 20 μm beryllium disk. The tube-disk interface is made gas-tight and filled to near one atmosphere with xenon gas. Ten OMEGA beams deliver 3.8 kJ of laser energy at 353 nm in a one nanosecond square pulse. This incident energy ablates a fraction of the Be disk, accelerating the remaining portion into the shock tube. The Be acts as a piston, driving a strong shock into the stationary

[1]See Appendix section of Ref. [55]

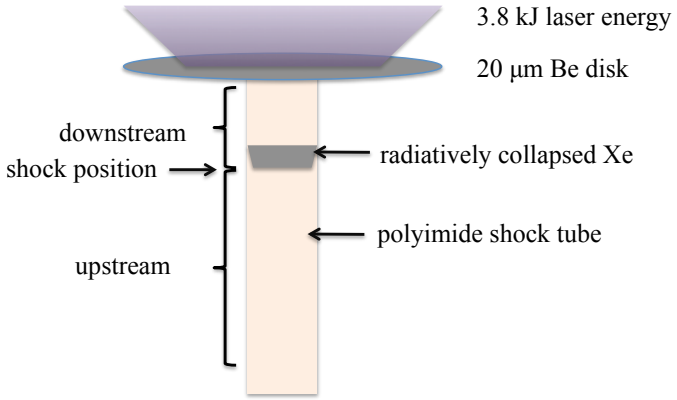

Figure 3.1: The fundamental components of the Xe radiative shock experiments are shown. A 20 μm-thick Be disk is affixed to a polyimide (plastic) tube so as to be gas tight. The tube is filled with $\sim$ 1.1 atm of Xe gas. Laser irradiation of the Be disk leads to a shock traveling down the tube. (Note that the diagram is not to scale, and similarly that the laser pulse ends *before* the shock propagates appreciably into the Xe.)

gas. The shock serves to heat and compress the gas, which ionizes and radiates away much of the incoming energy. Understanding this hot, compressed, radiating xenon layer that is formed by the shock has been the focus of the radiative shock campaign at OMEGA. Figure 3.1 is a diagram of the system showing the components common to all of the radiative shock experiments described herein.

The primary diagnostic for this system has been 2-dimensional (2D) x-ray radiography. The "camera" is operated in a point-projection configuration, where a detector is left un-apertured and the source of photons is made to be nearly point-like. To produce a high-contrast image the photons must be strongly attenuated in select regions of the target, while passing largely impeded in others. A brighter source decreases noise, and like any photograph of a rapidly evolving structure, the x-ray camera must have a sufficiently fast "shutter" to minimize motion blurring. All of these factors have been individually studied in the references listed above, and these efforts have yielded repeatable images of the quality seen in Fig. 3.2.

To understand the dynamics of the system, images were taken at a range of times.

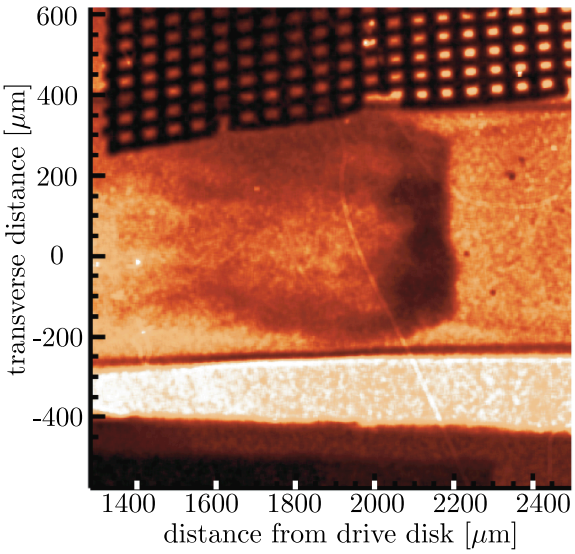

Figure 3.2: Transmission x-ray radiograph of a radiative shock in xenon gas. The shock is traveling left-to-right down the shock tube, which is partially obscured on the upper side by an opaque grid used for spatial calibration of the image. *Image credit Doss et al., [53]*

At "early time," less than approximately 10 ns after the drive pulse, the shock is moving its fastest, and is also very thin, as it has not passed through and compressed an appreciable amount of gas. A thin, fast shock will tend to produce blurred, low-contrast images. At "late-time," roughly 20 ns or more after cessation of the laser pulse, the shock has passed through much of the xenon and created a large, dense layer behind it. As it decelerates, the shock front and collapsed layer are susceptible to instabilities, the scope of which could fill a thesis [52]. These instabilities distort the planar shock front the late-time images, and also believed to account for the variation in structure between images taken at the probe time at 13 ns post-drive.

The utility of 2D imaging is apparent from Fig. 3.2. Taken at 14 ns, the shock has progressed approximately 2.2 mm down the shock tube, and the compressed layer has reached a thickness of $\approx$ 120 μm. Assuming that this layer contains all of the xenon that has passed through the shock front, and that it is homogeneous in density, the compression is then 2200 μm / 120 μm $\approx$ 18. Observations of this

dense layer is an important signature of a system that is strongly radiative. Beyond this example, detailed analysis of the shock compression has been performed based on repeated measurements, with attention paid to the asymmetric effect of shock tilt on the inferred compression [53]. The results of that analysis is consistent with compressions around 20×, which are also expected from the analysis in the following section. Gaining a better understanding of the plasma properties in this layer was the goal of the x-ray Thomson scattering measurements described in Chap. V.

3.2 Temperature and density in the shocked xenon

Estimating the parameters one would hope to measure, namely electron temperature and density, can be done largely from simple energy balance and equation of state arguments. The laser intensity delivered by the ten beams is $\sim 7 \times 10^{14}$ W/cm^2, which is in the range where the ablative acceleration analysis of §2.4 is applicable. We begin after the laser has turned off and ablative acceleration has launched the remaining mass of Be into the Xe-filled shock tube. From Eqn. 2.13d one estimates that the areal mass corresponding to 6.3 μm of Be is ablated, which can be used in the rocket equation (2.11) to find an ablation velocity of ~ 250 km/s [2].

Launched at such a high velocity, the Be piston drives a *strong shock* in the gas. In a strong shock the Mach number squared – the Mach number being simply the ratio of shock speed to the sound speed, $M = v_s/c_s$ – is much greater than unity. Anticipating our goals of performing x-ray Thomson scattering measurements of electron temperature and ionization state, it is useful to estimate these parameters here (along with density, which is a crucial parameter for any x-ray-matter interaction analysis).

[2] Observations of this experiment both early and late in time, as well as simulations of the shock breakout, suggest that the Be may not quite reach this velocity. The shock in the Xe does remain > 100 km/s for the length of the experiment (up to 26 ns), confirming an initial velocity well in excess of this [59].

In the strong shock limit, the density ratio of shocked (ρ_f) to unshocked material (ρ_0) tends to a value determined only by the adiabatic index γ:

$$\frac{\rho_f}{\rho_0} = \frac{\gamma + 1}{\gamma - 1}. \tag{3.1}$$

The specific value of γ depends on the system and the shock, and is commonly 5/3 (for a polytropic gas) or 4/3 (for a radiation-dominated plasma). From Eqn. 3.1, these values imply material compressions of 4 and 7, respectively. However, in the case of a high-Z, ionizing gas, the effective γ may be nearer to unity and the compression of Eqn. 3.1 is greater. We work here with some simple assumptions to assess the material compression and temperature independent of the specific value of γ.

Following the launch of the Be piston, the shock heats and compresses the gas, which is initially near atmospheric pressure ($\rho = 0.006$ g/cm^3 at standard temperature and pressure). Taking $v \approx 200$ km/s, the pressure in the shock heated region is then $P \sim \rho v^2 \approx 2.4$ Mbar. The ions are heated by the shock front, and their temperature can be found from an ideal gas equation of state, where A is the atomic weight of the element:

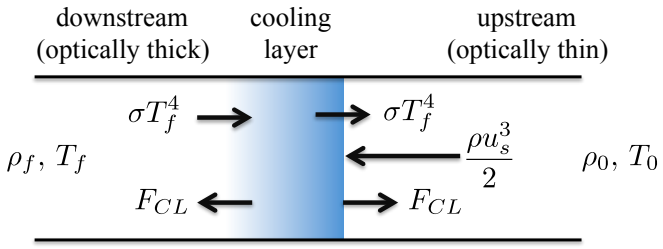

Figure 3.3: Energy flux vectors for a thick-thin system, shown in the shock frame. The final state in the downstream region is taken to be in equilibrium, which implies radiation flux balance at the rear edge of the cooling layer. Energy is provided to the shock by the incoming kinetic energy flux $\rho u_s^3/2$. (note: not to scale).

$$p = \frac{\rho k_B T(1+Z)}{A m_p} \rightarrow k_B T \approx \frac{A m_p v^2}{(1+Z)} \tag{3.2}$$

To solve Eqn. 3.2 for temperature, the degree of ionization Z is needed, and can be found via myriad models. Regardless of the model, the values of n_e and T_e are central to finding an average ionization. Here we approximate energy transfer such that that the ions share their energy with the electrons via collisions (and no energy is lost to other mechanisms, like radiation), so that $T_e = T_i/(Z+1)$. The electron density is taken to be the average value $n_e = Z n_i$, and with these two estimates one can solve the Saha equation to find [59]

$$Z = \sqrt{\frac{k_B T_e}{E_H}} \sqrt{\ln\left[\frac{1}{n_e}\frac{1}{4a_0^3}\left(\frac{k_B T_e}{\pi E_H}\right)\right]} - \frac{1}{2} \tag{3.3a}$$

$$Z = 19.7 \sqrt{\frac{T_i}{(Z+1)}\left[1 + 0.19\,\ln\left(\frac{10^{24} T_i^{3/2}}{(Z+1)^{3/2} Z n_i}\right)\right]} - \frac{1}{2}. \tag{3.3b}$$

Equation 3.3b evaluates to $Z = 10.3$, implying that the collisional transfer of energy from T_i to T_e yields $T_s \simeq 180$ eV, where we have used the subscript to indicate the approximate temperature at the shock front.

Because the upstream optical depth is long[3], the energy radiated by the shock-heated electrons serves to cool them. The temperature profile thus decreases from T_s at the shock front to a final downstream temperature T_f over a region called the *cooling region*. If the final downstream system is to be in steady state, the radiation flux in the region – including at the boundary of the final region and the cooling layer – must be zero [153]. This is depicted in Fig. 3.3, and leads to the condition $\sigma T_f^4 = F_{CL}$, where F_{CL} is the radiation flux emitted in the downstream direction from the cooling layer.

[3]See the discussion of §1.1.1.

In the approximation that the cooling layer is optically thin to the right-moving radiation flux σT_f^4, then at the upstream boundary of the cooling layer (ie. at the shock front) we have in the right-moving direction $F = \sigma T_f^4 + F_{CL} = 2\sigma T_f^4$. In the limit that all of the incoming kinetic energy goes into radiation, one then has $\rho u_s^3/2 = 2\sigma T_f^4$. For a shock speed of 150 km/s, assuming an optically thick downstream region, this equality yields a final temperature T_f of $\sim 47\ eV$. Though simplistic, this analysis provides estimates of the electron temperature one might hope to measure in an x-ray Thomson scattering experiment.

If the details of the temperature profile in the cooling layer are neglected and the total right-moving radiation flux is taken to be the product of an electron population at an effective temperature T_{eff}, then the normalized flux at the shock is

$$F_n = \frac{\sigma T_{\text{eff}}^4}{\rho_o u_s^3/2} \tag{3.4}$$

$$= \frac{2\sigma u_s^5}{\rho_0 R^4} \left(\frac{R^4 T_{\text{eff}}}{u_s^2} \right)^4 \tag{3.5}$$

$$= \frac{2\sigma u_s^5}{\rho_0 R^4} \left(\frac{R^4}{u_s^2} \frac{\rho_0 u_s^2}{\rho_f R(1+Z)} \right)^4 \tag{3.6}$$

$$= \frac{2\sigma u_s^5}{\rho_0 R^4} \left(\eta \frac{1}{(1+Z)} \right)^4 . \tag{3.7}$$

Here we have made liberal use of the ideal gas equation of state (Eqn. 3.2), and denote the inverse compression $\eta = \rho_0/\rho_f$. From Eqn. 3.7, we define the radiation strength parameter $Q = 2\sigma u_s^5/(\rho_0 R^4 (1+Z)^4)$. Upon consideration of the conservation equations for the system (analysis similar to §2.4), the value of η is found to be dependent only on Q, which we note is independent of γ. The solution for inverse compression in terms of Q is [54] :

$$\eta = \sqrt{\frac{\sqrt{1+8Q}-1}{4Q}}. \tag{3.8}$$

For values of Z and u_s discussed earlier for xenon gas, one finds shock compressions on the order of 20 - 30. These are several times higher than the compressions expected for customary values of γ from the strong shock relations (Eqn. 3.1). This dense, *radiatively collapsed* Xe layer has important implications for the x-ray transmission and scattering diagnostics used to probe the experiment.

3.3 Contributions to xenon x-ray opacity

The discussion of optical depth (recall Eqn. 1.2) and the arguments of the previous section speak of the opacity of the system at various points. Opacity, also known as the material *absorption coefficient*, is related to the fraction of radiation that is attenuated as it passes through a material. The transmission T is given by the Beer Lambert Law, $T = \exp[-\alpha_{abs}x]$, where α_{abs} is the absorption coefficient and x is the length of material traversed. Evidently the absorption coefficient has units of l^{-1}, and is the product of the *mass attenuation coefficient* – written as μ/ρ with units of area per unit mass – and the density of the material.

While it is often useful to perform calculations using the mass density, the interaction of x-rays with matter is fundamentally a quantum process. As such, the mass attenuation coefficient is equal to the per-atom cross section for scattering and absorption over the atomic mass of the element. This tour of nomenclature is relevant when one is designing an experiment with both x-ray radiography and x-ray scattering diagnostic components, as is described subsequently. The total, frequency dependent, per-atom cross section σ_{tot} for photon-matter interaction is

$$\sigma_{\text{tot}} = \sigma_{pe} + \sigma_{incoh} + \sigma_{coh} + \sigma_{pair} + \sigma_{trip} + \sigma_{ph.n.} \tag{3.9}$$

where σ_{pe} is photon absorption by the photoelectric effect and inverse bremsstrahlung processes, σ_{coh} and σ_{incoh} are coherent and incoherent scattering, σ_{pair} and σ_{trip} rep-

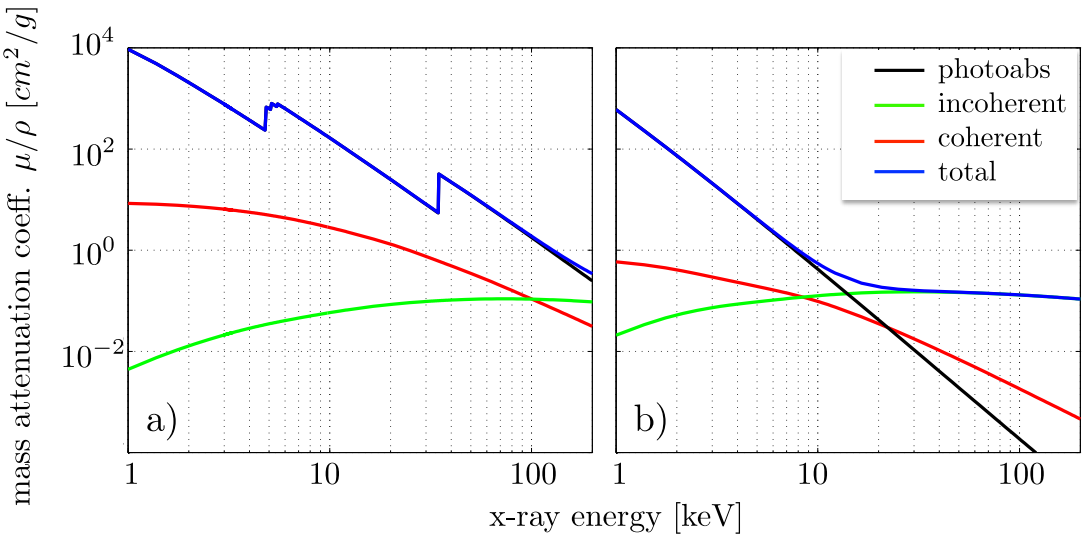

Figure 3.4: Mass attenuation coefficients for photon attenuation processes important to radiative shock diagnostics for a) xenon, and b) beryllium. Attenuation via mechanisms not plotted here are negligible for this energy range ($<$ 200 keV).

resent electron-positron pair and triplet production, and $\sigma_{ph.n.}$ is photonuclear absorption [106]. At low energies, the cross section is dominated by photoabsorption, with contributions from coherent and incoherent scattering decreased from this by several orders (Fig. 3.4). At higher energies the cross section for incoherent scattering (Compton scattering) increases, while the photoabsorption cross section drops sharply with increasing photon energy.

The abrupt jumps in attenuation coefficient (corresponding to a decrease in transmission via the Beer Lambert Law) are due to photoionization of inner shell electrons. For Xe, the L-shell binding energy is near 5 keV, and K-shell ionization at 34.5 keV. It is the L-shell absorption feature that is used to produce the high-contrast images seen in Fig. 3.2 and published in Refs. [180, 59, 53, 50, 178, 51]. These features are not seen in beryllium (Fig. 3.4(b)) because it lacks the electronic structure of xenon. Also noteworthy is the fact that at $\approx$ 20 keV, Compton scattering becomes the dominant attenuation process in Be (with similarly values for other low-Z materials). This

has enabled Compton radiography of inertial confinement fusion capsules [209], and should be exploited by any future efforts aimed at *imaging* of scattered x-ray radiation [112]. However, absorption remains the dominant process for photon energies below 200 keV in Xe. The implication for scattering experiments is that while it is beneficial to avoid peaks in absorption (like the Xe L-edge), the input signal will always be attenuated, sometimes substantially, by photoabsorption.

CHAPTER IV

X-ray Thomson scattering theory

4.1 Framing the problem at hand

Collecting the particles scattered from a system of interest to better understand the constituents of the scatterer is a proven and powerful method in the physicists toolbox. In the 1909 "gold foil experiment," Rutherford, Geiger, and Marsden bombarded a gold foil with α particles [185]. Observation of large-angle scattering of these particles led to the modern theory of an atomic nucleus of positively charged particles surrounded by electrons. A century later, scientists at the European Center for Nuclear Research (CERN) use similar principles, at orders of magnitude greater energy, when they collide protons and collect the scattered remnants to investigate the fundamental building blocks of our universe.

The gold foil experiment, high energy particle collisions, and x-ray Thomson scattering experiments are each a paragon of inverse problems. In a general sense, inverse problems arise in any system where one desires to infer the parameters of that system based on observations. They involve the formulation of two problems, denoted as the *forward* or *primary* problem, and its complement, the *inverse* problem. These are related by the fact that a complete formulation of one involves finding a solution to the other [64]. Examples abound in physics, and include tomography, medical and other non-invasive imaging, geophysical location of seismic activity, and scattering

experiments of all types.

Here I present the investigation of a system with x-ray Thomson scattering (XRTS) in the qualitative framework of inverse problem theory[1]. Clearly the accuracy of the inferred plasma parameters is a function not only of the resolution of the measurements, but also of the accuracy of the inverse model. The focus of this chapter is to introduce the methods used to map a measured spectrum back to physical parameters like temperature, density, and ionization level. Attention is paid to the approximations inherent in each of the models, as these serve to define the regimes of validity for different manifestations of the inverse problem. This framework is useful in the discussion that follows, where aspects of the analysis can be understood as belonging to one or more of the following three steps of scientific measurement. Broadly, these are [202] :

1. *Parameterization*: A system must be divided into a set of *model parameters*. For a given physical process, these parameters should completely characterize the system.

2. *Forward modeling*: The model parameters must be related to the system via a set of *physical laws*. Given the model parameters and the physical laws, one is able to predict the outcome of measurements to a degree of accuracy dependent on the input parameters and the completeness of the model.

3. *Inverse modeling*: Solving the *inverse problem* involves using the observations of a system to determine the model parameters. Data collected to do this are called *observable parameters*.

[1]Generally, Thomson scattering is the elastic wave-particle interaction wherein a charged particle oscillates in an applied electromagnetic field, and in doing so accelerates and remits radiation. The corresponding quantum mechanical description of Thomson scattering, where a photon bounces off a charged particle, is elastic given $\hbar\omega \ll mc^2$. When this is not the case and the probe photon has non-negligible energy relative to the scattering particle, the inelastic scattering process is called Compton scattering. Compton scattering plays an essential role in the process, though the diagnostic is generally refered to as "Thompson scattering."

These steps are clearly related, and a satisfying scientific theory cannot be formulated without progress on all three. Here, we are motivated by the desire to understand radiative shocks for reasons described in the introductory section 1.1.1. By "understand," one would like to know the macroscopic properties of the system, namely parameters such as pressure, temperature, density, and shock speed the (*model parameters*). These variables are related through the fluid equations of Chapter III, which constitute the laws of the forward problem. Given a subset of the model parameters as inputs, one can use the fluid equations to calculate other values (ie. these equations constitute the *forward model*). Alternatively, given a complete set of model parameters, the future state of the system can be predicted.

To improve the accuracy of the forward model, experiments are done on the system. Some experiments require the solution of only a simple inverse problem; using near-coincident imaging to measure the instantaneous shock velocity is an example of this. In this case, the relation between position and velocity, $x(t) = x_0 + v_s t$, constitutes the forward model and two pairs of position vs. time measurements are the observables. The model and observables allow the calculation of v_s. The errors inherent in a simple inverse problem of this type are generally well expressed by the familiar mean squared error. More complex inverse problems require careful consideration of the inputs. Inferring the density of the shocked xenon from radiographs is an example of this. In this case the observable is a map of photon density on a piece of film. To make an estimate of the gas density one must have (at least) an estimate of the source x-ray spectrum, a model of the x-ray transmission through the target, and a model of the film response function. One is referred to Ref. [50] for the description of a forward model for inferring density from x-ray radiographs that incorporates aspects of the problem beyond these limited inputs.

4.2 Plasma coupling

One of the primary ways that plasmas can be categorized is by the degree of interparticle interaction. Intuitively, at low temperatures and high densities, Coulomb effects between particles will influence their collective behavior. This is known as *plasma coupling* and the *plasma coupling parameter* Γ quantifies this effect. For coupling between ions, this is given by:

$$\Gamma_{ii} = \frac{Z^2 e^2}{d_i T_i}, \tag{4.1a}$$

$$d_i = \left(\frac{4\pi n_i}{3}\right)^{-1/3}, \tag{4.1b}$$

and similarly for electrons by

$$\Gamma_{ee} = \frac{e^2}{d_e T_e}, \tag{4.2a}$$

$$d_e = \left(\frac{4\pi n_e}{3}\right)^{-1/3}. \tag{4.2b}$$

The coupling constant is the ratio of the potential energy to kinetic energy between particles of a given species. The potential is given by $Z^2 e^2/d_k$, where $Z = 1$ for electrons and d_k is the particle spacing, with $k = e$ or i for electrons or ions. In either case the kinetic energy goes like T_k. In an ideal plasma the ions are uncorrelated and $\Gamma \ll 1$. At the opposing extreme, when $\Gamma \gg 1$, the motion of one particle is conferred to neighboring particles via their electrostatic repulsion. For very dense and cold plasmas, the total energy of the system is minimized by the ions assuming a lattice structure. This is predicted to occur at $\Gamma \geq 172$ ($T = 100$ eV, $n_i = 4 \times 10^{32}$ cm^{-3}) for an ionized hydrogen plasma [114]; this is approximately 10 orders of magnitude higher in density than the gas in the present experiments.

A second important metric in the classification of plasmas is the *degeneracy parameter*. Because electrons are fermions they are governed by Fermi-Dirac statistics and obey the Pauli exclusion principle. As $T_e \to 0$, electrons successively fill the lowest unoccupied energy state. The highest occupied energy at $T = 0$ is the *Fermi energy* and is given by

$$\epsilon_F = \frac{\hbar^2}{2m_e}(3\pi^2 n_e)^{2/3}. \tag{4.3}$$

The degeneracy parameter Θ is simply the ratio of the thermal kinetic energy of the electrons to the Fermi energy:

$$\Theta = \frac{k_B T_e}{\epsilon_F}. \tag{4.4}$$

In ideal plasmas ($\Gamma \ll 1$) the electron density is low enough and/or temperature high enough that the kinetic energy is greater than the Fermi energy and $\Theta \gg 1$. Such a system is said to be "classical," as quantum effects are negligible in describing the electrons.

Contours of constant plasma coupling parameter Γ_{ee} are shown in Fig. 4.1. Also plotted are the lines of $\Theta = 1$ and $d_e = \lambda_D$. As discussed in the following sections, the Debye length and the related Debye-Hückel potential represent the limiting behavior of a weakly coupled system. Finally, Fig. 4.1 also shows regions of parameter space accessed by recent experiments where XRTS was a primary diagnostic.

4.3 Structure in a plasma

The response of a system to a small perturbation requires knowledge of the spatial and temporal structure of the system. Here we establish first the spatial component, given by the static structure factor $S(\mathbf{k})$, followed by the frequency dependance cap-

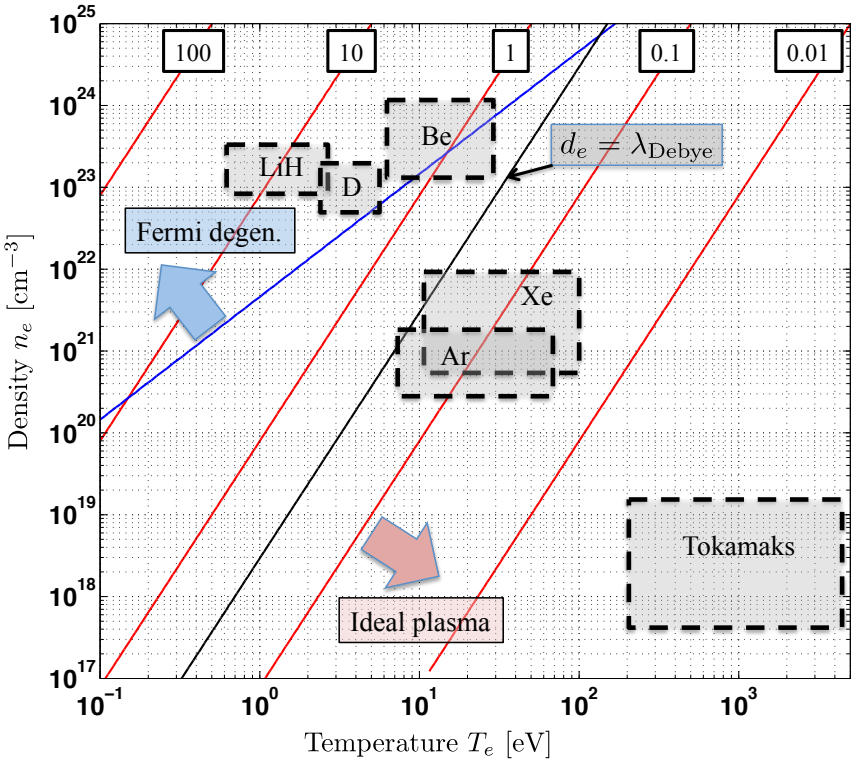

Figure 4.1: Electron temperature-density parameter space, with several important values for XRTS shown. Contours of the coupling parameter Γ_{ee} are shown in red. Fermi degenerate plasmas exist in the upper-left region, above $\Theta = 1$ (blue line). The region of ideal plasmas is indicated where $\Gamma_{ee} \ll 1$, which also corresponds to an inter-electron spacing $d_e > \lambda_{\mathrm{Debye}}$ (where λ_{Debye} is given later by Eqn. 4.11b). Also shown are approximate parameter ranges of several experiments where XRTS has been used. The Xe radiative shock tube experiments discussed in Chapter III are similar to the argon work of Visco *et al.* [213]. Most experiments have been performed in the warm dense matter regime; shown are the compressed Be experiments by Lee *et al.* 2009 [141], and the compressed lithium hydride experiments of Kritcher *et al.* [128].

tured by the dynamic structure factor $S(\mathbf{k}, \omega)$. This is developed from the poorly-named theory of *classical simple liquids* [212, 102], which assumes a total of N point-like particles of mass m, momentum p, and position $\mathbf{r}$, governed by a Hamiltonian of the form

$$\mathcal{H} = \sum_{i=1}^{N} \frac{p_i^2}{2m} + V(\mathbf{r}^N), \tag{4.5}$$

where $V(\mathbf{r}^N)$ is the interatomic potential energy. Using n for the average particle density and explicitly writing $n^(k)(\mathbf{r})$ for the position-dependent local density between k particles, we have the probability of finding those k particles in the fractional volume $d\mathbf{r}^k = \prod_{i=1}^{k} d\mathbf{r}_i$ given by the density distribution:

$$n^{(k)}(\mathbf{r}^k) = \frac{N!}{(N-k)!} \frac{\int \cdots \int exp(-\beta V(\mathbf{r}^N)) d\mathbf{r}^{N-k}}{Z_N(T,V)}. \tag{4.6}$$

Here $\beta = 1/kT$ is the Boltzmann constant and $Z_N(T,V)$ is the configuration integral:

$$Z_N(T,V) = \int \cdots \int d\mathbf{r}^N exp(-\beta V(\mathbf{r}^N)). \tag{4.7}$$

Equation 4.6 is normalized such that the number of ways to find one ($k = 1$), two ($k = 2$), or k particles is

$$\int n^{(1)}(\mathbf{r}^1) d\mathbf{r}^1 = N, \tag{4.8a}$$

$$\int \int n^{(2)}(\mathbf{r}^2) d\mathbf{r}^2 = N(N-1), \text{ or} \tag{4.8b}$$

$$\int \cdots \int n^{(k)}(\mathbf{r}^k) d\mathbf{r}^k = \frac{N!}{(N-k)!}. \tag{4.8c}$$

The second of these, Eqn. 4.8b, gives the total number of pairs of particles in the entire volume. The arrangement of these particles is described by the *pair distribution function*. This function describes the likelihood of finding nearby particles at a

specific location, relative to the particle of interest. Pair distribution functions can be developed for both ion-ion and ion-electron pairs, where the former predicts the structure of the material as a whole (isotropic vs. lattice-like) and the latter is a measure the polarization of the electrons around an ion. For isotropic fluids the pair distribution function depends only on the interparticle spacing $r = |\mathbf{r}_1 - \mathbf{r}_2|$, and in this case is referred to as the *radial distribution function* [102]. This is denoted by $g_\alpha(r)$, where $\alpha = i$ or e for ions or electrons, and has has the general form

$$g_\alpha(r) = \frac{n_\alpha^{(2)}(r)}{n_\alpha^2}, \tag{4.9}$$

where n_α is the average species density. For an ion at the origin one would expect $n_i(\mathbf{r}) \to 0$ for $r \to 0$, reflecting repulsion of ions at close range. For weakly coupled plasmas the value of $g_i(\mathbf{r})$ increases monotonically to unity. For strongly coupled plasmas the energy of the system is minimized when ions occupy specific regions relative to one another. This gives the plasma structure, and can be seen in Fig. 4.2 for several values of the coupling parameter Γ.

The *pair correlation function* is simply the deviation of the radial distribution function from the ideal plasma limit, given by $h(r) = g(r) - 1$. One can take the Fourier transform of $h(r)$ to find the static structure factor [114]:

$$S(k) = 1 + n \int d^3r \; [g(r) - 1] e^{-i\mathbf{kr}}. \tag{4.10}$$

The static structure factor quantifies the density response (ie. scattering) of a system as a result of a small perturbation of wavelength $\mathbf{k}$. For a given system, the spatial distribution of particles $n(r)$ can be calculated via Monte-Carlo or molecular dynamics simulations, from which $h(r)$ can then be computed. This is commonly done in the one-component plasma (OCP) approximation, where calculation of the electron radial distribution function (Eqn. 4.9) is neglected and the electrons are taken to

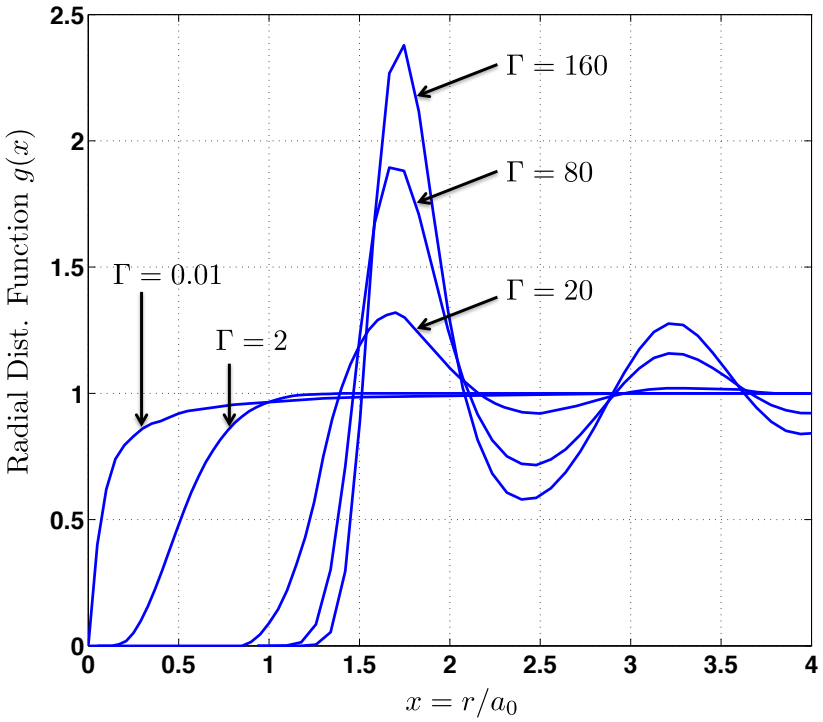

Figure 4.2: Radial distribution functions, $g(r)$, for several values of the coupling parameter Γ. Weakly coupled plasmas exhibit a dip in $g(r)$ at the origin and trend to unity with increased distance. The ions in strongly coupled plasmas have clear preferential positions relative to each other, and are predicted to settle into a lattice for $\Gamma \geq 172$. Data for this plot from Monte Carlo simulations by: ($\Gamma = 0.01, 2$) Brush, Sahlin, and Teller (1966) [24], ($\Gamma = 20$) Hansen (1973) [101], and ($\Gamma = 80, 160$) Slattery, Doolen, and DeWitt (1980) [194].

be a mobile, uniform, neutralizing background ($n_e(\mathbf{r}) = n_e$). In the limit of weakly coupled plasmas ($\Gamma_{ii} \ll 1$), the potential between particles is given by the *Debye-Huckel potential*

$$V(r) = \frac{Ze}{r} e^{-r/\lambda_D} \tag{4.11a}$$

$$\lambda_D = \sqrt{\frac{kT}{4\pi n Z e^2}}. \tag{4.11b}$$

The *Debye length* λ_D is the characteristic screening length for weakly coupled plasmas, and in this limit the static structure factor has the form

$$S(k) = \frac{k^2}{k^2 + k_D^2}, \tag{4.12}$$

where $k_D^2 = 4\pi n_e e^2/kT$ is the Debye wave number. Equation 4.12 serves as the starting point for more detailed calculations of the static structure factor used in scattering experiments, details of which are presented in Gregori *et al.* (2003) [96].

To understand the scattering of photons from a plasma, the static structure factor must be extended to the frequency domain. This is done in a manner similar to the development of the static structure factor. Noting that the density distribution function $n^{(k)}$ for an isotropic fluid can be recast from Eqn. 4.6 using delta functions as

$$n^{(1)}(r) = \left\langle \sum_{i=1}^{N} \delta(r_i) \right\rangle \text{and,} \tag{4.13a}$$

$$n^{(2)}(r_1, r_2) = \left\langle \sum_{i=1}^{N} \sum_{j=1, j\neq i}^{N} \delta(r - r_i + r_j) \right\rangle, \tag{4.13b}$$

the pair distribution function can then be expressed as [219]

$$g(r_1, r_2) = \frac{1}{n^2} \left\langle \sum_{i=1}^{N} \sum_{j=1, j\neq i}^{N} \delta(r - r_i + r_j) \right\rangle . \tag{4.14}$$

In Eqns. 4.13a - 4.14 brackets indicate an average over the canonical ensemble. The time-dependent version of this is the *van Hove equation* [211, 102], given by

$$G(r, t) = \frac{1}{N} \left\langle \sum_{i=1}^{N} \sum_{j=1, j\neq i}^{N} \delta(r - r_i(t) + r_j(0)) \right\rangle . \tag{4.15}$$

The dynamic structure factor is then the space-time Fourier transform of this,

$$S(k, \omega) = \frac{1}{2\pi} \int \int G(r, t) exp(-i(kr - \omega t)) dr dt. \tag{4.16}$$

In a scattering experiment, the dynamic structure factor describes the response of the plasma as a function of k and ω. It can be cast in a number of forms depending on the probe (x-rays, optical photons, electrons, neutrons, etc), and various plasma approximations, often relating directly to the degree of coupling (through $g(r)$, see Fig. 4.2) in a system of interest.

4.4 X-ray Thomson scattering

Using electromagnetic radiation to probe a plasma is an attractive diagnostic technique because it is minimally perturbing to the system, can be used to probe a wide range of plasma densities and temperatures, and has the potential to directly measure the electron distribution function of a system [113]. Thomson scattering proved to be a powerful diagnostic less than a decade after the invention of the laser when Peacock *et al.*, in collaboration with Russian physicists, used it to probe the confined plasma in the T3 Tokamak [170]. The method has since been extended

significantly, with x-ray Thomson scattering joining laser scattering as a method to probe dense plasmas.

Thomson scattering is used to probe plasma experiments in two fundamentally different regimes: collective and non-collective (sometimes referred to as coherent and incoherent) scattering. In collective scattering, incident photons couple to and scatter from electron-plasma and ion-acoustic waves. Conversely, non-collective scattering probes the plasma at smaller length scales, bypassing the collective fluctuations and instead interacting with the individual particles in the system. The collective versus non-collective regimes are quantified by the scattering parameter α:

$$\alpha = \frac{\lambda}{2\pi\lambda_S}. \tag{4.17}$$

In this equation, λ is the probe wavelength, and is computed in terms of the x-ray wavelength λ_0 and the scattering direction θ as $\lambda = \lambda_0/(2\sin(\theta/2)$ [140]. This is compared to the plasma scale length λ_S of the system under investigation. The scale length of the plasma is quantified by the usual Debye length in weakly coupled plasmas, but must be refined for strongly coupled plasmas. In the latter case, λ_S is given by the Thomas-Fermi screening length [89]:

$$\lambda_{TF} = \sqrt{\frac{\hbar^2}{4m_e e^2}\left(\frac{\pi}{3n_e}\right)^{1/3}}. \tag{4.18}$$

When $\alpha \ll 1$, the incident light probes the individual (non-collective) electron thermal motion, as opposed to the bulk (collective) plasma motion when α is greater than one.

In the non-collective regime, x-ray Thomson scattering (XRTS) can be thought of as collisions between photons and the particles in the plasma. Each particle has a cross section for scattering, and each collision must conserve energy and momentum. Assuming they are not promoted to a higher energy level or liberated from the atom

(*bound-free*), electrons which are bound to an ion respond elastically in a collision, resulting in a scattered photon with the same energy as before the interaction. Free electrons, however, will recoil and take some energy from the photon, which results in a red-shifted scattered wave.

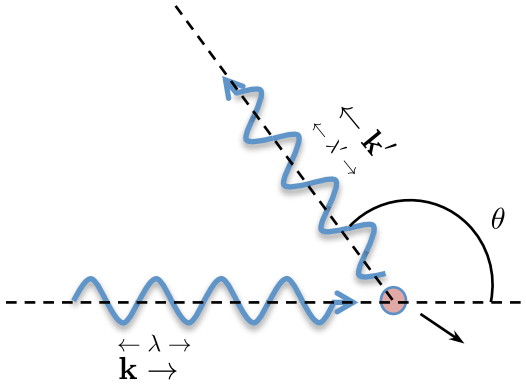

Figure 4.3: A photon with initial wavelength λ scatters from an electron at scattering angle θ. The scattered wavelength λ' is longer than λ, as energy has been transferred to the electron in the collision.

For a free electron initially at rest with energy $m_e c^2$ and a photon with energy $h\nu$, energy conservation requires that

$$h\nu + m_e c^2 = h\nu' + \sqrt{p^2 c^2 + m_e^2 c^4}, \tag{4.19}$$

where p is the electron momentum after the collision. Conserving momentum gives

$$\mathbf{q} = \mathbf{p} + \mathbf{q}', \tag{4.20}$$

where $q = h\nu/c$ for the photon. Solving 4.20 for the square of the electron momentum p^2 introduces the cosine of the angle θ between the incoming and outgoing photon via the cross term:

$$p^2 = \left(\frac{h\nu}{c}\right)^2 + \left(\frac{h\nu'}{c}\right)^2 - 2\left(\frac{h\nu}{c}\right)\left(\frac{h\nu'}{c}\right)\cos\,\theta. \tag{4.21}$$

The energy equation (Eqn. 4.19) can also be expressed in terms of the electron momentum

$$p^2 + m_e^2 c^2 = \left(\frac{h\nu}{c} - \frac{h\nu'}{c} + m_e c \right)^2, \tag{4.22}$$

$$p^2 = \left(\frac{h\nu}{c} \right)^2 + \left(\frac{h\nu'}{c} \right)^2 - 2 \left(\frac{h\nu}{c} \right) \left(\frac{h\nu'}{c} \right) + 2m_e h(\nu - \nu') + m_e^2 c^2. \tag{4.23}$$

Together, Eqn. 4.21 and 4.23 yield the Compton formula, which expresses the shift in energy (or wavelength, as $\nu = c/\lambda$) in terms of the photon deflection angle θ:

$$2 \left(\frac{h\nu}{c} \right) \left(\frac{h\nu'}{c} \right) (1 - \cos\,\theta) = 2m_e hc \left(\frac{\nu}{c} - \frac{\nu'}{c} \right) \tag{4.24}$$

$$\lambda' - \lambda = \frac{h}{m_e c} (1 - \cos\,\theta)\,. \tag{4.25}$$

This shift in the scattered photon energy is a signature of a free electron population in XRTS data. In any real system the electrons are not stationary, but have a distribution of velocities. In the scattering process, this electron motion Doppler shifts the scattered photon and adds a term proportional to the inner product of the x-ray and electron wave vectors to the solution for the shifted photon. Expressing Eqn. 4.25 in terms of energy shift ΔE via $\mathrm{E} = hc/\lambda$ and wavevector $k = (2E_o/\hbar c)\sin(\theta/2)$ gives

$$\Delta E = \frac{\hbar^2 k^2}{2m_e} \pm \hbar \mathbf{k} \cdot \mathbf{v}. \tag{4.26}$$

The Compton-shifted photon signal from free electrons is a fundamental observable and can be understood from first principles. As such, it is a powerful diagnostic for the electron distribution function. However, Eqn. 4.26 is appropriate only for an isolated free electron. As developed in the previous section, the total scattered signal is given by the dynamic structure factor. For a multi-species plasma, $S(k, \omega)$ is a

convolution of numerous sources which contribute to varying degrees depending on the plasma conditions.

A model for the total scattering from a plasma which separates contributions from free electrons and bound electrons, as well as separating the motion of electrons and ions, has been developed by Chihara [37, 38]. The result is the dynamic structure factor $S(\omega, k)$:

$$\begin{aligned} S(\omega,k) = |f_I(k) + q(k)|^2 S_{ii}(k,\omega) + Z_f S^o_{ee}(k,\omega) \\ + Z_c \int S_c e(k, \omega - \omega') S_s(k,\omega') d\omega'. \end{aligned} \tag{4.27}$$

In this form, the contribution from free electrons which scatter inelastically (proportional to Z_f) is given by the second term. The function S^0_{ee} is the electron-electron correlation function, and describes the motion of the electrons relative to one another. The third term is proportional to Z_c, the number of core electrons, and describes inelastic scattering by electrons undergoing Raman transitions to the continuum. Finally, the first term represents scattering from electrons that follow the ion motion, which is given by S_{ii}. This includes bound electrons described by the ion form factor $f_I(k)$, as well as weakly bound electrons within the ion sphere. These "free" electrons are given by $q(k)$, and also follow the ion motion but may scatter inelastically [93].

The designation of "free" electrons with respect to Eqn. 4.27 requires further description. In the process of x-ray scattering, an electron is *kinematically* free if it experiences a (negative) Coulomb potential with magnitude that is less than the energy of the Compton shift given by Eqn 4.26 [93]. These weakly bound valence electrons contribute to the scattering in the same manner as free electrons, but are not free in the usual sense that they are not associated with any ion. For an isolated atom in the hydrogenic approximation, the binding energy of an atom in quantum level n is given roughly by $E_n = Z_A^2 E_H / n^2$, where $E_H = 13.6$ eV is the binding energy of hydrogen and Z_A is the nuclear charge of the atom of interest. However, the many-

particle interactions in a plasma distort this simple analysis and the descriptions of atomic models in Chap. II are relevant here. In this document Z_f indicates kinematically free electrons (electrons which scatter inelastically), Z refers to the actual (average) charge state, and Z_A refers to the total nuclear charge of an atom.

4.5 Measurements from x-ray Thomson scattering

Analysis of the scattered x-ray spectrum has the potential to yield information on the plasma temperature T_e, the electron density n_e, and the number of electrons which are kinematically free Z_f. The forward model governing the measurement of T_e is the simplest, as was shown in Eqn. 4.19 - 4.26. In particular, for a monoenergetic source $E = hc/\lambda$, Eqn. 4.25 gives exactly the scattered wavelength, with the second term in Eqn. 4.26 fully capturing the dependence of the inelastic peak on the electron distribution function. Indeed, in analysis of some experiments the elastic peak is subtracted and analysis of the scattered signal is reduced to a calculation of $\mathbf{v}$ or, equivalently, the average temperature T_e [213].

Inference of the electron density from a scattered spectrum can be made in two ways. First, the total scattered power into a solid angle $d\Omega d\omega$ is given by

$$P_S(\mathbf{R},\omega)d\Omega d\omega = \frac{P_o r_0^2 d\Omega}{4\pi A} N S(\mathbf{k},\omega) d\omega \times (1+\cos^2\theta). \tag{4.28}$$

Here P_0 is the incident power, A is the area being probed, r_0^2 is the classical electron radius, N is the total number of scatterers (electrons), and the factor $1/2(1+\cos^2\theta)$ is valid for unpolarized light. In principle, from Eqn 4.28 one could solve for N if the other values of the equation were well known. However, beyond the model-dependent approximations incorporated in $S(\mathbf{k},\omega)$, one would need one or more detectors capable of accurately measuring P_S and P_0, including understanding the frequency-dependent detector quantum efficiency. These experimental challenges, compounded with errors

associated with measurement of the solid angles and the area A, make this inverse problem very difficult and it has yet to be attempted in HED XRTS experiments.

A method to determine the electron density which has proven more fruitful is via analysis of the density dependence on the "effective temperature". When a system transitions from an ideal plasma to the warm dense matter (WDM) regime, the system can no longer be considered classical (quantified by $\Theta \leq 1$). We repeat here the Fermi energy, noting the dependance on the parameter of interest, n_e:

$$\epsilon_F = \frac{\hbar^2}{2m} \left(3n_e\pi^2\right)^{(2/3)}. \tag{4.29}$$

In a degenerate electron system the thermal temperature T_e is comparable to T_F (given $T_F = \epsilon_F/k_B$), and T_e alone does not fully characterize the particle motion. In XRTS experiments, this is accounted for by following the work of Perrot and Dharma-wardana [171], who describe the fluid by an effective temperature $T_{cf} \simeq (T_e^2 + T_q^2)^{1/2}$ (the subscripts here indicate "Coulomb fluid," "electron (thermal)," and "quantum," respectively). The form of T_q was found to be $T_q = T_F/(1.3251 - 0.1779\sqrt{r_s})$, where $r_s = d/a_o$, $d = (3/4\pi n_e)^{1/3}$, and a_o is the Bohr radius. This fitting was shown to reproduce the Monte-Carlo predications of the pair distributions ($g(r)$) of the $T_e = 0$ quantum fluid, while having the correct asymptotic behavior for small Θ. Through T_q, which is proportional to T_F and thus (from Eqn. 4.29) $n_e^{2/3}$, the electron density affects the width of the Compton peak. For experiments with $\Theta \geq 1$, the electron density has been measured in this way [129, 128].

In addition to measurements of temperature and density, the potential to use XRTS as a diagnostic for ionization of a material was described by Landen *et al.* [140]. This measurement is made by comparing the intensities of the elastic and inelastic peaks of the scattered spectrum, as the inelastic peak is produced by scattering from Z_f electrons, while the elastic peak is from $Z_A - Z_f = Z_c$ core electrons. The intensity

of the electron feature from Eqn. 4.27 is given by [93]

$$I_e(k) = Z_f \int_0^\infty S^0_{ee}(k,\omega) \left[1 + \exp\left(\frac{-\hbar\omega}{T}\right)\right] \, d\omega = Z_f S^0_{ee}(k), \tag{4.30}$$

while the ion feature intensity is

$$I_i(k) = |f_I(k) + q(k)|^2 S_{ii}(k,\omega). \tag{4.31}$$

Following Ref. [37], the free electron density correlation function $S^0_{ee}(k)$ is related to the electron structure factor by

$$S^0_{ee}(k) = S_{ee}(k) - \frac{|q(k)|^2}{Z_f} S_{ii}(k). \tag{4.32}$$

In the case of $\alpha \ll 1$ and $\Gamma \ll 1$ (*ie* the non-collective scattering regime in a weakly coupled plasma) then $q(k) \ll 1$ and $S^0_{ee}(k) = S_{ee}(k) = S_{ii}(k) \approx 1$. The ratio of inelastic to elastic scattering is then [140]

$$\frac{I_{inel.}(k)}{I_{el.}(k)} \approx \frac{Z_f}{|f_I(k)|^2} \geq \frac{Z_f}{Z_c^2}. \tag{4.33}$$

In the Xe radiative shock experiment, $\alpha = .02$ and $\Gamma_{ee} \approx .08$, so Eqn. 4.33 is valid and the ratio of the inelastic scattered intensity over elastic will tend to Z_f/Z_c^2. In principle, but comparing elastically and inelastically scattered signals one can make an estimate of $Z_f : Z_c$. However, the Doppler broadening through the electron temperature, as well as blurring of the collected spectrum from the instrument response function, make determination of the free electron function more challenging than it may appear from Eqn. 4.33.

CHAPTER V

X-ray Thomson scattering experiments

5.1 Experimental overview

The radiatively-collapsed Xe shock system consists of three distinct regions: the upstream, unshocked gas, the radiatively-collapsed dense Xe layer, and the downstream region of entrained xenon and beryllium. The goal of the radiative shock x-ray Thomson scattering campaign was to measure the plasma conditions (electron temperature, density, degree of ionization, and possibly the detection of ions other than xenon in the entrained flow) in each of the these regions. Ideally the data would be of sufficient resolution to discern the scattered signal from each of the regions, and would complement the numerous previous x-ray radiography observations. Additionally, the ability to analyze the data from the regions individually builds on XRTS work by Visco *et al.*, who measured spatially integrated scattering spectra from radiative shocks in argon gas [213]. In that work, the same disk-tube system was filled with Ar, and data was collected at two different times. For each time, 1D radiative hydrodynamic simulations were used to estimate the plasma temperature and density profile in the scattering volume. These profiles were convolved to produce a weighted "effective electron temperature T_{eff}," and the data was seen to agree well with the simulated T_{eff}. However the error bars associated this complex average over plasma conditions are large, and it was a further goal of the work described here to reduce

these errors.

Collecting scattered x-ray signal from the radiatively-collapsed dense Xe layer, which has an axial extent of $\approx 150\mu m$, requires spatial "resolution" of this same order in the collected spectrum. This requirement is complicated by an inherent shot-to-shot variation in the shock speed of approximately 5% [53]. This uncertainty is the result of several factors, including variations in laser energy, Be disk thickness, and gas pressure, among others. Thus, at the chosen time point of the experiment –13 ns after the drive laser – the shock front has progressed nearly 2 mm $\pm 100\mu$m. As this is also approximately the spatial extent of the dense Xe layer, knowing what region of the shock was passing through the scattering volume at the time of the Thomson scattering probe was an important consideration when designing these experiments. Different approaches to solving this problem were taken in each of the experiments, and are detailed in their respective sections.

An additional consideration in the design of the XRTS experiments was the need to probe the experiment at 13 ns after the drive. At times much earlier than this the amount of Xe compressed behind the shock front is less, giving less material to scatter from. The shock is also moving faster earlier in time, and both of these factors make accurately probing a precise region of the system difficult. Finally, the majority of radiographic data from previous experiments was taking at 13 ns post-drive, further motivating probing at this time. However, the ability to efficiently utilize the 60 beams available at OMEGA is difficult for delays of this length. At the time of this writing, this restriction is based on the following:

- The thin Be drive disk must be irradiated with a uniform intensity. Failure to do this would imprint laser "hot-spots" on the 20 μm-thick disk, seed Rayleigh-Taylor growth, and add unwanted structure to the Be ablator as it is driven into the Xe gas [195, 175].

- The smoothest possible beam at OMEGA is produced through a process called

"smoothing by spectral dispersion" (SSD) [177]. SSD improves the uniformity by oscillating the speckle pattern in the laser profile, thereby time-averaging the non-uniformity [1].

- The electro-optic phase modulation that produces the smoothed pulse is done before prior to beam amplification, at the level of the beam *drivers*. The drivers produce the shaped pulses that go on to be amplified and delivered to the target. One of the three drivers is devoted to the SSD system, and produces seed pulses for two *legs* of beams. Each leg is made up of a specific set of 20 beams; ie. the 60 beams are divided into three legs.

- To achieve the necessary 13 ns delay the SSD driver must be offset from another driver, in this case the *backlighter driver*. As such, there will be 40 beams available to irradiate the Be disk and 20 available for all diagnostic probes at 13 ns.

The nominal Xe radiative shock experiment is driven with 10 beams. In the design for each shot day one must find these ten beams, within the constraints of the diagnostics and x-ray sources. In practice, this becomes an effort to maximize the number of the 20 backlighter beams which can be brought to bear on the x-ray source foils, to maximize probe signal. It is an ongoing effort of the Laboratory for Laser Energetics and the Omega Laser User Group to modify the driver hardware to permit SSD to be run on only one leg, allowing the remaining 40 beams to be dedicated to probing at a delay. Such a capability would permit more energy and much greater flexibility in planning experiments where low probe signal, like XRTS, is a primary concern.

The three experiments in the following sections were carried out in the the spring months of 2010, 2011, and 2012, respectively. Each target shared the same fundamental Be disk and Xe shock tube described in Chap. III, and the goal of each was

the same, namely collecting XRTS spectra from the individual regions of the shock system. However, each experiment was unique and designed to leverage XRTS diagnostics that improved year-to-year. This work is presented chronologically, with data and conclusions following each experimental description.

5.2 2010 Campaign

5.2.1 2010 Experimental design and diagnostics

The primary diagnostic for the 2010 XRTS experiments was the Zinc Spectrometer (ZSPEC), designed and maintained by Lawrence Livermore National Laboratory. The diagnostic relies on a Highly-Ordered Pyrolytic Graphite (HOPG) crystal to disperse x-rays onto a detector consisting of a microchannel plate (MCP) coupled to a CCD camera. The energy resolution of the instrument is determined by the properties of the crystal, while a coarse ability to perform time gating is provided by the strips of the MCP. The spectrographic properties of the diagnostic can be modified by changing the crystal; at the time of the 2010 experiments a flat, high-mosaicity HOPG crystal was available. A rendering of the diagnostic is shown in Fig. 5.1.

Owing to the small cross section for Thomson scattering, photometric estimates motivated the incorporation of two zinc x-ray source foils, to increase the source photon count. The placement of the sources relative to the vector to the spectrometer defines the Compton angle, as given by Eqn. (4.25). Increasing the scattering angle increases the separation between elastic and inelastic (λ and λ') peaks on the detector and facilitates analysis, so effort was made to maximize this angle. To minimize the number of separate $\mathbf{k}$ vectors in the scattered signal, the two sources were positioned at equal angles to the scattering volume and spectrometer. A scattering angle for both sources of $\approx 130^\circ$ was achieved by affixing the source foil to precisely aligned gold "wings," which also served to shield the spectrometer from the zinc plumes.

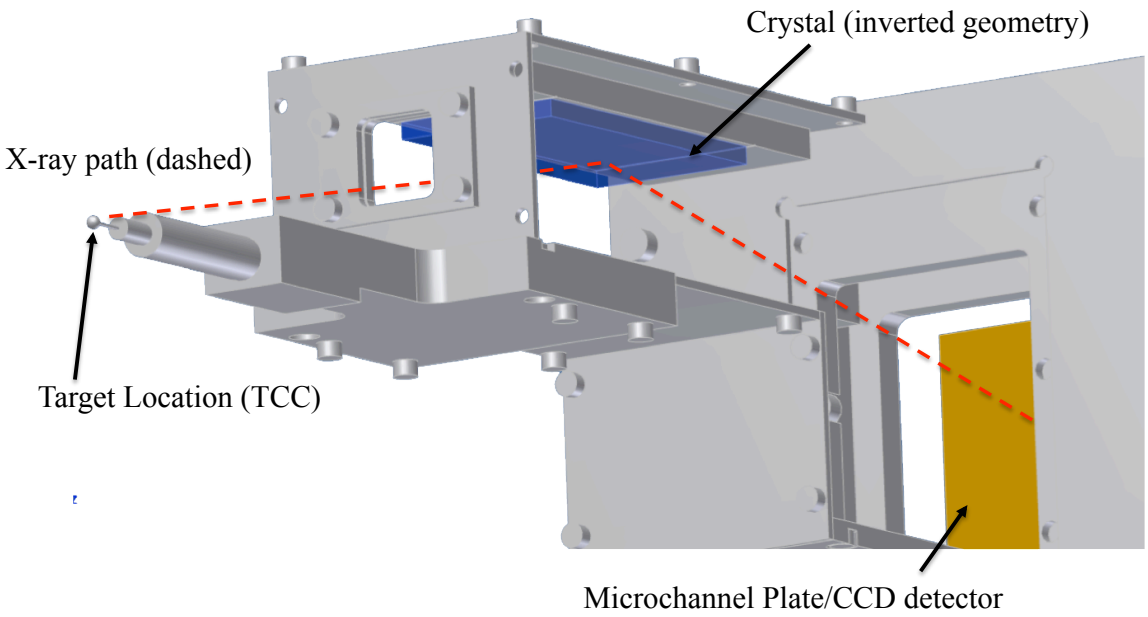

Figure 5.1: Rendering of the ZSPEC diagnostic in the "inverted" geometry. Much of the housing has been hidden to show the position of the crystal and detector. An example of the path of a scattered photon is depicted by the dashed ray.

These shields are clear in the annotated target diagram (Fig. 5.2).

The pair of zinc source foils needed to be shielded from the spectrometer, and were located behind 50 μm of gold. The two source foils were illuminated with 4 and 5 beams respectively, with the normal vector of the source foil offset at an oblique angle of $\approx 70^\circ$ to the shock tube. The spectrum from the laser-irradiated face of a source foil includes emission from cooler, low-density plasma. These plasma conditions exist in the regions that have expanded laterally, out of the field of the laser, as well as in the cooling, rarefied plasma after the laser pulse has turned off [110]. The ionization is lower in these regions and the emission lines peak at lower energies than the primary He_α peaks, which complicates analysis of XRTS data. However, this configuration was chosen for this initial experiment based on concerns about photometrics.

As described previously, data from a flat-crystal spectrometer provides no indication of the shock position, i.e. what region of the shock was interrogated by the

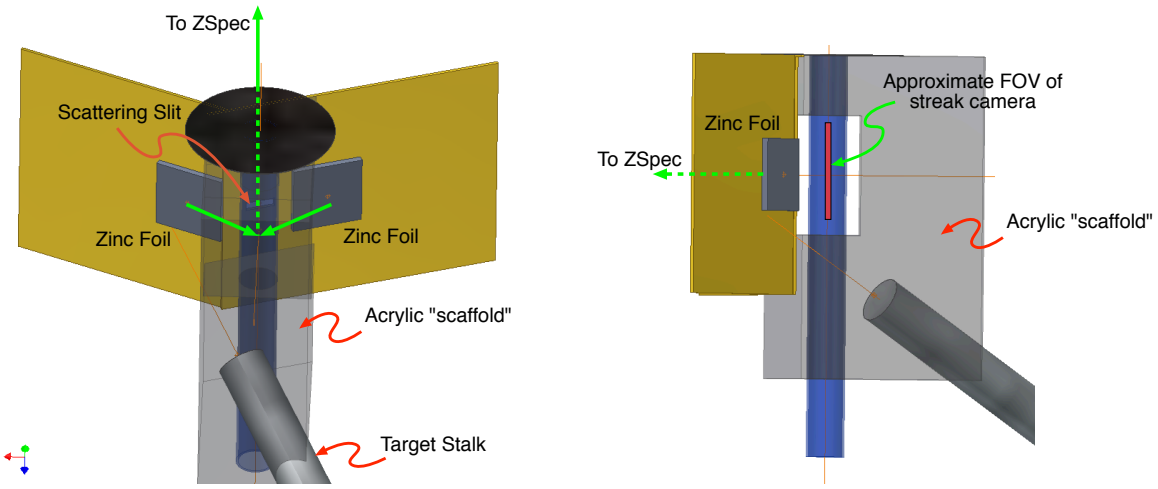

(a) View in the plane of the vector to the ZSPEC.

(b) View along SSC line of sight.

Figure 5.2: Views depicting the relevant vectors for Thomson scattering and radiography.

scattering diagnostic. Despite its proven utility in previous experiments, ungated x-ray radiography was not an option to monitor the shock position because the high-energy zinc source used for XRTS would saturate the film. Instead, an x-ray streak camera was enlisted (denoted as *SSC*, for historical reasons). This instrument sacrifices one of the spatial dimensions of imaging radiography, but is able to monitor a 1D image as it evolves in time. This is done by converting the photons collected from the 1D image to electrons via a photocathode, and then using a pulsed electric field to "sweep" the electrons across the detector. To measure the position of the shock in this experiment, the SSC was pointed to image a "slice" in the central region of the shock tube where the shock front is nearly planar, as shown in Fig. 5.3. The streak camera provides no data regarding the 2D structure of the system, but is capable of recording the variation in x-ray transmission along chords through the field of view (ie., record the density variation created by the shock) with time. Additionally, because it is time-resolved, the bright x-ray signal generated by the lasers striking the zinc foil is separated on the film from the earlier vanadium signal. This effectively

overcomes the limitations of the ungated detectors for tracking the shock position in this experiment.

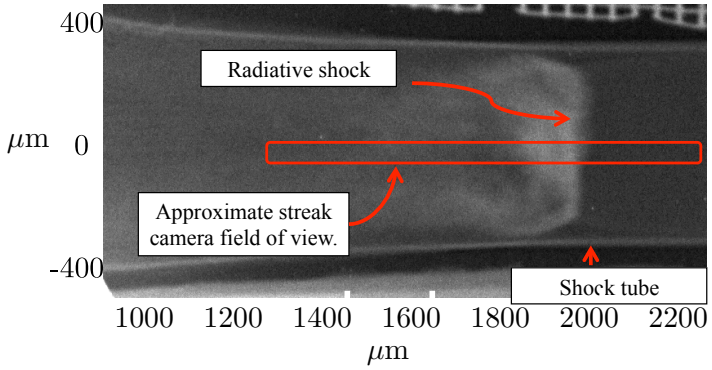

Figure 5.3: The field of view of the streak camera is shown overlaid on a radiograph from previous experiments. The image of the shock front is swept in time, providing data on the position of the shock front with time.

Figure 5.4 shows the spatial and temporal relationship of the streak camera, ZSPEC, and their associated target features. The ordinate shows increasing distance from the drive disk, while the abscissa shows time elapsed since the drive pulse. The shock front travels at $\approx 100\mu$m/ns after 10 ns, and forms the leading edge of the dense xenon layer, shown in green. Two x-rays sources are shown, labeled as V Bl (backlighter) and Zn Bl, providing 5.2 and 9.0 keV x-rays for the streaked radiography and Thomson scattering diagnostics, respectively. Both sources are created by striking a foil with several 1 ns OMEGA beams. The laser intensity for maximal conversion efficiency is informed by the literature. For vanadium, we have had success with irradiance of 2.3×10^{14} W/cm^2, which can be achieved with 2 beams. For this experiment we used three pairs of beams staggered in time to form a total pulse of several ns in duration.

The vertical extent of the red regions in Fig. 5.4 represent the collection field-of-view of the streak camera, which images a strip of the target approximately 0.8 mm along the tube axis. To calibrate the absolute position of the shock, a 100μm-thick tungsten wire was affixed to each target and measured precisely during pre-shot

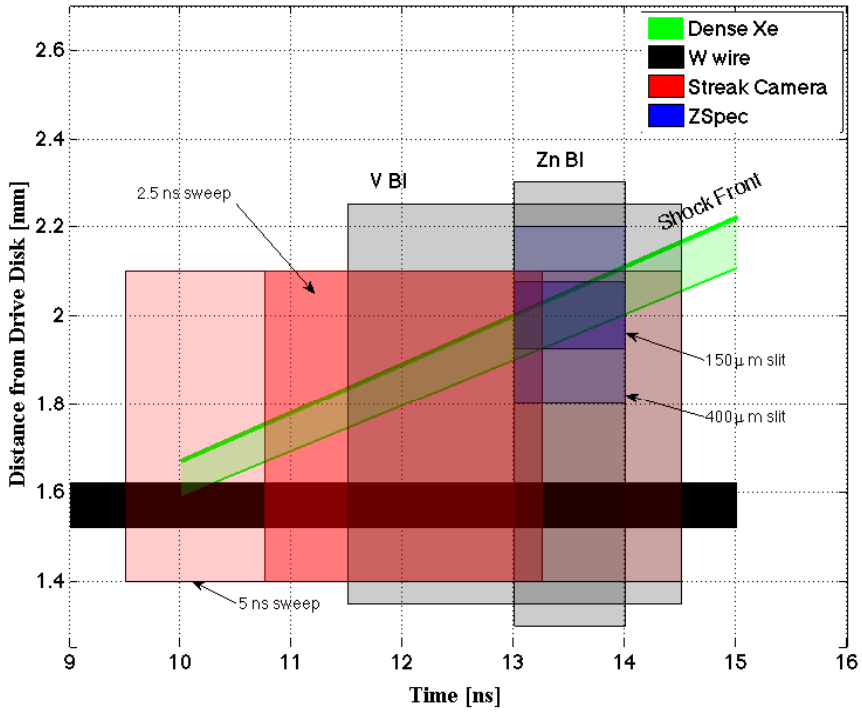

Figure 5.4: Both 2.5 ns and 5 ns streak camera sweep speeds are shown. The height of the streak camera boxes are determined by the extent of the uniform vanadium backlighter spot size, while the height of the ZSpec collection region is determined by the slit width, either 150 or 400 μm.

metrology. This is shown in black in Fig. 5.4. (For orientation, it is useful to note that the wire exists in the same place, 1.55 mm from the disk, for the duration of the experiment.) The streak camera was positioned to capture the shock when it had reached the scattering volume, centered at 2 mm down the shock tube. The electron optics of the streak camera can be pulsed with a 2.5 or 5.0 ns pulse, indicated by the two red regions in the Fig. 5.4. Because stacked 1 ns backlighter beams must be used to create a longer pulse, it is difficult to create x-rays for the full extent of the 5 ns sweep speed, but the increased data collection has generally motivated the use of the longer sweep for most shots.

5.2.2 2010 Data analysis

Typical data from the SSC collected with a 5 ns sweep is shown in Fig. 5.5. It is oriented to match the diagram in Fig. 5.4, with the shocked Xe passing the opaque tungsten wire as it progresses in time from the bottom to the top of the image. Analysis of several such images yielded a shock velocity of $u_s = 110 \pm 15 \mu$m/ns. Deviation of the shock front from a straight line in $x-t$ space indicates shock deceleration. However, quantifying this was found to be highly-variable, possibly due to non-linearity in the streak camera electron optics.

Analysis of the scattering data begins with the input spectrum. Ideally, this is a measurement of the x-ray spectrum "seen" by the scattering volume. To measure it as accurately as possible, a simple zinc foil target was constructed and oriented at the same 70° angle to the ZSPEC as the target sources were to the shock tube. The integrated opacity of the plasma plume influences the emitted spectrum, and this configuration was chosen to produce the same opacity and angular effects as the sources on the target [105]. The gain of the microchannel plate detector was varied to capture a range of features in the spectrum, which is seen in Fig. 5.6.

The MCP strip with the highest voltage setting (corresponding to the lowest gain)

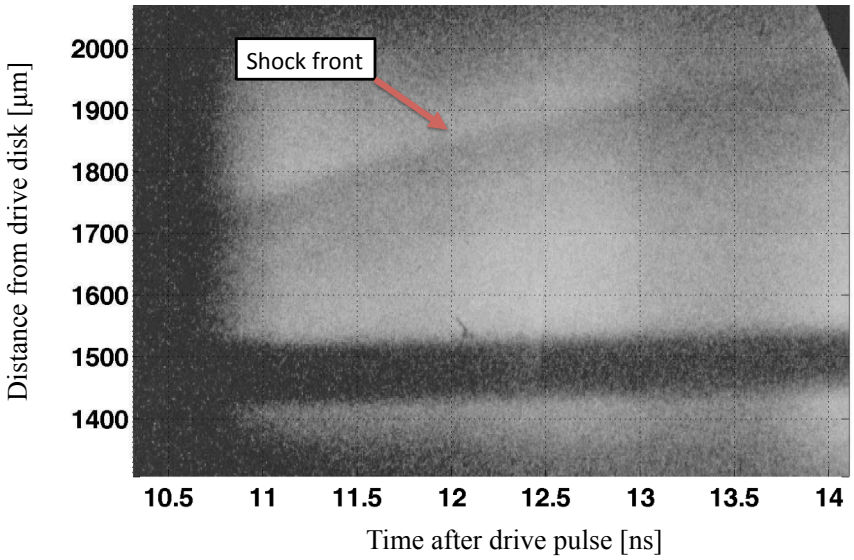

Figure 5.5: Five nanosecond streak camera image. Oriented as in Fig. 5.4, the fiducial wire is opaque to x-rays and appears as a dark bar between $\approx 1425 - 1525\mu$m. The shock is also partially opaque to x-rays, and is seen passing by the fiducial wire. Modulation in the intensity of the backlighter pulse in time is a result of the staggered laser beams irradiating the vanadium foil.

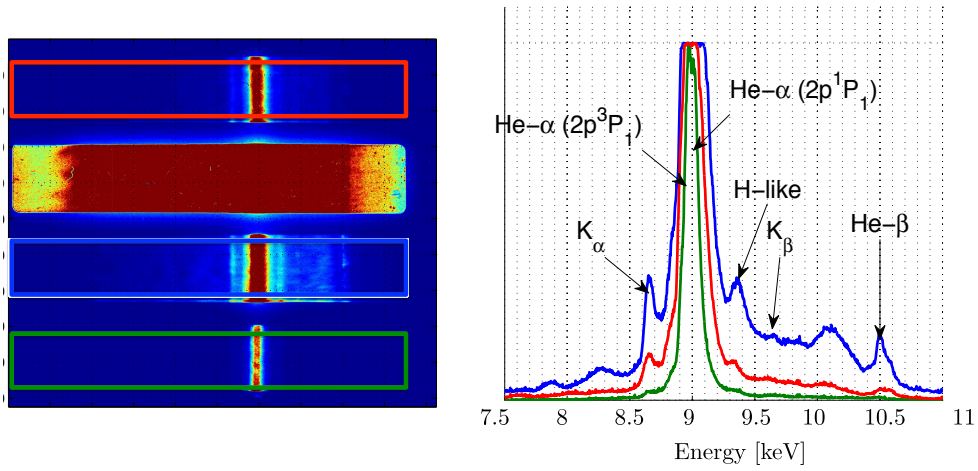

(a) Microchannel plate image.

(b) Integrated spectra from (a).

Figure 5.6: Integrated energy spectra from three strips of the MCP (a) are shown in (b), for the zinc disk shot. The colored boxes in (a) show the regions where spectra in (b) are taken from.

in on the bottom of Fig 5.6 a) and highlighted in green. In frame (b), the two peaks of the He_α lines can be seen at the maximum point of the green trace, just below the saturation limit. A low intensity foot extends from 8.6-9.4 keV. At higher gain these features are more prominent, as shown in in the red and blue curves corresponding to the top and second-to-bottom strips in (a). X-ray Thomson scattering is concerned primarily with the signal that is downshifted from the input x-rays (primarily the He_α lines here), and as such the K_α peak has the greatest potential to obscure data. In the data from full shots, it is possible that the K_α radiation from hot electron-matter interaction partially obscured the desired scattered signal.

An instance of the scattering data collected on the 2010 shot day is shown in Fig. 5.7. The input spectrum is shown in blue and the collected spectrum in green. All of the data collected on this day showed evidence of line emission peaks *in addition to* the desired He_α elastic scattering peaks. Unlike a uniform background that can be accounted for without significantly changing the shape of the scattered spectrum, line emission (especially from unknown sources) cannot be precisely removed. Additionally, a large background was seen on the high energy side (near 9.5 keV in Fig. 5.7). Because this was not uniform through the spectra (not evident at 8.5 keV, for example) and of unknown origin, it is also unclear how intense this signal is in the Compton energy range. These inconsistent features in the collected signal precluded accurate fitting of the data from this shot day.

5.2.3 2010 Conclusions

The two primary diagnostics for the 2010 campaign – x-ray Thomson scattering and streaked radiography – produced mixed results. The radiography was successful, yielding data on every shot and proving the utility of the diagnostic for shock velocity and acceleration measurements. Data from the spectrometer differed greatly from the predicted scattering spectra from Xe gas, which is expected to be dominated

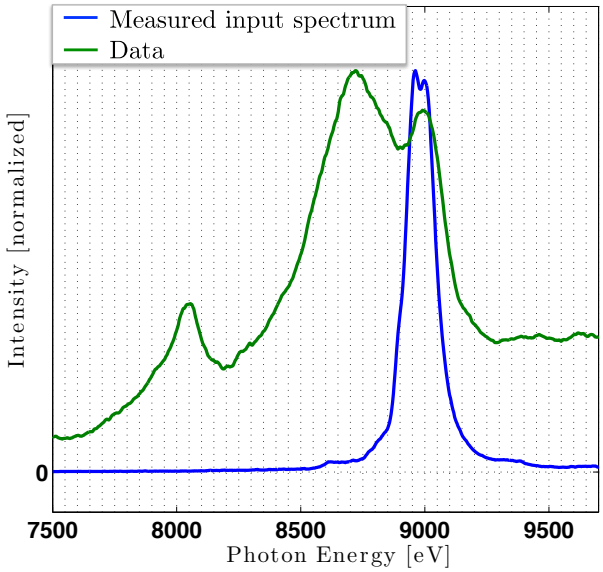

Figure 5.7: Integrated data from a full target shot (green) shown with the input x-ray spectrum (blue). Significant, non-uniform background was seen on both the high and low energy sides of the He_α peaks in the scattered data.

by an elastic peak. The high inelastic peak lead us to conclude that x-rays were scattering from a low-Z source in the target; likely culprits were the acrylic body and the polyimide tube containing the Xe gas. It is possible that hot electrons were produced in the interaction of the lasers and the zinc source foils, and that these were directed along a vector through the zinc and into the gold shielding where they interacted to create background signal. Furthermore, 50 μm of gold shielding may have been transmissive to a fraction of the zinc x-ray signal capable of distorting the measurement. Designs for future experiments would need to remove low-Z material from the scatterinyhg volume and better shield the diagnostic from plasma plumes, potential hot electron-generated radiation, and the x-ray sources themselves.

5.3 2011 Campaign

5.3.1 2011 Experimental design and diagnostics

In 2011, investigation of the radiatively collapsed dense Xe layer with x-ray Thomson scattering remained the focus of the experiment, but several substantive changes were made. A pair of collimating slits – one for the input and one for the outgoing x-rays – served to define the scattering volume (See Fig. 5.8). This had two benefits: the remediation of **k**-vector blurring in the scattered signal, and the minimization of radiation scattered from the polyimide shock tube. The first effect can be understood by reference to Fig. 4.3. If the incoming and outgoing vectors, $\mathbf{k}$ and $\mathbf{k}'$ in the figure, are not unique but vary over a range of vectors, then the collected signal will represent scattering from a related range of angles θ. This can be accounted for in data analysis by convolving the intensity-weighted signals from an appropriate range of angles to produce a final scattered spectrum. However, in practice it is very difficult to quantify the incoming x-ray intensity as it varies over the solid angle represented by the source-tube-detector system. Incomplete determination of these effects can produce into erroneous temperature measurements because Compton peak which is blurred by a range of k-vectors will be fit by a hotter electron temperature profile.

The second advantage to collimating both the incoming and outgoing x-rays is that this affords control over the number of x-rays scattering from the tube that can reach the detector. Each slit, as seen from the side opposite the tube (ie, as seen from the detector and the x-ray source, respectively) projects a volume into the target. Only x-rays scattering from the region where these solid angles overlap are able to reach the detector. In practice, it is relatively simple to anticipate the projection of the scattering slit, because the diagnostic-to-slit distance is much greater than the slit-to-tube distance. However, the slit collimating the x-ray source is approximately equidistant from the source and tube. Additionally, the emitting plasma on the x-

ray side is known to expand greatly during and after the laser pulse, and does not emit uniformly. These factors make determination of the regions of the tube that are exposed to x-rays harder to determine). Despite these factors, the incoming and outgoing collimation of the 2011 target represents an improvement over the "open input" design of 2010.

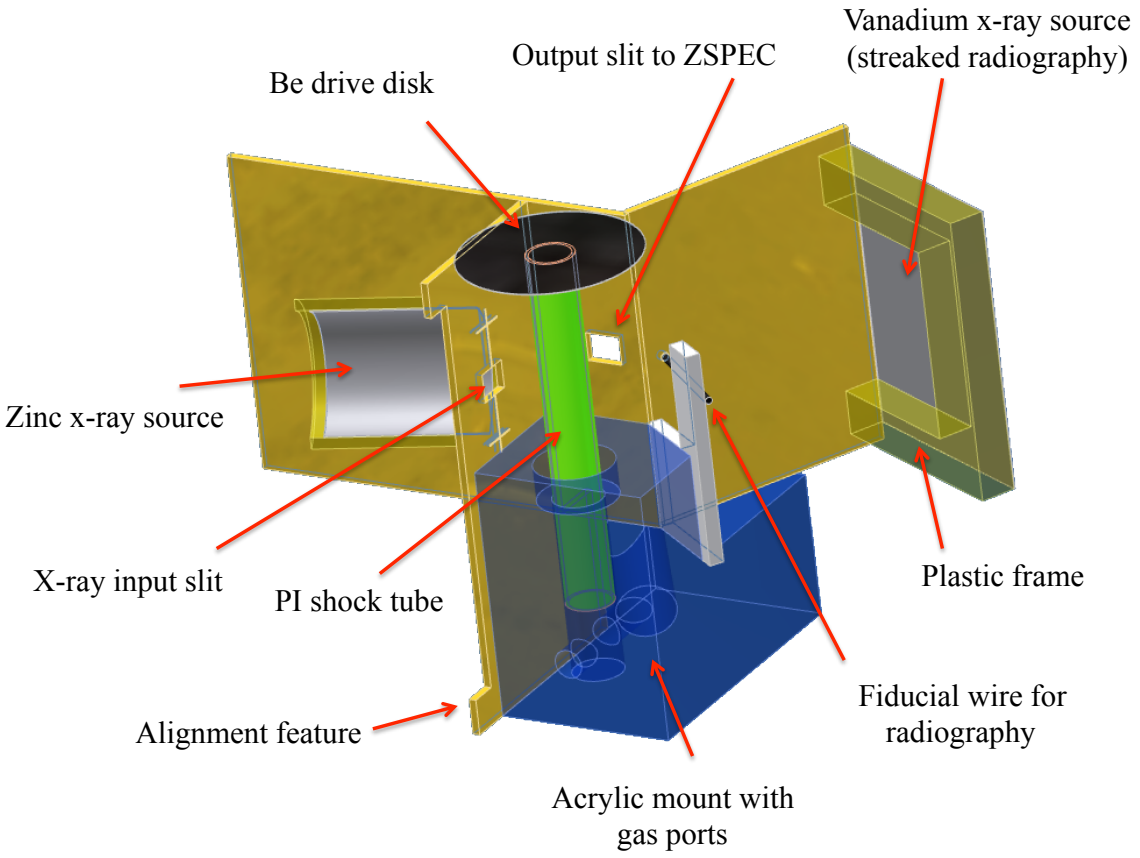

Figure 5.8: The 2011 x-ray Thomson scattering target. The PI tube (shown in green) is capped with a Be drive disk (black) and again supported by an acrylic body (blue). A pair of gold shields, each with a laser-cut slit, serve to define the scattering volume.

The slits defining the scattering volume were laser-cut into 100 μm gold foils, twice the thickness of the shields in the 2010 experiment. The increase in foil thickness decreased the transmission of 9 keV x-rays by a factor of $\sim 3\times10^{6}$ (to $\sim 1.5\times10^{-13}$), and by a factor of 10 for 30 keV hard x-rays (to $\sim 6.3\times10^{-3}$). Only a single x-ray

source foil was used, positioned at an angle of $\approx 100^{\circ}$ to the detector (as defined by the pair of scattering slits). The second x-ray source was dropped based on the 2010 results, where signal intensity was high, but background was a significant problem. It was thought that a single source could be better shielded, and that the extra signal from a second source may not be necessary. Additionally, the incorporation of a streak-camera line of sight precluded the use of two incoming x-ray collimation foils.

Initial designs and construction specified a curved zinc foil, as shown in Fig. 5.8. The thought was that the shaped foil (or, more accurately, the arc-shaped segment of the thick plastic tube that the zinc was mounted on) would impede the lateral flow of plasma over the top of the gold shielding where it could affect the data collection. To keep plasma from passing through the scattering slit, this was also covered with a thin layer of plastic (20μm, 99% transmissive at 9 keV). Both the plastic supporting the zinc foil and the plastic covering the slit were also intended to mitigate hot electron interaction with the gold shields. The zinc structure was to be be affixed at a "floating" position, out of contact with the gold shield, limiting any conductive paths between the laser-irradiated surface and the shielding. Several prototypes of this target were made, but it was determined that the shape and position of the curved foils was too variable, and the targets fielded on this shot day replaced the curved foil with a flat, 25μm-thick zinc foil.

The primary diagnostics were again the zinc spectrometer (ZSPEC) and the streak camera (SSC). In 2011 a second zinc spectrometer was also available, and could be fitted with a range of crystals. The target was oriented in the OMEGA chamber to allow use of both ZSPEC instruments – one acting as the primary data collector, and the second as a "source monitor," with a line of sight to the zinc foil. For improved signal gathering the primary instrument was fielded with a cylindrically curved crystal. In this configuration, the x-rays impinging on the crystal are scattered towards the axis of the crystal radius of curvature. This effectively collapses the four

MCP strips seen in Fig. 5.6 (a) onto one strip, increasing the signal-to-noise at the sake of timing information provided by the four-strip MCP. The source monitor was configured with a flat crystal like that used in the 2010 experiment.

To accommodate the pair of ZSPEC instruments and find beams sufficient for the drive, zinc x-ray source, and vanadium x-ray source, the streak camera imaging axis could not be made perpendicular to the tube axis. Instead, it was at 97°, 7° from the ideal position. This oblique view had the effect of blurring the edges of the dense layer and changing the line-integrated mass density through which the x-rays traveled. In this configuration a uniform dense layer of xenon 120 μm thick and 500 μm in diameter appears, "corner-to-corner," to be 207 μm thick. Because the x-rays traverse varying lengths of the dense plasma, the image, especially at the leading edge, is expected to less sharp than in a perpendicular configuration. However, with a tilt of 7° there is a $\sim$ 60 μm-thick region where the x-rays pass through *greater* than 500 μm of dense xenon. The attenuation of this region should be greater than the attenuation in the 2010 data (Fig. 5.5), and should have been observable with the SSC.

5.3.2 2011 Data analysis

An example of the SSC data foreshadowed in the previous paragraph is shown in Fig. 5.9. The fiducial wire is clear, with no evidence of the minor distortions seen in the 2010 data. Ostensibly the camera setup was the same as the 2010 campaign, but on this day there was no evidence of a shock in the SSC image. During the shot day large adjustments were made to the spatial and temporal field of view, but no shock was observed. Possible explanations include a systematic error in the diagnostic configuration that was not detected (mispointed, miscalibrated), an incorrectly designed target (the tube did not fall in the SSC field of view, or that the above analysis of the 7° tilt is incomplete), or that the diagnostic was working properly but no shock

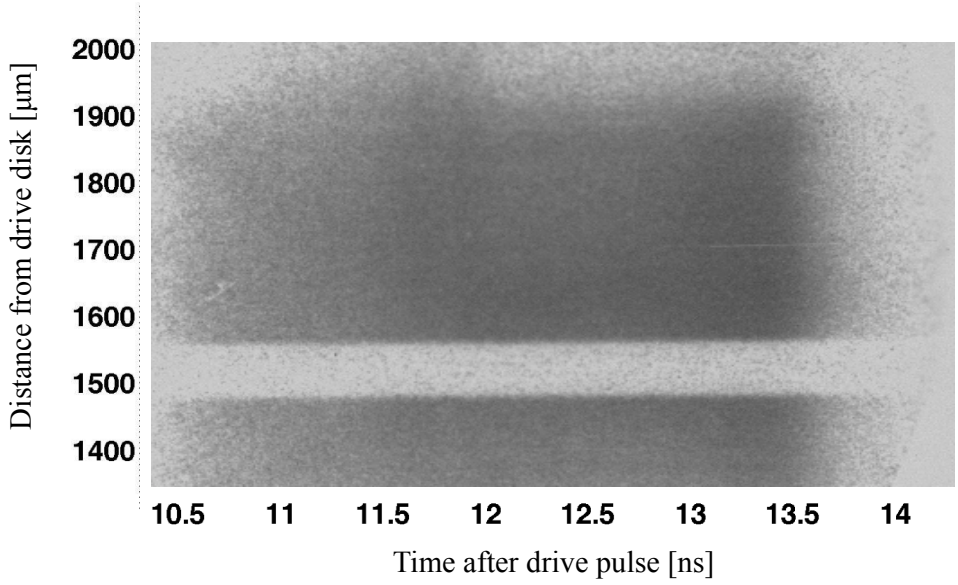

Figure 5.9: Negative image from the 5 ns sweep on the streak camera from the 2011 OMEGA campaign. The fiducial wire is clearly visible at the bottom of the image, but the dense xenon layer was not observed.

was produced (possible if the target was not driven properly, the tube was not filled with gas, etc). This final point is the most likely, as there is evidence in other experiments that relied on the same gas-fill system that the tubes were not filled with Xe gas. Instead of Xe the tubes were filled with pressurized air, which does not have the optical properties to produce an image of the shock.

Because only one curved crystal was available, the first several shots were taken with flat crystals in both the "primary" and "monitor" ZSPEC instruments. This was done to facilitate direct comparison between the x-ray input and and scattered signal. The data from the primary instrument was of generally poor quality for these shots, and during the second half of the day the curved crystal was used. It is data from the latter half of the day that is analyzed here, though all spectra are given in Appendix F.

An example of the data recorded from the primary ZSPEC (with the curved crystal) is shown in Fig. 5.10 (a). Distinct peaks are seen, offset from one another

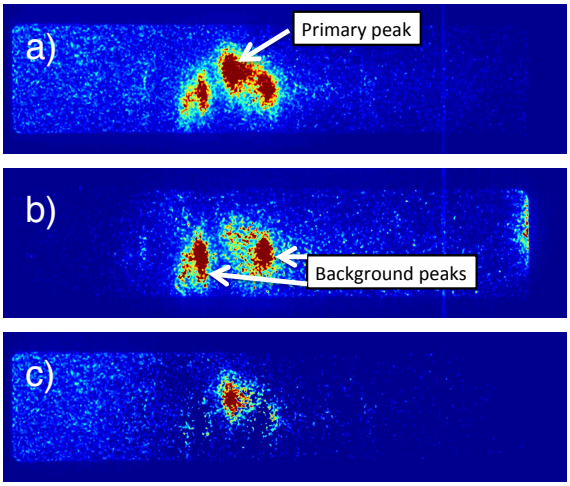

Figure 5.10: Scattered signal recorded on the central MCP strip of the ZSpec (color indicates signal intensity). a) Uncorrected data from a driven Xenon experiment. b) Data from a non-driven shot. The two background peaks are prominent, while minimal signal is recorded from the scattering volume at TCC. c) Subtracting b) from a) removes much of the background, leaving the central peak corresponding to signal from the scattering volume.

in both directions (note the horizontal axis is the dispersive direction). This can be understood as follows: for both a flat or curved crystal, deviation from a point source in the dispersive direction (vertical axis in the target plane, as seen from the spectrometer) leads to blurring of the spectrum if the source is spatially continuous, or the illusion of distinct energy bands if multiple sources are distinct and spatially separated. This is illustrated in Fig. 5.11, which shows the target as it was oriented relative to the crystal, though otherwise not to scale. The scattering slit on the target is not visible in this view, but is cut at the point on the shield indicated by the green ray in the figure.

The peaks on either side of the central peak were identified as originating from secondary sources by comparing the signal from a "full" shot (Fig. 5.10 (a)), when the target is driven and the x-ray source beams fire, with a "disk" shot, which is simply a flat zinc foil placed at TCC. This made clear that the central peak in Fig.

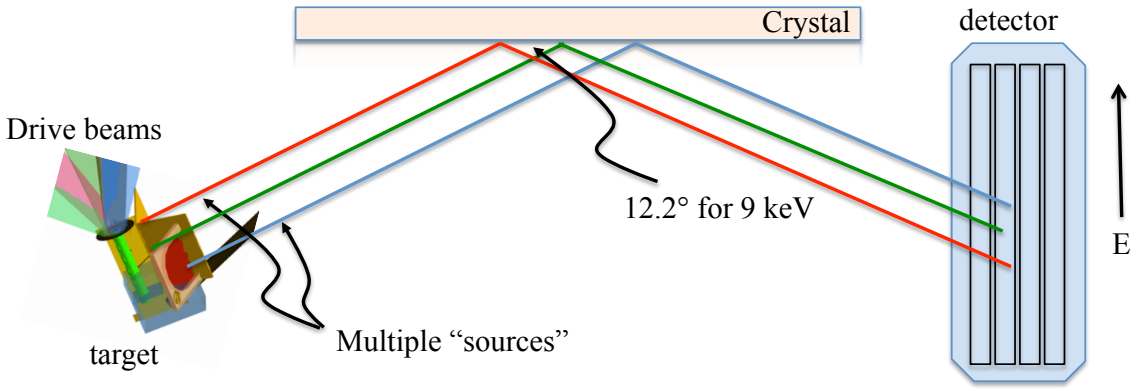

Figure 5.11: Relation of the target shields to the spectrometer, with rays from multiple sources. Note that the line colors are solely to aid the eye in this case, and do not correspond to energies. All of these rays represent 9 keV x-rays, but at distinct locations – the scattering slit, and above and below the shield.

5.10 (a) originated at TCC, the same location as the zinc foil shot. The secondary sources are the result of lateral expansion of the zinc plasma above and below the edge of the gold shielding, resulting in the signal on either side of the central peak in Fig. 5.10 (a) and (b). This was partially mitigated on one shot by adding extra shielding during the shot day (further confirming our understanding of the secondary sources), but is still present to some degree on that and all other shots.

Despite the insufficient shielding, it remains the case that the central peak in Fig. 5.10 (a) shows scattering from the scattering volume at TCC. To improve signal to noise in the data, one would like to integrate across the spatial axis (vertical in Fig. 5.10). To do so, the central peak must be isolated from the the secondary sources of signal. This was done by subtracting the signal collected from an undriven target (Fig. 5.10 (b)), from the data collected from a full (driven) target. The result of this subtraction is seen in Fig. 5.10 (c). Importantly, the undriven target had a 150 μm scattering aperture, and one would expect less intensity in the scattered (central) peak for this reason alone. Comparison of the data in the subtracted image (Fig. 5.10 (c)) with models of the predicted scattering was then performed to infer the plasma

conditions.

Model scattered spectra were generated using the XRTS computational program written by Gianluca Gregori (hereafter, "xrts code"). This code constitutes the forward model, requiring as inputs the parameters needed to generate the dynamic structure factor $S(k, \omega)$. Several static structure models can be chosen, including one-component plasma (OCP), screened OCP (SOCP), and SOCP with negative screening (SOCPN), and Debye-Hückel (DH) models. However, because the xenon radiative system is weakly coupled ($\Gamma \ll 1$) and the electron kinetic temperature is much greater than the Fermi temperature ($\Theta > 1$) there is not a significant difference in the calculated dynamic structure factor between models[1]. Based on the discussion in §4.5, the normalized spectra are thus not sensitive to electron density n_e.

Regardless of the static model, the result of the dynamic structure factor calculation must be convolved with a spectrum representing the incoming x-rays in the experiment. Ideally this is measured during the experiment, because the ratio of line intensities is a complex sum over the emission from many plasma conditions [110, 95, 168, 169]. The spectrum used in the calculation must also take into account the resolution of the detector, further motivating a measurement of the source spectrum during the experiment. In the xrts code, this instrument-dependent spectrum is termed the *instrument function*. Here, because the ZSPEC intended to serve as a source monitor employed a flat crystal, while the data was collected with the curved crystal, the detector response was significantly different between these two instruments. The instrument function used for fitting was instead collected from a single zinc foil shot, recorded using the primary ZSPEC with the curved crystal. The same instrument function is used to produce model curves in Fig. 5.12.[2]

[1]The DH model is the simplest model, and represents the limiting behavior for an ideal plasma, which the system under investigation is not. The calculations shown here were performed with the OCP model, and the results shown were nearly unchanged under any set of plasma coupling assumptions more sophisticated than DH (i.e. SOCP or SOCPN).

[2]The xrts code calculations were also performed using an ideal (analytic Gaussian) instrument response function and an instrument response generated with FLYCHK in a similar method as Ref.

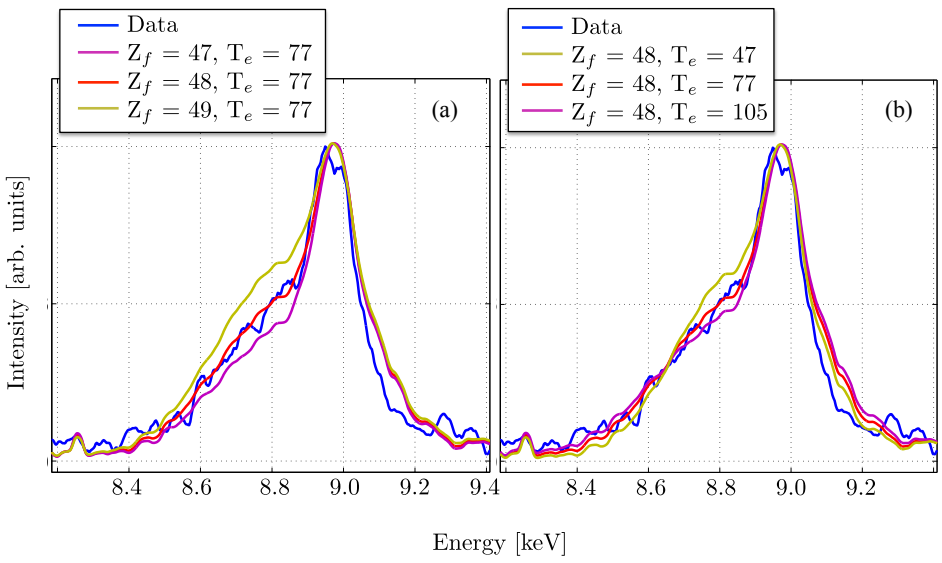

Figure 5.12: Data from a 400 μm-slit scattering target is shown in blue in both sub figures. The least-squares best fit, with parameters T_e = 77 eV, Z_f=48, is shown in red in both sub figures. The subfigures show: a) variation in free electron number (constant T_e) , and b) variation in electron temperature (constant Z_f). Each of the model curves is indicated on Fig. 5.13.

Then, for a given instrument function, the shape of the Compton peak is a function of the free electron fraction Z_f and the electron temperature T_e. To understand the dependance on these parameters, several thousand xrts runs were performed over a range of Z_f and T_e. Using a least-squares difference between the data and the model result, a best fit was found at T_e = 77 eV, Z_f = 48. This is shown as the red curve overlying the blue data in Fig. 5.12 (a) and (b). Variations around these parameters are also plotted, and shown overall by the contour plot in Fig. 5.13. The location of each curve is indicated in the T_e - Z_f parameter space of the contour plot. The fit is relatively sensitive to Z_f, but large changes in T_e still produce reasonable fits to the data. Additionally, this analysis assumes only one homogeneous plasma condition throughout the entire scattering volume, which is known to be a simplification based

[110]. The difference in goodness of fit between the model spectra produced with this array of input functions and the data was essentially uniform over parameter space. Thus, the choice of instrument function did not significantly change the results presented below.

on spatial dimensions of the dense Xe layer measured in 2D radiographs.

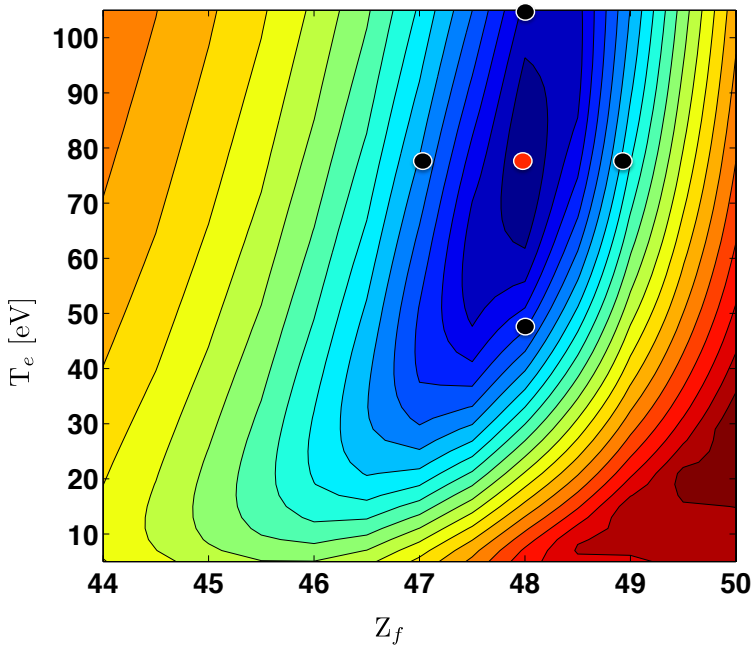

Figure 5.13: Model spectra over the T_e - Z_f parameter space is compared to the data via simple least-squares differencing. This converges to a minimum at $T_e = 77$ eV, $Z_f = 48$. This point is indicated by the red dot. Each of the black points is the displayed in Fig. 5.12.

Comparison of the inverse problem results with the calculations of Chap. III draw into question the design of the experiment as having probed Xenon. The large error bars in the XRTS temperature measurement permits agreement with the analytic estimates, but the value of Z_f higher than expected. For conditions of $n_e = 5 \times 10^{22}$ cm^{-3} and $T_e = 100$ eV, the Thomas Fermi model predicts an average ionization state of ~ 18. This is the electron configuration of the nobel gas krypton, and as such represents a relatively stable state[3]. However, because of the screening of the inner electrons, six electrons (in addition to the outer 18) have binding energies less than the Compton shift (≈ 169 eV) of the 9 keV probe electrons. (These six are the $4p^6$ electrons, with binding energies of 145 eV. The outer 18 are the $5s^2$ level at 23 eV,

[3]Note that this is a coincidental prediction of the TF model, which does not take into account the electron shell structure of atoms. See Appendix A for details of this model.

$4d^{10}$ at 67-145 eV, and $5p^6$ at 12-13 eV, [2]). This Z_f value of 24 may be considered kinematically free with respect to the XRTS probe, but is still well short of the 48 needed to fit the data.

Reprinted here for convenience, the ratio of inelastic scattering intensity to the elastic intensity is given by Eqn. 4.33:

$$\frac{I_{inel.}(k)}{I_{el.}(k)} \approx \frac{Z_f}{|f_I(k)|^2} \geq \frac{Z_f}{Z_c^2}. \tag{5.1}$$

It is clear that theory predicts the scattered spectrum for a high-Z system, where more than half of the electrons remain tightly bound, will be dominated by elastic scattering. In a low-Z system, particularly when is hydrogen present, it is possible to ionize a significant fraction of the electrons and increase the inelastically scattered signal. In the experiment here it must be considered that the polyimide tube, with chemical formula $C_{22}H_{10}N_2O_5$, contributed to the scattered signal.

Comparison of the data with model scattering curves from xenon yielded a best-fit temperature of 77 eV. This value is independent of the scatterer; any optimum fit to the data will be at this temperature. If one assumes that this represents the actual temperature of the scattering material, the ionization of polyimide can be found using an appropriate model. Applying the Thomas Fermi model with a solid density of 1.4 g/cm^3, on finds average ionizations for each of the constituent elements to be C (Z_f= 4.1), H (0.9), N (4.6), and O (5.0). These are subject to the validity of the model, discussed further in the appendix on the topic, but represent reasonable starting values. Beginning with the same instrument function used to generate the xenon curves of Figs. 5.12 and 5.13, the xrts code calculation for scattering from PI was carried out. This is shown in black in Fig. 5.14, plotted with the data (blue) and the best-fit model curve from Xe scattering (red). Notably, air is also primarily N and O and produces a similar curve to the polyimide and highly-ionized Xe models. The

striking similarity between calculated scattering spectra from xenon at unphysical conditions and plastic or air at reasonable ones precludes making strong claims about the model parameters in the system of interest.

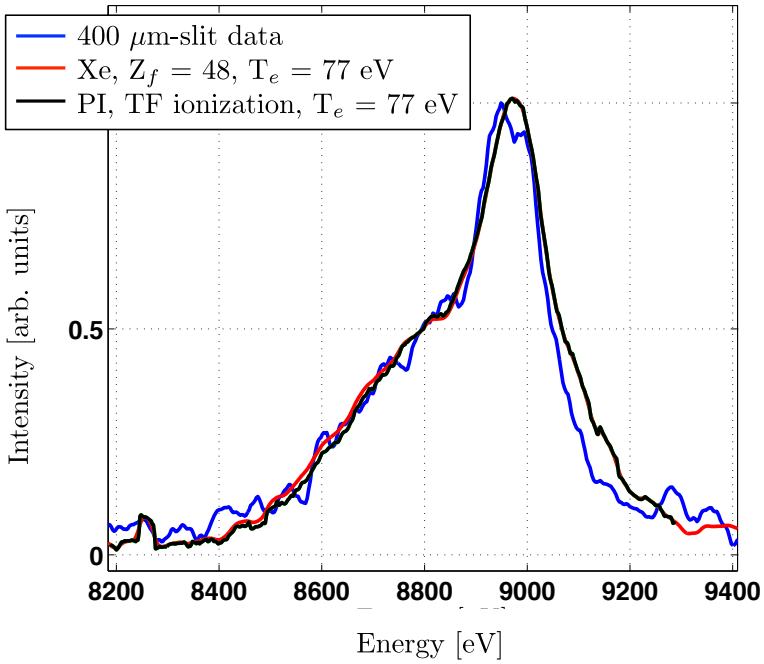

Figure 5.14: The measured data spectrum is shown in blue, with the best fit xenon spectrum overlaid in red. Plotted in black is the xrts calculation for scattering from polyimide ($C_{22}H_{10}N_2O_5$) at 77 eV. The ionization states are determined from the Thomas-Fermi model to be C (Z_f= 4.1), H (0.9), N (4.6), O (5.0).

5.3.3 2011 Conclusions

Using the cylindrically curved crystal in the zinc spectrometer, we were able to identify the sources of background in the 2011 experiment. Isolation of the scattered signal from the signal from multiple sources was roughly achievable, and permitted the comparison between the data and model spectra calculated with the xrts code. Using an instrument function recorded from the zinc disk x-ray source, the data is well-fit by scattering from xenon with an unrealistically high ionization state. Because of the ill-posed nature of the XRTS analysis method, the data was also well-fit by

scattering from the plastic shock tube. In reality the measured spectrum is almost certainly an average of scattering from electrons bound to xenon atoms, electrons bound in the plastic, and free electrons from all sources. This experiment made several key improvements over the 2010 effort, and permitted the inference of a free electron temperature, albeit with large error bars. It also convincingly illustrates the stringent requirements on shielding and experimental design when attempting to probe a low-density, high-Z material with XRTS.

5.4 2012 Campaign

5.4.1 2012 Experimental design and diagnostics

In April of 2012 a new diagnostic had been completed to measure spatially resolved x-ray Thomson scattering. The "imaging x-ray Thomson spectrometer," or *ixts*, was designed by E.J. Gamboa and collaborators at Los Alamos National Laboratory. Central to the ixts is a torriodially-bent crystal with high-resolution spectral dispersion along one axis and spatial resolution afforded by a Von Hamos geometry on the orthogonal axis. The crystal is aligned for use with a nickel He_α x-ray source with characteristic lines at 7766 and 7806 eV. A diagram of the instrument is shown in Fig. 5.15; full specifications can be found in Ref. [79] and [78].

Building on the previous experiments and working to take advantage of the new diagnostic, several changes were made to the target design. These included tighter collimation of the input x-rays, using a laser-cut 300 μm-diameter hole to limit the irradiance of the tube walls. The imaging capabilities of the ixts diminished the importance of a streak camera and relieved the need for a second x-ray source. As such, the vector approximately 180° to the ixts direction was designed to accommodate the curved-crystal ZSPEC in a configuration similar to 2011. This provided a complementary diagnostic for comparison to previous data, with minimal additional

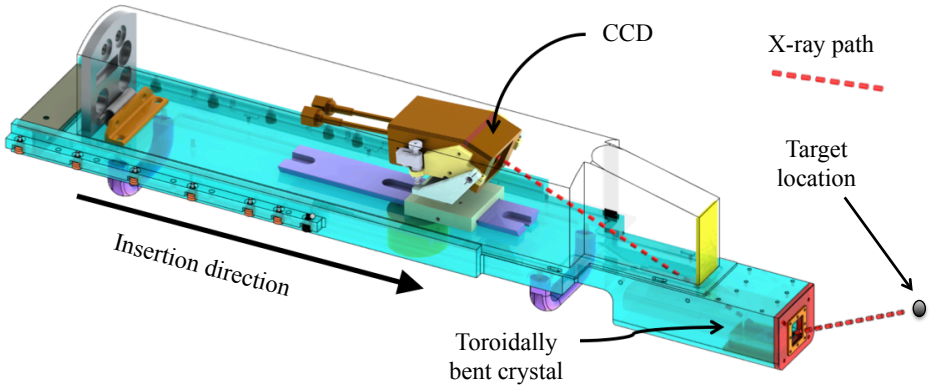

Figure 5.15: Diagram of the imaging x-ray Thomson spectrometer. *Image credit: Gamboa et al.* [78]

experimental requirements. An annotated photograph of the target is shown in Fig. 5.16.

Relative to the ZSPEC, the ixts has significantly higher resolution and photon-gathering capabilities. Owing to this, we were able to decrease the width of the scattering slit from 500 μm to 300 μm. This is approximately half of the tube diameter, and eliminates the collection of any photons scattered from the tube walls with normal vector parallel to the incident x-rays. The slit was lengthened to 1 mm along the direction of the shock tube to guarantee the presence of the dense xenon layer during the probing time. The ixts imaging capability was relied upon to monitor the shock position.

Not unexpectedly, the lateral expansion of the x-ray source plasma once again extended beyond the shields. Emission from the Be disk also produced strong emission in the energy range of interest (7400 – 7900 eV), which was collected by the time-integrating CDD. However, with the spatial discrimination of the ixts this background was trivially cropped out and did not interfere with the scattered data[4].

[4]This understates the issue somewhat. The first shot of the day produced background bright enough to saturate and possibly endanger the CCD detector if repeated. This motivated the attachment additional gold shielding to subsequent targets, which is generally considered a "last-resort" solution. Still, it remains the case that the saturated shot did produce viable data. This highlights the power of the instrument and the yet-unachieved amount of shielding needed to eliminate the collection of direct x-ray emission in these sensitive XRTS measurements.

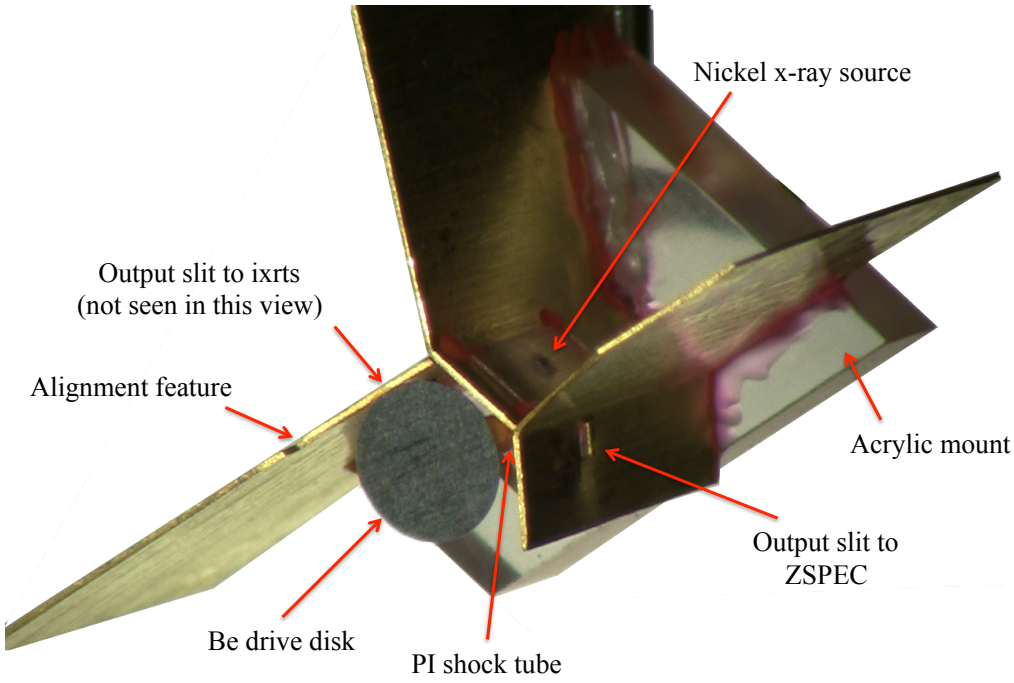

Figure 5.16: Photograph of the 2012 target, with important features labeled. Significant improvements in the target viewing and metrology system in the Drake lab between 2011 and 2012 enabled this image.

5.4.2 2012 Data analysis

Data from this day is shown in Appendix G, and an example is given in Fig. 5.17. The plot on the left of this figure shows the spatial variation recorded by the ixts (integrating both elastic and inelastic scattering). A region of enhanced signal is seen between 350 and 550 μm from the edge of the scattering slit, or 1850 – 2050 μm from the drive disk. This is scattering from a region of higher density, and is consistent with the plethora of shock position measurements at 13 ns. Spatial modulation was not seen in the scattering from an undriven experiment, shown in Fig. 5.18. indicating that the structure is the result of the shock in the xenon gas.

To account for background scattering, the signal collected from the undriven target was subtracted from the full target data. Subtraction was performed in 2D (pixel-by-pixel image subtraction) and in 1D (subtraction of lineouts taken at the same spatial coordinate in the scattering slit), with negligible difference in the qualitative results.

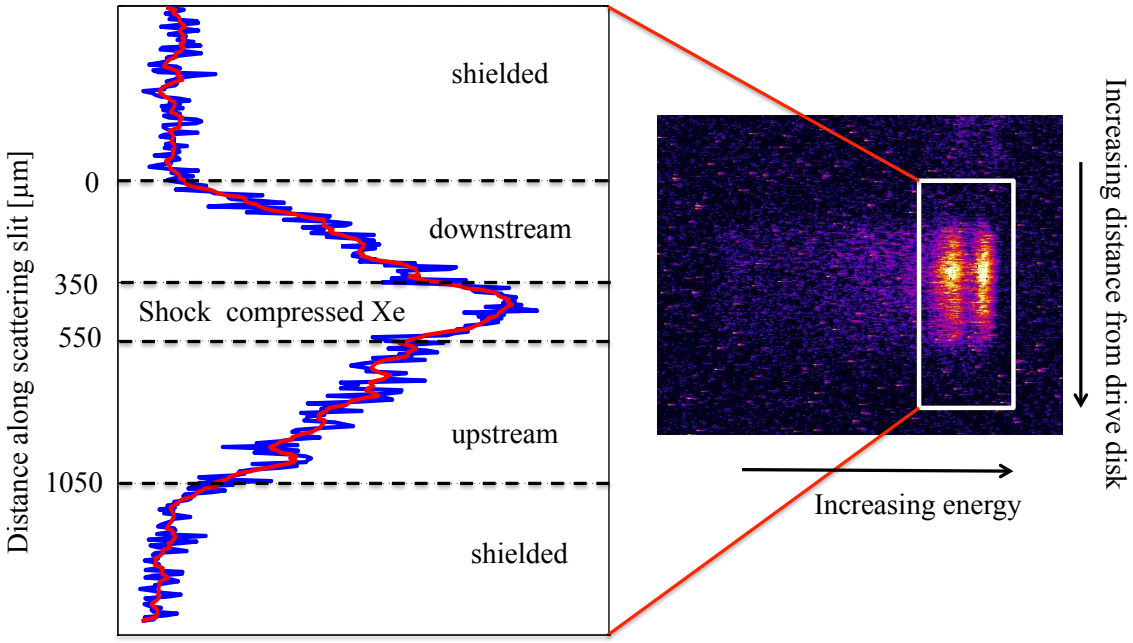

Figure 5.17: Raw data is shown in false color on the right. Integration over all energies gives the spatial scattering profile on the left (blue is the sum, red is smoothed slightly) where upstream, compressed, and downstream regions are indicated.

There was not a shot dedicated to measurement of the Ni x-ray spectrum on this shot day, so an instrument function had to be developed. A zeroth order approximation uses a pair of Gaussians fit to the two clear Ni He_α peaks in the data. This represents a best-case scenario, as the spectrum from a real laser-produce plasma will have lower-charge state populations emitting at lower energy than the He-lines. Similarity to the experiment described in §2.5 motivated the use of FLYCHK to produce an input x-ray spectrum. Convolving the results of such a calculation with a simulated instrument response function so as to match the measured He_α lines produces the instrument function used in the xrts calculations. This is shown in gray in Fig. 5.19, with data plotted in red.

The power of x-ray Thomson scattering comes from the fitting of inelastically scattered signal. However, it is clear that a radiative shock in a high-Z systems may not sufficiently ionize the system to produce a measurable down-scattered signal. In

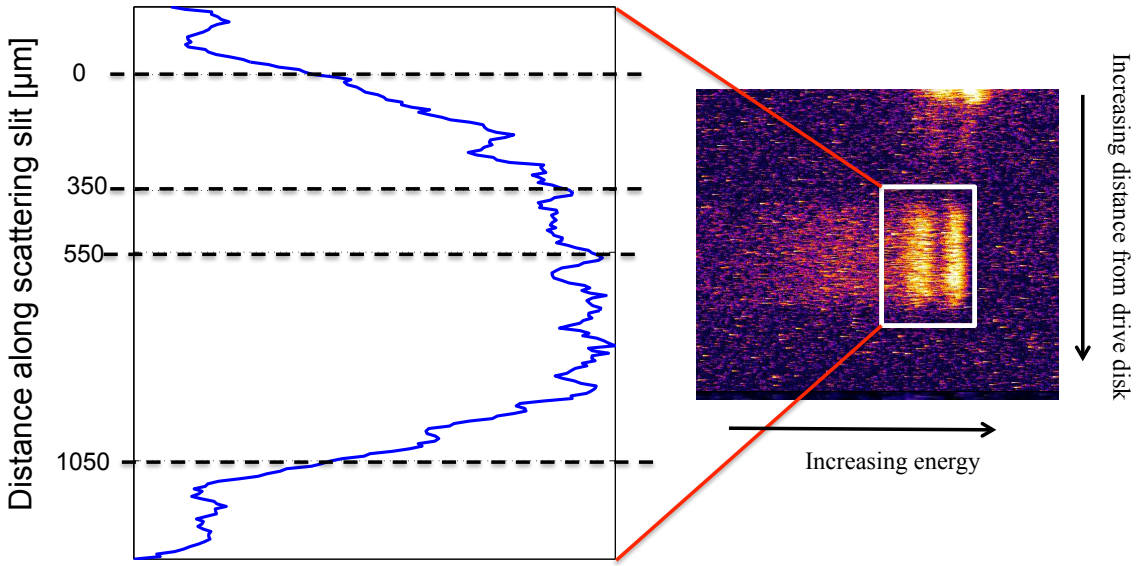

Figure 5.18: Raw data from a null (undriven) shot is shown in false color on the right. Integration over all energies gives the spatial scattering profile on the left. The signal intensity is approximately half of that in Fig. 5.17, and there is very little spatial modulation. The signal here is thus attributed to scattering from the PI tube walls, and can be subtracted from the full-shot signal.

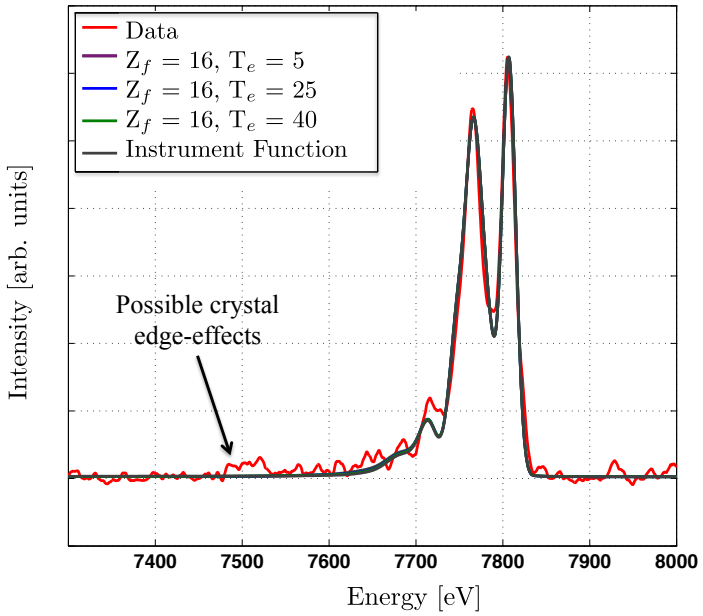

Figure 5.19: Data is shown in red, with several calculated scattering spectra shown. Because of the low Z_f fraction all of the spectra are dominated by elastic scattering and are indistinguishable from the instrument function (shown in thick gray).

such a case the input spectrum matches the data over the entire parameter space. Notably, nature is nearly as uncooperative for low-Z materials. Figure 5.20 shows the predicted scattering from beryllium at density $n_e = 1.2 \times 10^{23}$ cm^{-3} and $T_e = 5$ eV for two different ionization states, $Z_f = 0$ and $Z_f = 2$. (Other parameters, like instrument function and coupling model, are also the same). This indicates that the inverse problem results are non-unique for the parameter Z_f in low-Z materials, making inference of this parameter difficult. Despite this, the presence of *an* inelastic signal allows for fitting of other parameters, which is not possible for moderately ionized high-Z materials.

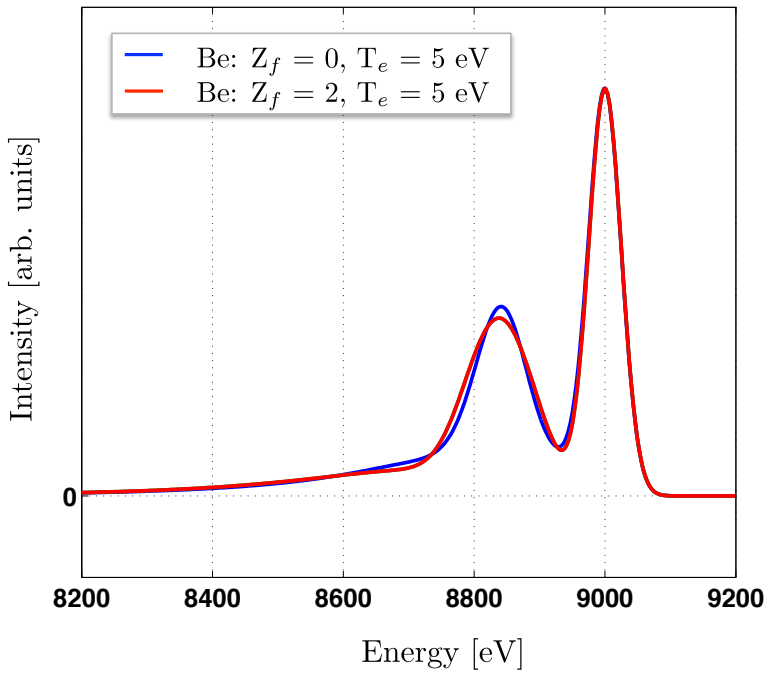

Figure 5.20: Scattering response from Be at solid density, 5 eV, and ionization of 0 and 2, as calculated by the xrts code. For a 50 eV full-width-half-max Gaussian instrument function at 9 keV, the expected scattering is not sensitive to the ionization to within errors in typical experimental data.

5.4.3 2012 Conclusions

The 2012 radiative shock campaign made use of the ixts instrument. This spectrometer uses a toroidially-bent crystal in the von Hamos geometry to spatial resolve input x-rays in one dimension while spectrally dispersing them in the other. The high-resolution spatial discrimination allowed complete separation of background x-ray sources that plagued earlier efforts. Additionally, the subtraction of signal from an undriven, evacuated shock tube – representing scattering entirely from the PI tube, acrylic housing, and other uninteresting sources – yielded the scattered signal from the xenon gas. This signal was dominated by elastic scattering, a result that is in keeping with the limiting behavior of the scattering theory and the calculations of the xrts code, which uses more advanced models.

Future efforts to use XRTS to probe a high-Z gas will require improvements in experimental design. In particular, a brighter, higher energy x-ray source will be needed to increase the total number of scattered x-rays and improve the signal-to-noise. Continuing to reduce background sources–scattering from the tube or other target elements, plasma expansion beyond the shields, and signal produced by hot electrons–will be necessary. Finally, improvements in detector dynamic range will be required to resolve both the elastic and inelastic scattering peaks. These issues are discussed further in Chap. VIII: Conclusions and future directions.

CHAPTER VI

Laser wakefield acceleration and current filamentation instabilities

6.1 Introduction

The physics of relativistic charged particle beams is of central importance to gamma ray bursts, as introduced in Chapter I, as well as astrophysical jets of other types. During these events, tremendous fluxes of charged particles are accelerated into the interstellar media (ISM). It was shown in 1959 by Erich Weibel that such a system may be unstable in the presence of thermal anisotropies, evolving into a series of current filaments via a process which now bears his name [214]. In addition to the Weibel instability, several other phenomenologically similar mechanisms can also cause filamentation of the charged particle flow [77, 22], all of which can lead to the formation of strong magnetic fields. Deflection of charged particles from the small-scale magnetic fields created by the Weibel instability have been suggested as the origin of the late-time emission (*afterglow*) of the gamma ray burst radiation spectrum [155, 154, 183].

The process can be understood as follows. Assume equal fluxes of electron traveling in the $\pm\hat{\mathbf{x}}$ directions and a stationary proton background, yielding global charge neutrality and a net current of zero. The electrons will respond to an infinitesi-

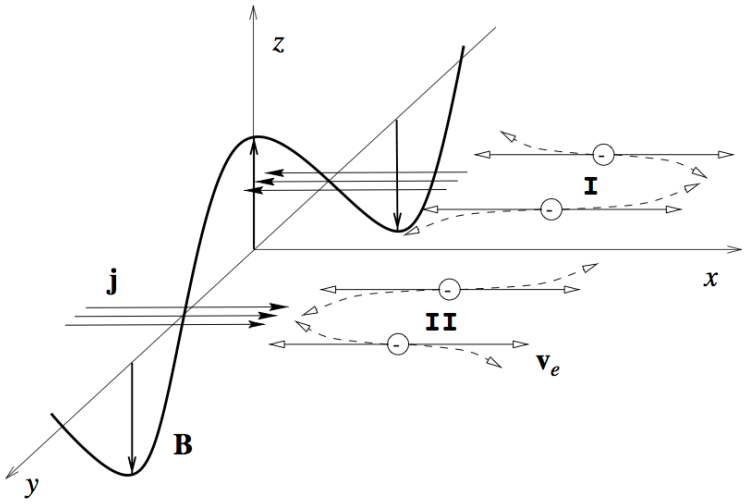

Figure 6.1: An initially uniform flux of electrons flowing in the **x** direction will tend to form current sheets at locations I and II in the presence of a magnetic field **B**. From Ref. [155].

mal magnetic field fluctuation of the form $B = \hat{\mathbf{z}} B_z \cos(ky)$ via the Lorenz force, $F = -e/c(\mathbf{v} \times \mathbf{B})$. With reference to Fig. 6.1, electrons traveling in the $+\hat{\mathbf{x}}$ direction will be deflected, as shown by the dashed arrows. The electrons bunch into sheets, indicated by I and II, which serve to enhance the magnetic field. By similar analysis, electron motion along $\hat{\mathbf{y}}$ tends to quench the process, while motion in $\hat{\mathbf{z}}$ does not contribute to the instability as it is depicted (though the perpendicular component of velocity can contribute to stabilization of Weibel instabilities, as described by Su *et al.* [199]). Initially filaments grow at wavelengths on the order of the skin depth c/ω_p, where c is the speed of light and ω_p is the plasma frequency. The instability progresses as co-propagating currents attract and coalesce, increasing the local electron density and furthering the anisotropy.

Numerous sources report on variations to the fully-kinetic, relativistic treatment of the Weibel instability, and are summarized in the review by Tautz and Lerche [203]. As alluded to previously, there are a multitude of related instabilities that have been identified; these arise from subtly different conditions and compete with

(or reinforce) the Weibel instability. Equation 6.4 (a) quotes the maximum growth rate for the Weibel instability, along with those of the two-stream (ts), oblique (o), and filamentation (f) instabilities [23]:

$$\omega_W = \left(\frac{n_b}{n_0\gamma}\right)^{1/2} \omega_p, \tag{6.1}$$

$$\omega_{ts} \propto (n_b/n_0)^{1/3}\gamma^{-1} \tag{6.2}$$

$$\omega_o \propto (n_b/n_0)^{1/3}\gamma^{-1/3} \tag{6.3}$$

$$\omega_f \propto \sqrt{(n_b/n_0)/\gamma}. \tag{6.4}$$

In each case, γ is the relativistic factor, n_b is the beam electron density, and n_o is the background electron density. All of the instabilities grows faster for low energy, high density beams. This set of growth rates is presented to show the similarity between the instabilities, and because in most experiments, including the one detailed later in this chapter, it is not possible to distinguish the specific mechanism that leads to beam filamentation.

In addition to aiding in understanding the radiation signatures of astrophysical objects, the physics of electron beams is also relevant to the fast ignition concept of inertial confinement fusion. In this scheme, the heating of the fuel is separated from the process of fuel compression (*isochoric* heating). This differs from so-called "hot-spot" (or, *isobaric*) ignition (described in Chap. VII), when these steps are performed at the same time. In fast ignition (FI), a capsule of DT fuel is compressed to high density, either by x-ray ablation or direct laser irradiation. When the fuel is near maximum compression, a pulse of charged particles is provided to create the "spark" needed to reach fusion conditions. In principle, FI relaxes the stringent requirements on the symmetry of the spherically compressed fuel and thereby lessens the detrimental effects of Rayleigh-Taylor instabilities (see Chap. VII).

Fast ignition is not without stability issues, however, and suffers from breakup of the particle beam intended to spark fusion. This is ameliorated, in part, by the introduction of a cone into the capsule, providing an avenue free of plasma for the beam to reach to the dense fuel [164, 126, 208]. Despite this, deposition of energy in the dense fuel remains challenging, and the same beam instabilities present in electrons streaming through the ISM also serve to filament and disperse the energy of the FI heater beam. To investigate the physics of relativistic electron beam propagation, a source of energetic electrons is needed. Laser wakefield acceleration of electrons provides such a beam.

6.2 Laser Wakefield Acceleration

In a process called laser wakefield acceleration (LWFA), electron bunches can be accelerated to relativistic energies by "surfing" on electron-plasma waves generated by an ultra-intense laser pulse as it propagates through a low-density plasma [148, 80, 67]. This was proposed conceptually in 1979 [200], but was not realized until several years later when the necessary laser intensities could be reached. In particular the invention of chirped pulse amplification (CPA), where a frequency dependent delay is introduced to a short laser pulse prior to amplification [198], led to gain increases of several orders of magnitude in ultra-fast pulses. The development of CPA enabled the construction of several high-intensity lasers during the 1990's, and aided by progress in parallelized particle-in-cell (PIC) code development, laser wakefield acceleration has been a prolific area of research in the last two decades.

The process of LWFA relies on the focusing of an intense laser into a plume of neutral gas. As the leading edge of the laser ionizes the gas, the high electric field gradients expel the electrons via the ponderomotive force, leaving behind a bare ion cavity. The resulting electron density profile resembles a near-spherical "bubble" following the laser pulse. The space-charge separation at the rear of the

bubble can produce electric fields of tens or hundreds of GeV/m and can be used to accelerate trapped electrons to near the speed of light. These electric field strengths are significantly higher than those used in traditional radio-frequency cavities, and for this reason, laser wakefield accelerators are a promising avenue in the search for next-generation accelerators.

To achieve the greatest energy gain, it is necessary to increase the length of the accelerating region, maximizing the distance over which electrons can extract energy from the driving laser pulse. However, as the laser pulse propagates it continuously loses energy to the plasma in generating the wakefield. The length over which the laser pulse can sustain a wakefield is given by the pump depletion length. In the non-linear 3D regime, this is given as $L_{pd} = (n_{cr}/n_0)c\tau_p$, where $n_{cr} = \omega_0^2 m_e \epsilon_0 / e^2$ is the critical density for a laser of angular frequency ω_0, τ_p is the pulse duration, and n_0 is the unperturbed plasma electron density [146]. This length is shown in Figure 6.2, along with several other important points along the plasma channel.

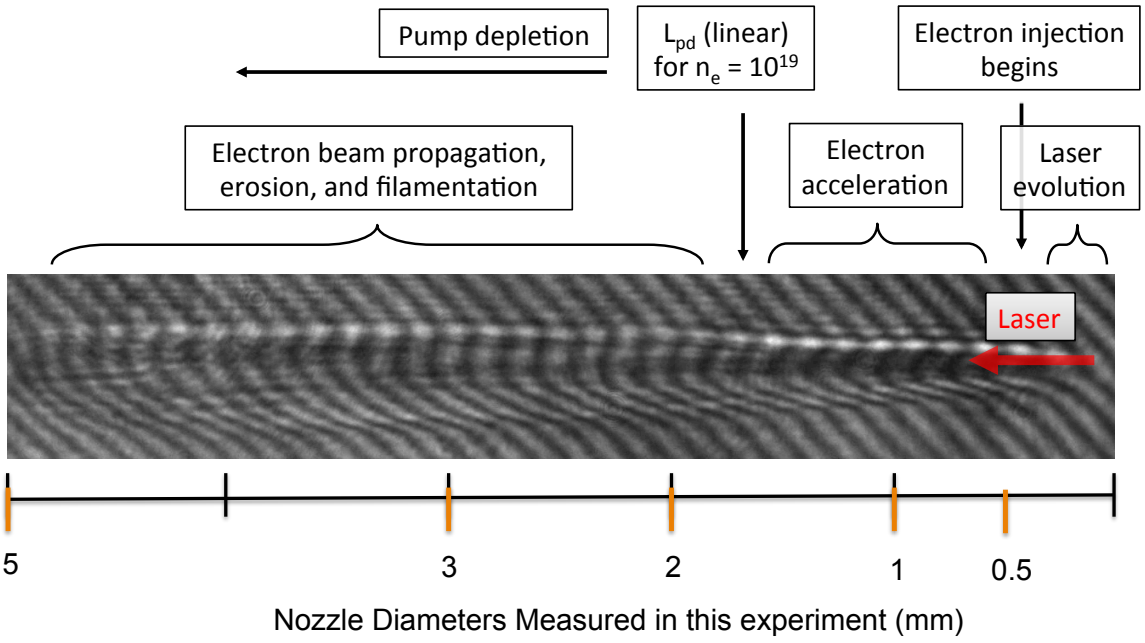

Figure 6.2: The stages of electron beam formation and propagation are shown on an interferogram of the plasma channel.

If the length of the gas target used exceeds the pump depletion length, the electron beam will subsequently propagate through an approximately uniform, quasineutral plasma, instead of the bare ion channel generated by the plasma bubble. As well as driving its own wakefield [34], the electron beam may be susceptible to filamentation and propagation instabilities. Weibel [214] first discovered that an electron distribution with an anisotropic temperature can lead to the growth of self-excited transverse electro-magnetic waves. A related transverse instability for relativistic electron *beams* is the current filamentation instability [29], which occurs when the magnetic field generated by the beam causes an initial seed modulation in the transverse current profile to be amplified by the Lorentz force, $\mathbf{j} \times \mathbf{B}$. The evolving current filaments produced by these instabilities leads to a densely tangled magnetic field structure that serves to "jitter" the electrons. In astrophysics, observations of gamma-ray bursts can be characterized by the spectra of the long-duration afterglow, which may be the result of such jitter radiation [154, 163].

6.3 Electron Beam Filamentation Experiments

To investigate current filamentation, we conducted experiments using the 30 fs, $\lambda_0 = 0.8$ μm HERCULES laser at the University of Michigan [221] to generate relativistic electron beams. The laser wave front was corrected using a deformable mirror, and the beam was focused to approximately 10 μm FWHM spot size using an $f/10$ off-axis parabola. Shots were taken with 28 ± 3 TW peak power with a focused intensity of 4×10^{19} W/cm^2, resulting in a normalized vector potential $a_0 = 4.4$. The pulse was focused onto the front edge of an expanding helium gas plume created by the flow of gas through a supersonic conical nozzle. To vary the length of the plasma channel a range of gas nozzles were used, with diameters of 0.5, 1, 2 , 3, and 5 mm. The set of nozzles were shot on sequential shot days, during which the laser parameters and major alignment remained the same. The repeatability of the pulse

was checked by imaging the laser immediately before beginning the experiment. The backing pressure was varied during each shot cycle, with electron densities ranging from 1×10^{19} - 2.6×10^{19} during the experiment.

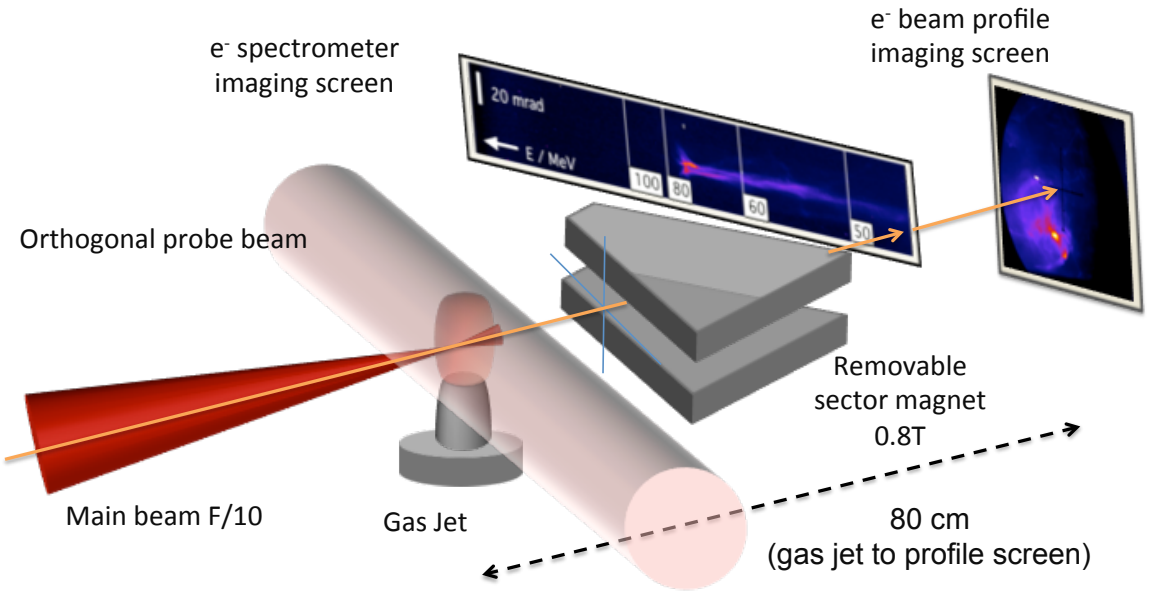

Figure 6.3: Diagram of the laser wakefield accelerator geometry and electron imaging diagnostics (not to scale).

To measure electron density and image the plasma channel structure, we employed a transverse interferometer beam orthogonal to the main laser pulse direction. The length of the plasma column was measured directly from a calibrated image, while the density measurement was made via Abel inversion of the interferometer image. The error associated with the Abel inversion process was estimated by dividing the interferometer image along the laser axis and separately mirroring the top and bottom images using image processing software. For the cylindrically symmetric Abel calculation, the pair of mirrored images should produce equal results, and the maximum density values produced in this way were seen to agree to within ten percent.

The energy of the electron beam was measured with a spectrometer using a 0.8 T sector magnet placed in the path of the electron beam. The magnet served to disperse

the beam onto a scintillator screen, which was imaged with a high-resolution camera. When the magnet was removed from the beam path a beam profile image was recorded by a second screen, placed on-axis approximately 90 centimeters beyond the gas nozzle, providing a measure of the electron beam divergence. A removable optical imaging system was in place to monitor the laser light after passing through the plasma. This confirmed that the laser pulse was self-focused through the gas jet and did not filament in a manner that would affect the observed electron beam.

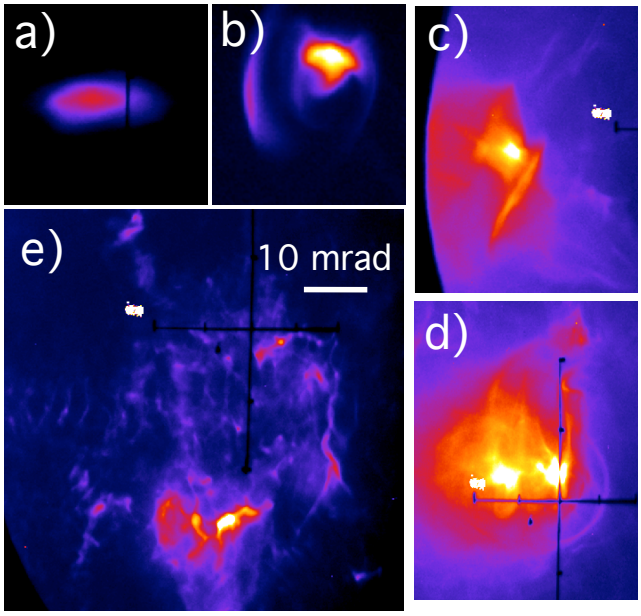

Figure 6.4: Representative electron beam profile images in the transverse ($x_2 - x_3$, horizontal-vertical) plane. a) 500μm nozzle: single, localized filament. b) 1 mm nozzle: generally a single beam, with larger divergence than the 500 μm nozzle. c) 2 mm nozzle: beam divergence increased d) 3 mm nozzle: significantly divergent beam e) 5 mm nozzle: beam is non-local and heavily filamented. The spatial scale shown applies in both vertical and horizontal axes, and is equal for all subfigures.

Reconstructed density maps confirmed the increasing plasma interaction length as the nozzle diameter increased. The narrowest nozzle used was 500 μm and produced a plasma channel of nearly 380 μm. At this length a single electron beam with a broad energy between 20 and 50 MeV was consistently produced (51 of 62 shots). The

beam was elliptical and showed no evidence of multiple bunches (Fig. 6.4a). At this length beam-loading has not yet occurred and injection at the back of the bubble is continuous, resulting in the broad energy spectrum observed [149]. From the scalings described previously, the plasma channel is too short for maximum acceleration and the electron population does not rotate in phase space, explaining the low maximum energy achieved with this nozzle.

Using a 1 mm conical nozzle to lengthen the plasma channel, electron beams were often produced with broad spectra, though monoenergetic beams were also observed. The channel was sustained for 880 μm, which was long enough to accelerate the electron beam to approximately 190 MeV. These high-energy beams are the result when electrons have gained maximum energy from the laser-sustained plasma wave, but before dephasing slows and spreads the beam.

The 2 mm nozzle produced a plasma channel of approximately 1800 μm. The electron spectrometer reveals quasi-monoenergetic or dual-peaked spectra with initial signs of transverse beam spread. Figure 6.5c) shows an energy spectrum from this plasma length. Although little off-axis signal is observed on the spectrometer images, the profile images show either one or two beam main filaments surrounded by a disperse 'halo' (Fig. 6.4 c-e). Because these electrons are not seen on the spectrometer, they are likely below 20 MeV and thus outside of the spectrometer energy detection range. The pump depletion length can be estimated at 1.1 mm for an electron density of 1.4×10^{19} cm^{-3}, which was the density observed for this nozzle. Consequently, significant charge at higher energies was not observed for lengths longer than this nozzle in this experiment.

At 3 mm, both the profile and spectra images showed increased beam divergence (Fig 6.4 d and 6.5 d). Beams were created consistently, but no mono-energetic spectra were recorded. It is expected that after propagation through this length of gas target the laser pulse is depleted far below the the intensity necessary to drive a wake. As

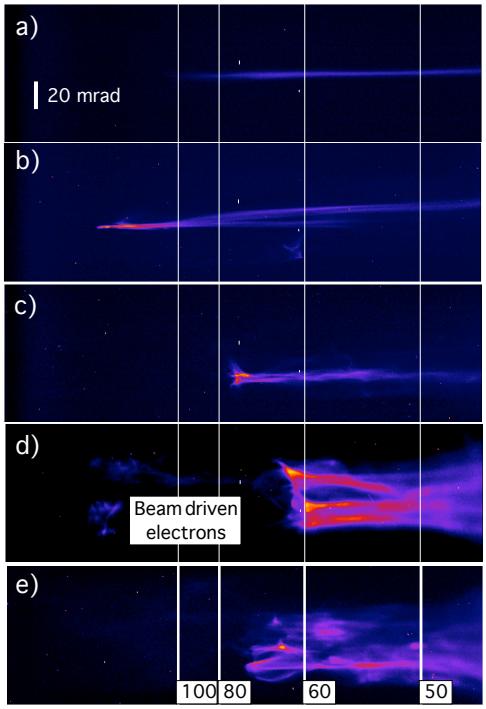

Figure 6.5: Representative electron spectrometer images. Energy increases from right to left, and is indicated in MeV by the vertical bars. Tother axis is the angular distribution in the x_2 direction. The spatial scale shown is equal for all subfigures. The spectra are from: a) 500μm nozzle, b) 1 mm nozzle, c) 2 mm nozzle, d) 3 mm nozzle, e) 5 mm nozzle. The maximum energy shown in frame b is approximately 190 MeV.

a result, the profile images showed a 'halo' on all shots. This effect is evident in the spectrometer images as well, where filaments with nearly equal energy are displaced in space (vertical separation in Fig. 6.5 d-e). In this case, the leading electron bunch is propagating through the He plasma and begins to drive its own plasma wake. It subsequently starts to become susceptible to current filamentation instabilities as the fast electron beam is neutralized by upstream electrons. There is also evidence of small bunches of electrons with energies near 200 MeV, consistent with beam driven acceleration of a small portion of the rear of the bunch or trapping of secondary bunches [210].

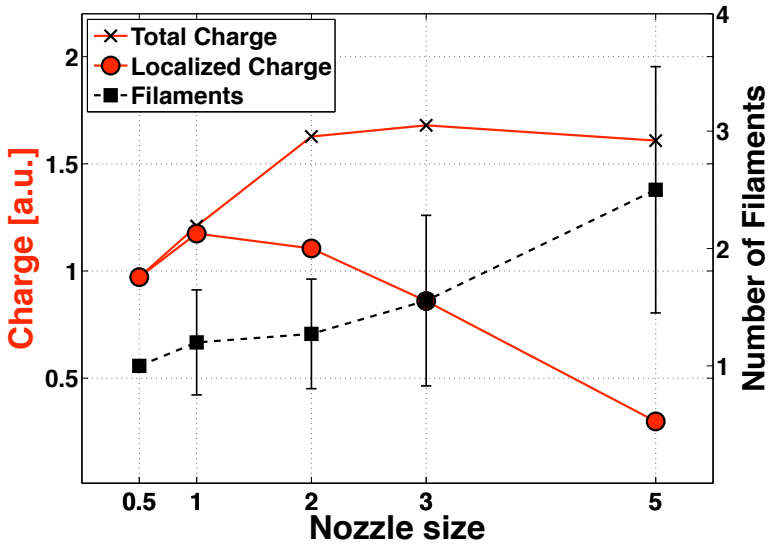

Figure 6.6: Plot of total charge, localized charge, and number of filaments per image. Localized charge is defined as integrated intensity when electrons outside of filament bunches (as identified algorithmically based on intensity) are excluded. The charge in the beam shows an inflection around the 2 mm length, while the number of filaments and the charge in the halo both increase with plasma length.

The largest diameter nozzle used was 5 mm, and yielded a plasma channel of nearly 4500 μm. The beam profile at this stage is highly filamented, with multiple bunches evident in the beam profile, Fig. 6.4e. Integrating the total charge collected

on the profile LANEX suggests a saturation in the number of electrons injected (Fig 6.6). This was quantified by integrating the charge on the profile LANEX in the regions identified as primary beams. This analysis shows the effect of beam erosion, as indicated by the halo and decrease in localized charge, at plasma lengths beyond the dephasing length. In addition, there are a large number of small filaments observed in the beam profile for this propagation length, qualitatively different from structures seen in the shorter plasma lengths. Modifications to the plasma channel profile at this length affected electron production, but beam filamentation was evident whenever electrons were observed, regardless of the details of the plasma profile.

The main filament is not susceptible to the instability as it is both very relativistic, $\gamma_b > 100$, and has small transverse extent compared with c/ω_p. However, for the 'halo', which has particle energies below 20 MeV, a larger divergence and a beam density not far below the background density, the growth-rate can be estimated, for $\gamma = 16$ and $n_b/n_p = 1/100$, as $\Gamma = \omega_p/40$. The length propagated to achieve 8 e-foldings, corresponding to a gain of 3000, is $50 \cdot 2\pi c/\omega_p$, or 500 μm for a density of 1.1×10^{19} cm^{-3}. This 1D estimate suggests that filamentation is qualitatively feasible given the parameters of this experiment. However, 3D effects and saturation of the instability will affect the quantitative degree of growth measured in experiment.

6.4 Simulations

Computer modeling of relativistic particle beams proceeds in a fundamentally different way than the radiation hydrodynamic simulations described in Chap. VII. Instead of calculating the properties of a "large" fluid element as it convects through the system, simulations of LWFA experiments solve Maxwell's equations for the fields and resultant motions of individual particles. In particular, in addition to Maxwell's

equations, the motion of each particle j is described by the equation set

$$\frac{\mathrm{d}\mathbf{r}_j}{\mathrm{d}t} = \mathbf{v_j} \tag{6.5a}$$

$$\frac{\mathrm{d}\mathbf{v}_j}{\mathrm{d}t} = \frac{q_j}{m_j}\left(\mathbf{E} + \frac{\mathbf{v}_j \times \mathbf{B}}{c}\right) \tag{6.5b}$$

$$\rho_e = \sum_j q_j \delta(\mathbf{r}_j - r) \tag{6.5c}$$

$$\mathbf{J} = \sum_j q_j \mathbf{v}_j \delta(\mathbf{r}_j - \rho), \tag{6.5d}$$

where $\mathbf{E}$, $\mathbf{B}$, and $\mathbf{J}$ are the electric field, magnetic field, and charge density, respectively. The process is iterated through cycles depicted by [63]

$$\{\mathbf{r}_j, \mathbf{v}_j\} \rightarrow (\rho_e, \mathbf{J}) \rightarrow (\mathbf{E}, \mathbf{B}) \rightarrow \{\mathbf{r}_j, \mathbf{v}_j\} \rightarrow \text{etc..} \tag{6.6}$$

This type of simulation is known as particle-in-cell (PIC), indicative of the strategy of following individual particles through the computational mesh [45]. Only the negligible effects of quantum mechanical corrections and particle collsions are omitted from the self-consistent PIC calculations, making these codes potentially very accurate [70]. However, individual particle tracking quickly becomes computationally expensive, and modern PIC codes rely on massive parallelization in modeling fully 3D systems.

One widely-used PIC code is the *OSIRIS*, developed by researchers at the Insituto Superior Tecnico, University of California, Los Angles, and the University of Southern California. Version 2.0 of the code was employed by Dr. Alec Thomas to model the conditions in the experiment described in §6.3. Two simulations were run. The first, denoted as "Simulation 1", modeled the propagation of gaussian laser pulse with pulse duration 29 fs FWHM, beam waist $w_0 = 10$ μm and normalized vector potential of $a_0 = 4$ in a helium plasma with a fully ionized electron density of $0.005 n_c$. The density profile consisted of a vacuum region followed by a short linear ramp of length 63.7 μm

and then a region of constant density. This simulation was run using 2 particles per cell with a resolution of 6π cells per λ_0 in the propagation direction (x_1) and $2\pi/3$ cells per λ_0 in both directions perpendicular to propagation (x_2 and x_3).

Fig. 6.7(a-b) shows the longitudinal current density in a window moving at c, after propagation of (a) 0.84 mm and (b) 2.9 mm of the laser. In (a), the laser pulse drives a region of strong electron cavitation, forming an accelerating bubble structure. Significant electron charge is self-trapped and accelerated in the bubble to an energy exceeding 300 MeV in a quasi-monoenergetic peak with a broad energy spread. Depletion of the laser driver occurs subsequently, and after 2.9 mm propagation (b) the laser no longer generates a wakefield. However, the electron beam driver itself now generates its own wakefield through space-charge repulsion [34]. This serves to accelerate of a small group of electrons from the rear of the electron bunch to energies in excess of 400 MeV. Simultaneously, erosion of the electron beam driver head occurs, the latter resulting in a lower energy and more diffuse cloud of electrons, as seen in the experiments. The beam driven wakefield is unstable to the electron beam hosing instability in an ion channel [49, 47], which ultimately results in filamentation and destruction of the beam structure.

By 3.5 mm the beam structure is sufficiently fragmented and/or eroded to such an extent that the beam charge profile is indistinguishable from noise, as the density has fallen to below the background level. Phase-spaces indicate that there is a significant population of the original beam in the diffuse cloud with an average forward momentum distribution below 20 MeV. To model the behavior of this low energy 'halo,' "Simulation 2" was run without a laser pulse, with a resolution of $\pi/3$ cells per λ_0 in x_1 and π cells per λ_0 in x_2, x_3. An initially spatially uniform electron beam of density $0.0005n_c$ with a Gaussian temporal profile of duration $150/\omega_0$ average momentum $p_{x_1} = 20m_ec$, and a thermal distribution with $\Delta p_{x_1} = 20m_ec$, $\Delta p_{x_2,3} = 2m_ec$ was propagated in a uniform plasma of density $n = 0.005n_c$. The

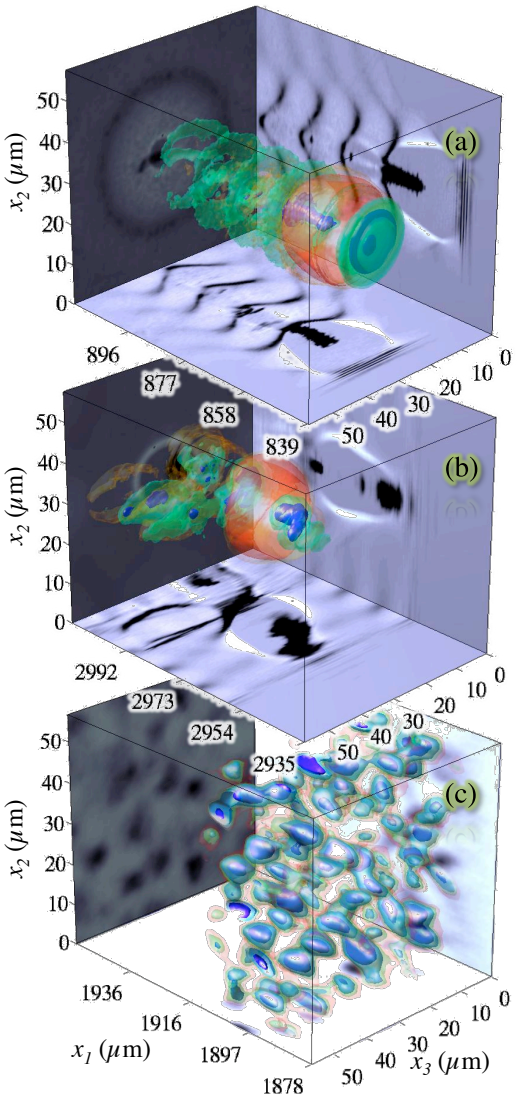

Figure 6.7: Isosurface plots from 3D OSIRIS 2.0 [70] simulations in a window moving at c with side panels displaying slices through the center of the box. (a-b) The longitudinal *current density* in simulation 1 after laser propagation of (a) 0.84 mm and (b) 2.9 mm. Isosurfaces are at (blue, green) 10% and 2% of minimum and (red, orange) 25% and 50% of maximum current. (c) Final *charge density* of the electron beam of simulation 2, with isosurfaces at 75%, 70%, 65% and 50% maximum.

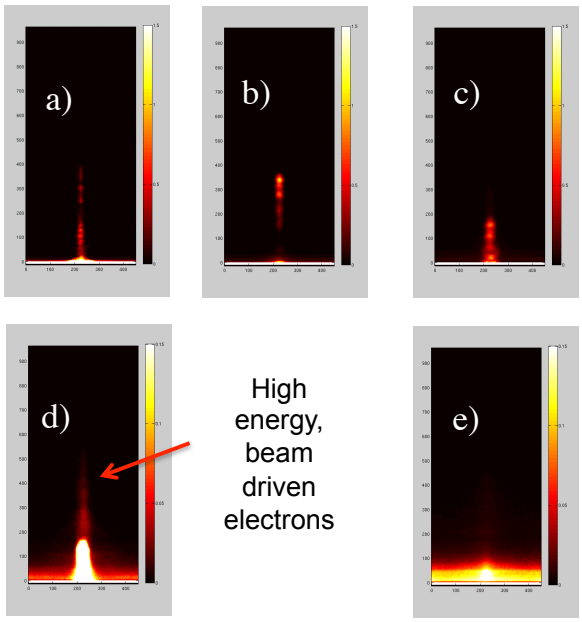

Figure 6.8: The corresponding $p_z - x$ phase spaces of the frames shown in Fig. 6.7. They correspond to propagation lengths of: a) 1 mm, b) 2 mm, c) 3 mm, d) 3 mm, with intensity adjusted to show beam-driven electron population, and e) 5 mm.

beam density and temporal profile was taken to be similar to those observed in simulation A at 3.5 mm. Being a separate population from the background electrons allowed the easy identification of structures formed in the beam from filamentation instabilities. After 1.9 mm of beam propagation the instability had saturated, and the area A of the filaments projected onto a 2D grid were analyzed using a threshold image at half maximum intensity. Their diameter, defined as $d = 2\sqrt{A/\pi}$ was found to vary between $0.57c/\omega_p$ and $1.74c/\omega_p$ with a mean of $1.07c/\omega_p$, consistent with the current filamentation instability.

These experiments were motivated by recent theories regarding the radiation signatures from gamma-ray bursts. At the longer gas target lengths, this work demonstrates a potential test bed for such laboratory astrophysics research. However, the sensitivity of the electron beam properties to the plasma conditions in the shorter length nozzles highlight the narrow range of parameter space one must work in to

achieve a consistent electron beam. Before a full-scale laboratory astrophysics experiment can be realized, instabilities like hosing and filamentation must be *controlled*, and then made to grow in a manner well-scaled to the astrophysical system. Finally, we note encouraging results from X-ray measurements under these conditions [125], which showed an increase in x-ray flux for up to a 10 mm nozzle, beyond the point where betatron radiation from the wakefield would be expected. This indicates radiation generation in the filamented region, and motivates further investigation into the radiation produced by relativistic charged particle beams in the laboratory and in astrophysics.

CHAPTER VII

Radiative Rayleigh Taylor instabilities

7.1 Background

As alluded to in Chap. I, the ICF capsule implosion process is hampered by instability growth, primarily the Rayleigh-Taylor instability (RTI). Rayleigh-Taylor is the mechanism by which layers of fluids of differing densities minimize potential energy in the presence of a pressure gradient. The instability is characterized by "bubbles" and "spikes" of interpenetrating fluids, and was first described by Lord Rayleigh in 1900 and later by Geoffrey Taylor in 1950 [173, 206]. In addition to its effect on ICF capsule implosion, as described below, RTI can also occur at the contact surfaces in exploding stars and may be responsible for the mixing observed in the ejecta from supernova 1987A [61, 99].

During capsule implosion, opposing pressure and density gradients occur at two stages, both of which are prone to RTI. "Acceleration phase" RT occurs during ablative acceleration, at which time perturbations on the outer surface of the capsule may seed RT growth. Later, "deceleration phase" RT can occur when the pressure gradient in the compressed, low-density fuel opposes the dense, incoming shell. This stagnation event proceeds over ≈ 200 ps, during which time the fuel-shell interface is susceptible to Rayleigh-Taylor growth [145].

This latter configuration has been studied as it pertains to ICF both numerically

[7, 189] and experimentally [25, 151, 124, 182]. Additional experiments, designed to be relevant to astrophysics, also provide data on deceleration phase RTI [136, 135, 84]. The work of Kuranz *et al.* explores deceleration phase-like RTI in a hydrodynamic context [1]. However, the conditions in an ICF capsule are not purely hydrodynamic, and radiation in particular plays a significant role in the dynamics.

To understand the mechanisms by which radiation can stabilize a Rayleigh-Taylor unstable system, it is useful to work from the non-radiative Rayleigh Taylor growth rate. A simple derivation of the linear, inviscid, non-radiative, uniform fluid Rayleigh-Taylor growth rate follows. Beginning the conservation equations for mass and momentum:

$$\frac{\partial \rho}{\partial t} + \mathbf{u} \cdot \boldsymbol{\nabla} \rho = 0 \tag{7.1}$$

$$\rho \frac{\partial \mathbf{u}}{\partial t} + \rho \mathbf{u} \cdot \boldsymbol{\nabla} \mathbf{u} = -\boldsymbol{\nabla} p + \rho \mathbf{g} \tag{7.2}$$

where g is the effective acceleration, taken to be in the -$\hat{\mathbf{z}}$ direction, as shown in Fig 7.1. In laboratory experiments, however, the acceleration is rarely gravity, but instead a gradient in pressure. In this geometry $p = p(z)$ and $\rho = \rho(z)$. Perturbing the system slightly takes this quantities from the rest values to $p = p_0 + p_1$, $\rho = \rho_0 + \rho_1$, and $u = u_1$, where the subscript 1 denotes a small value (the system is initially at rest, $u_0 = 0$).

To linearize, we substitute the perturbed quantities into equations 7.1-7.2 and discard terms that are second order in smallness. Doing this, and using the incom-

[1] While the design and subsequent analysis of these experiments assumed a purely hydrodynamic system, this is under further investigation. It is thought that some structure observed in data suggests the presence of magnetic fields, a result of the Biermann-Battery effect, which play a role in the density profile of the spikes. This is under investigation in ongoing experiments by Di Stefano.

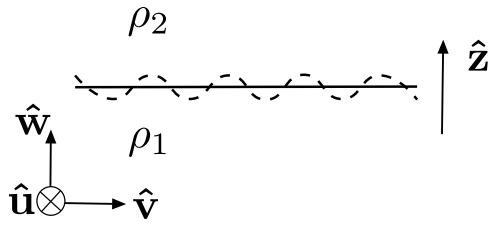

Figure 7.1: System for RT analysis. The perturbed interface is shown as dashed variation from the solid, unperturbed interface.

pressibility condition $\boldsymbol{\nabla} \cdot \mathbf{u} = 0$:

$$\frac{\partial}{\partial t}(\rho_0 + \rho_1) + \mathbf{u} \cdot \boldsymbol{\nabla}(\rho_0 + \rho_1) = 0 \tag{7.3}$$

$$\frac{\partial \rho_1}{\partial t} + \mathbf{u} \cdot \boldsymbol{\nabla}\rho = 0 \tag{7.4}$$

and

$$(\rho_0 + \rho_1)\frac{\partial \mathbf{u}}{\partial t} + (\rho_0 + \rho_1)\mathbf{u} \cdot \boldsymbol{\nabla}\mathbf{u} = -\boldsymbol{\nabla}(p_0 + p_1) + \rho\mathbf{g} \tag{7.5}$$

$$\rho_0 \frac{\partial \mathbf{u}}{\partial t} = -\boldsymbol{\nabla} p_1 + \rho_1 \mathbf{g} \tag{7.6}$$

From Fig. 7.1, one can evaluate the derivatives of these equations along the orthogonal velocity vectors shown. Dropping the subscript on non-perturbation terms for brevity, Eqn. 7.4 becomes

$$\frac{\partial \rho_1}{\partial t} + w \cdot \frac{\partial \rho}{\partial z} = 0 \tag{7.7}$$

and Eqn. 7.6 has components:

$$\rho\frac{\partial u}{\partial t} = -\frac{\partial p_1}{\partial x} \tag{7.8}$$

$$\rho\frac{\partial v}{\partial t} = -\frac{\partial p_1}{\partial y} \tag{7.9}$$

$$\rho\frac{\partial w}{\partial t} = -\frac{\partial p_1}{\partial z} - \rho_1 g \tag{7.10}$$

$$\tag{7.11}$$

With these equations we look for waves with represent surface waves in x and y, growing in time with growth exponent γ. Notably, this modification of this growth rate is the primary metric for our experimental design of a radiative RT system. Assuming a form proportional to $\exp(ik_x x + ik_y y + \gamma t)$ for $\mathbf{u}$, ρ_1, and p_1, we have:

$$\gamma\rho_1 = -w\frac{\partial \rho}{\partial z} \tag{7.12}$$

$$\gamma\rho u = -ik_x p_1 \tag{7.13}$$

$$\gamma\rho v = -ik_y p_1 \tag{7.14}$$

$$\gamma\rho w = -\frac{\partial p_1}{\partial z} - \rho_1 g \tag{7.15}$$

With the notation $\mathrm{k}^2 \equiv k_x^2 + k_y^2$ one has

$$\gamma\rho(ik_x u + ik_y v) = k^2 p_1. \tag{7.16}$$

Applying the incompressibility condition, Eqn 7.16 can then be written

$$-\gamma\rho\frac{\partial w}{\partial z} = k^2 p_1.. \tag{7.17}$$

Use of Eqn. 7.12 in Eqn. 7.15 gives

$$\gamma\rho w = -\frac{\partial p_1}{\partial z} + \frac{gw}{\gamma}\frac{\partial \rho}{\partial z}, \tag{7.18}$$

and the quantity p_1 can be solved by taking a derivative of 7.17, yielding

$$\frac{\partial p_1}{\partial z} = \frac{-\gamma}{k^2}\frac{\partial}{\partial z}\left(\rho\frac{\partial w}{\partial z}\right). \tag{7.19}$$

One then has the set of equations:

$$\gamma\rho w = \frac{\gamma}{k^2}\frac{\partial}{\partial z}\left(\rho\frac{\partial w}{\partial z}\right) + \frac{gw}{\gamma}\frac{\partial \rho}{\partial z}, \tag{7.20}$$

$$\rho = \frac{1}{k^2 w}\frac{\partial}{\partial z}\left(\rho\frac{\partial w}{\partial z}\right) + \frac{g}{\gamma^2}\frac{\partial \rho}{\partial z}, \tag{7.21}$$

$$k^2 w\rho - \frac{k^2 gw}{\gamma^2}\frac{\partial \rho}{\partial z} = \frac{\partial}{\partial z}\left(\rho\frac{\partial w}{\partial z}\right). \tag{7.22}$$

Although $\mathbf{u}$ and w are continuous at z=0 (in order for the fluid on either side to remain in contact), other quantities need not be. To derive jump conditions at the interface, we must difference and integrate equations 7.17 and 7.18, respectively. These quantities are continuous and differentiable everywhere except z=0, and thus can be described by the sum of two functions multiplied by the Heavyside step function $\Theta(z)$ at the interface. Taking the bounds of the integral to be vanishingly small increments above and below the interface yields a non-zero integral only in cases where the integrand is described by $\Theta(z)$ With the notation $\Delta f \equiv f(0)_+ - f(0)_-$, where subscripts indicated approaching the interface from the positive and negative directions, then across the interface Eqn. 7.17 becomes

$$k^2\Delta p_1 = -\gamma\Delta\left(\rho\frac{\partial w}{\partial z}\right) \tag{7.23}$$

and integration of Eqn. 7.18 gives

$$\Delta p_1 = \frac{g}{\gamma}\Delta(w\rho) \tag{7.24}$$

where the first term in Eqn. 7.18 is zero because w is continuous across the interface, as described above. These can be combined to form the jump condition:

$$k^2 g\Delta(w\rho) = -\gamma^2\Delta\left(\rho\frac{\partial w}{\partial z}\right). \tag{7.25}$$

The simplest case one can analyze are two different, uniform density fluids. In this case, Eqn. 7.22 becomes:

$$k^2 w = \frac{\partial^2 w}{\partial z^2} \tag{7.26}$$

which is easily solved with

$$w = Ae^{kz} + Be^{-kz} \tag{7.27}$$

where A and B are constants. Enforcing that $w = 0$ as $z \to \pm\infty$ and requiring continuity at the interface leads to:

$$\begin{aligned} w_1(z) &= Ae^{kz} \quad (z < 0) \\ w_2(z) &= Ae^{-kz} \quad (z > 0) \end{aligned} \tag{7.28}$$

where the subscripts are the same as those given for ρ in Fig. 7.1. The fact that these solutions decay as $|z|$ increases will be utilized below in our description of ablative stabilization of a Rayleigh Taylor unstable front. For the non-ablative case, using this solution for $w(z)$ in the jump condition 7.25, and noting that $w_1(0) = w_2(0) = 1$,

gives

$$k^2 g \left(w_2(z)\rho_2 - w_1(z)\rho_1\right)\Big|_{z=0} = -\gamma^2 \left(\rho_2 \frac{\partial w_2}{\partial z_+} - \rho_1 \frac{\partial w_1}{\partial z_-}\right) \tag{7.29}$$

$$k^2 g(\rho_2 - \rho_1) = -\gamma^2(\rho_2(-k) - \rho_1 k) \tag{7.30}$$

or, rearranging:

$$\gamma = \sqrt{kg\left(\frac{\rho_2 - \rho_1}{\rho_2 + \rho_1}\right)} = \sqrt{A_n k g}. \tag{7.31}$$

The Atwood number, $A_n = (\rho_2 - \rho_1)/(\rho_2 + \rho_1)$, is a measure of the magnitude of the density jump. From 7.31 one can see that the solutions for w and ρ, assumed to be proportional to $\exp(\gamma t)$, are unstable for $\rho_2 > \rho_1$. This is the linear Rayleigh-Taylor growth rate solution for uniform fluids, which can be modified to include effects from viscosity, density gradients, ablation, and several other mechanisms affecting RT growth.

Radiation in particular has been investigated as a means of controlling instability growth in ICF. One effect of radiation in the context of RTI is to ablate material from the unstable surface. Extensive work has been performed to study ablatively stabilized Rayleigh-Taylor growth, much of which has been framed in the context of an applied heat source in the form of a laser or thermal x-ray source [121]. In seminal work on ICF, Nuckolls and Bodner described RT instabilities on the outer surface of the capsule which are ablatively stabilized by temperature gradients in a process deemed "fire-polishing" [165, 18, 17]. More recently, numerous experiments have investigated ablative RT in a variety of geometries [86, 85, 182, 124, 25, 92, 8, 196].

Accompanying the experimental effort, a fully self-consistent theoretical model of radiative stabilization has been developed by Betti, Goncharov, and others,which includes thermal conduction and radiation transport through the ablation surface

[189, 218, 91, 90, 16, 145, 190, 90, 60]. The applicability of these theories to a given experiment depends on the details of the hydrodynamic profiles and energy fluxes in the system. While exploring the full breadth of ablative RT theory is beyond the scope of both this document and often experimental analysis, Eqn. 7.31 can be modified in a systematic way to capture the physics at work in the experiment described hereafter.

An version of Eqn. 7.31 was proposed by Takabe in 1985, and is often referred to as the Takabe RT growth rate [201, 132]. Slightly modified from this original form, the radiatively stabilized RT growth rate is given by:

$$\gamma = \alpha\sqrt{\frac{kg}{1+kL_m}} - \beta k v_a. \tag{7.32}$$

It is also noted that this form of γ has been shown to be an appropriate simplification of the full Betti-Goncharov treatment in cases where the Froude number (given by $v_a^2/(gL)$, the ablation velocity squared on acceleration times scale length) is low and one limits analysis to long wavelengths ($kL << 1$).

A phenomenological description of the modifications to the simple $\sqrt{Akg}$ growth rate captured by Eqn. 7.32 was given by Kilkenny [121]. The first term reflects the dependancies of the linear growth rate, except that the Atwood number has been modified to reflect a gradient in densities between the materials. Approximating the shape of this interface by e^{-kL_m} and taking $kL_m << 1$, then to first order the effective Atwood number can be expressed as $(1+kL_m)^{-1}$. The density gradient scale length L_m quantifies this effect. This expansion of the interface will occur at very small scales for common systems that form an abrupt density jump, but can have a significant stabilizing effect when radiation is being deposited near the interface.

The second stabilizing effect of energy deposition at the unstable interface captured in Eqn. 7.32 is to effectively "move" the interface, via ablation, to a region

where the instability is less pronounced. This effect can be understood by recalling that RT waves are surface waves which decay away from the interface as $e^{-k|z|}$. If one thinks of ablation–whether it be from x-rays or another source–as a mechanism that moves the interface at the ablation velocity v_a, then the position of the interface after some time δt is $v_a \delta t$. Thus, the amount of RT growth after a given time is $\exp(\gamma \delta t - k v_a \delta t)$, which motivates the ablatively-stabilized growth rate given Eqn. 7.32.

7.2 Proposed Experiment

As cited previously, numerous experiments have been conducted to measure the stabilizing effects of radiation in a Rayleigh-Taylor unstable system. However, none of these experiments has produced an embedded, unstable interface which is being heated by an upstream, self-generated radiation source. To investigate the stabilization of RT growth in such a system, an experiment has been designed for the National Ignition Facility (NIF).

The NIF is uniquely suited to perform such an experiment as it is capable of launching a shock fast enough to produce observable radiative effects in materials dense enough to be diagnosed with x-ray diagnostics [133]. The pressure pulse used to launch the driving shock will be created using a hohlraum–a cylinder of high atomic number material with open ends, into which the laser beams of the NIF are pointed. The beams irradiate the interior walls, heating the walls and creating a high-Z (often gold) plasma which radiates into the hohlraum. Hohlraums have been shown to be relatively efficient converters of laser light to near-Planckian thermal radiation, and these thermal x-rays are used to ablatively drive the experiment.

In order to use the thermal x-rays created in the hohlraum to drive a planar target, a section of the cylindrical hohlraum wall is removed and a target is attached. The target consists of a 180 μm thick polyimide (PI) ablator disk, followed by a 10 μm

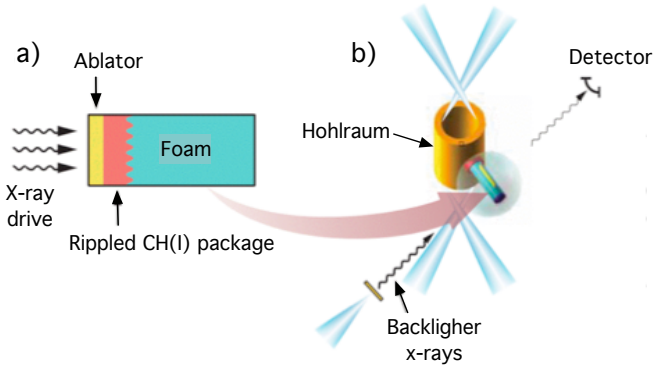

Figure 7.2: a) Experimental target consists of a plastic (CH) ablator strip followed by an iodine-doped tracer layer with machined perturbations to seed RT growth. this is mated to a low density foam. b) The target is mounted to a NIF hohlraum, where thermal x-rays are used to drive the system. Adapted from Kuranz *et al.* [133]

thick gold layer to provide shielding from gold M-band x-ray radiation (2 - 5 keV) from the hohlraum drive. Adjoining is a 150 μm PI disk with a 75 μm thick inset strip of iodine-doped plastic (CHI) at nearly the same density, approximately 1.4 g/cm^3. This iodinated plastic tracer provides a high-opacity material to attenuate diagnostic x-rays at the center of the target, essentially specifying what region of the target is being imaged. On the CHI/polyimide face a 2-D sinusoidal ripple with peak-to-valley amplitude of 7 μm and wavelength of 100 μm is machined to seed RT growth. Mated to the rippled surface is 20 mg/cm^3 SiO_2 foam, which fills the remaining several millimeters of the shock tube.

The x-ray irradiance from the hohlraum which creates the ablative pressure pulse scales as the hohlraum blackbody temperature to the fourth power. Thus, varying the maximum temperature reached by the hohlraum has a significant effect on the strength of the shock which is launched into the polyimide. The temperature is a function of hohlraum size, laser-wall coupling efficiency, and input laser energy, the latter of which can be easily changed in the design of an experiment [144]. Referred to as "drive temperature" in this work, hohlraum blackbody spectra have been recorded

up to $T_R \approx 325$ eV on the National Ignition Facility, representing an upper limit for practical experimental designs in the present context [133, 88].

As the shock front passes through the interface between the higher density PI and lower density foam, Richtmyer-Meshkov [184, 156] and Rayleigh-Taylor instabilities occur. At the seed perturbation wavelength of 100 μm, Rayleigh-Taylor growth is expected to be stabilized by both finite density gradient scale lengths and ablative stabilization. Simulations were performed to understand the density and pressure profiles for a range of drive temperatures.

7.3 Simulations

The specific regime of applicability of ablative Rayleigh Taylor theory is determined by the experimental conditions. In particular, the dimensionless Froude number Fr is significant. With the ablation front width defined as the minimum value of the density gradient scale length [16], $L_m = \rho/\nabla\rho$, each of the parameters needed to calculate Fr can be found from numerical simulations over a range of hohlraum drive temperatures.

Simulations were performed in 1D with the radiation hydrodynamics code HYDRA [152]. Multigroup radiation diffusion was used with tabulated EOS values and opacities generated from the LLNL opacity libraries. Although the RT instability in a physical system is a 2/3D effect, one can extract parameters from a 1D simulation which inform the degree of instability (as discussed in Sec. 7.4). In light of this, the speed of 1D simulations facilitate large parameter scans, motivating their use as a tool for initial experimental design.

One-dimensional HYDRA simulations were initiated with a time-dependent radiation temperature (T_R) profile produced by a 2D HYDRA simulation. This 2D simulation employed implicit Monte Carlo radiation transport, allowing for a non-Planckian energy distribution. This was converted to a time-dependent Planckian

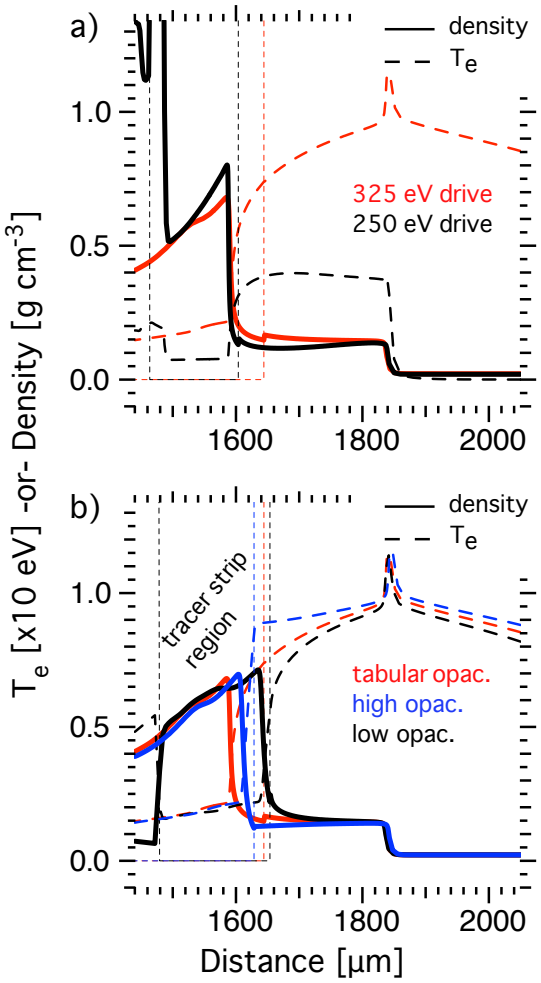

Figure 7.3: Density and electron temperature profiles for various conditions. The time for each was selected to align the shock to the same position down the tube, approximately 1850 μm. a) Material density and temperature from high (325 eV) and low (250 eV) drive simulations, at 12 and 21.5 ns after the drive begins, respectively. b) The same parameters for simulations with artificially high and low CHI tracer strip opacities. Note that the red curves in (a) and (b) are identical.

spectrum with equal total energy, and the resulting T_R profile was used to drive the 1D simulations. This profile was in good agreement with measurements made during a previous test of the hohlraum for this experiment. In this experiment, 600 kJ of laser energy was used to irradiate the hohlraum. The radiation temperature profile was measured with the soft x-ray diagnostic DANTE [48] and was seen to reach a peak temperature of 325 eV [133].

For a 325 eV drive temperature, simulations show that a pressure pulse exceeding 200 Mbar is launched into the polyimide. Figure 7.3(a) shows the material density and electron temperature for the high and low drive cases, 325 eV and 250 eV, respectively. The results are plotted at different times, chosen such that the shock front has progressed an equal distance into the foam (as measured from the irradiated plastic surface) in both cases. In addition to the shock front, located at nearly 1850 μm in each case, there are two significant spatial points of reference. The first is the steep density transition, located at $\approx$1600 μm in Fig. 7.3(a). Specifically, the point behind the shock where the scale length L_m is a minimum is maximally unstable to Rayleigh Taylor. The second spatial point of note is the 1D material interface, indicated by the vertical dashed line in Fig. 7.3. This interface separates the SiO_2 foam from the CHI, which do not mix in the simulation. In the undriven target the density transition and material interface position coincide, but after the shock has passed through this point, the density transition lags behind the material interface. The degree of separation between these features is dependent on the strength of the shock and resultant radiation and material temperatures, as described below.

Examining first the electron temperature, the low drive case shows a rapid heating at the shock front relative to the cold, upstream foam. This temperature is approximately constant in the foam, and cools at the dense plastic layer, as is necessary to maintain a continuous pressure profile across the interface. The high-drive case shows a local temperature spike (a *"Zel'dovich spike"*) at the shock [224]. The temperature

decreases slowly toward the dense plastic, where it cools as in the previous case. Upstream of the shock the temperature remains high and only gradually decreases. This upstream region is heated by the radiation streaming forward from the shock front, forming a radiatively heated precursor.

The difference in drive temperature between the cases results in markedly different density profiles. The increased energy deposited in the plastic in the high drive case ablates material from the dense surface. This decreases the magnitude of the density jump, which is quantified by an increased density gradient scale length L_m. In the high-drive simulation of Fig. 7.3(a), the material interface, indicated by the vertical dashed line, has advanced away from the density transition. The rate at which the point of minimum density gradient recedes from the material interface is the ablation velocity used to calculate Fr in Table 7.1, and in subsequent calculations.

To understand the effects of radiation on the dense, unstable plastic layer, simulations were performed with unphysically high and low tracer strip opacity. In each case, the peak in electron temperature reaches the same value at the shock front. However, in the artificially high opacity case (blue curves in Fig. 7.3(b)), radiation couples very strongly to the material and is absorbed over a short distance at the plastic/foam interface. It is then re-radiated ahead of the interface without significantly lengthening L_m. In the artificially low case (black curves in Fig. 7.3(b)), radiation reaching the plastic-foam interface from the shock streams through the plastic without depositing significant energy (note the spike in T_e is seen at $\sim$1500 μm in the figure, in the plastic drive disk material, which is modeled with a realistic opacity). The point of maximum density gradient remains closer to the interface than the realistic case, as the decreased radiation coupling lessens the ablative effects. The simulations performed with a realistic tracer strip opacity show the longest gradient in material temperature at the interface, and an increased density gradient scale length.

Table 7.1: Parameters derived from 1D HYDRA simulations necessary for calculation of the Froude number Fr and the RT growth rate through the modified Takabe formula.

Peak Drive (eV)	Time (ns)	Interface Position (μm)	Acceleration (um/ns^2)	Min. Density Grad. Scale Length (μm)	Ablation Velocity (μm/ns)	Froude number Fr
225	25.5	1508	0.52	2.8	0.0	0.00
250	21.5	1604	0.94	2.9	0.4	0.06
275	17	1610	1.66	3.7	0.6	0.06
300	14	1636	2.49	4.1	1.6	0.25
325	11.5	1570	3.54	6.7	2.8	0.33
340	11	1616	4.16	8.7	3.3	0.30

7.4 Growth Rate Parameters

From Table 7.1 it is seen that the geometry of the proposed experiments leads to relatively low ablation velocity and long density gradient scale lengths, resulting in Fr < 1. For the initial design of an experiment with a unique geometry, the simplified Betti-Goncharov treatment discussed in section 7.1 and given by Eqn. 7.32 is appropriate.

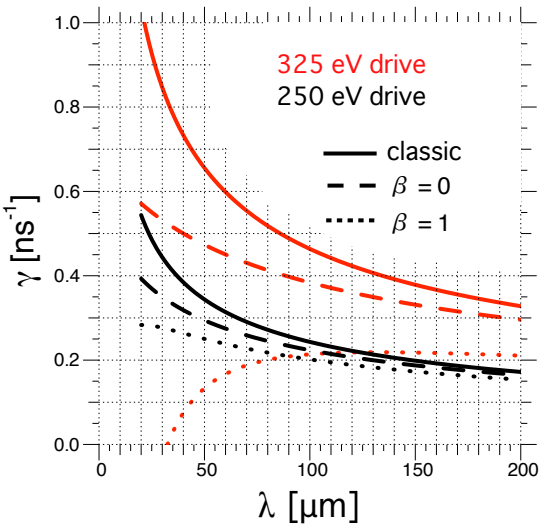

Figure 7.4: Instantaneous growth rates for high and low drive cases, as calculated from the simplified Betti-Goncharov model (Eqn. 7.32). Parameters used were inferred from the 1D simulations for the time at which the shock progressed an equal distance, approximately 1600 microns.

From the 1D simulations all of the parameters needed to evaluate Eqn. 7.32 can be calculated. The instantaneous growth rate γ is shown for low and high drive cases in Fig. 7.4. They are compared at 21.5 ns for the 250 eV drive case and 11.5 ns for 325 eV, when the interface is approximately in the middle of the experimental field of view, as in Table 7.1. The curve labeled "classic RT" shows $(kg)^{1/2}$ growth, where the Atwood number had been taken to be unity, expressing the maximal possible growth rate. The density gradient stabilized term reflects Eqn. 7.32 with $\beta = 0$ (no ablative stabilization), while the final curve reflects this same equation with $\beta = 1$ (both use

$\alpha = 1$). The high-drive conditions are seen to have a significantly higher instantaneous growth rate, while wavelengths below a few tens of microns are predicted to be stabilized. It is noted that for small wavelengths the simplifying assumptions of Eqn. 7.32 are not strictly valid, and the growth rate must be modified [91]. However, in the proposed experiment using a doped tracer strip and a seeded, long-wavelength perturbation, high-wavenumber modes will not be diagnosable and the details of their evolution in the presence of a strongly radiative shock are left as future work.

Although the growth will be strongly non-linear at the time of observation, calculation of the growth exponent is often still a useful parameter [57]. Defined by the integration of the the instantaneous growth rate,

$$G = \int_{t_0}^{t} \gamma(t')dt', \tag{7.33}$$

the growth exponent is the number of e-folding by which initial perturbations would grow if the system remained in the linear regime. Performing this integral numerically for the experimentally-relevant 100 μm wavelength yields $\mathrm{G}_{250eV} = 2.5$ and $\mathrm{G}_{325eV} = 1.6$ after each interface has reached 1600 μm. This suggests approximately a factor of 2.5 larger amplitude growth for the 250 eV drive experiment than the 325 eV drive case. Although this is a simplified analysis, this predicted growth matches well to 2D simulations performed for this system. In these simulations the half-width spike length at the same 1600 μm interface position in high drive case was 42 μm, compared to 87 μm in the low drive case, corresponding to a growth ratio of 2.1.

These simulations serve to aid in understanding the basic physics mechanisms in the upcoming Rayleigh-Taylor experiment on the National Ignition Facility. The novel conditions of the experiment—a strongly radiative shock crossing a plastic-foam interface, with ablation occurring from the upstream side of the unstable interface—will test the applicability of the simplified RT growth rate formula (Eqn. 7.32) for this set

of conditions. Upon performing the experiment, measurements of spike growth should provide data needed to inform selection of α and β in Eqn. 7.32. Additionally, measurements will inform future work investigating the stabilization mechanisms which may play a role in RT growth of this unique system, including the possible coupling of unstable modes at the shock front with those at the ablating material interface [60]. Such efforts will likely also require 2 or 3-D simulations and additional experiments, and should result in improved models for radiatively stabilized Rayleigh-Taylor growth in a variety of cases.

CHAPTER VIII

Conclusions and future directions

This document describes several laboratory-based, astrophysically-relevant experiments that I have played a leading role in. All of these projects – the investigation of radiative shocks with x-ray Thomson scattering on the OMEGA laser, the exploration of electron beam formation, acceleration, and filamentation on the HERCULES laser, and the design of radiative Rayleigh-Taylor experiments to be performed at the National Ignition Facility – are somewhat different from one another. However, each is motivated by the desire to bring an important astrophysical phenomenon into the laboratory where the scientific method can be brought to bear. Each project was conducted in previously unexplored regimes or configurations, and each provides a clear point from which to move forward. A brief summary and future direction for the central topics are provided below.

8.1 Astrophysical Radiative Shocks

The experiments performed using shocked xenon gas represent the most complex atomic structure yet probed with x-ray Thomson scattering. This work was undertaken not as a test of the diagnostic principle, but in an effort to better understand a specific system of interest. During this process, advances were made in plasma modeling, experimental design, and diagnostic capabilities. The work of the author was

devoted largely to experimental design and data analysis, a year-by-year summary of which is provided in Tbls. 8.1-8.3. The most recent designs illustrate the difficulty of applying XRTS to the xenon radiative shock system, but also provides a framework from which to design future experiments.

In particular, the successful application of XRTS to low-density, high-Z systems requires complete mitigation of low-Z contributions to scattering. For the xenon radiative shock system at the University of Michigan, this may involve replacing the narrow shock tube with a gas cell, or allowing the shock to expand into a cavity where no low-Z material is present. This certainly requires one to revisit the analysis of Chap. III, and would likely result in a different set of plasma conditions than those described here. Additionally, measurement of free electron fraction in a hot, high-Z material necessitates an as yet unachieved detector resolution and dynamic range. Despite these challenges, XRTS allows for the measurement of parameters of crucial importance to understanding radiative shocks. Continued improvement in x-ray sources, detectors, driver facilities, and experimental design will all contribute to the successful application of XRTS to radiative shock systems in the future.

8.2 Current Filamentation instabilities

The past two decades have seen tremendous advances in laser technology, with the advent of laser chirped-pulse amplification of specific importance for ultra-intense laser physics. This has led to an explosion of research in the field of ultrafast laser-plasma interaction, including the realization of laser wakefield acceleration. The LWFA technique has great potential, and has been proposed as the driving mechanism for next generation particle colliders [28]. Additionally, the relativistic charged particle beams produced via LWFA are central to fast-ignition ICF concepts [172], and have also been used as a generating mechanism for bright, coherent x-ray sources [125]. However, the motivation of the experiment detailed here – to compare the

2010	
Key Features	Results and Conclusions
· First attempt at XRTS in Xe. · Two equal-angle zinc x-ray sources to increase input photon count. · Same-shot measurements with flat-crystal zinc spectrometer and x-ray streak camera · Laser-cut gold shields for highly accurate scattering volume	· Recored scattered zinc spectrum, including detailed source spectrum. · First use of streak camera to measure shock position and acceleration of Xe system · Unexpectedly high x-ray flux on detector · Evidence of line emission from unidentified materials made fitting difficult, but unexpectedly high elastic scattering was clear.

Table 8.1: Summary of 2010 Xe x-ray Thomson scattering experiments.

2011	
Key Features	Results and Conclusions
· Thicker shielding (100 μm) to decrease background · Additional shielding added to limit the extent of the input x-ray source · Slightly off-perpendicular x-ray streak camera · Pair of ZSPEC instruments: primary with curved crystal and monitor with flat crystal	· Curved crystal allowed for us to determine the location of secondary sources, in addition to scattering from the scattering volume · Scattering from an undriven target was compared to full data, to isolate scattering from the scattering volume · Reduced data is well fit by xenon with anomalously-high Z_{free} fraction, but also by scattering from polyimide (shock tube) at reasonable conditions · Despite seeming to function properly, no shock observed with streak camera

Table 8.2: Summary of 2011 Xe x-ray Thomson scattering experiments.

2012	
Key Features	Results and Conclusions
· Fielded the imaging x-ray Thomson scattering (ixts) spectrometer with toroidally-bent crystal · Single x-ray source was collimated with 300 μm-diameter laser-cut aperture · Gold shielding was coated in plastic to mitigate hot electrons · Scattering slit made much narrower than the shock tube, to exclude the strongest scattering from plastic	· The familiar structure of the Xe radiative shock system is seen in the 1D imaging of the ixts · Extra sources were completely isolated from the data of interest · Undriven target used to subtract background from the driven-target measurement · Comparison of the reduced data to the inverse model, through the xrts code, is in good agreement · The small inelastic peak precludes a temperature measurement of the system

Table 8.3: Summary of 2012 Xe x-ray Thomson scattering experiments.

observed radiation signature from gamma-ray bursts to the radiation produced by relativistic electrons under controlled conditions in the laboratory – remains a novel use of the technology.

The experiments of Chap. VI entailed a systematic varying the gas jet length and measuring the effect on the electron beam. The measurements are well-supported by analytic and computational predictions for the plasma conditions of the experiment, and may be used to optimize LWFA electron beams in future experiments. Additionally, beam filamentation was directly observed. This is thought to occur in gamma-ray bursts, mediated by Weibel or other current filamentation instabilities, and lead to the observed signal from these astrophysical explosions. Building on the work described here, an experiment with a moderate-energy electron beam made to pass through extended lengths of neutral gas (beyond the longest, 5 mm nozzle used here) may allow measurement of the filamentation growth rate and discrimination of the specific mechanism at work. The addition of a broadband x-ray spectrometer would enable direct comparison between the radiation produced by these electrons and the forward-directed "jitter radiation" that has been proposed in the literature. Finally, if such a testbed can be produced, it may be possible to create a configuration with more direct applicability to the astrophysical system. Interesting conditions would include colliding beams, beam-clump interactions, or beam interactions with imposed magnetic fields.

8.3 Radiative Rayleigh Taylor Instability

The radiative Rayleigh-Taylor experiment detailed in Chap. VII represents unexplored regime of hydrodynamics and radiation transport in a near-solid density material. Only on the National Ignition Facility can such an experiment be performed [133], and as such it marks the first of many experiments that will touch novel parameter space using this new scientific tool. The work presented here was

undertaken both to aid in the design of the experiment, but also to establish an understanding of this unique system *before* the observations are made. Upon completion of the experiment, the comparison of data to the quantitative and qualitative conclusions developed here will provide a roadmap for future efforts. In the end, beyond code development and experimental design improvements, the best possible outcome would be that the experiment will raise new questions about the physics at work in the system.

APPENDICES

APPENDIX A

The Thomas-Fermi model

Several methods have been developed for solving the many-body problems that arise naturally in plasma physics. In particular, the problem of solving for the potential resulting from a complex system of ions and electrons has been addressed many ways. The simplest common method is the Debye-Hückel model (DH), which begins with the Poisson equation and assumes a Boltzmann distribution for the electrons and ions. The resulting potential is exponentially decreasing, $V(r) \propto (1/r)\ \exp[-r/\lambda_D]$, and the Debye screening length λ_D arises naturally from the calculation. The use of Boltzmann statistics in DH is only appropriate for weakly coupled plasmas, making these results the limiting behavior for $\Gamma \ll 1$.

One method developed treat systems high-Z, moderately coupled systems that goes beyond the DH theory is the venerable Thomas-Fermi (TF) model. The TF model is widely used, owing to the fact that it is analytically tractable, can be modified for many special cases of interest, and agrees well with calculations from more complicated Hartree-Fock simulations [158]. It is one example of a broad set of models called *ion sphere models*, which establish around each ion a set volume and impose that the potential at and beyond the boundary of the volume exactly cancel. This condition requires charge neutrality within the volume, implying that the nuclear charge Z_A is equal to the bound and free charge $Z_A = Z_B + Z_F$, all of which reside within the ion sphere. More advanced ion sphere models solve the Schrödinger or Dirac equations and thus take into account the atomic structure of the atoms, a feature which is lacking in the TF model. Despite this, a the Thomas-Fermi model illustrates several important features of strongly-coupled plasma descriptions. A short description is given here (following Salzmann [188] and More [158]) to complement the discussions of Chap. IV and motivate the estimates of ionization used in several chapters.

As J.D. Jackson taught us, most problems involving potential begin with the Poisson equation,

$$\nabla^2 V(\mathbf{r}) = -4\pi e[Z\delta(\mathbf{r}) - n_e(\mathbf{r})]. \tag{A.1}$$

The goal here is to solve for the potential $V(\mathbf{r})$ created by the electrons with density $n(\mathbf{r})_e$ and the point-like ions of charge Z. The potential can be separated into a ion (nuclear) contribution $V_N(r) = Ze/r$ and an electronic contribution that itself satisfies the Poisson equation:

$$\nabla^2 V_e(\mathbf{r}) = 4\pi e n_e(\mathbf{r}). \tag{A.2}$$

Jackson also showed us the solution to Eqn. A.2, given by [116]:

$$V_e(\mathbf{r}) = -\int_V \frac{e\ n_e(\mathbf{r})}{|\mathbf{r}-\mathbf{r}'|} d^3\mathbf{r}' \tag{A.3}$$

As stated previously, one assumption of the TF model is an isotropic electron distribution within the ion sphere. This removes the vector dependance of n_e in Eqn. A.3, allowing the denominator of the integrand to be expanded into Legendre polynomials as

$$\frac{1}{|\mathbf{r}-\mathbf{r}'|} = \sum_{k=0}^{\infty} \frac{r_<^k}{r_<^{k+1}} P_k(\cos\ \theta) \tag{A.4}$$

where $r < (r >)$ is the smaller (larger) of r and r'. The electronic part of the potential is then

$$V_e(r) = -e\sum_{k=0}^{\infty} \int_0^{\infty} r'^2 dr' \int_0^{\pi} \sin\ \theta d\theta \int_0^{2\pi} d\phi n_e(r') \frac{r_<^k}{r_<^{k+1}} P_k(\cos\ \theta) \tag{A.5}$$

$$= -2\pi e \sum_{k=0}^{\infty} 2\delta_{k,0} \int_0^{\infty} r'^2 dr' n_e(r') \frac{r_<^k}{r_<^{k+1}} \tag{A.6}$$

$$= -4\pi e \int_0^{\infty} n_e(r') \frac{r'^2 dr'}{r_>} \tag{A.7}$$

$$= -4\pi \left(\frac{1}{r} \int_0^{r} n_e(r') r'^2 dr' + \int_r^{R_i} n_e(r') r' dr' \right) \tag{A.8}$$

where we have made use of the orthogonality of Legendre polynomials to perform the integration over θ:

$$\int_0^{\pi} d\theta\ \sin\theta\ P_k(\cos\ \theta) = \int_{-1}^{1} dx\ P_k(x) = \int_{-1}^{1} dx P_k(x) P_0(x) = \frac{2}{2k+1}\delta_{k,0} = 2\delta_{k,0}. \tag{A.9}$$

$$\tag{A.10}$$

In Eqn. A.8 we have introduced the ion sphere radius R_i, and for $r = R_i$ the second integral in this equation is zero and $V_e(R_i) = -Ze/R_i$ This exactly opposes the nuclear potential at $r = R_i$, ensuring the potential is zero at the boundary.

On the question of the electron density n_e, the TF model departs from the DH theory and accounts for degenerate electrons through the use of Fermi-Dirac statistics. This extends the range of validity to strongly coupled plasmas, where DH fails to apply. The electron density is found by integration of the Fermi-Dirac electron momentum distribution

$$f_e(r,p)dp = \frac{1}{\pi^2\hbar^2}\frac{p^2dp}{1+exp\left([p^2/2m - eV(r) - \mu]/T_e\right)} \tag{A.11}$$

over all momentums. Note that the electron distribution includes the chemical potential μ (equal to the Fermi energy, Eqn. 4.3, for degenerate systems), and for $\mu \to -\infty$ the Fermi-Dirac distribution reduces to the Maxwell-Boltzmann distribution used in DH theory. Also, the momentum distribution explicitly includes the local microfield $V(r)$, making the resulting potential self-consistent in $V(r)$.

Denoting the chemical and potential energies together as $y = [eV(r)+\mu]/T_e$ (using T_e in energy units) and replacing the momentum with $x = p^2/(2mT_e)$, the density is found from

$$n_e(r) = \int dp\ f_e(r,p) \tag{A.12}$$

$$= \frac{(2mT_e)^{3/2}}{2\pi^2\hbar^3}\int_0^\infty \frac{x^{1/2}\ dx}{1+exp(x-y)} \tag{A.13}$$

$$= \frac{1}{2\pi^2}\left(\frac{2mc^2T_e}{\hbar^2c^2}\right)^{3/2} F_{1/2}\left(\frac{\mu+eV(r)}{T_e}\right). \tag{A.14}$$

Here $F_{1/2}$ is the *Fermi integral*, which has the general form $F(\phi) = \int_0^\infty x^n[\exp(x-\phi)+1]^{-1}\mathrm{d}x$. The set of TF equations is completed by ensuring charge neutrality within the ion sphere,

$$Z = \int_0^{R_i} n_e(r,\mu)d^3r. \tag{A.15}$$

Solving the system can be done numerically and results in values for $V(r)$, $n(e)$, and μ. These estimates from the TF theory have proven remarkably robust over a wide range plasma parameter space.

An additional feature of the TF model is its capacity to calculate an average ionization. This is not done directly because electrons are never explicitly separated into bound and free contributions, and it is also worth repeating that atomic structure (quantum shells, explicit binding energies, etc) are not part of the TF theory. However, the electron distribution function defines a range of energies, and electrons with

energy greater than the local binding potential can be considered free:

$$\frac{p^2}{2m} - eV(r) \geq 0. \tag{A.16}$$

The density of these free electrons is given by

$$n_{e,f}(r) = \frac{1}{2\pi^2}\left(\frac{2mc^2T_e}{\hbar^2c^2}\right)^{3/2} F_{1/2}\left(\frac{\mu + eV(r)}{T_e}; \left|\frac{eV(r)}{T_e}\right|\right). \tag{A.17}$$

Similar to the Fermi-Dirac integral except in the lower limit of integration, this equation has the form of the *incomplete Fermi-Dirac integral*: $F(\phi;\beta) = \int_\beta^\infty x^n[\exp(x-\phi)+1]^{-1}\mathrm{d}x$. The bound electron population is, expectedly, the rest of them, and given by

$$n_{e,b}(r) = \frac{1}{2\pi^2}\left(\frac{2mc^2T_e}{\hbar^2c^2}\right)^{3/2}\left[F_{1/2}\left(\frac{\mu + eV(r)}{T_e}\right) - F_{1/2}\left(\frac{\mu + eV(r)}{T_e}; \left|\frac{eV(r)}{T_e}\right|\right)\right] \tag{A.18}$$

To calculate a per-ion free electron value, the electron density from Eqn. A.17 need only be integrated over the ion sphere volume,

$$\bar{Z}(T_e, n_i) = \int_V n_{e,f}(r,\mu)d^3r. \tag{A.19}$$

A useful algorithm for calculation of $\bar{Z}$ was developed by R. More and is given in Ref. [158]. This algorithm that was used for the calculations of polyimide ionization in Chap. 5.3.2, and is presented below as a vectorized Matlab function, useable as is or easily converted to one's language of choice.

```
%% Thomas Fermi numerical solver.
% Based on work by R. More (1981), accurate to a few
% percent over a large range or T and rho
function [ionize] = TF(rho, T, Z, AtomicNum)
if ¬all(size(T) == size(rho))
    error('Temperature and density can be matrices, but must be ...
       the same shape!')
else
    R = rho /(Z * AtomicNum);
    T0 = T / Z^(4/3);

    alpha  = 14.3139;
    beta = 0.6624;
    a1 = 3.323E-3;
    a2 = 0.971832;
    a3 = 9.26148E-5;
    a4 = 3.10165;
    b0 = -1.7630;
    b1 = 1.43175;
    b2 = 0.315463;
    c1 = -0.366667;
    c2 = 0.983333;

    f = inline('x ./ (1 + x + sqrt(1 + 2*x))');

    if T == 0
        x = alpha * R .^ beta;
        ionize = f(x) .* Z;

    elseif T > 0
        T_F = T0 ./ (1 + T0);
        A = a1 * T0.^ a2 +  a3 * T0.^ a4;
        B = -exp(b0 + b1* T_F + b2* T_F.^7);
        C = c1 * T_F + c2;
        Q1 = A .* R.^B;
        Q = (R.^C + Q1 .^ C) .^ (1./C);
        x = alpha * Q .^ beta;
        ionize = f(x) * Z;

    else
        error('Enter a positive temperature.')
    end
end
```

APPENDIX B

Omega shot day critique forms

After each shot day on the OMEGA or OMEGA EP laser, the facility requests that the principle investigator for complete a shot critique form. This is an opportunity for PIs to describe problems encountered, compliment work well done, and generally provide feedback regarding his or her experience. The shot critique form for each shot day is provided here.

Experimental Critique Sheet
Laboratory for Laser Energetics, University of Rochester

Week of:	March 16, 2009
Experiment Date:	March 18, 2009
Principle Investigator:	R. P. Drake, S. Glenzer, J. Knauer, C.C Kuranz, C.M. Huntington
Experimental series:	NLUF Radiative Gas Thomson Scattering
Primary diagnostics:	Gated Thomson Scattering spectrometer, XRFC 1, XRFC 3

Primary objectives: This experimental series was intended to build on a 2008 shot series by improving the resolution of incoherent Thomson scattering signal from radiative shocks in argon. Additional objectives for the day included using tin L-shell and the He-like chlorine lines for radiographic backlighting, both new techniques for our group. The final configuration was an initial attempt at imaging Thomson scattered light for shock density measurements.

- Problems encountered:
  - Laser Software issues and laser problems, resulted in the delay of the first shot.
  - Experimental diagnostics
    - Target debris broke through blast shields on 3 shots, damaging a XRFC on one of the shots.
    - A software problem during shot 53949 prevented the primary diagnostic, XRFC 1, from triggering. No data primary data was recorded from this shot.
    - The nosecone installed for shot 53946 was not correct. The SRF for this shot specified a 6X-16, but a 2X-16 was installed. This resulted in the wrong magnification for that shot and a minor delay while the nose cone was changed and the camera was repointed.
  - Experimental problems (including design)
    Significant shrapnel was produced by the Thomson scattering and tin flag backlighter targets designs. Shrapnel twice damaged the front filter of the Thomson Scattering diagnostic and also damaged the MCP in XRFC 3 during shot 53948.
  - Target problems
    The target metrology and reticle calculation procedure for several of the targets was flawed. This resulted in difficult alignments and the need to modify the target alignment procedure on shot day.

- Suggestions for improvements
  Discussions have been had between our group and Jim Knauer regarding the target design and how to prevent debris from damaging diagnostics. In the future targets will be designed with the intention of creating minimal debris, or with careful consideration to the direction of component normal vectors. The metrology procedure that lead to the shot-day errors is also being investigated here at Michigan so as to not repeat these mistakes.

- Positive feedback
  Good area radiographic images were obtained. Also, the first data from imaging Thompson Scattering was obtained. Jack Armstrong and the ESO team provided excellent support throughout the day. On the shots that the blast shields were damaged, the Omega team was helpful in looking for solutions so that we could continue with our experiments.

Experimental Critique Sheet
Laboratory for Laser Energetics, University of Rochester

Week of:	March 8, 2010
Experiment Date:	March 11, 2010
Principle Investigator:	R. P. Drake, S. Glenzer, J. Knauer, C.C Kuranz, C.M. Huntington
Experimental series:	NLUF Radiative Gas Thomson Scattering
Primary diagnostics:	SSC-A streak camera, ZSpec spectrometer, Henway

Primary objectives: For each shot, we hoped to collect incoherent Thomson scattered signal and use the SSC to record absolute shock position and velocity.

- Problems encountered:
  - Laser
    At one point a laser cluster was subdivided, with the intention of PLAS delaying the subgroups individually. When this was done, the resulting SRF default called for DPRs to be inserted, whereas, they were previously specified as out. This introduced an additional component into the optical path, which changed the pointing of 4 beams. These beams were off target by several millimeters, and minimal data was collected for the associated diagnostic. Thankfully, the intended target was a large area backlighter, and x-ray pinhole images confirmed that the beams did intersect some part of the target, causing no damage to the facility. The subtle change in the setup was overlooked by everyone in the process, including the shot director, beam operators, and PI, who signed off on the modified RID.
  - Experimental diagnostics
    * SSC: Collecting timing fiducials for the streak camera was important for each streak sweep speed used. However, the position of the fiducial marks interfered with our data, so the fiducials needed to be collected on separate shots, when no experimental data was collected. On one shot where we intended to forgo SSC data, we requested the fiducials be run. The fiber optic was correctly in place, but the driver for the beam was not initialized. There were no other shots where we could forgo data collection, so no fiducials were collected for this sweep speed.
    * ZSpec: The spectrometer was imaged onto a 4-strip MCP, namely XRFC 4. It was only discovered by us, though it had been noted previously at LLE, that one strip could not be biased above 200 V. Thus, for strong signals, including our spectrometer calibration shots, this strip was completely saturated.

- Experimental problems (including design)
  The main target was gas-filled and required a pressure readout, as noted in the SRF. However, the incorrect TIM TPS (one that did not have a pressure readout) was loaded. This TIM TPS needed to be removed and the correct one loaded. Once the correct TIM TPS was loaded there was a short. After some troubleshooting, the problem was corrected.
- Target problems
  One set of our targets was designed and built incorrectly, and only realized too late in the process to correct the problem. They required a new alignment procedure, and were only able to be shot because of their exceedingly simple geometry (flat foils at TCC). We appreciate these being supported (see Positive Feedback below).

- Suggestions for improvements
  A method for PIs to access LLE notes, like the observation that XRFC 4 had a broken strip, may eliminate some surprises that have been overlooked.

  It is unclear to me at what stage it could be implemented, but it may be useful to have some equivalent of an SRF change auditor which highlights changes from previous shots, to catch errors like the DPR default.

- Positive feedback
  This was a very complicated experiment, with many changes made shot-to-shot based on the data collected immediately previous. Aside from the noted concerns, this was accommodated quickly and efficiently.

  We appreciate the help of Jack Armstrong in the days leading up to the experiment to support targets which differed from the proposed geometry.

  Many discussions regarding debris mitigation with Jim Knauer and Chuck Sorce in the design phase resulted in a design which, though massive, was relatively well controlled and presented no major risks to the facility.

  Essential to the collection of good streak camera data was a tutorial provided to me by Ray Bahr. This was a new diagnostic for these experiments and excellent data was collected. It also has great potential for future experiments and will likely be employed for future experiments.

Experimental Critique Sheet
Laboratory for Laser Energetics, University of Rochester

Week of:	April 18, 2011
Experiment Date:	April 20, 2011
Principle Investigator:	C. Kuranz, RP Drake, C Sorce, SH Glenzer, CM Huntington
Experimental series:	2011 NLUF Radiative Shock experiments
Primary diagnostics:	Two zinc spectrometers, imaging SSC

Primary objectives: Collect simultaneous x-ray Thomson scattering and streaked radiography from radiatively-collapsed xenon shock system.

- Problems encountered:
  - Laser
    After several shots we dropped one beam (66) which passed close to a piece of gold shielding, on the chance that it was striking the gold and creating the background seen on the zinc spectrometer diagnostic. Dropping the beam made no observable difference in the recorded spectra.

    Additionally, it was realized during the day (approximately 13:00, shot 5) that beam 30 was striking the housing of the Zspec in TIM 3, and was dropped on all subsequent shots. This interference does appear in the documentation for the ZSpec, but is not flagged by the SRF auditor.
  - Experimental diagnostics
    At the beginning of the day, the primary ZSpec was recording significant background signal. Despite trying to maximize shielding of this instrument, the problem persisted until we changed from a flat crystal to a curved crystal, which afforded us a higher signal with some spatial resolution.
  - Experimental problems (including design)
    Images recorded on the streak camera showed insufficient contrast. We believe that this is a result of a slightly-non-orthogonal view of the shock tube axis, off of orthogonal by approximately 8 degrees. In target design this was not expected to be as significant an issue as it appears to have been.
  - Target problems
    During the shot day, additional shielding was added to the target in attempt to reduce the background recorded on the TIM 1 zinc spectrometer. The added shielding did not have the desired effect, and was not continued.

- Suggestions for improvements
  This experiment will benefit from new diagnostics (currently under development by UM, LANL, and LLE), which will offer spatial and spectral resolution. This may decrease the need for such substantial shielding, which is a major challenge in this design. Additionally, the proposed reconfiguration of driver legs to allow SSD to be run on a single, advanced leg and backlight with the remaining two legs will be a major advantage for this experiment.

- Positive feedback
  Having the ability to change from a flat to curved crystal in the primary (TIM 1) ZSpec during the shot day was an important modification. Also, in response to the data we were seeing, numerous additional changes to beam groups and spot sizes during the day, not all of which were explicit in the SRFs. These were accommodated, and lead to a better understanding of what we were seeing. Finally, having access to the lab space in DSDL again proved essential both for our gas-fill operations and also when target modifications needed to be made, and we appreciate the continued support of our group using that space.

Experimental Critique Sheet
Laboratory for Laser Energetics, University of Rochester

Week of:	March 19, 2012
Experiment Date:	March 20, 2012
Principle Investigator:	Channing Huntington, Eliseo Gamboa
Experimental series:	Other
Primary diagnostics:	LANL Imaging X-ray Thomson Spectrometer (IXTS)

Primary objectives: The goal of this experimental day was to use the IXTS to measure the spatial temperature profile of shocks in two different materials. One portion of the day used several beams to irradiate a sample of low density carbon foam, launching a shock. A second set of beams struck a nickel foil, creating the x-ray source for the Thomson scattering diagnostic. The second system probed was a radiative shock in xenon gas. This experiment was similar to earlier campaigns, but again focused on using the new diagnostic to capture the spatial temperature profile.

- Problems encountered:
  - Laser
    No issues were encountered with the laser system.
  - Experimental diagnostics
    The ZSpec (zinc spectrometer) was used as a secondary diagnostic on the xenon gas experiment. Several pointing changes were made to try to improve the focusing of the x-ray signal. This was expected and discussed before the shot, and was the result of using a nickel x-ray source (8 keV) with a diagnostic designed for zinc (9 keV). The data is not directly comparable with previous shot days (which did use zinc), but the diagnostic did prove useful as a secondary monitor of the scattered x-ray signal.
  - Experimental problems (including design)
    The design of this experiment proved largely successful, especially with respect to the primary diagnostic. The data collected was of high quality, and will inform future experiments. As it was designed, some improvements could have been made to the use of secondary diagnostics on this day. The film-based imager had an insufficient field of view to capture the desired views of the target, which lead to some confusion during shot day (as mentioned below, help from Chuck Sorce was appreciated in understanding this).
  - Target problems
    One target design (shocked carbon foam) produced significant shrapnel, which required frequent replacement of blast shields and filters. It will be redesigned for future shot days with the goal of minimizing spall.

The second design, investigating the shock in a xenon gas tube, resulted in very high (saturating) background levels from the beryllium drive disk. This was observed on the first shot, at which time shielding was added to the target and the high levels of background were suppressed.

- Suggestions for improvements
  The XOP operators indicated that the YTVS camera is preferred for alignment as the XTVS camera has a vertical offset error. If this is a rigorously examined issue at LLE, it would be beneficial to convey this to PIs before the shot day, as target alignment is a priority and such surprises are disconcerting.

- Positive feedback
  We are thankful for the support from LLE with respect to the gas fill operation that is necessary to field the xenon experiments. Additionally, it was very useful on this shot day to be able to modify our targets (specifically, to add shielding) in response to the data collected. Having both capabilities required a significant time commitment from Sallee Klein at Michigan and the safety personnel, namely Douglas Jacobs-Perkins and Milton Shoup, at LLE. Their efforts are appreciated.

APPENDIX C

2010 Target Drawings

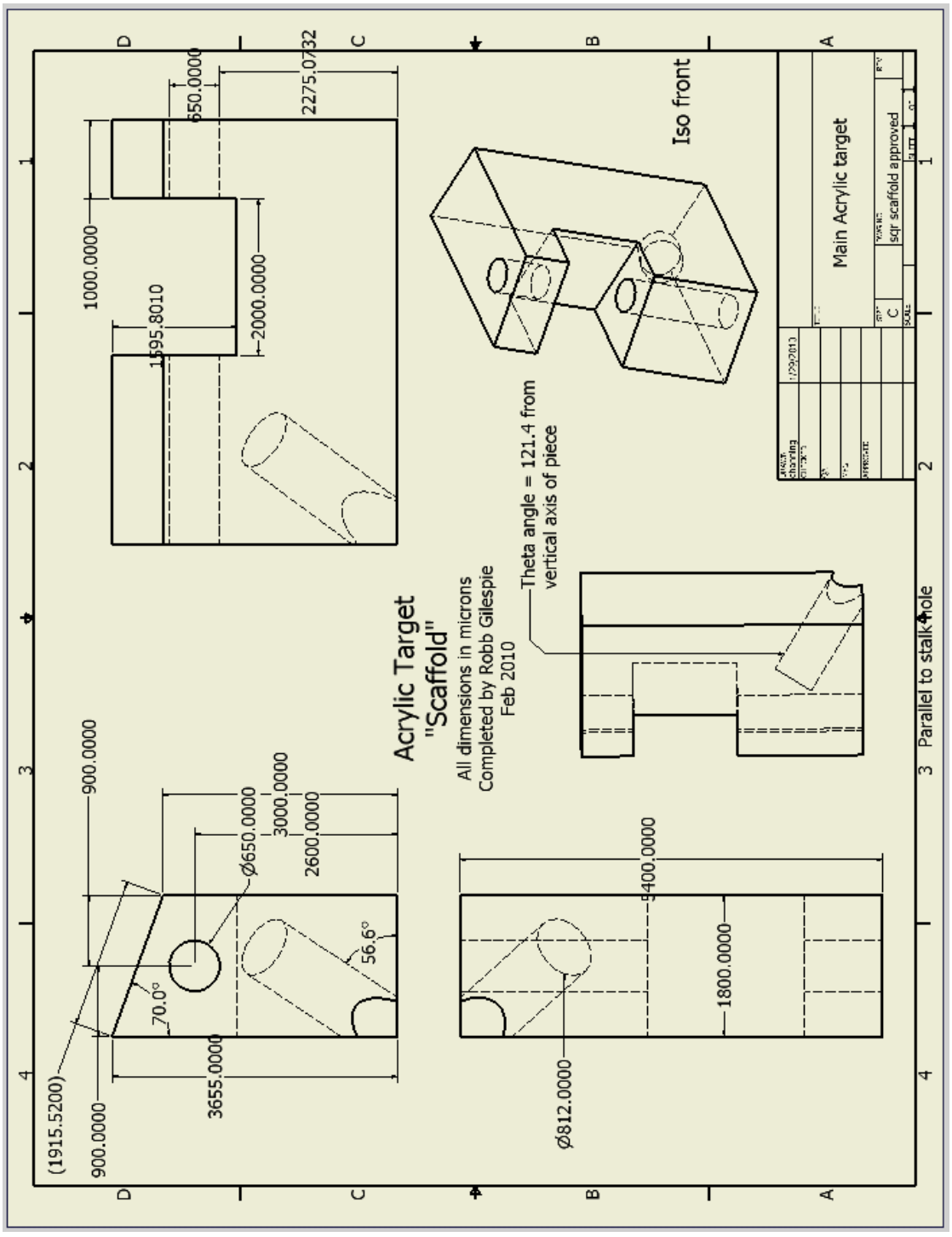
Acrylic Target
"Scaffold"
All dimensions in microns
Completed by Robb Gilespie
Feb 2010
Theta angle = 121.4 from
vertical axis of piece
Iso front
Main Acrylic target
sqr scaffold approved
Parallel to stalk hole
(1915.5200)
900.0000
900.0000
3655.0000
70.0°
Ø650.0000
3000.0000
2600.0000
56.6°
Ø812.0000
400.0000
1800.0000
1000.0000
1595.8010
2000.0000
650.0000
2275.0732

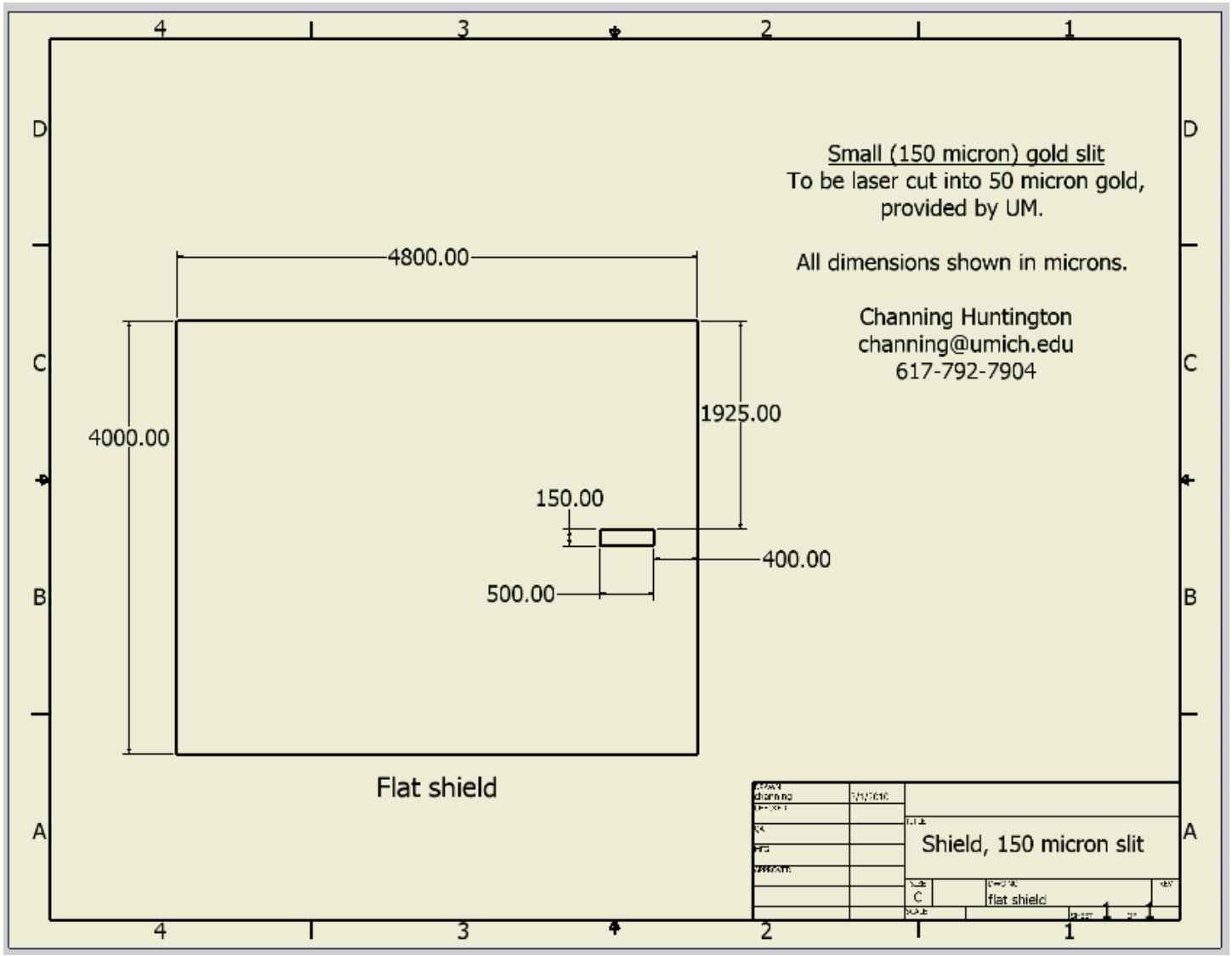
Small (150 micron) gold slit
To be laser cut into 50 micron gold,
provided by UM.
All dimensions shown in microns.
Channing Huntington
channing@umich.edu
617-792-7904
4800.00
4000.00
1925.00
150.00
400.00
500.00
Flat shield
Shield, 150 micron slit
flat shield

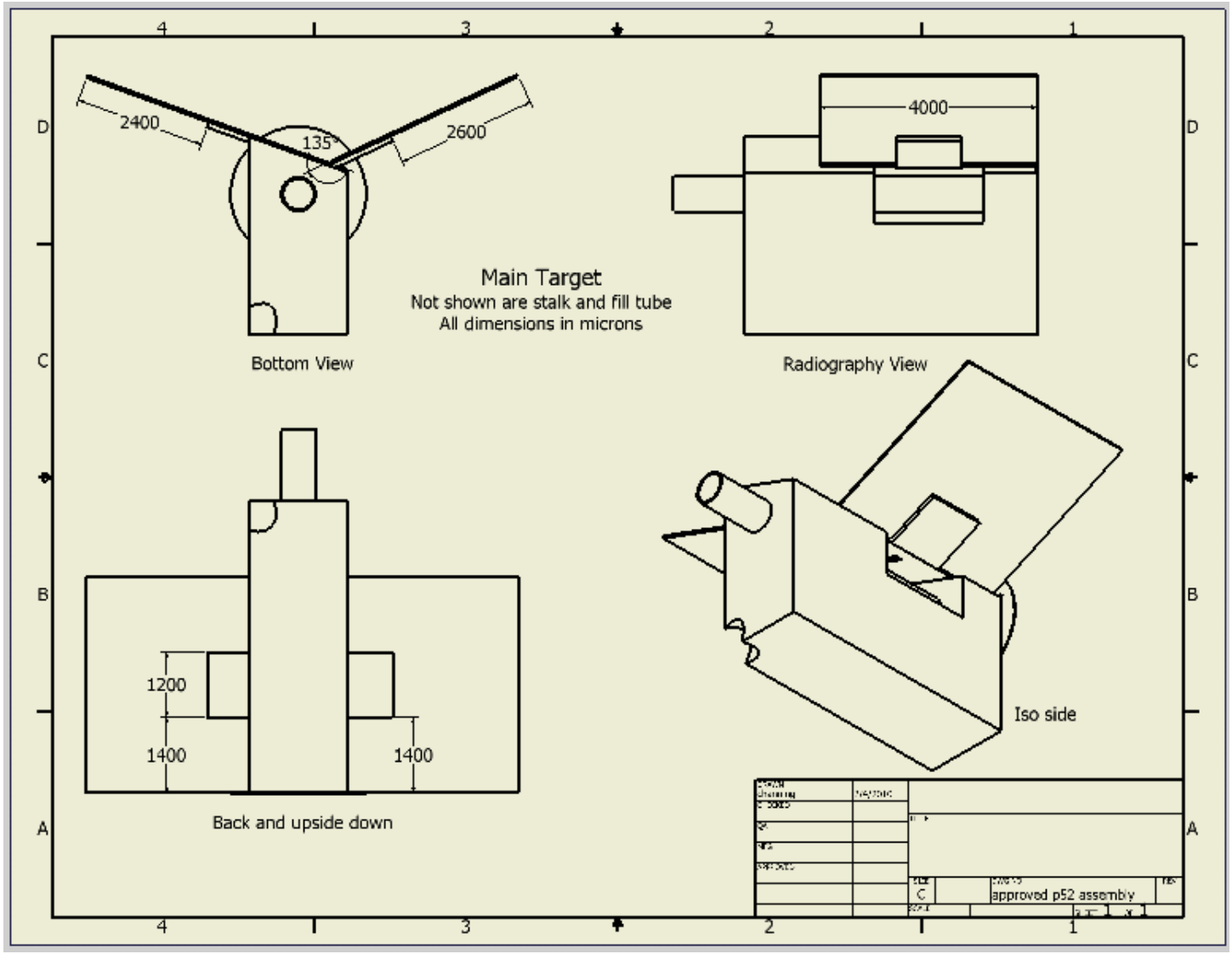
2400
135°
2600
Bottom View
Main Target
Not shown are stalk and fill tube
All dimensions in microns
4000
Radiography View
1200
1400
1400
Back and upside down
Iso side
approved p52 assembly

APPENDIX D

2011 Target Drawings

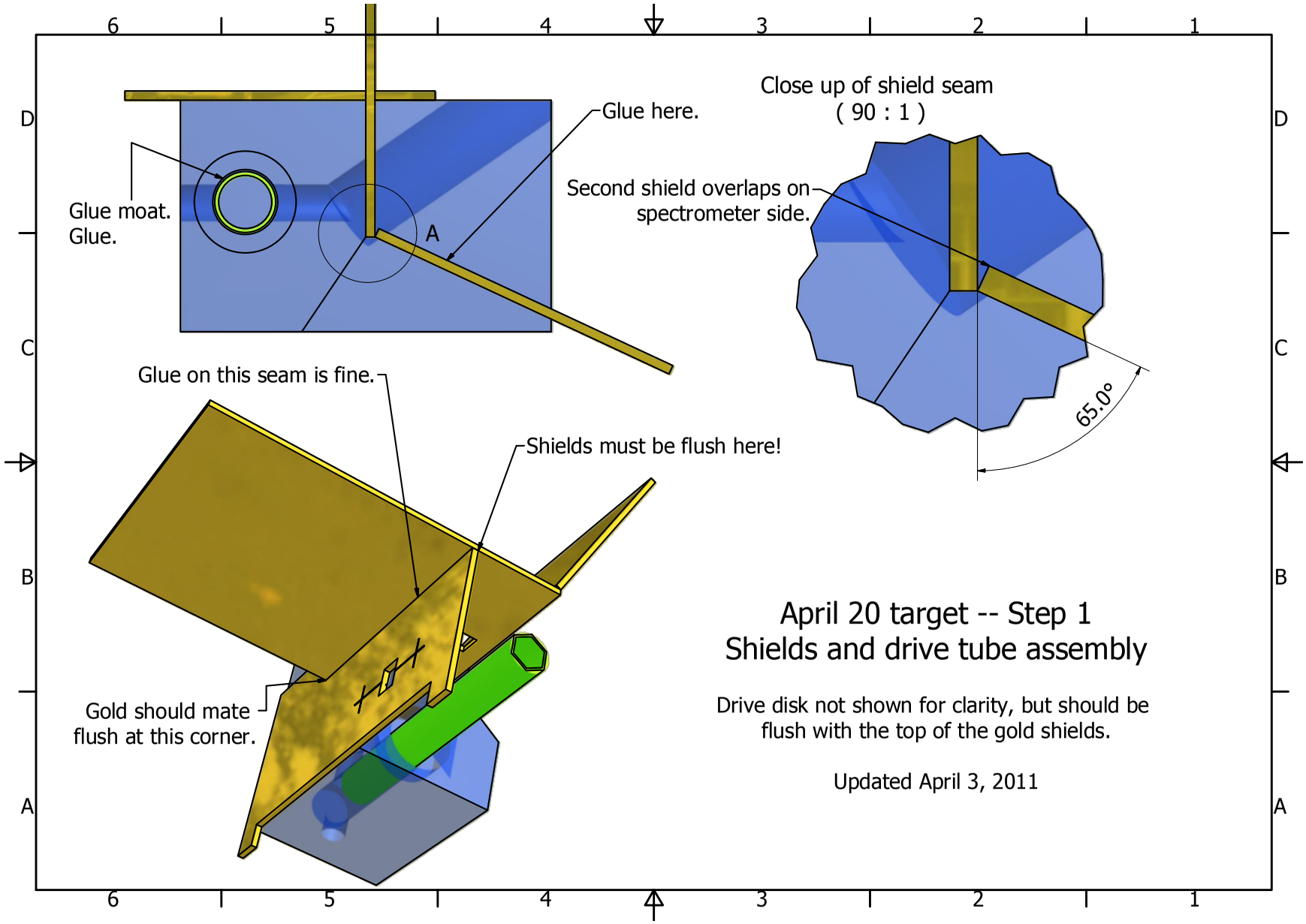
Glue here.
Glue moat.
Glue.
A
Close up of shield seam
(90 : 1)
Second shield overlaps on
spectrometer side.
65.0°
Glue on this seam is fine.
Shields must be flush here!
Gold should mate
flush at this corner.
April 20 target -- Step 1
Shields and drive tube assembly
Drive disk not shown for clarity, but should be
flush with the top of the gold shields.
Updated April 3, 2011

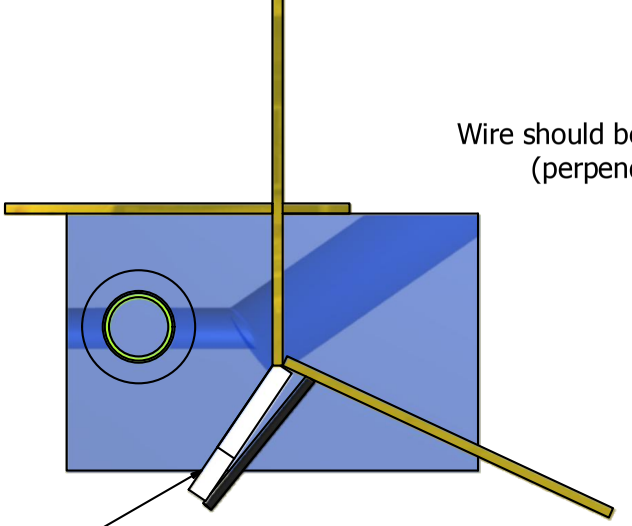

Wire support sits flush on ledge (bottom),
acrylic face, and gold shield (on the corner).

Wire should be a level as possible
(perpendicular to the tube).

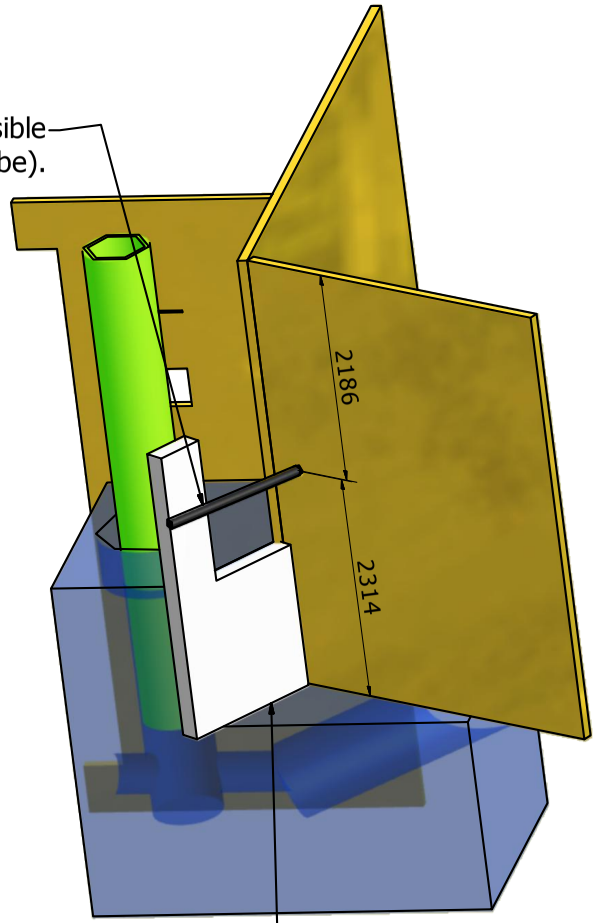

Glue on the acrylic is fine.

April 20 target -- Step 2
Fiducial wire

Drive disk (and others) not shown for clarity.

Updated April 3, 2011

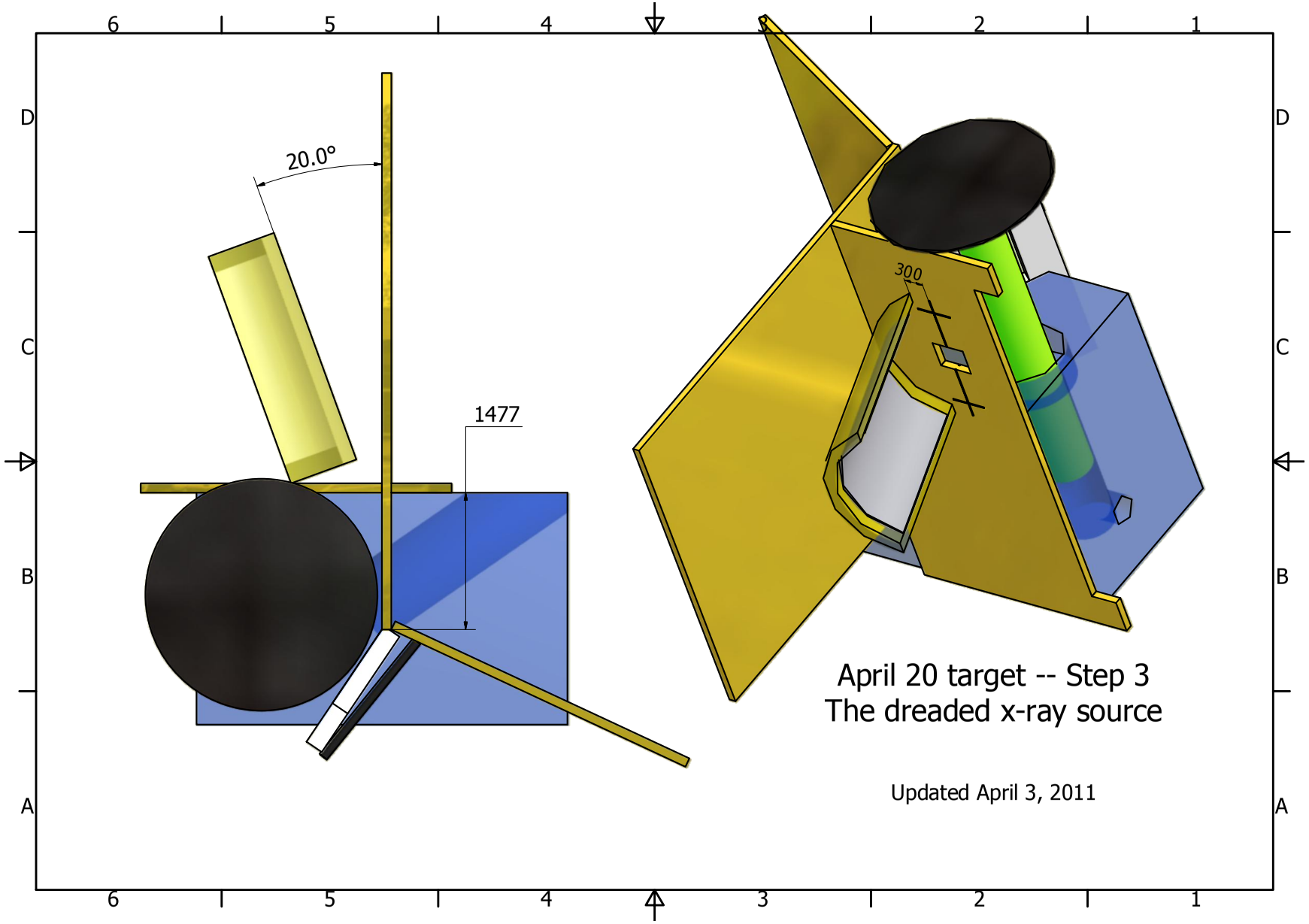
6
5
4
3
2
1
D
C
B
A
20.0°
1477
300
April 20 target -- Step 3
The dreaded x-ray source
Updated April 3, 2011

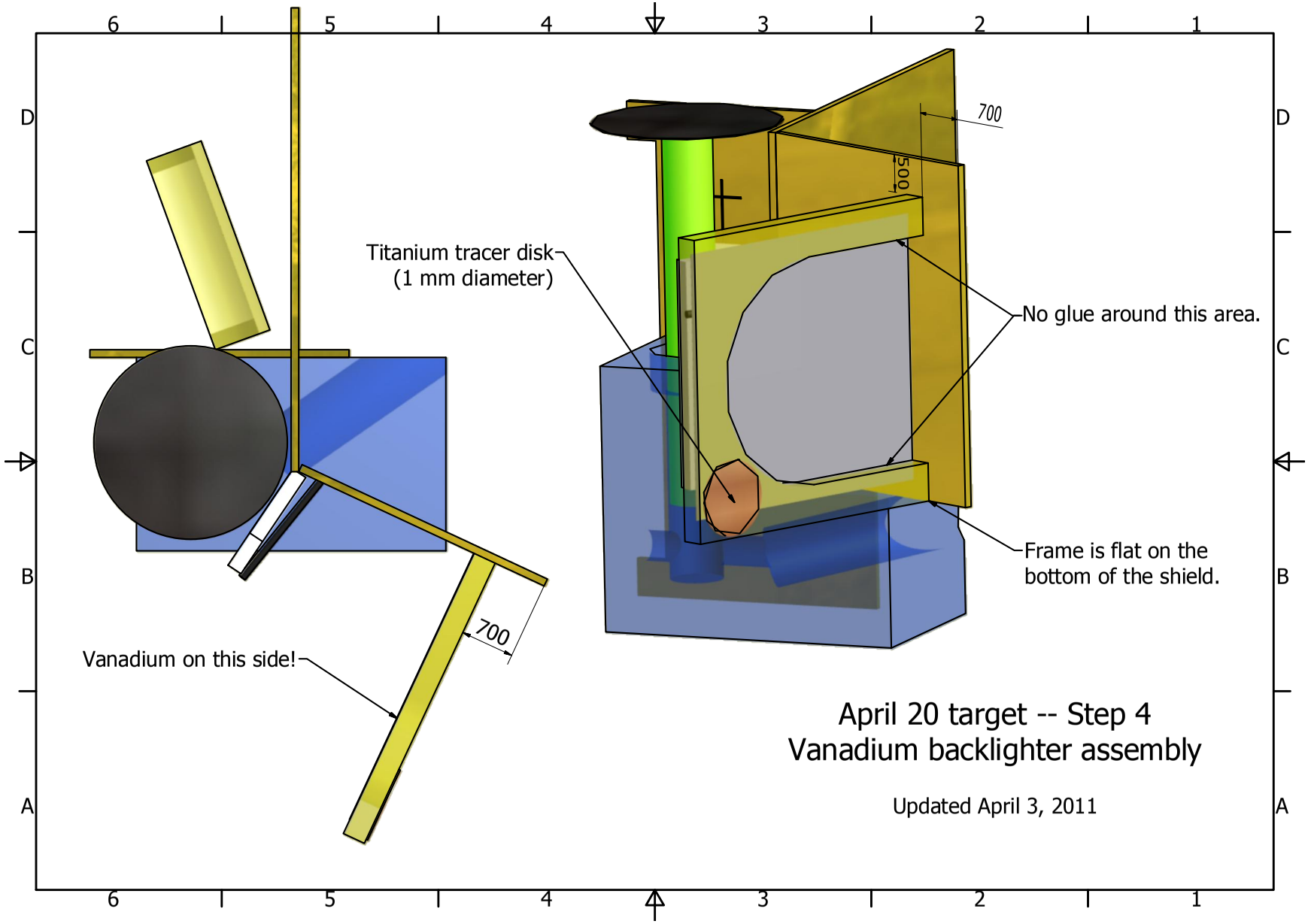
6
5
4
3
2
1
D
C
B
A
Titanium tracer disk
(1 mm diameter)
Vanadium on this side!
700
700
500
No glue around this area.
Frame is flat on the
bottom of the shield.
April 20 target -- Step 4
Vanadium backlighter assembly
Updated April 3, 2011

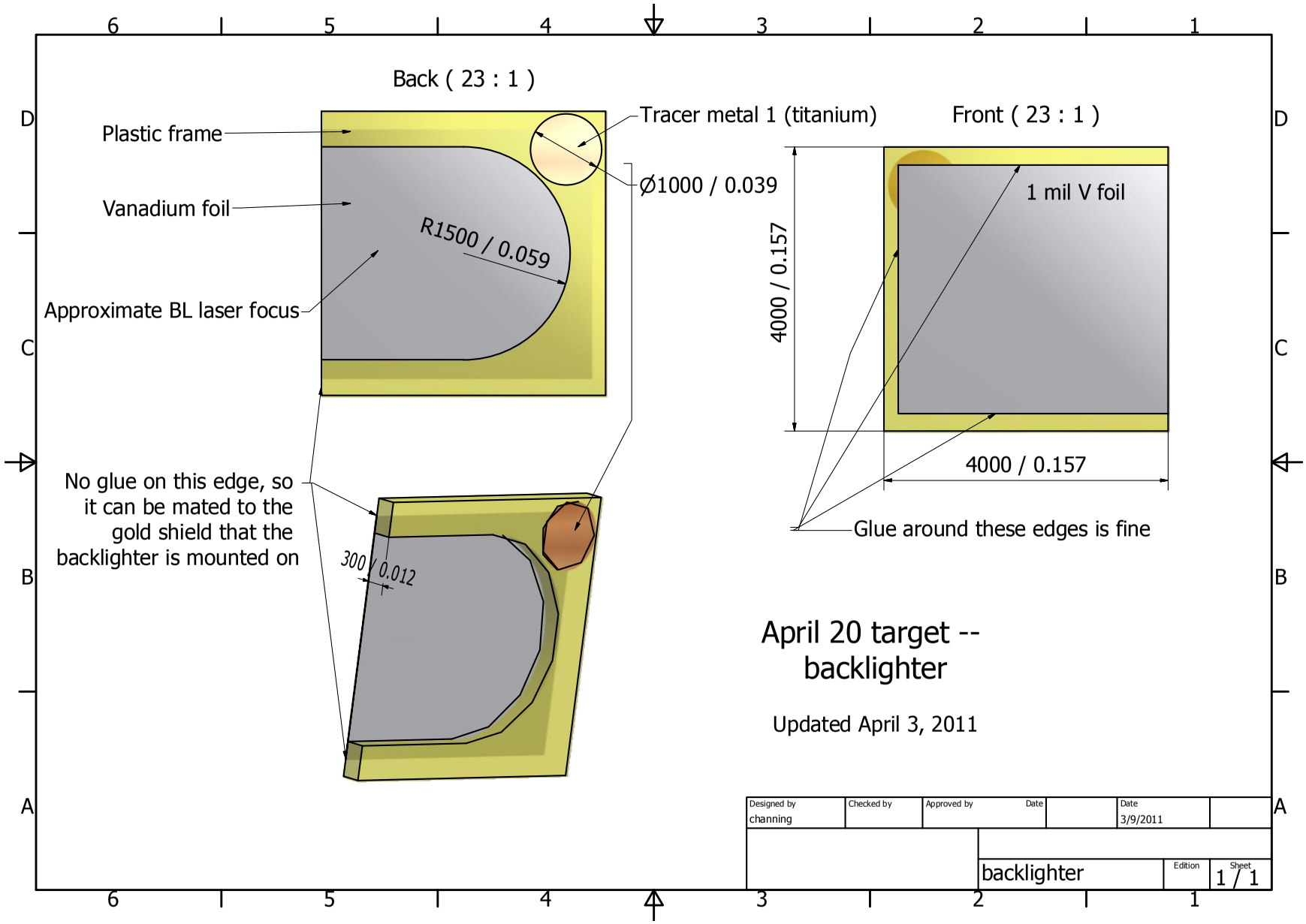
Back (23 : 1)
Plastic frame
Vanadium foil
Approximate BL laser focus
R1500 / 0.059
Tracer metal 1 (titanium)
Ø1000 / 0.039
No glue on this edge, so it can be mated to the gold shield that the backlighter is mounted on
300 / 0.012
Front (23 : 1)
1 mil V foil
4000 / 0.157
4000 / 0.157
Glue around these edges is fine
April 20 target -- backlighter
Updated April 3, 2011
Designed by
channing
Checked by
Approved by
Date
Date
3/9/2011
backlighter
Edition
Sheet
1 / 1

Gold shield designs for Gateway Laser-- 150 micron slits

Channing Huntington
University of Michigan

All dimensions in microns.

Parts to be made from 100 micron thick gold, provided by U of M.

Updated 3/14/11

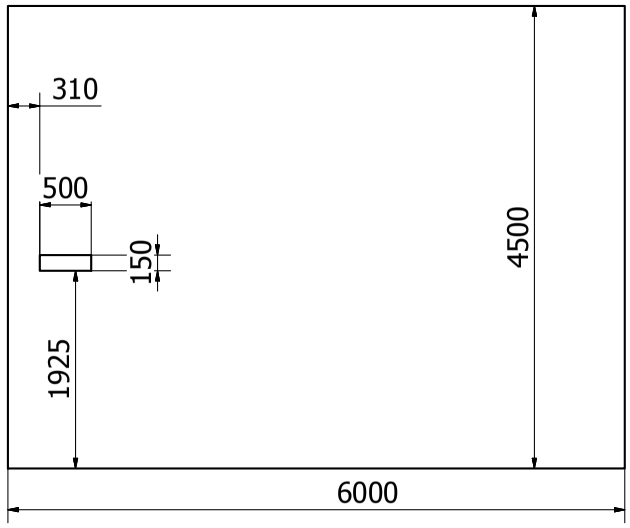

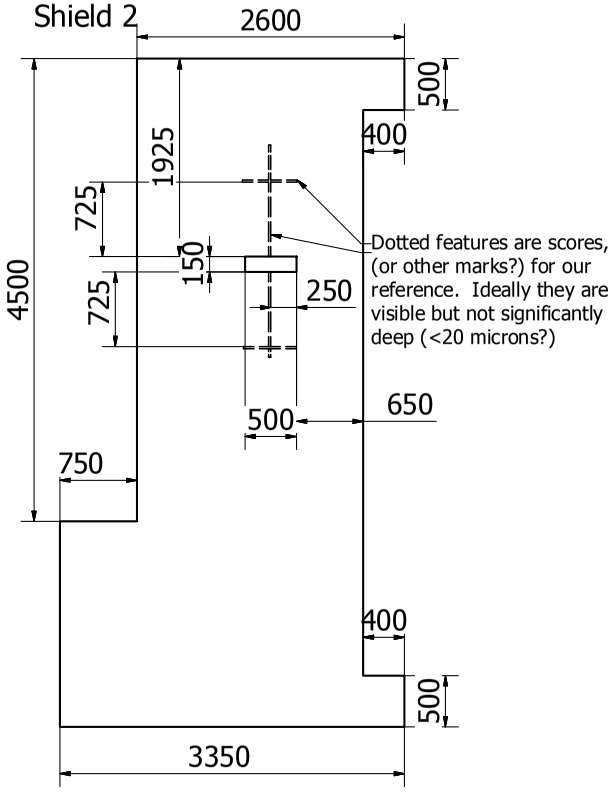

Designed by	Checked by	Approved by	Date		Date
channing					3/9/2011

400 micron shields | Edition: final | Sheet: 1 / 1

APPENDIX E

2012 Target Drawings

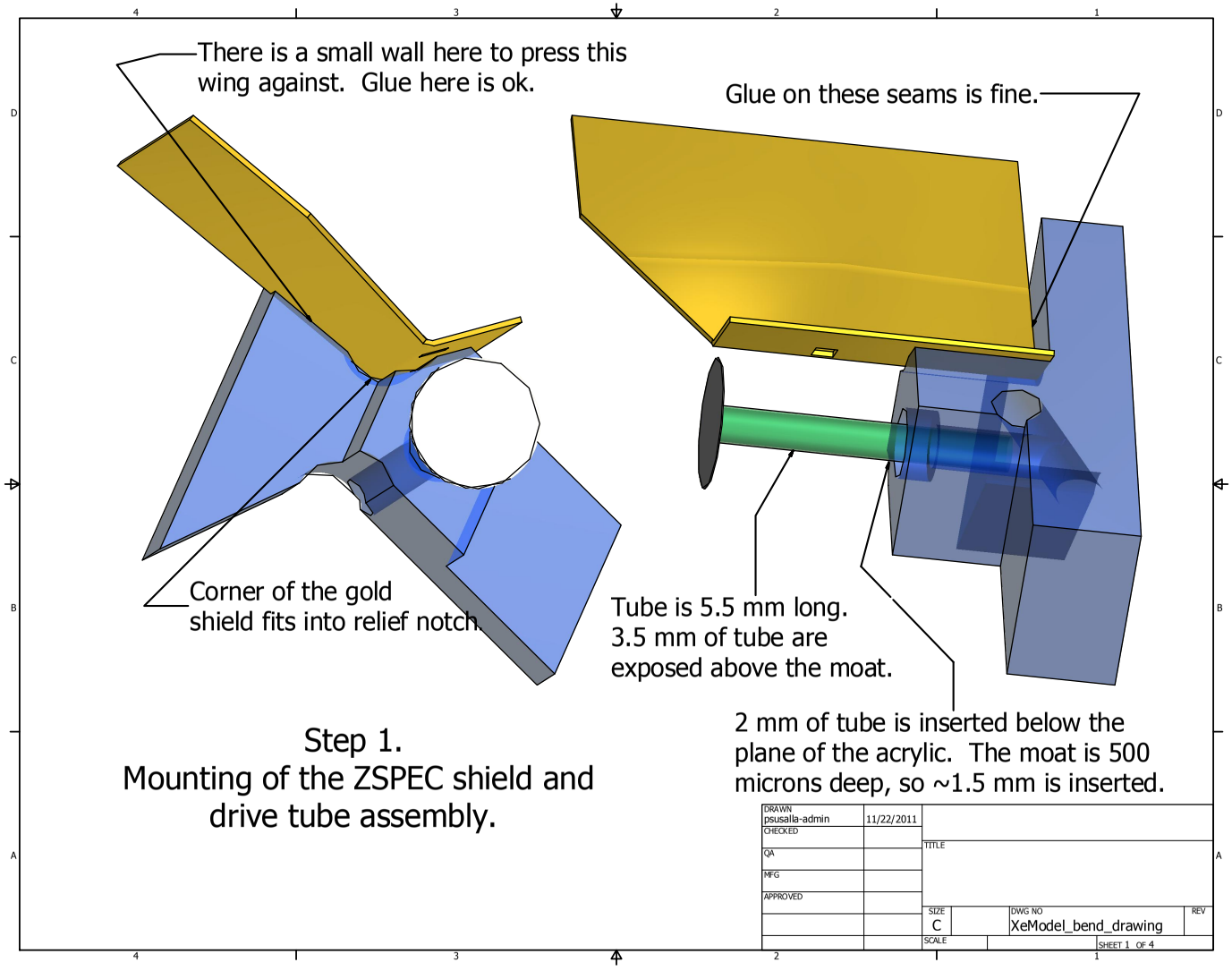
There is a small wall here to press this wing against. Glue here is ok.
Glue on these seams is fine.
Corner of the gold shield fits into relief notch.
Tube is 5.5 mm long. 3.5 mm of tube are exposed above the moat.
2 mm of tube is inserted below the plane of the acrylic. The moat is 500 microns deep, so ~1.5 mm is inserted.
Step 1.
Mounting of the ZSPEC shield and drive tube assembly.
DRAWN psusalla-admin 11/22/2011
CHECKED
QA
MFG
APPROVED
TITLE
SIZE C
DWG NO XeModel_bend_drawing
REV
SCALE
SHEET 1 OF 4

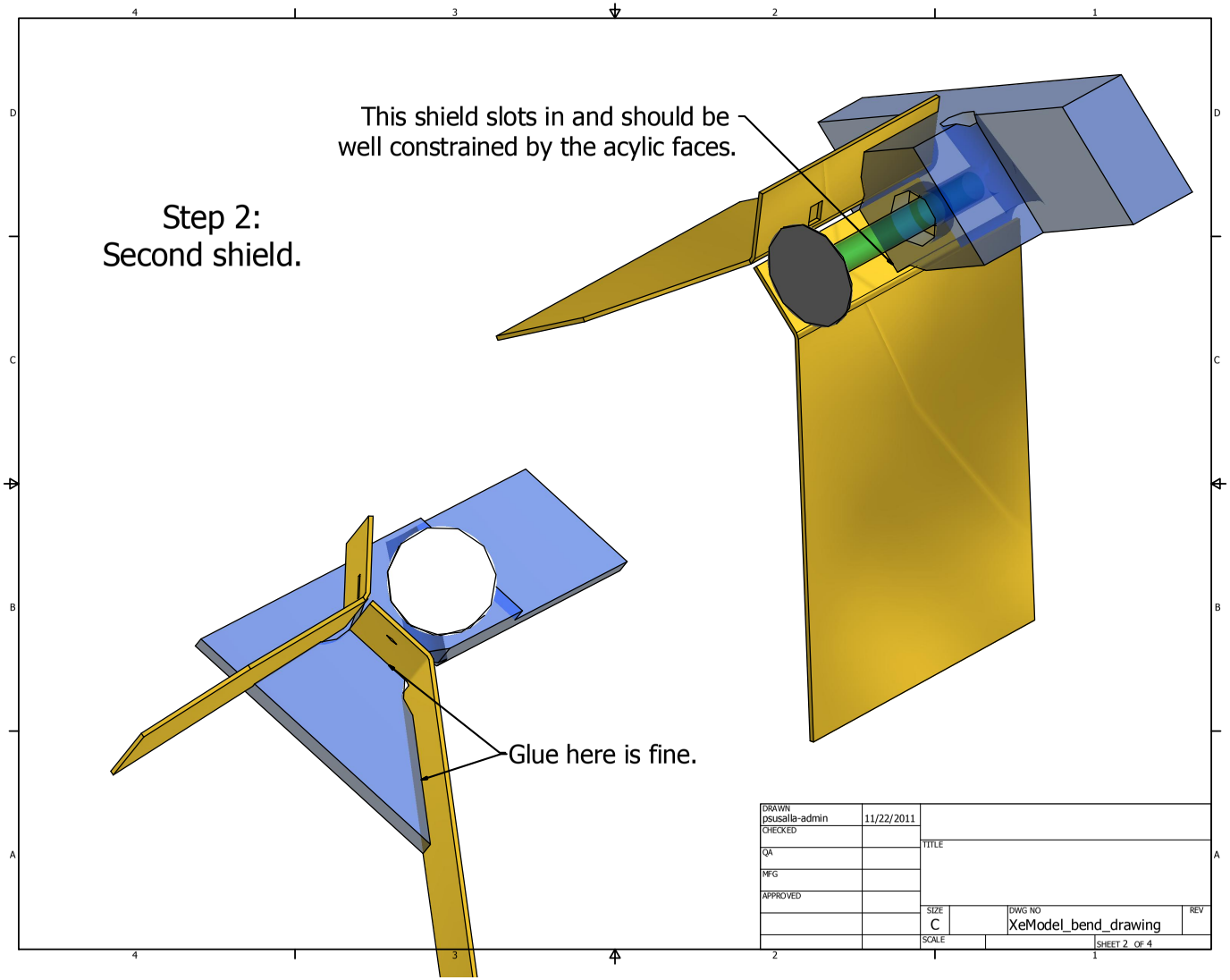
This shield slots in and should be
well constrained by the acylic faces.
Step 2:
Second shield.
Glue here is fine.
DRAWN
psusalla-admin
11/22/2011
CHECKED
QA
MFG
APPROVED
TITLE
SIZE
C
DWG NO
XeModel_bend_drawing
REV
SCALE
SHEET 2 OF 4

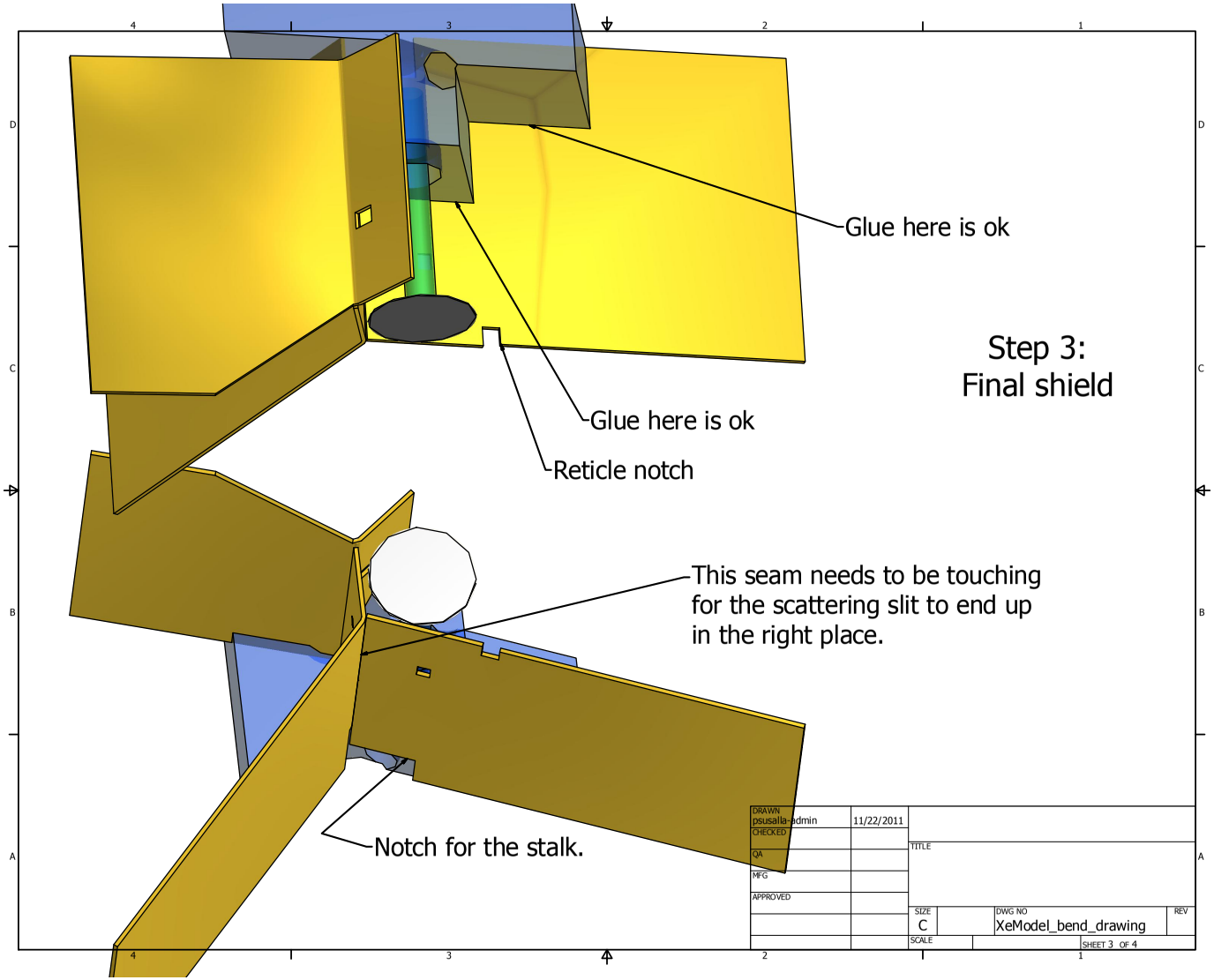
Glue here is ok
Glue here is ok
Reticle notch
Step 3:
Final shield
This seam needs to be touching
for the scattering slit to end up
in the right place.
Notch for the stalk.
DRAWN
psusalla-admin
11/22/2011
CHECKED
QA
MFG
APPROVED
TITLE
SIZE
C
DWG NO
XeModel_bend_drawing
REV
SCALE
SHEET 3 OF 4

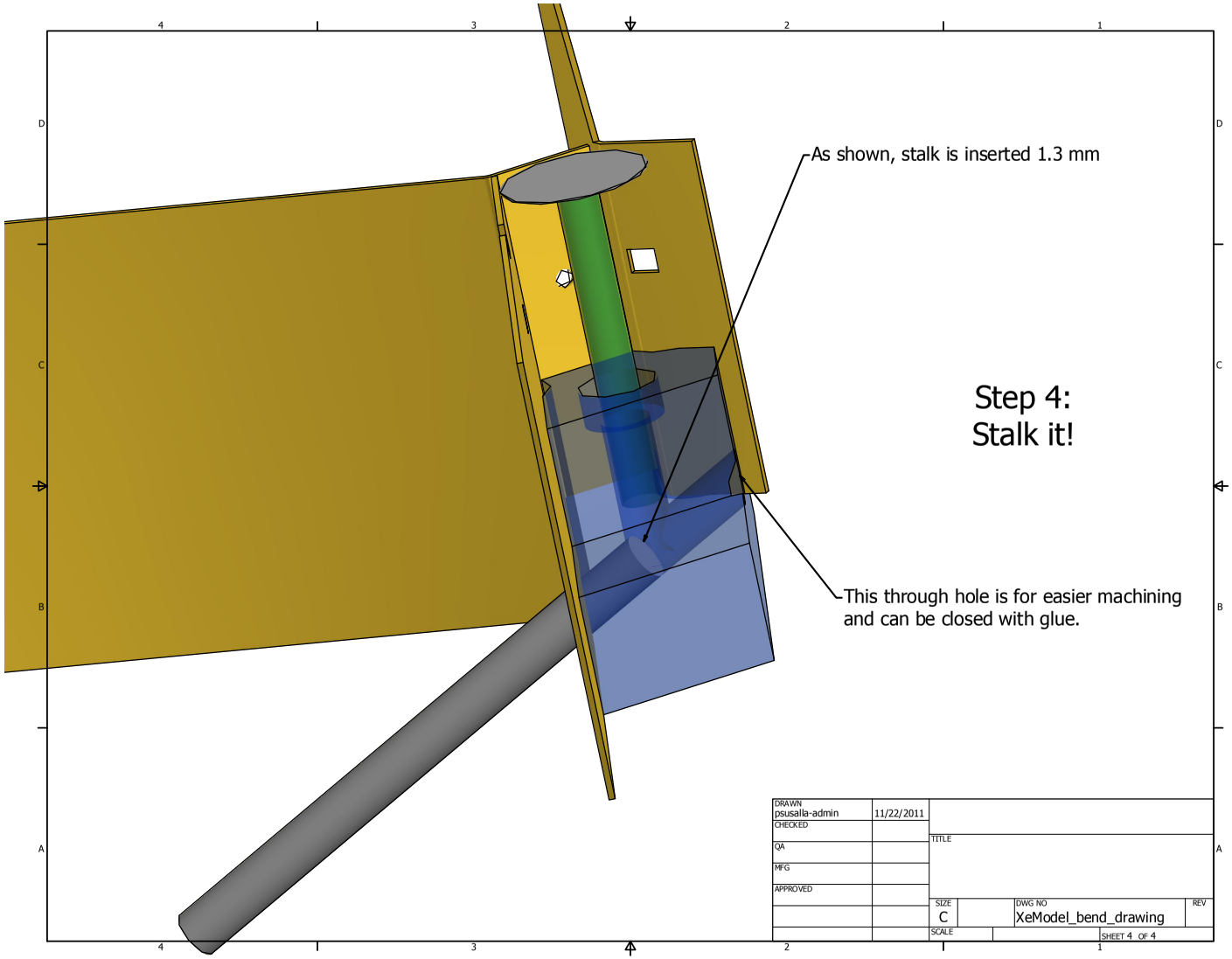
As shown, stalk is inserted 1.3 mm
Step 4:
Stalk it!
This through hole is for easier machining
and can be closed with glue.
DRAWN
psusalla-admin
11/22/2011
CHECKED
QA
MFG
APPROVED
TITLE
SIZE
C
DWG NO
XeModel_bend_drawing
REV
SCALE
SHEET 4 OF 4

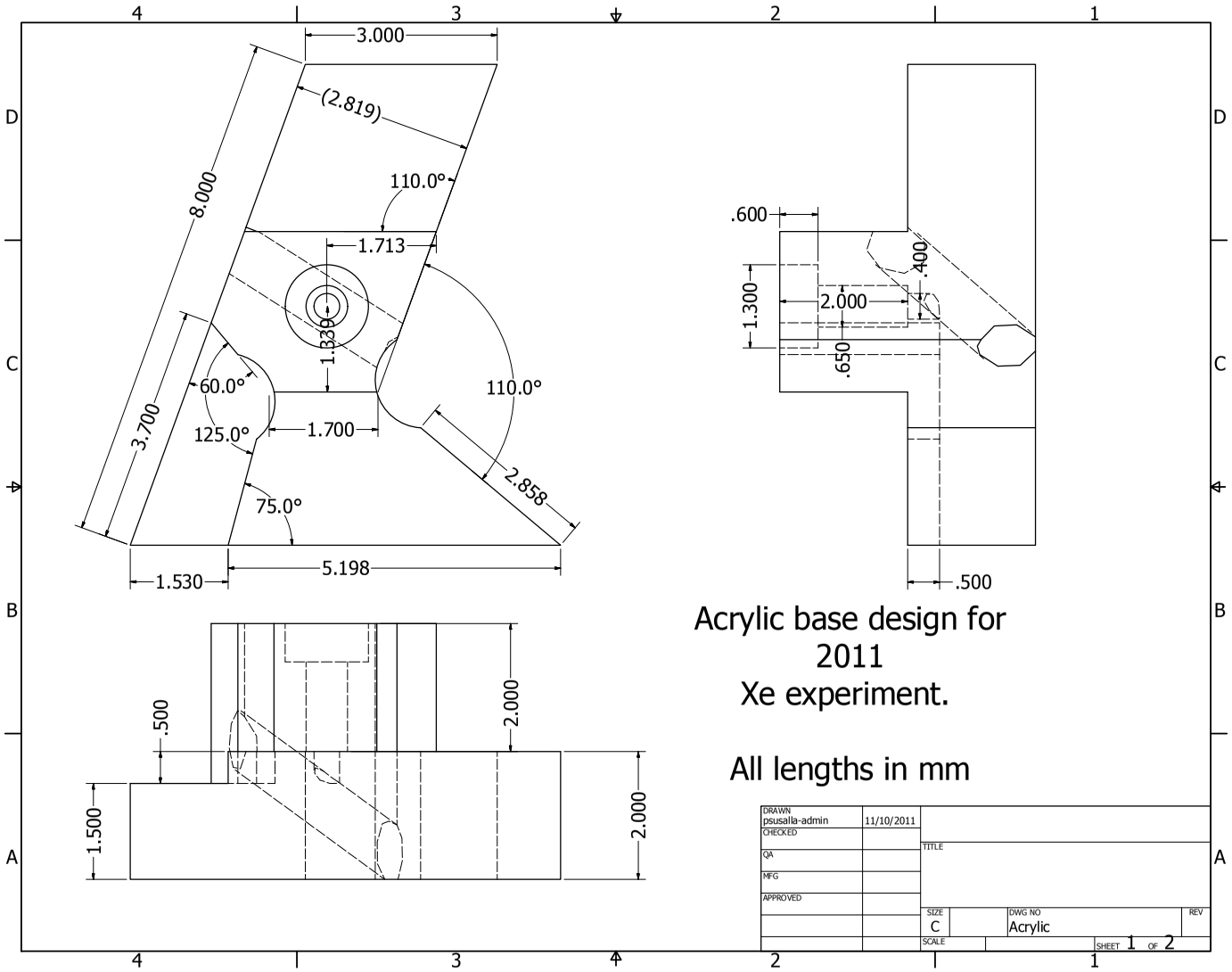
3.000
(2.819)
8.000
110.0°
1.713
1.330
60.0°
110.0°
3.700
125.0°
1.700
2.858
75.0°
1.530
5.198
.600
.400
1.300
2.000
.650
.500
.500
2.000
1.500
2.000
Acrylic base design for
2011
Xe experiment.
All lengths in mm
DRAWN
psusalla-admin
11/10/2011
CHECKED
QA
MFG
APPROVED
TITLE
SIZE
C
DWG NO
Acrylic
REV
SCALE
SHEET 1 OF 2

Stalk angles.
All lengths in mm

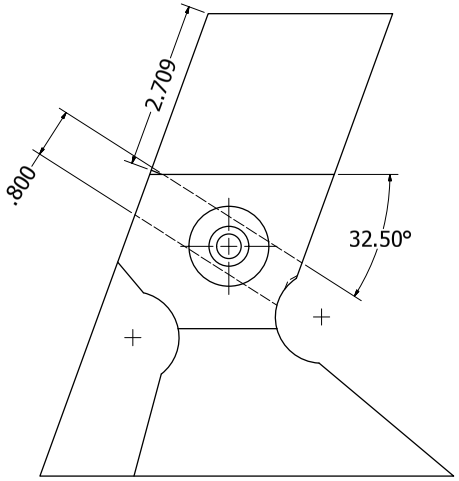

Azimuthal angle

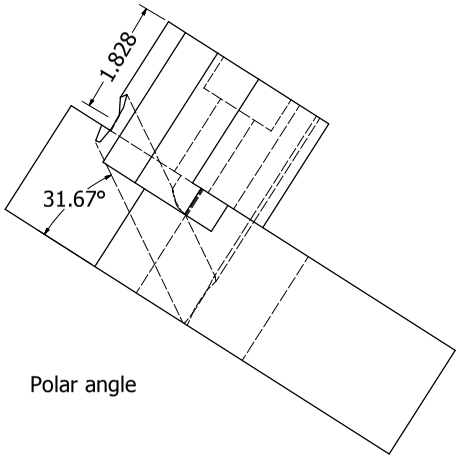

Polar angle

DRAWN psusalla-admin	11/10/2011		
CHECKED		TITLE	
QA			
MFG			
APPROVED		SIZE C	DWG NO Acrylic REV
		SCALE	SHEET 2 OF 2

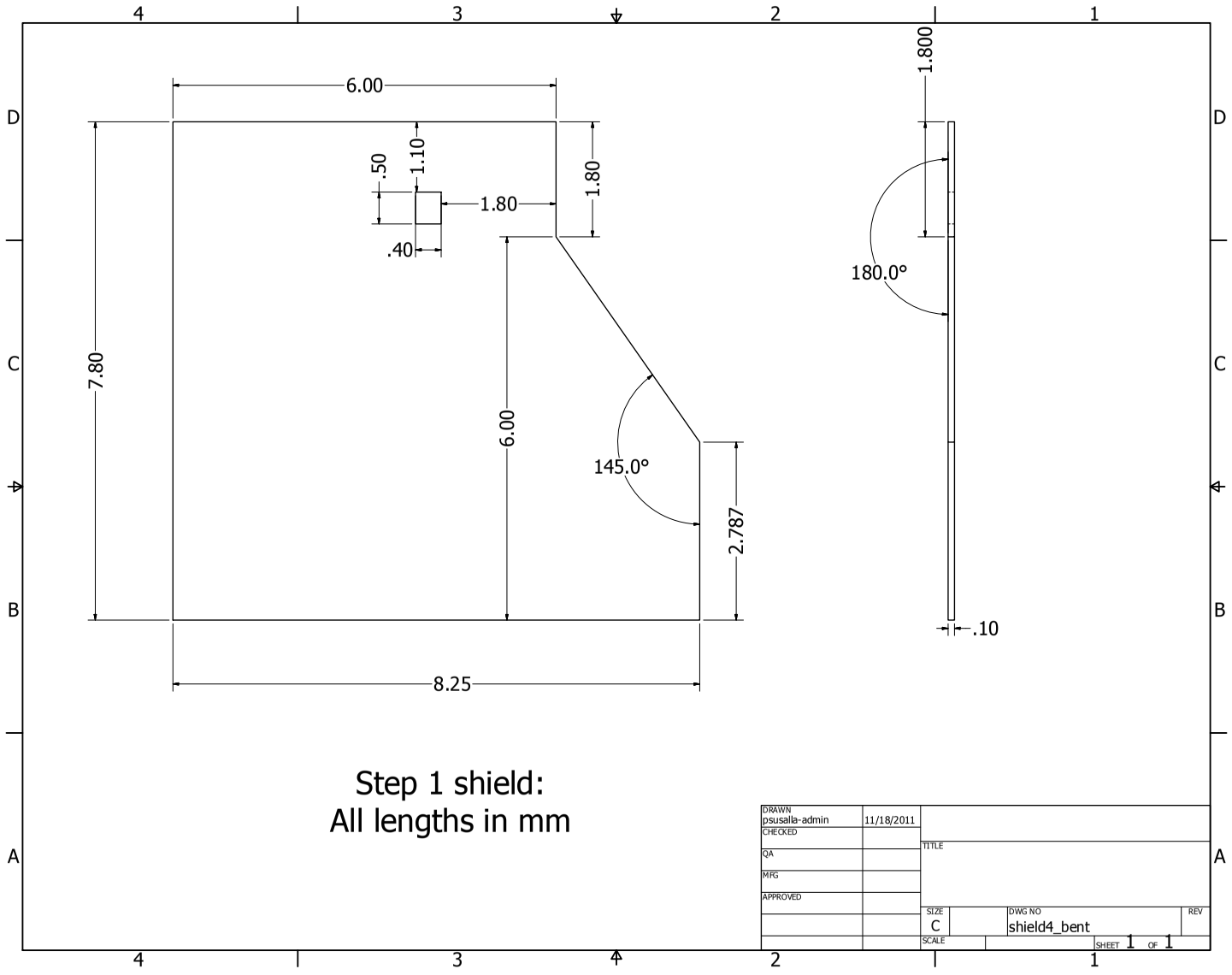
6.00
.50
1.10
1.80
1.80
.40
7.80
6.00
145.0°
2.787
8.25
1.800
180.0°
.10
Step 1 shield:
All lengths in mm
DRAWN
psusalla-admin
11/18/2011
CHECKED
QA
MFG
APPROVED
TITLE
SIZE
C
DWG NO
shield4_bent
REV
SCALE
SHEET 1 OF 1

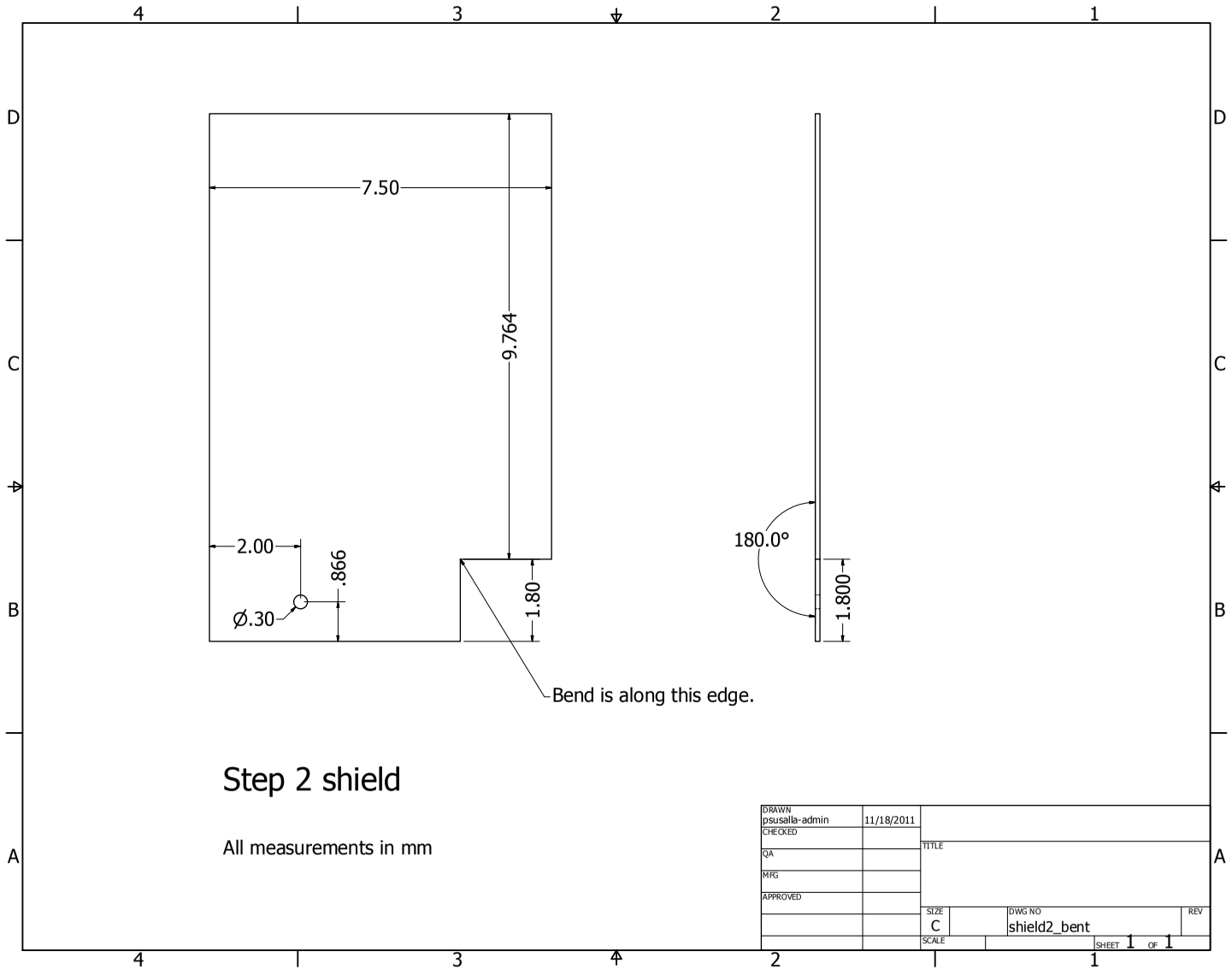
7.50
9.764
2.00
.866
Ø.30
1.80
180.0°
1.800
Bend is along this edge.
Step 2 shield
All measurements in mm
DRAWN
psusalla-admin
11/18/2011
CHECKED
QA
MFG
APPROVED
TITLE
SIZE
C
DWG NO
shield2_bent
REV
SCALE
SHEET 1 OF 1

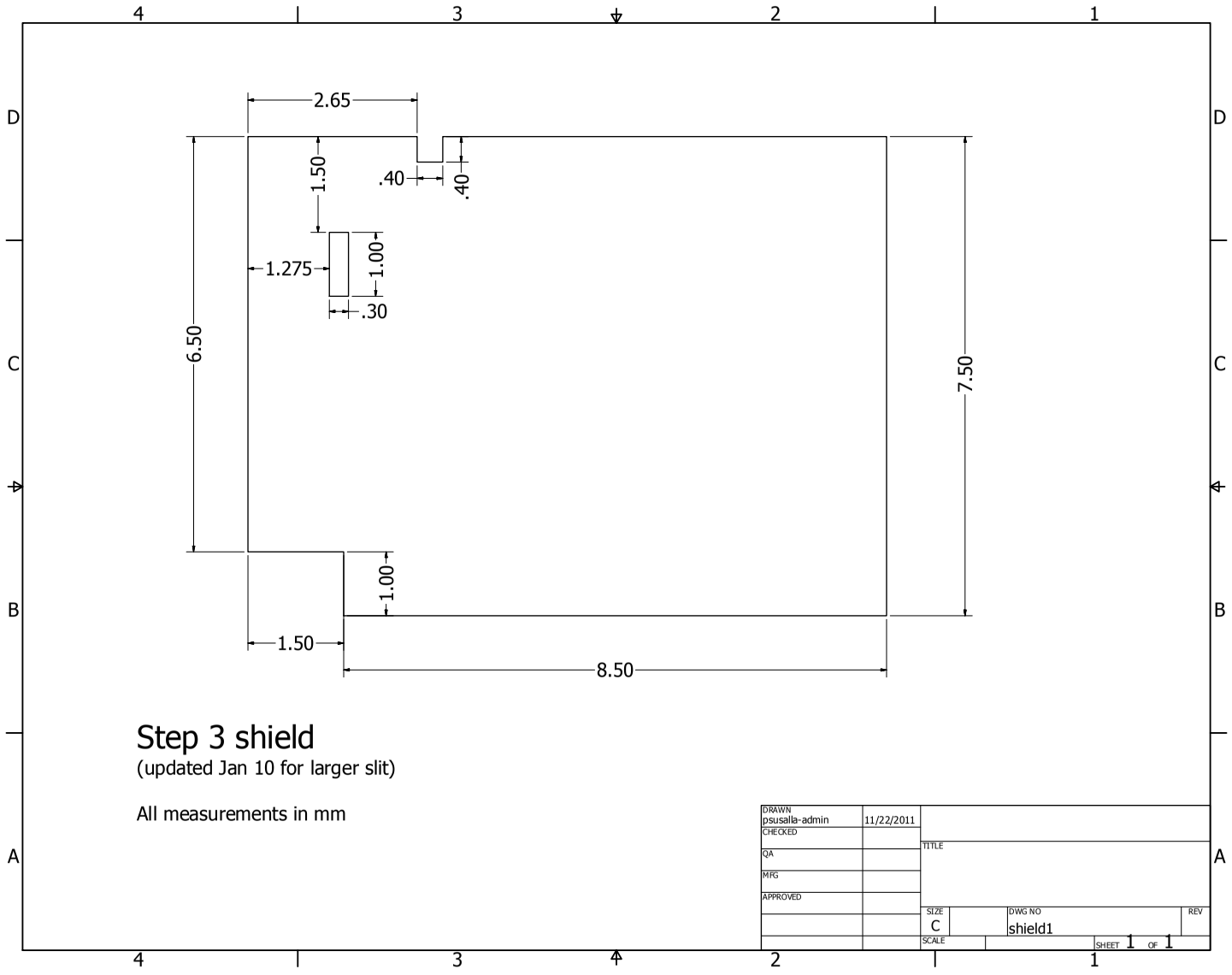
4
3
2
1
D
C
B
A
2.65
1.50
.40
.40
1.275
1.00
.30
6.50
7.50
1.00
1.50
8.50
Step 3 shield
(updated Jan 10 for larger slit)
All measurements in mm
DRAWN
psusalla-admin
11/22/2011
CHECKED
QA
MFG
APPROVED
TITLE
SIZE
C
DWG NO
shield1
REV
SCALE
SHEET 1 OF 1

APPENDIX F

2011 Data

Raw data is shown here for each shot taken in the 2011 OMEGA campaign. Links in the shot number and SRF number provide access to the specific setup and results of each shot through the LLE Omega User website (LLE login required).

Zinc disk target

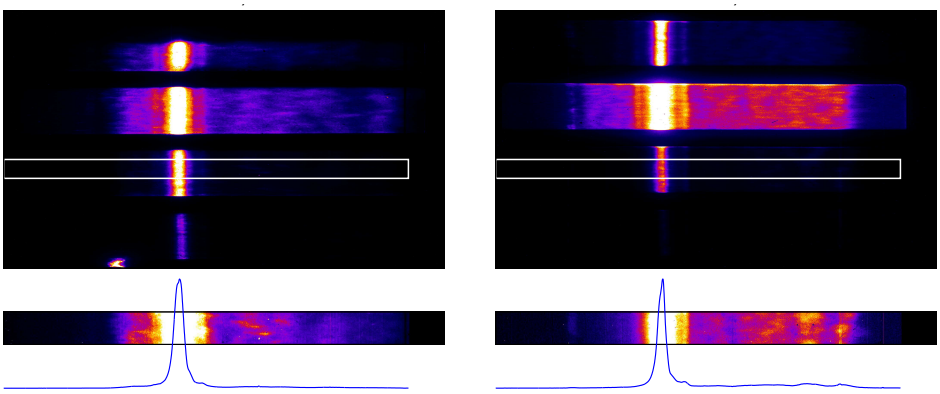

(a) TIM 3 (b) TIM 1

Figure F.1: Raw MCP data.

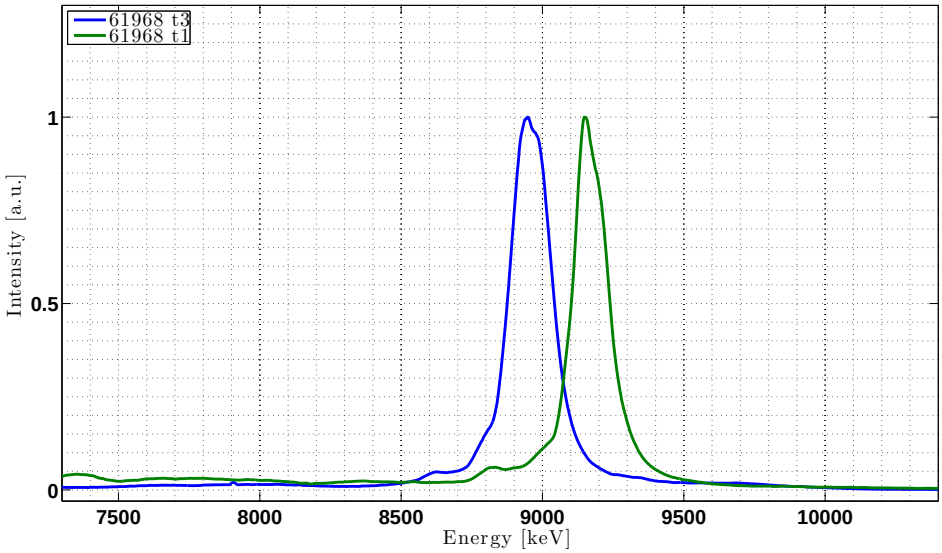

Figure F.2: Lineouts from selected regions.

Target: 16, 400 μm slit
SRF 35382
Shot 61969
Notes:
Target images: Target: 16

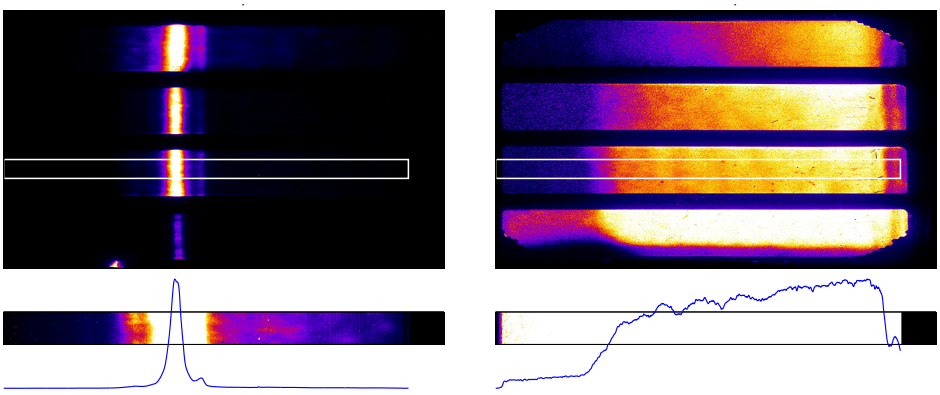

(a) TIM 3 (b) TIM 1

Figure F.3: Raw MCP data.

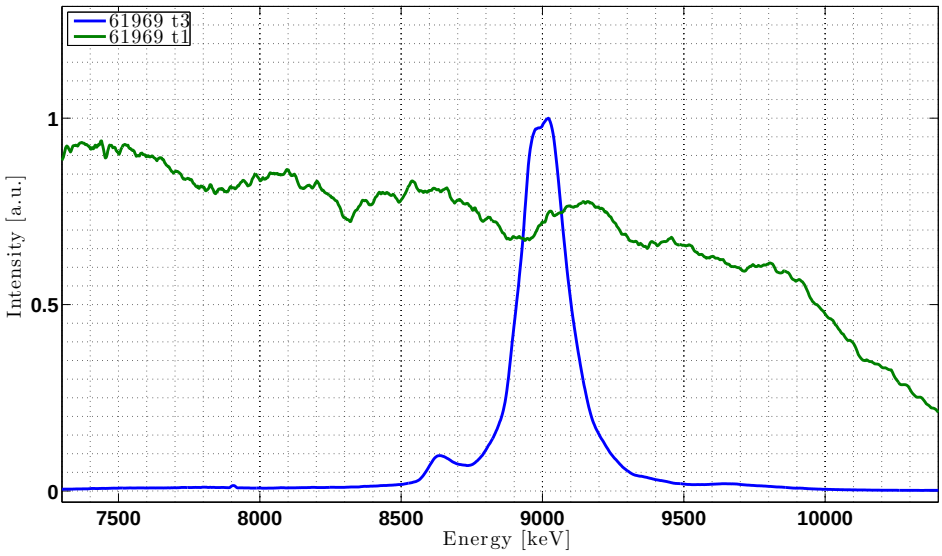

Figure F.4: Lineouts from selected regions.

Target: 23, 400 μm slit
SRF 35123
Shot 61970
Notes: Drive and Zn only (no SSC)
Target images: Target: 23

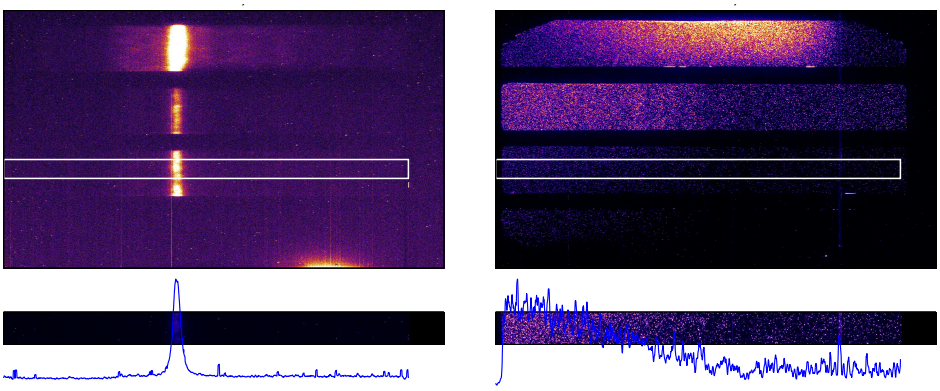

(a) TIM 3 (b) TIM 1

Figure F.5: Raw MCP data.

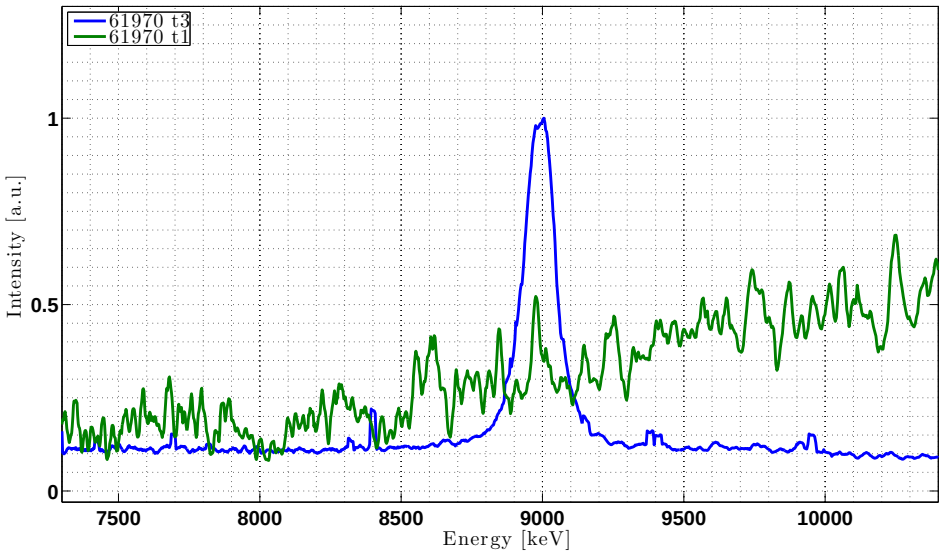

Figure F.6: Lineouts from selected regions.

Target: 44, 150 μm slit
SRF 35384
Shot 61971
Notes: All beams fired
Target images: Target: 44

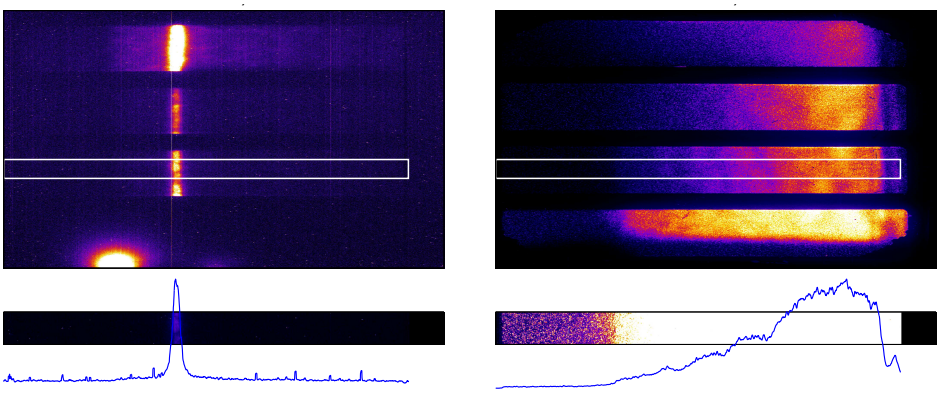

(a) TIM 3 (b) TIM 1

Figure F.7: Raw MCP data.

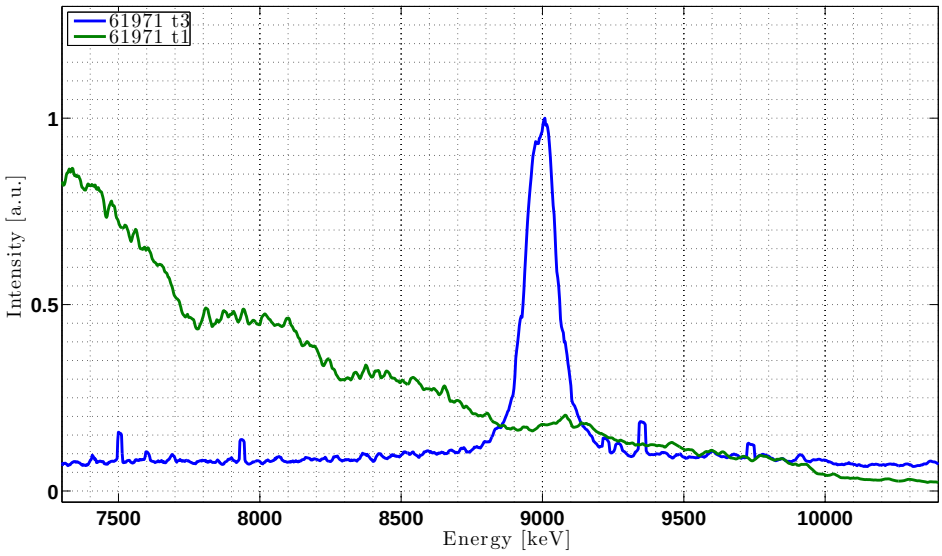

Figure F.8: Lineouts from selected regions.

Target: 21, 150 μm slit
SRF 35385
Shot 61972
Notes: Added shielding, Zn only (no drive, no SSC)
Target images: Target: 21

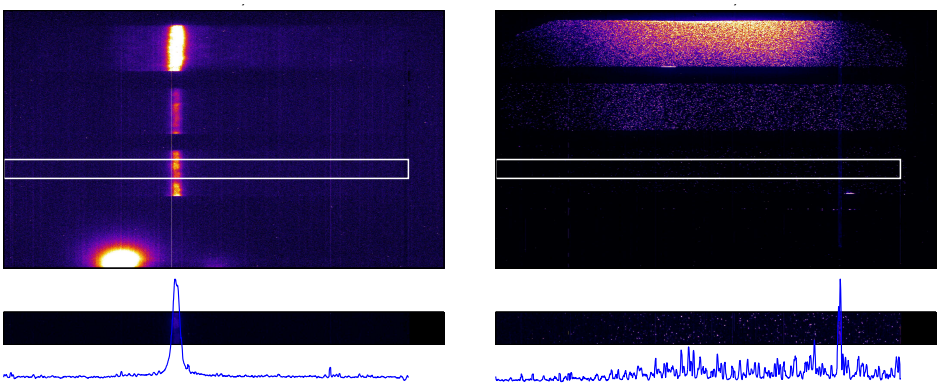

(a) TIM 3 (b) TIM 1

Figure F.9: Raw MCP data.

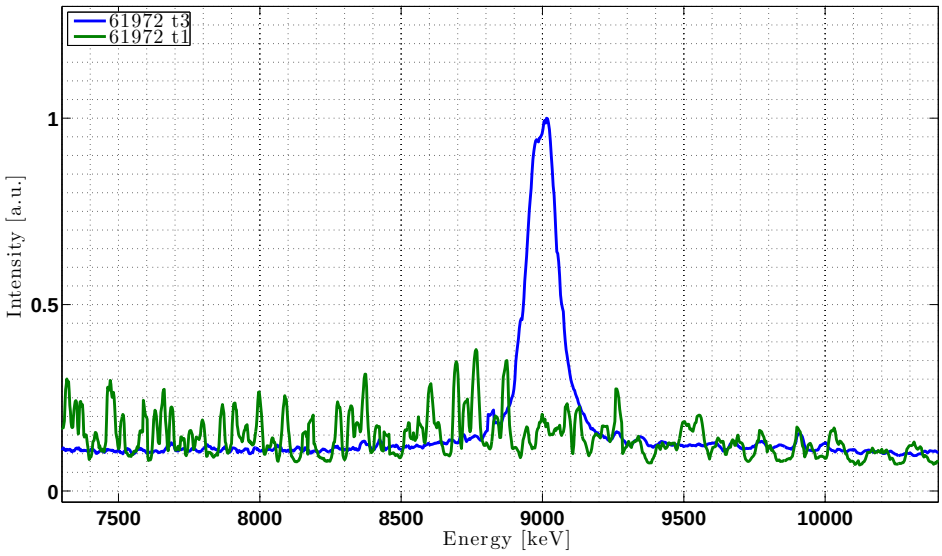

Figure F.10: Lineouts from selected regions.

Target: 24, 150 μm slit
SRF 35386
Shot 61973
Notes: Added shielding, SSC only (no Zn)
Target images: Target: 24

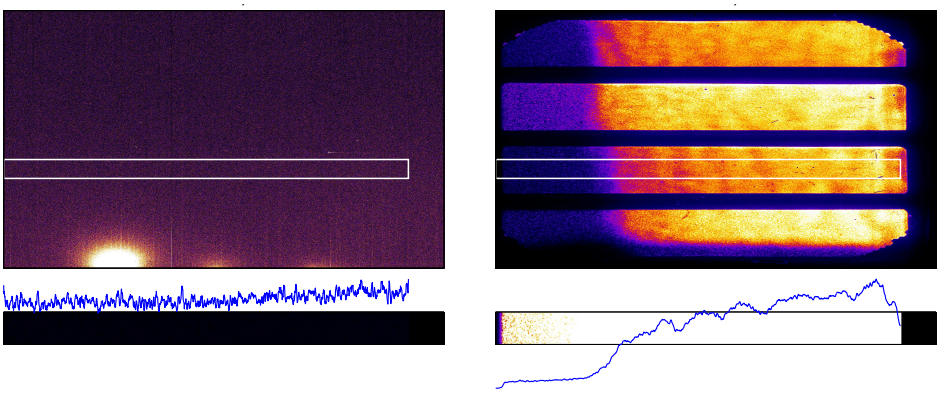

(a) TIM 3 (b) TIM 1

Figure F.11: Raw MCP data.

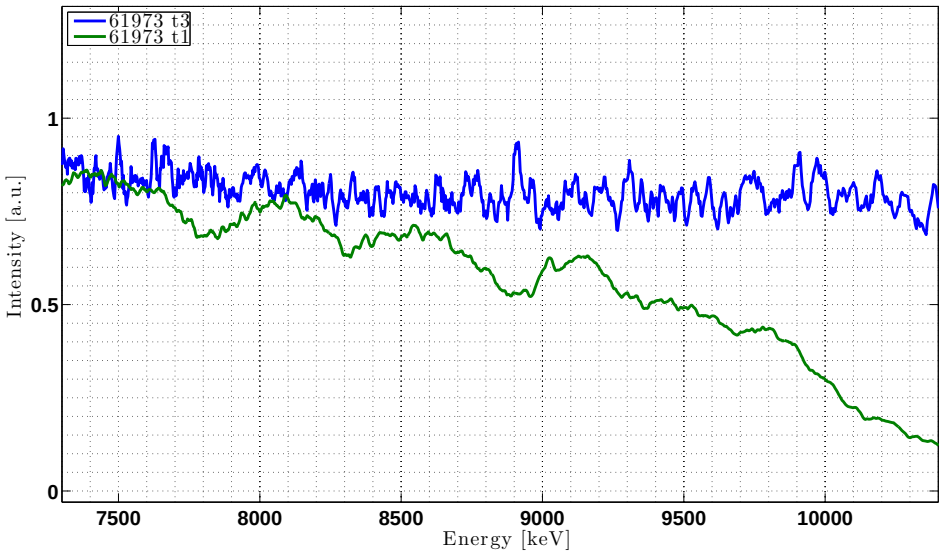

Figure F.12: Lineouts from selected regions.

Target: 36, 150 μm slit
SRF 35387
Shot 61974
Notes: Added shielding, Drive and Zn only (no SSC)
Target images: Target: 36

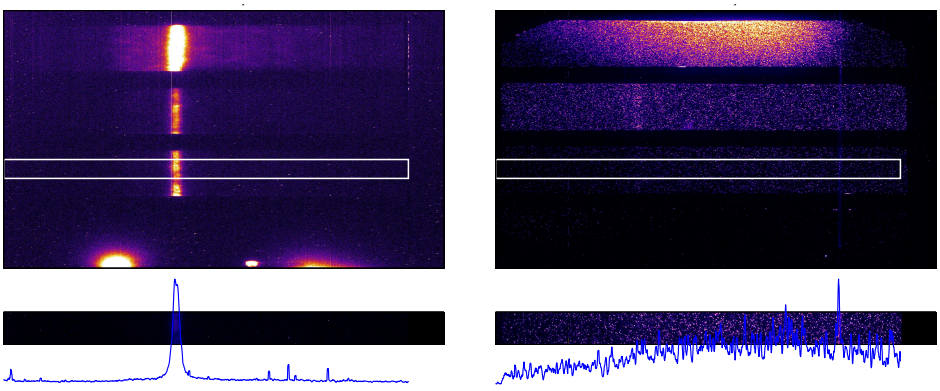

(a) TIM 3 (b) TIM 1

Figure F.13: Raw MCP data.

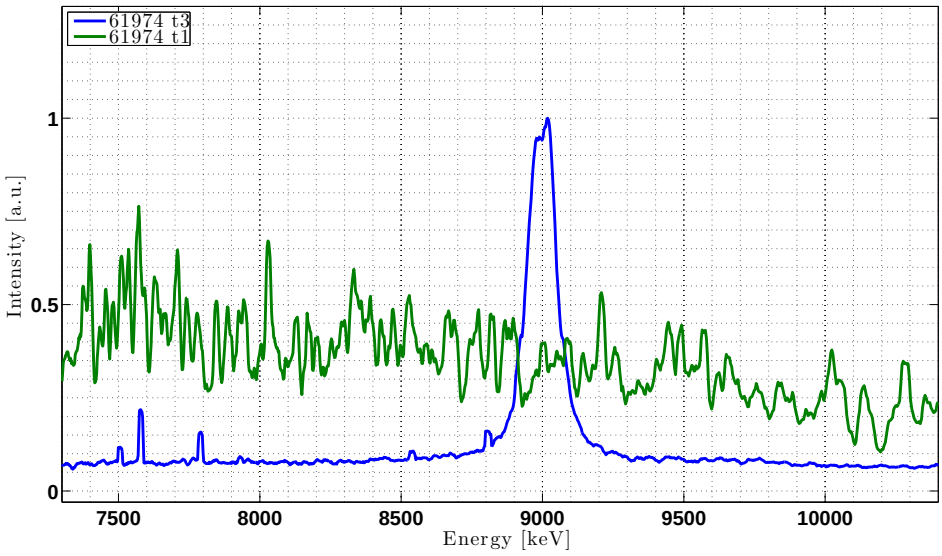

Figure F.14: Lineouts from selected regions.

Target: 22, 150 μm slit
SRF 35348
Shot 61976
Notes: Extra shielding added, drive and Zn only (no SSC)
Target images: Target: 22

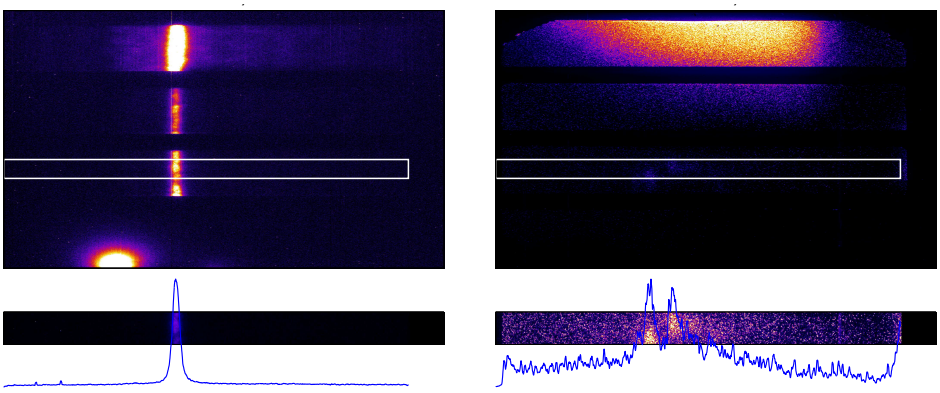

(a) TIM 3 (b) TIM 1

Figure F.15: Raw MCP data.

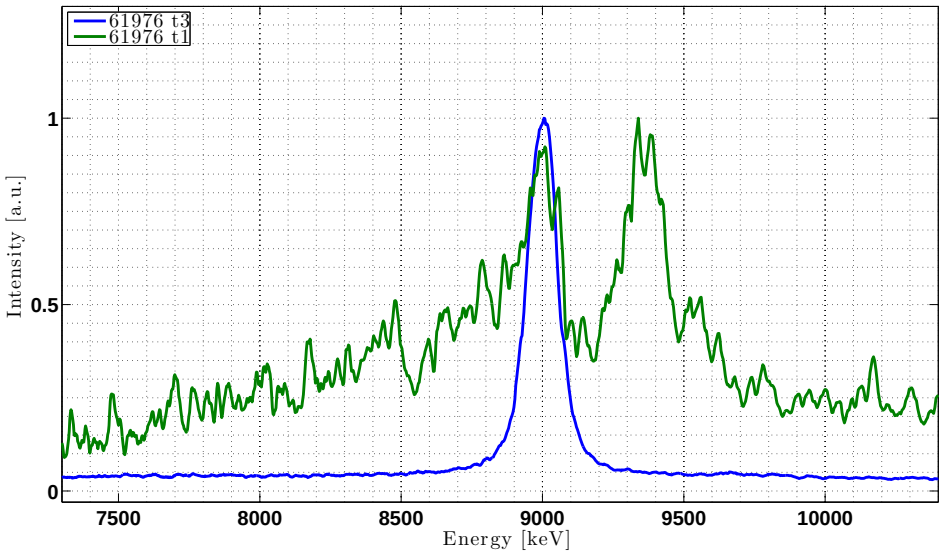

Figure F.16: Lineouts from selected regions.

Target: 19, 400 μm slit
SRF 35488
Shot 61977
Notes: Curved crystal, no added shielding, drive and Zn source (no SSC)
Target images: Target: 19

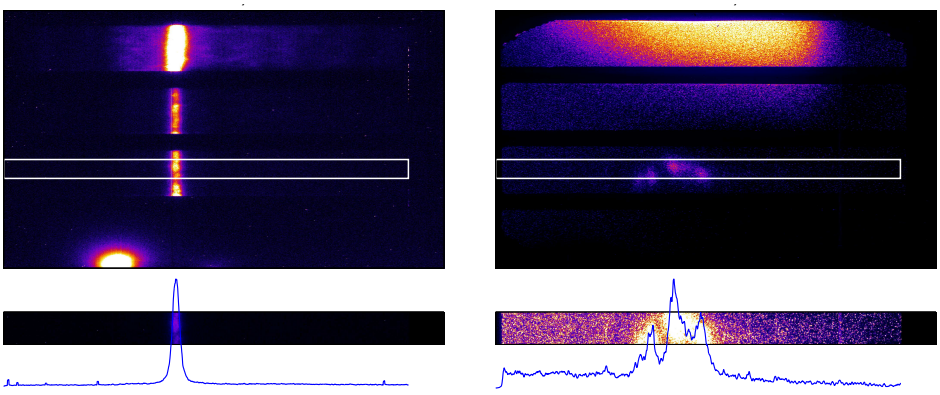

(a) TIM 3 (b) TIM 1

Figure F.17: Raw MCP data.

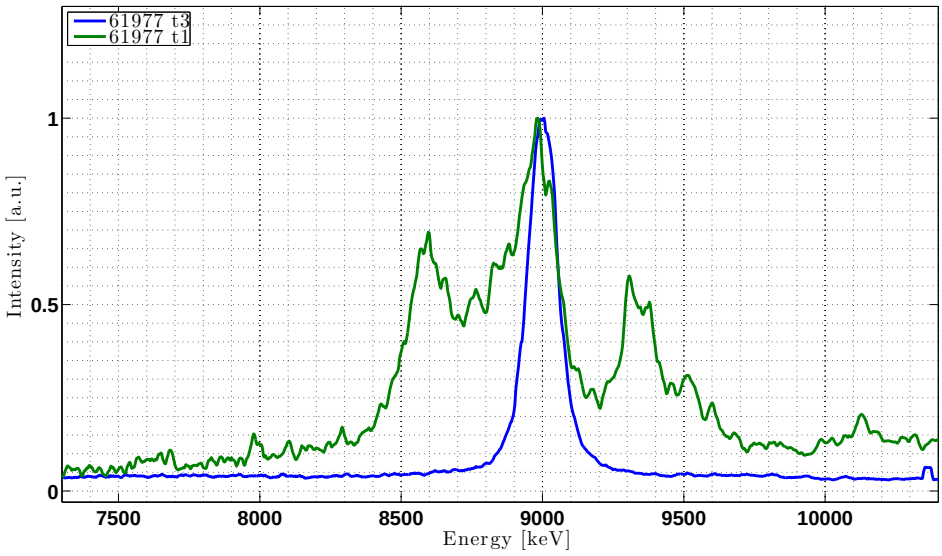

Figure F.18: Lineouts from selected regions.

Target: 17, 400 μm slit
SRF 35489
Shot 61978
Notes: Curved crystal, drive and Zn source (no SSC)
Target images: Target: 17

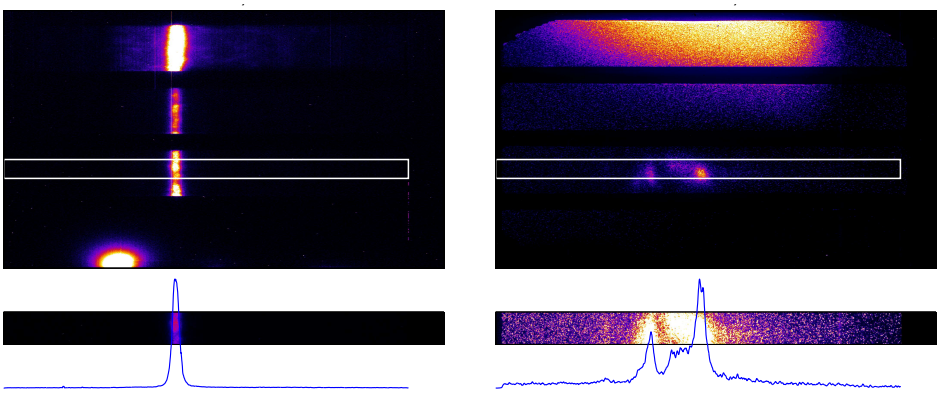

(a) TIM 3 (b) TIM 1

Figure F.19: Raw MCP data.

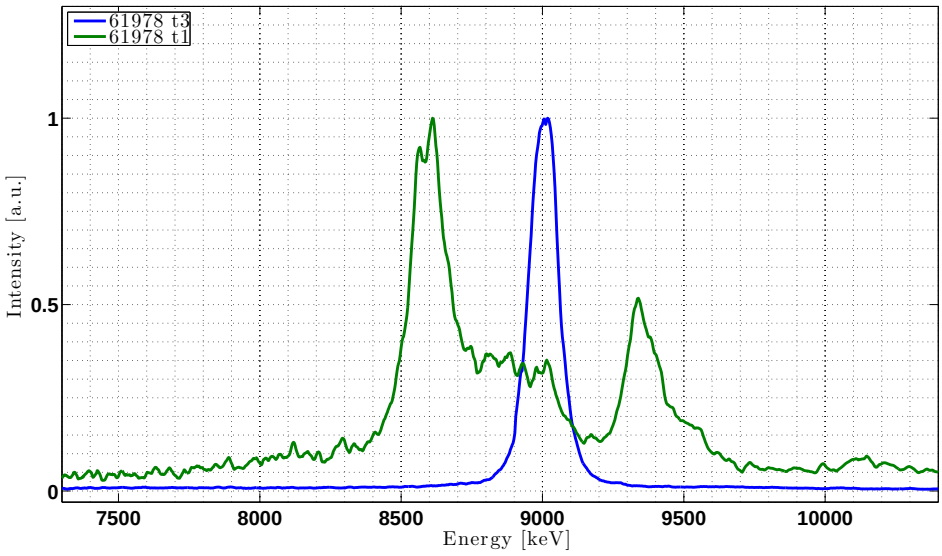

Figure F.20: Lineouts from selected regions.

Target: 40, 150 μm slit
SRF 35490
Shot 61979
Notes: Zn only (no drive, no SSC). Target did not hold gas well
Target images: Target: 40

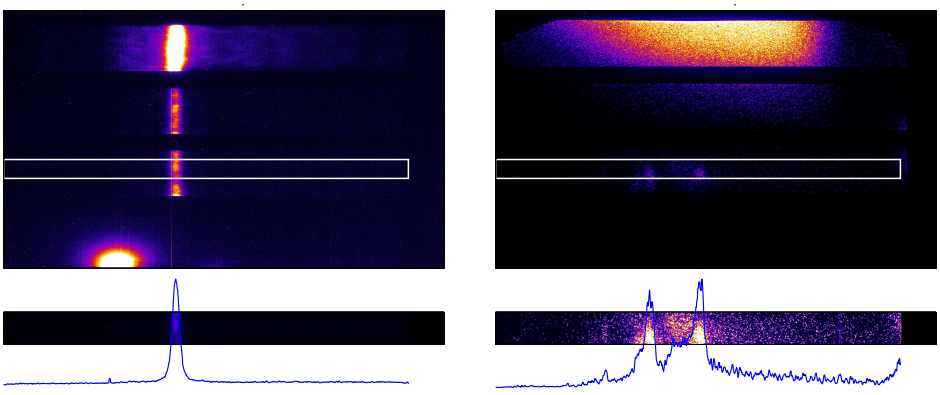

(a) TIM 3 (b) TIM 1

Figure F.21: Raw MCP data.

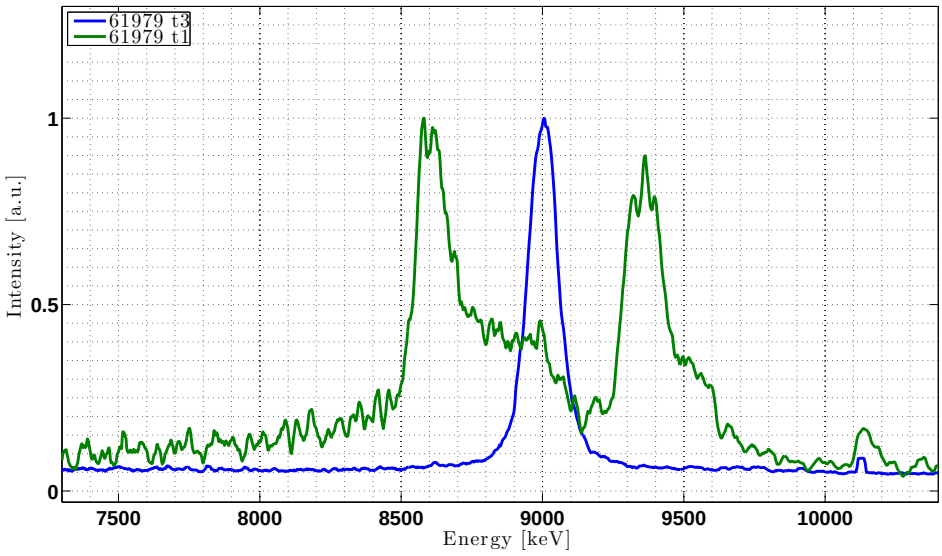

Figure F.22: Lineouts from selected regions.

Zinc disk target

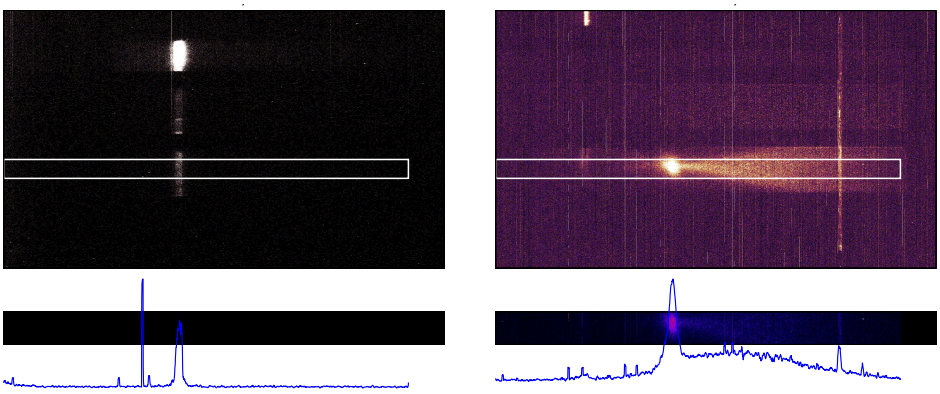

(a) TIM 3 (b) TIM 1

Figure F.23: Raw MCP data.

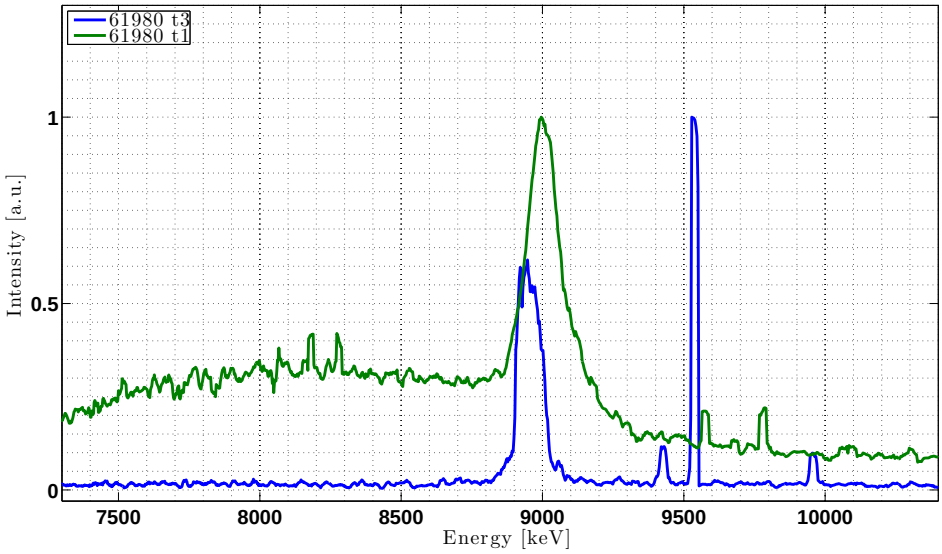

Figure F.24: Lineouts from selected regions.

APPENDIX G

2012 Data

Raw data is shown here for each shot taken in the 2012 OMEGA campaign. Links in the shot number and SRF number provide access to the specific setup and results of each shot through the LLE Omega User website (LLE login required).

Target: 45
SRF 37404
Shot 65404
Notes: Null shot (undriven). Saturated by the Be plume emission.

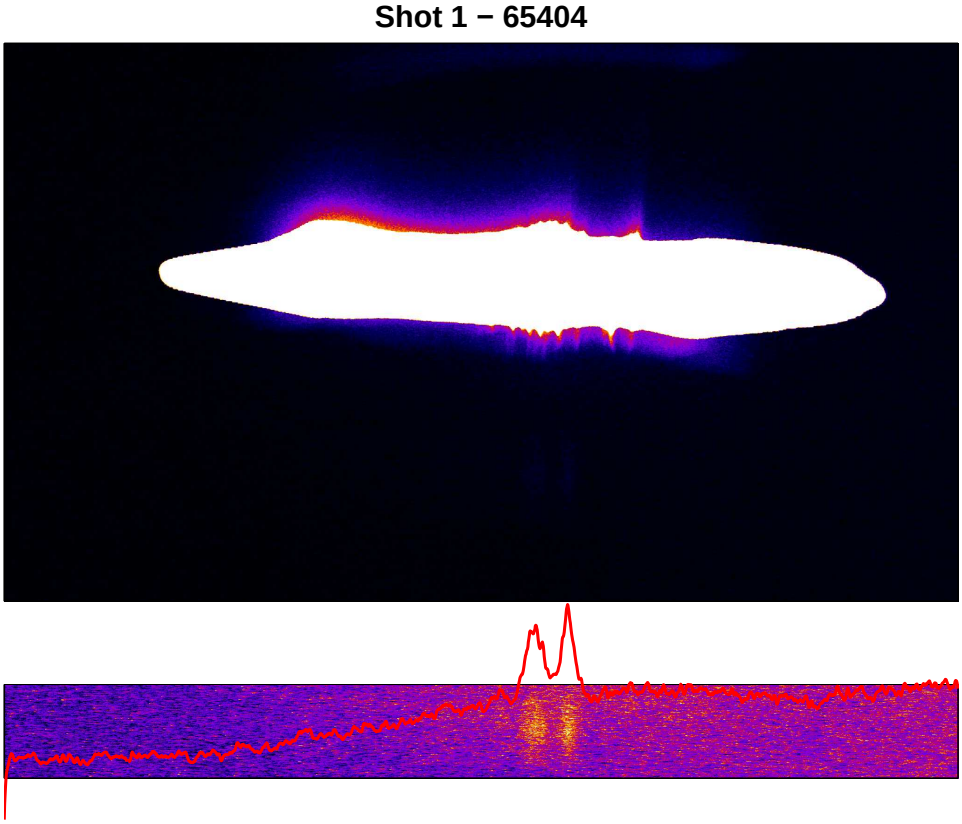

Target: 15
SRF 38917
Shot 65406
Notes: Null shot (undriven)

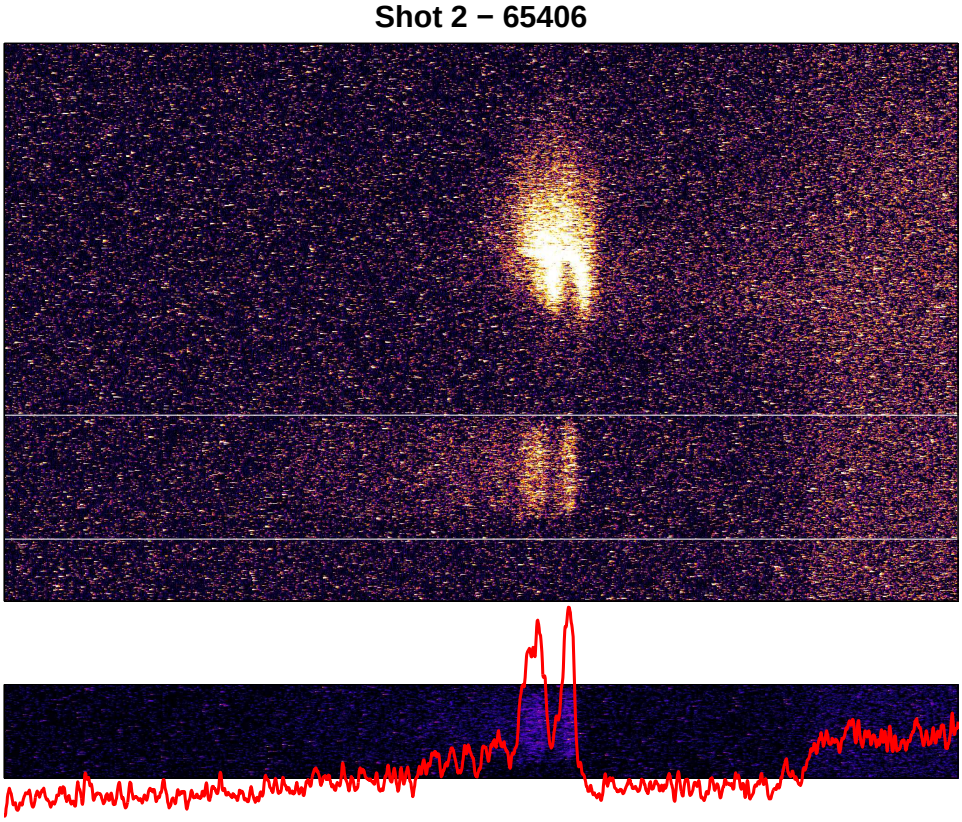

Target: 28
SRF 39035
Shot 65409
Notes:

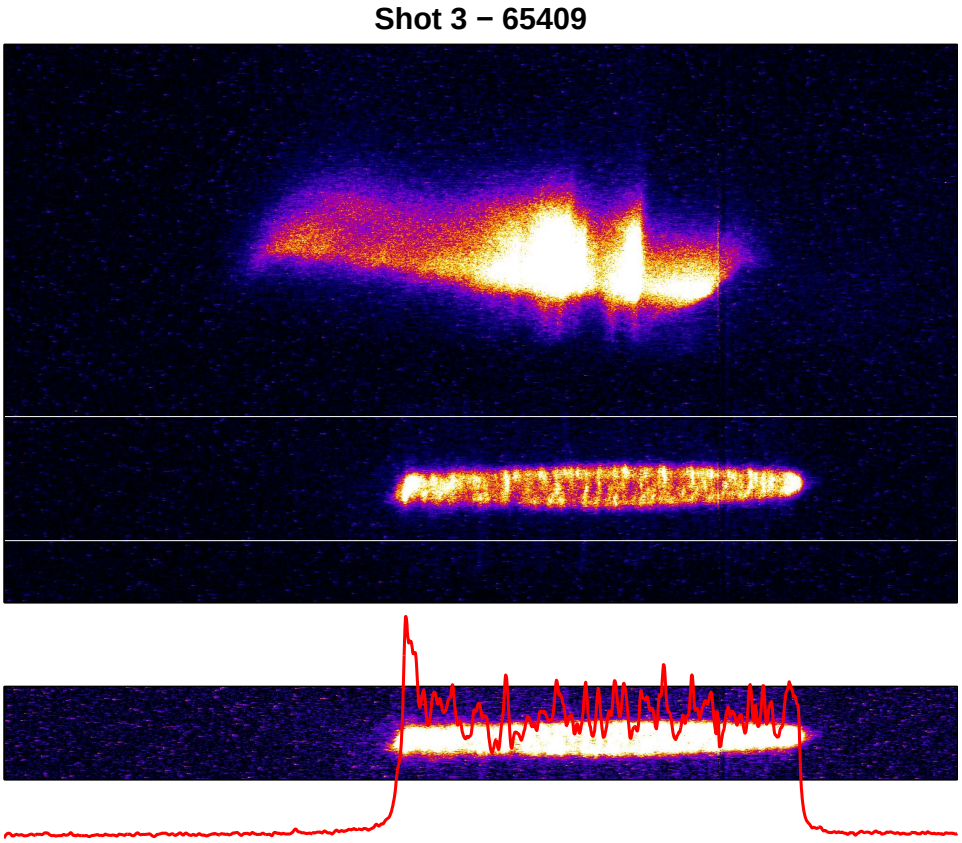

Target: 33
SRF 39036
Shot 65411
Notes:

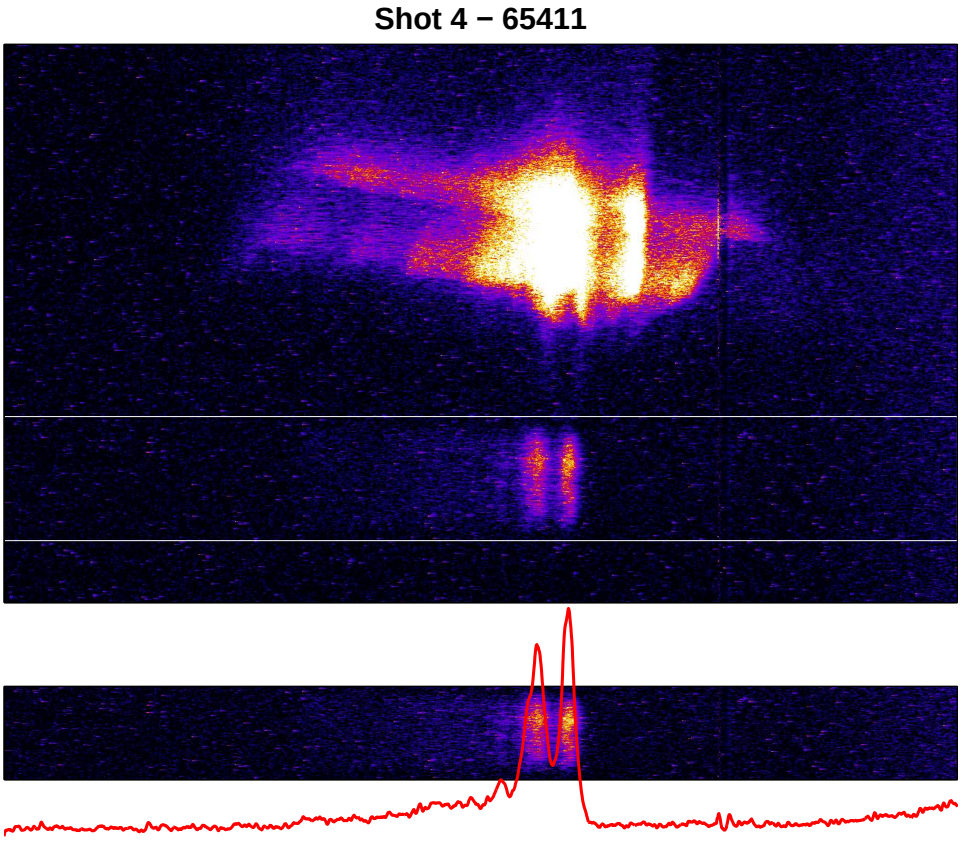

Target: 19
SRF 39033
Shot 65412
Notes:

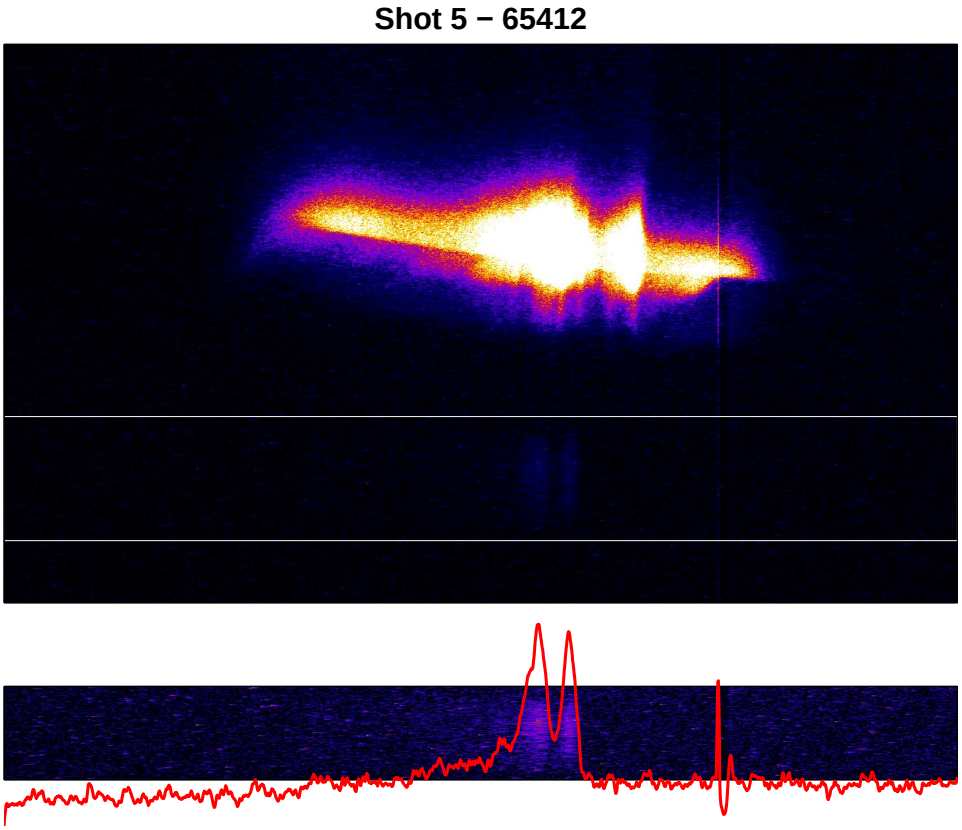

Target: 16
SRF 39034
Shot 65413
Notes:

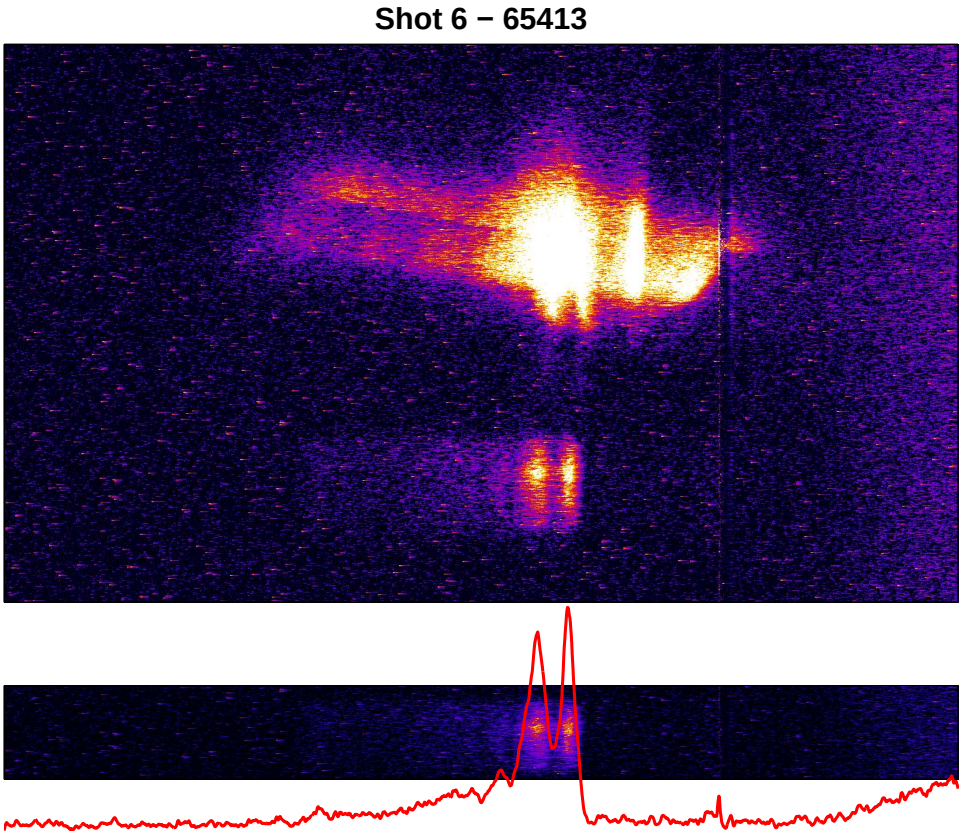

Target: 38B
SRF 39037
Shot 65414
Notes:

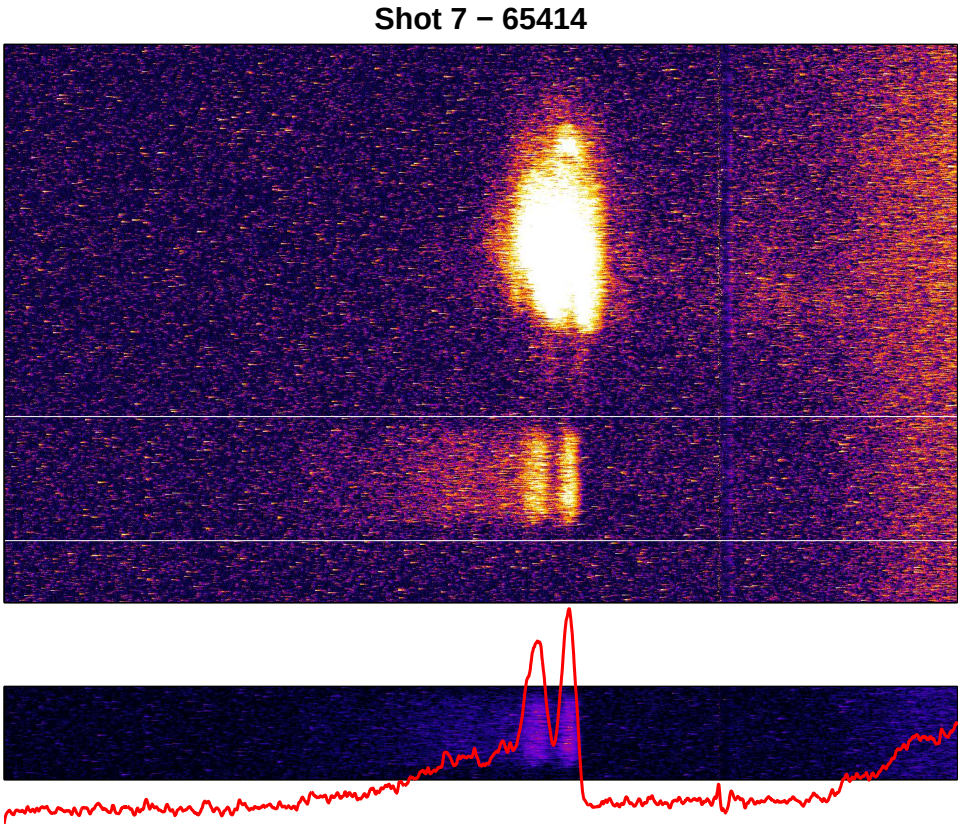

BIBLIOGRAPHY

BIBLIOGRAPHY

[1] Broadband beam smoothing on omega with two-dimensional smoothing by spectral dispersion. In *LLE 1999 Annual Report*, vol. 99. University of Rochester for the US Department of Energy, Jan. 2000.

[2] A. Thompson *et al.* X-ray data booklet. Center for X-ray Optics and Advanced Light Sources, Lawrence Berkeley National Lab, Berkeley, USA, Oct. 2009.

[3] Balza Achmad and Esam M. A. Hussein. An x-ray compton scatter method for density measurement at a point within an object. *Applied Radiation and Isotopes*, 60(6):805 – 814, 2004.

[4] K. U. Akli, P K Patel, R Van Maren, R B Stephens, M H Key, D P Higginson, B Westover, C D Chen, A J Mackinnon, T Bartal, F N Beg, S Chawla, R Fedosejevs, R R Freeman, D S Hey, G E Kemp, S LePape, A Link, T Ma, A G MacPhee, H S McLean, Y Ping, Y Y Tsui, L D Van Woerkom, M S Wei, T Yabuuchi, and S Yuspeh. A dual channel x-ray spectrometer for fast ignition research. *Journal of Instrumentation*, 5(07):P07008, 2010.

[5] D. Arnett, B. Fryxell, and E. Mueller. Instabilities and nonradial motion in SN 1987A. *ApJ*, 341:L63–L66, June 1989.

[6] Stefano Atzeni and Jurgen Meyer-Ter-Vehn. *The Physics of Interial Fusion*. Oxford University Press, 2004.

[7] Stefano Atzeni, Angelo Schiavi, and Mauro Temporal. Converging geometry Rayleigh–Taylor instability and central ignition of inertial confinement fusion target. *Plasma Phys. Control. Fusion*, 46:B111–B120, 2004.

[8] H. Azechi, T. Sakaiya, S. Fujioka, Y. Tamari, K. Otani, K. Shigemori, M. Nakai, H. Shiraga, N. Miyanaga, and K. Mima. Comprehensive diagnosis of growth rates of the ablative Rayleigh-Taylor instability. *Phys. Rev. Lett.*, 98(4):045002, Jan. 2007.

[9] D. Babonneau, M. Primout, F. Girard, J.-P. Jadaud, M. Naudy, B. Villette, S. Depierreux, C. Blancard, G. Faussurier, K. B. Fournier, L. Suter, R. Kauffman, S. Glenzer, M. C. Miller, J. Grün, and J. Davis. Efficient multi-kev x-ray sources from laser-exploded metallic thin foils. *Phys. Plasmas*, 15(9):092702, 2008.

[10] C. A. Back, J. Davis, J. Grun, L. J. Suter, O. L. Landen, W. W. Hsing, and M. C. Miller. Multi-kev x-ray conversion efficiency in laser-produced plasmas. *Phys. Plasmas*, 10(5):2047–2055, 2003.

[11] C. A. Back, J. Grun, C. Decker, L. J. Suter, J. Davis, O. L. Landen, R. Wallace, W. W. Hsing, J. M. Laming, U. Feldman, M. C. Miller, and C. Wuest. Efficient multi-kev underdense laser-produced plasma radiators. *Phys. Rev. Lett.*, 87(27):275003, Dec. 2001.

[12] C. A. Back, J. L. Davis, J. Grun, O. L. Landen, M. C. Miller, and L. J. Suter. Multi-kilovolt x-ray conversion efficiencies. In George A. Kyrala and Jean-Claude J. Gauthier, editors, *Applications of X Rays Generated from Lasers and Other Bright Sources II*, vol. 4504, pp. 133–142. SPIE, 2001.

[13] S. Barwick and J. Beacom. Aps neutrino study: Report of the neutrino astrphysics and cosmology working group. Technical report, American Physical Society, Oct. 2004.

[14] F. N. Beg, A. R. Bell, A. E. Dangor, C. N. Danson, A. P. Fews, M. E. Glinsky, B. A. Hammel, P. Lee, P. A. Norreys, and M. Tatarakis. A study of picosecond laser–solid interactions up to 10^{19} w cm^{-2}. *Phys. Plasmas*, 4(2):447–457, 1997.

[15] D Berenyi, G Hock, S Ricz, B Schlenk, and A Valek. K_α/K_β x-ray intensity ratios and k-shell ionisation cross sections for bombardment by electrons of 300-600 kev. *J. Phys. B: Atom. Molec. Phys.*, 11(4), 1978.

[16] R. Betti, V. N. Goncharov, R. L. McCrory, and C. P. Verdon. Growth rates of the ablative Rayleigh–Taylor instability in inertial confinement fusion. *Phys. Plasmas*, 5(5):1446–1454, 1998.

[17] Stephen E. Bodner. Rayleigh-Taylor instability and laser-pellet fusion. *Phys. Rev. Lett.*, 33(13):761–764, Sep 1974.

[18] Stephen E. Bodner. Critical elements of high gain laser fusion. *Journal of Fusion Energy*, 1(3):221–240, May 1981.

[19] K. J. Borkowski, J. M. Blondin, and R. McCray. X-rays from the impact of sn 1987a with its circumstellar ring. *The Astrophysical Journal*, 477(1):281, 1997.

[20] S. Bouquet, C. Stéhlé, M. Koenig, J.-P. Chièze, A. Benuzzi-Mounaix, D. Batani, S. Leygnac, X. Fleury, H. Merdji, C. Michaut, F. Thais, N. Grandjouan, T. Hall, E. Henry, V. Malka, and J.-P. J. Lafon. Observation of laser driven supercritical radiative shock precursors. *Phys. Rev. Lett.*, 92:225001, Jun 2004.

[21] D. K. Bradley, O. L. Landen, A. B. Bullock, S. G. Glendinning, and R. E. Turner. Efficient, 1-100-keV x-ray radiography with high spatial and temporal resolution. *Optics Letters*, 27:134–136, 2002.

[22] A. Bret, M.-C. Firpo, and C. Deutsch. Characterization of the initial filamentation of a relativistic electron beam passing through a plasma. *Phys. Rev. Lett.*, 94:115002, Mar. 2005.

[23] A. Bret, L. Gremillet, and J. C. Bellido. How really transverse is the filamentation instability? *Phys. Plasmas*, 14(3):032103, 2007.

[24] S. G. Brush, H. L. Sahlin, and E. Teller. Monte carlo study of a one-component plasma. i. *The Journal of Chemical Physics*, 45(6):2102–2118, 1966.

[25] K. S. Budil, B. Lasinski, M. J. Edwards, A. S. Wan, B. A. Remington, S. V. Weber, S. G. Glendinning, L. Suter, and P. E. Stry. The ablation-front Rayleigh–Taylor dispersion curve in indirect drive. *Phys. Plasmas*, 8(5):2344–2348, 2001.

[26] A. B. Bullock, O. L. Landen, and D. K. Bradley. 10 and 5 mu m pinhole-assisted point-projection backlit imaging for the national ignition facility. *Review of Scientific Instruments*, 72(1):690–693, 2001.

[27] N. H. Burnett and G. D. Enright. Hot-electron generation and transport in high-intensity laser interaction. *Canadian Journal of Physics*, 64(8):920–931, 1986.

[28] A. Caldwell, K. Lotov, A. Pukhov, and F. Simon. Proton-driven plasma-wakefield acceleration. *Nature Physics*, 5:363–367, April 2009.

[29] F. Califano, F. Pegoraro, S. V. Bulanov, and A. Mangeney. Kinetic saturation of the weibel instability in a collisionless plasma. *Phys. Rev. E*, 57:7048–7059, Jun 1998.

[30] Nuria Calvet and Erik Gullbring. The structure and emission of the accretion shock in T Tauri stars. *The Astrophysical Journal*, 509(2):802, 1998.

[31] S. Chandrasekhar. The highly collapsed configurations of a stellar mass (Second paper). *MNRAS*, 95:207–225, Jan. 1935.

[32] C. D. Chen, P. K. Patel, D. S. Hey, A. J. Mackinnon, M. H. Key, K. U. Akli, T. Bartal, F. N. Beg, S. Chawla, H. Chen, R. R. Freeman, D. P. Higginson, A. Link, T. Y. Ma, A. G. MacPhee, R. B. Stephens, L. D. Van Woerkom, B. Westover, and M. Porkolab. Bremsstrahlung and k alpha fluorescence measurements for inferring conversion efficiencies into fast ignition relevant hot electrons. *Phys. Plasmas*, 16(8):082705, 2009.

[33] H. Chen, B. Soom, B. Yaakobi, S. Uchida, and D. D. Meyerhofer. Hot-electron characterization from $K\ \alpha$ measurements in high-contrast, p -polarized, picosecond laser-plasma interactions. *Phys. Rev. Lett.*, 70:3431–3434, May 1993.

[34] P. Chen, J. M. Dawson, Robert W. Huff, and T. Katsouleas. Acceleration of electrons by the interaction of a bunched electron beam with a plasma. *Phys. Rev. Lett.*, 54:693–696, Feb.. 1985.

[35] S. N. Chen, P. K. Patel, H.-K. Chung, A. J. Kemp, S. Le Pape, B. R. Maddox, S. C. Wilks, R. B. Stephens, and F. N. Beg. X-ray spectroscopy of buried layer foils irradiated at laser intensities in excess of 10[sup 20] w/cm[sup 2]. *Phys. Plasmas*, 16(6):062701, 2009.

[36] Roger A. Chevalier. Type ii supernovae sn 1987a and sn 1993j. *Science*, 276(5317):1374–1378, 1997.

[37] J Chihara. Difference in x-ray scattering between metallic and non-metallic liquids due to conduction electrons. *Journal of Physics F: Metal Physics*, 17(2):295–304, 1987.

[38] J Chihara. Interaction of photons with plasmas and liquid metals-photoabsorption and scattering. *J. Phys.: Condens. Matter*, 12, 2000.

[39] H.-K. Chung, M.H. Chen, W.L. Morgan, Y. Ralchenko, and R.W. Lee. Flychk: Generalized population kinetics and spectral model for rapid spectroscopic analysis for all elements. *High Energy Density Physics*, 1(1):3 – 12, 2005.

[40] J. D. Colvin, K. B. Fournier, J. Kane, S. Langer, M. J. May, and H. A. Scott. A computational study of x-ray emission from high-z x-ray sources on the national ignition facility laser. *High Energy Density Physics*, 7(4):263 – 270, 2011.

[41] Commerçon, B., Audit, E., Chabrier, G., and Chièze, J.-P. Physical and radiative properties of the first-core accretion shock. *A&A*, 530:A13, 2011.

[42] J. P. Conner, W. D. Evans, and R. D. Belian. The Recent Appearance of a New X-Ray Source in the Southern Sky. *Astrophys J. Lett*, 157:L157, Sept. 1969.

[43] E. Costa, F. Frontera, J. Heise, M. Feroci, J. in't Zand, F. Fiore, M. N. Cinti, D. Dal Fiume, L. Nicastro, M. Orlandini, E. Palazzi, M. Rapisarda, G. Zavattini, R. Jager, A. Parmar, A. Owens, S. Molendi, G. Cusumano, M. C. Maccarone, S. Giarrusso, A. Coletta, L. A. Antonelli, P. Giommi, J. M. Muller, L. Piro, and R. C. Butler. Discovery of an X-ray afterglow associated with the γ-ray burst of 28 Feb. 1997. *Nature*, 387:783–785, June 1997.

[44] A. Cucchiara, A. J. Levan, D. B. Fox, N. R. Tanvir, T. N. Ukwatta, E. Berger, T. Krühler, A. Küpcü Yoldas, X. F. Wu, K. Toma, J. Greiner, F. E. Olivares, A. Rowlinson, L. Amati, T. Sakamoto, K. Roth, A. Stephens, Alexander Fritz, J. P. U. Fynbo, J. Hjorth, D. Malesani, P. Jakobsson, K. Wiersema, P. T. O'Brien, A. M. Soderberg, R. J. Foley, A. S. Fruchter, J. Rhoads, R. E. Rutledge, B. P. Schmidt, M. A. Dopita, P. Podsiadlowski, R. Willingale, C. Wolf, S. R. Kulkarni, and P. DÄôAvanzo. A photometric redshift of z 9.4 for grb 090429b. *The Astrophysical Journal*, 736(1):7, 2011.

[45] J. M. Dawson. Particle simulation of plasmas. *Reviews of Modern Physics*, 55:403–447, April 1983.

[46] Michael A.B. Deakin. G.I. Taylor and the trinity test. *International Journal of Mathematical Education in Science and Technology*, 42(8):1069–1079, 2011.

[47] S. Deng, C. D. Barnes, C. E. Clayton, C. O'Connell, F. J. Decker, R. A. Fonseca, C. Huang, M. J. Hogan, R. Iverson, D. K. Johnson, C. Joshi, T. Katsouleas, P. Krejcik, W. Lu, W. B. Mori, P. Muggli, E. Oz, F. Tsung, D. Walz, and M. Zhou. Hose instability and wake generation by an intense electron beam in a self-ionized gas. *Phys. Rev. Lett.*, 96(4):045001, Jan. 2006.

[48] E. L. Dewald, K. M. Campbell, R. E. Turner, J. P. Holder, O. L. Landen, S. H. Glenzer, R. L. Kauffman, L. J. Suter, M. Landon, M. Rhodes, and D. Lee. Dante soft x-ray power diagnostic for national ignition facility. *Review of Scientific Instruments*, 75(10):3759–3761, 2004.

[49] E. S. Dodd, R. G. Hemker, C.-K. Huang, S. Wang, C. Ren, W. B. Mori, S. Lee, and T. Katsouleas. Hosing and sloshing of short-pulse gev-class wakefield drivers. *Phys. Rev. Lett.*, 88:125001, Mar. 2002.

[50] F. W. Doss, R. P. Drake, and C.C Kuranz. Statistical inference in the presence of an inclination effect in laboratory radiative shock experiments. *Astrophysics and Space Science*, 336:219–224, 2011. 10.1007/s10509-010-0579-4.

[51] F. W. Doss, H. F. Robey, R. P. Drake, and C. C. Kuranz. Wall shocks in high-energy-density shock tube experiments. *Phys. Plasmas*, 16(11):112705, 2009.

[52] Forrest W. Doss. *Structure in Radiative Shock Experiments*. PhD thesis, University of Michigan, 2011.

[53] F.W. Doss, R.P. Drake, and C.C. Kuranz. Repeatability in radiative shock tube experiments. *High Energy Density Physics*, 6(2):157 – 161, 2010. ICHED 2009 - 2nd International Conference on High Energy Density Physics.

[54] R. P. Drake. *High-Energy-Density Physics: Fundementals, Inertial Fusion, and Experimental Astrophysics*. Springer, 2006.

[55] R. P. Drake. Theory of radiative shocks in optically thick media. *Phys. Plasmas*, 14(4):043301, 2007.

[56] R. P. Drake. Simple Imaging of x-ray Thomson scattering. Unpublished memo, April 2009.

[57] R. P. Drake and P. A. Keiter. Rayleigh-Taylor growth at decelerating interfaces. *Phys. Plasmas*, 9(1):382–384, 2002.

[58] R. P. Drake, R. E. Turner, B. F. Lasinski, K. G. Estabrook, E. M. Campbell, C. L. Wang, D. W. Phillion, E. A. Williams, and W. L. Kruer. Efficient raman sidescatter and hot-electron production in laser-plasma interaction experiments. *Phys. Rev. Lett.*, 53:1739–1742, Oct 1984.

[59] R.P. Drake, F.W. Doss, R.G. McClarren, M.L. Adams, N. Amato, D. Bingham, C.C. Chou, C. DiStefano, K. Fidkowski, B. Fryxell, T.I. Gombosi, M.J. Grosskopf, J.P. Holloway, B. van der Holst, C.M. Huntington, S. Karni, C.M. Krauland, C.C. Kuranz, E. Larsen, B. van Leer, B. Mallick, D. Marion, W. Martin, J.E. Morel, E.S. Myra, V. Nair, K.G. Powell, L. Rauchwerger, P. Roe, E. Rutter, I.V. Sokolov, Q. Stout, B.R. Torralva, G. Toth, K. Thornton, and A.J. Visco. Radiative effects in radiative shocks in shock tubes. *High Energy Density Physics*, 7(3):130 – 140, 2011.

[60] V. Drean, M. Olazabal-Loumé, J. Sanz, and V. T. Tikhonchuk. Dynamics and stability of radiation-driven double ablation front structures. *Phys. Plasmas*, 17(12):122701–122701–14, 2010.

[61] T. Ebisuzaki, T. Shigeyama, and K. Nomoto. Rayleigh-Taylor instability and mixing in SN 1987A. *Astrophys J.*, 344:L65–L68, September 1989.

[62] K. Eidmann, U. Andiel, F. Pisani, P. Hakel, R. C. Mancini, G. C. Junkel-Vives, J. Abdallah, and K. Witte. K-shell spectra from hot dense aluminum layers buried in carbon and heated by ultrashort laser pulses. *Journal of Quantitative Spectroscopy and Radiative Transfer*, 81(1-4):133 – 146, 2003.

[63] Shalom Eliezer. *The Interaction of High-Power Lasers with Plasmas*. Institute of Physics Publishing, 2002.

[64] Heinz W. Engl and Philipp Kügler. Nonlinear inverse problems: Theoretical aspects and some industrial applications. In *Multidisciplinary Methods for Analysis Optimization and Control of Complex Systems*, vol. 6 of *Mathematics in Industry*, pp. 3–47. Springer Berlin Heidelberg, 2005.

[65] L. Ensman and A. Burrows. Shock breakout in SN 1987A. *ApJ*, 393:742–755, July 1992.

[66] K. Estabrook, W. L. Kruer, and B. F. Lasinski. Heating by raman backscatter and forward scatter. *Phys. Rev. Lett.*, 45:1399–1403, Oct 1980.

[67] J. Faure, Y. Glinec, A. Pukhov, S. Kiselev, S. Gordienko, E. Lefebvre, J.-P Rousseau, F. Burgy, and V. Malka. A laser-plasma accelerator producing monoenergetic electron beams. *Nature*, 431(7008):541–544, September 2004.

[68] G J Fishman and C A Meegan. Gamma-ray bursts. *Annual Review of Astronomy and Astrophysics*, 33(1):415–458, 1995.

[69] Gregory D. Fleishman. Diffusive synchrotron radiation from relativistic shocks in gamma-ray burst sources. *The Astrophysical Journal*, 638(1):348, 2006.

[70] R. Fonseca, L. Silva, F. Tsung, V. Decyk, W. Lu, C. Ren, W. Mori, S. Deng, S. Lee, T. Katsouleas, and J. Adam. Osiris: A three-dimensional, fully relativistic particle in cell code for modeling plasma based accelerators. *Computational*

Science, ICCS 2002, vol. 2331 of *Lecture Notes in Computer Science*, pp. 342–351. Springer Berlin / Heidelberg, 2002.

[71] K. B. Fournier, C. Constantin, J. Poco, M. C. Miller, C. A. Back, L. J. Suter, J. Satcher, J. Davis, and J. Grun. Efficient multi-kev x-ray sources from ti-doped aerogel targets. *Phys. Rev. Lett.*, 92(16):165005, Apr 2004.

[72] K. B. Fournier, M. Tobin, J. F. Poco, K. Bradley, C. A. Coverdale, D. E. Beutler, T. Vidnovic III, S. B. Hansen, M. Severson, E. A. Smith, and D. L. Reeder. Absolute x-ray yields from laser-irradiated ge-doped aerogel targets. In George A. Kyrala, Jean-Claude J. Gauthier, Carolyn A. MacDonald, and Ali M. Khounsary, editors, *Laser-Generated, Synchrotron, and Other Laboratory X-Ray and EUV Sources, Optics, and Applications II*, number 1, p. 59180N. SPIE, 2005.

[73] K.B. Fournier, C. Constantin, C.A. Back, L. Suter, H.-K. Chung, M.C. Miller, D.H. Froula, G. Gregori, S.H. Glenzer, E.L. Dewald, and O.L. Landen. Electron-density scaling of conversion efficiency of laser energy into l-shell x-rays. *Journal of Quantitative Spectroscopy and Radiative Transfer*, 99(1-3):186 – 198, 2006.

[74] Kevin B. Fournier, Camen G. Constantin, John Poco, Michael C. Miller, Christina A. Back, Larry J. Suter, Joe Satcher, John F. Davis, and Jacob Grun. Efficient multi-kev x-ray sources from ti-doped aerogel targets. vol. 5196, pp. 194–204. SPIE, 2004.

[75] P. C. Fragile, S. D. Murray, P. Anninos, and W. van Breugel. Radiative shock-induced collapse of intergalactic clouds. *The Astrophysical Journal*, 604(1):74, 2004.

[76] S. Fujioka, H. Takabe, N. Yamamoto, D. Salzmann, F. L. Wang, H. Nishimura, Y. T. Li, Q. L. Dong, S. J. Wang, Y. Zhang, Y. J. Rhee, Y. W. Lee, J. M. Han, M. Tanabe, T. Fujiwara, Y. Nakabayashi, G. Zhao, J. Zhang, and K. Mima. X-ray astronomy in the laboratory with a miniature compact object produced by laser-driven implosion. *Nature Physics*, 5(11):821–825, 2009.

[77] Y. Fujita, T. N. Kato, and N. Okabe. Magnetic field generation by the weibel instability at temperature gradients in collisionless plasmas. *Phys. Plasmas*, 13(12):122901, 2006.

[78] E. J. Gamboa, C. M. Huntington, M. R. Trantham, P. A. Keiter, R. P. Drake, D. S. Montgomery, J. F. Benage, and S. A. Letzring. Imaging x-ray Thomson scattering spectrometer design and demonstration (invited). *Review of Scientific Instruments*, 83(10):10E108, 2012.

[79] E J Gamboa, D S Montgomery, I M Hall, and R P Drake. Imaging x-ray crystal spectrometer for laser-produced plasmas. *Journal of Instrumentation*, 6(04):P04004, 2011.

[80] C. G. R. Geddes, Cs. Toth, J. van Tilborg, E. Esarey, C. B. Schroeder, D. Bruhwiler, C. Nieter, J. Cary, and W. P. Leemans. High-quality electron beams from a laser wakefield accelerator using plasma-channel guiding. *Nature*, 431(538-541), September 2004.

[81] Neil Gehrels. The CGRO mission. [Online] Available: http://heasarc.gsfc.nasa.gov/docs/cgro/index.html

[82] F. Girard, J. P. Jadaud, M. Naudy, B. Villette, D. Babonneau, M. Primout, M. C. Miller, R. L. Kauffman, L. J. Suter, J. Grun, and J. Davis. Multi-kev x-ray conversion efficiencies of laser-preexploded titanium foils. *Phys. Plasmas*, 12(9):092705, 2005.

[83] F. Girard, M. Primout, D. Babonneau, J.P. Jadaud, M. Naudy, B. Villette, M.C. Miller, L.J. Suter, R.L. Kaufmann, J. Grun, and J.F. Davis. Experimental multi-kev x-ray conversion efficiencies from laser exploded germanium foil. *32nd EPS Conference on Plasma Phys.*, 29, 2005.

[84] S. G. Glendinning, K. S. Budil, C. Cherfils, R. P. Drake, D. Farley, D. H. Kalantar, J. Kane, M. M. Marinak, B. A. Remington, A. Richard, D. Ryutov, J. Stone, R. J. Wallace, and S. V Weber. Experimental measurements of hydrodynamic instabilities on nova of relevance to astrophysics. *The Astrophysical Journal Supplement Series*, 127(2):325, 2000.

[85] S. G. Glendinning, S. N. Dixit, B. A. Hammel, D. H. Kalantar, M. H. Key, J. D. Kilkenny, J. P. Knauer, D. M. Pennington, B. A. Remington, R. J. Wallace, and S. V. Weber. Measurement of a dispersion curve for linear-regime Rayleigh-Taylor growth rates in laser-driven planar targets. *Phys. Rev. Lett.*, 78(17):3318–3321, Apr 1997.

[86] S. G. Glendinning, S. V. Weber, P. Bell, L. B. DaSilva, S. N. Dixit, M. A. Henesian, D. R. Kania, J. D. Kilkenny, H. T. Powell, R. J. Wallace, P. J. Wegner, J. P. Knauer, and C. P. Verdon. Laser-driven planar Rayleigh-Taylor instability experiments. *Phys. Rev. Lett.*, 69(8):1201–1204, Aug. 1992.

[87] S. H. Glenzer, G. Gregori, F. J. Rogers, D. H. Froula, S. W. Pollaine, R. S. Wallace, and O. L. Landen. X-ray scattering from solid density plasmas. *Phys. Plasmas*, 10(6):2433–2441, 2003.

[88] S. H. Glenzer, B. J. MacGowan, P. Michel, N. B. Meezan, L. J. Suter, S. N. Dixit, J. L. Kline, G. A. Kyrala, D. K. Bradley, D. A. Callahan, E. L. Dewald, L. Divol, E. Dzenitis, M. J. Edwards, A. V. Hamza, C. A. Haynam, D. E. Hinkel, D. H. Kalantar, J. D. Kilkenny, O. L. Landen, J. D. Lindl, S. LePape, J. D. Moody, A. Nikroo, T. Parham, M. B. Schneider, R. P. J. Town, P. Wegner, K. Widmann, P. Whitman, B. K. F. Young, B. Van Wonterghem, L. J. Atherton, and E. I. Moses. Symmetric inertial confinement fusion implosions at ultra-high laser energies. *Science*, 327(2970):1228–1231, 2010.

[89] S. H. Glenzer and R. Redmer. X-ray Thomson scattering in high energy density plasmas. *Rev. Mod. Phys.*, 81(4):1625–1663, Dec. 2009.

[90] V. N. Goncharov, R. Betti, R. L. McCrory, P. Sorotokin, and C. P. Verdon. Self-consistent stability analysis of ablation fronts with large froude numbers. *Phys. Plasmas*, 3(4):1402–1414, 1996.

[91] V. N. Goncharov, R. Betti, R. L. McCrory, and C. P. Verdon. Self-consistent stability analysis of ablation fronts with small froude numbers. *Phys. Plasmas*, 3(12):4665–4676, 1996.

[92] V. N. Goncharov, O. V. Gotchev, E. Vianello, T. R. Boehly, J. P. Knauer, P. W. McKenty, P. B. Radha, S. P. Regan, T. C. Sangster, S. Skupsky, V. A. Smalyuk, R. Betti, R. L. McCrory, D. D. Meyerhofer, and C. Cherfils-Clérouin. Early stage of implosion in inertial confinement fusion: Shock timing and perturbation evolution. *Phys. Plasmas*, 13(1):012702, 2006.

[93] G. Gregori, S. H. Glenzer, W. Rozmus, R. W. Lee, and O. L. Landen. Theoretical model of x-ray scattering as a dense matter probe. *Phys. Rev. E*, 67(2):026412, Feb. 2003.

[94] G. Gregori, S.H. Glenzer, H.-K. Chung, D.H. Froula, R.W. Lee, N.B. Meezan, J.D. Moody, C. Niemann, O.L. Landen, B. Holst, R. Redmer, S.P. Regan, and H. Sawada. Measurement of carbon ionization balance in high-temperature plasma mixtures by temporally resolved x-ray scattering. *Journal of Quantitative Spectroscopy and Radiative Transfer*, 99(1-3):225 – 237, 2006.

[95] G. Gregori, S. B. Hansen, R. Clarke, R. Heathcote, M. H. Key, J. King, R. I. Klein, N. Izumi, A. J. Mackinnon, S. J. Moon, H.-S. Park, J. Pasley, N. Patel, P. K. Patel, B. A. Remington, D. D. Ryutov, R. Shepherd, R. A. Snavely, S. C. Wilks, B. B. Zhang, and S. H. Glenzer. Experimental characterization of a strongly coupled solid density plasma generated in a short-pulse laser target interaction. *Contributions to Plasma Physics*, 45(3-4):284–292, 2005.

[96] G. Gregori, A. Ravasio, A. Hll, S.H. Glenzer, and S.J. Rose. Derivation of the static structure factor in strongly coupled non-equilibrium plasmas for x-ray scattering studies. *High Energy Density Physics*, 3(1-2):99 – 108, 2007. Radiative Properties of Hot Dense Matter.

[97] Hans R. Griem. *Principles of Plasma Spectroscopy*. Cambridge University Press, 1997.

[98] J. Grun, J. Stamper, C. Manka, J. Resnick, R. Burris, J. Crawford, and B. H. Ripin. Instability of Taylor-Sedov blast waves propagating through a uniform gas. *Phys. Rev. Lett.*, 66:2738–2741, May 1991.

[99] I. Hachisu, T. Matsuda, K. Nomoto, and T. Shigeyama. Nonlinear growth of Rayleigh-Taylor instabilities and mixing in SN 1987A. *Astrophys J.*, 358:L57–L61, Aug. 1990.

[100] J. F. Hansen, S. G. Glendinning, R. F. Heeter, and S. J. E. Brockington. Dynamic hohlraums as x-ray sources in high-energy density science. *Review of Scientific Instruments*, 79(1):013504, 2008.

[101] Jean Pierre Hansen. Statistical mechanics of dense ionized matter. i. equilibrium properties of the classical one-component plasma. *Phys. Rev. A*, 8:3096–3109, Dec. 1973.

[102] J.-P. Hansen and I. R. McDonald. *Theory of Simple Liquids, Third Edition*. Academic Press, 3 edition, April 2006.

[103] Patrick Hartigan. Shock waves in outflows from young stars. *Astrophysics and Space Science*, 287:111–122, 2003. 10.1023/B:ASTR.0000006209.56314.c8.

[104] S. P. Hatchett, C. G. Brown, T. E. Cowan, E. A. Henry, J. S. Johnson, M. H. Key, J. A. Koch, A. B. Langdon, B. F. Lasinski, R. W. Lee, A. J. Mackinnon, D. M. Pennington, M. D. Perry, T. W. Phillips, M. Roth, T. C. Sangster, M. S. Singh, R. A. Snavely, M. A. Stoyer, S. C. Wilks, and K. Yasuike. Electron, photon, and ion beams from the relativistic interaction of petawatt laser pulses with solid targets. *Phys. Plasmas*, 7(5):2076–2082, 2000.

[105] G.-Y. Hu, J.-Y. Zhang, J. Zheng, B.-F. Shen, S.-Y. Liu, J.-M. Yang, Y.-K. Ding, X. Hu, Y.-X. Huang, H.-B. Du, R.-Q. Yi, A.-L. Lei, and Z.-Z. Xu. Angular distribution and conversion of multi-kev l-shell x-ray sources produced from nanosecond laser irradiated thick-foil targets. *Laser and Particle Beams*, 26(04):661–670, 2008.

[106] J. H. Hubbell. Review and history of photon cross section calculations. *Physics in Medicine and Biology*, 51:245, July 2006.

[107] A. Hujeirat and J. C. B. Papaloizou. Shock formation in accretion columns - a 2D radiative MHD approach. *Astronomy and Astrophysics*, 340:593–604, Dec. 1998.

[108] C. M. Huntington, C. M. Krauland, C. C. Kuranz, R. P. Drake, H.-S. Park, D. H. Kalantar, B. R. Maddox, B. A. Remington, and J. Kline. Development of a short duration backlit pinhole for radiography on the national ignition facility. *Review of Scientific Instruments*, 81(10):10E536, 2010.

[109] C. M. Huntington, C. C. Kuranz, R. P. Drake, A. R. Miles, S. T. Prisbrey, H.-S. Park, H. F. Robey, and B. A. Remington. Design of experiments to observe radiation stabilized Rayleigh-Taylor instability growth at an embedded decelerating interface. *Phys. Plasmas*, 18(11):112703, Nov. 2011.

[110] C. M. Huntington, C. C. Kuranz, G. Malamud, R. P. Drake, H.-S. Park, and B. R. Maddox. Spectral analysis of x-ray emission created by intense laser irradiation of copper materials. *Review of Scientific Instruments*, 83(10):10E114, 2012.

[111] C. M. Huntington, A. G. R. Thomas, C. McGuffey, T. Matsuoka, V. Chvykov, G. Kalintchenko, S. Kneip, Z. Najmudin, C. Palmer, V. Yanovsky, A. Maksimchuk, R. P. Drake, T. Katsouleas, and K. Krushelnick. Current filamentation instability in laser wakefield accelerators. *Phys. Rev. Lett.*, 106(10):105001, Mar. 2011.

[112] C.M. Huntington, C.M. Krauland, C.C. Kuranz, S.H. Glenzer, and R.P. Drake. Imaging scattered x-ray radiation for measurement of local electron density in high-energy-density experiments. *High Energy Density Physics*, 6(2):194 – 199, 2010. ICHED 2009 - 2nd International Conference on High Energy Density Physics.

[113] I.H. Hutchinson. *Principles of Plasma Diagnostics*. Cambridge University Press, 2 edition, 2005.

[114] Setsuo Ichimaru. Strongly coupled plasmas: high-density classical plasmas and degenerate electron liquids. *Rev. Mod. Phys.*, 54:1017–1059, Oct 1982.

[115] N. Izumi, R. Snavely, G. Gregori, J. A. Koch, H.-S. Park, and B. A. Remington. Application of imaging plates to x-ray imaging and spectroscopy in laser plasma experiments (invited). *Review of Scientific Instruments*, 77(10):10E325, 2006.

[116] John David Jackson. *Classical Electrodynamics*. Wiley, 3rd edition, 1998.

[117] J. Kane, D. Arnett, B. A. Remington, S. G. Glendinning, J. Castor, R. Wallace, A. Rubenchik, and B. A. Fryxell. Supernova-relevant hydrodynamic instability experiments on the nova laser. *The Astrophysical Journal Letters*, 478(2):L75, 1997.

[118] J. I. Katz. Low-frequency spectra of gamma-ray bursts. *Astrophys J. Lett*, 432:L107–L109, Sept. 1994.

[119] P. A. Keiter, R. P. Drake, T. S. Perry, F. Robey, H. B. A. Remington, C. A. Iglesias, R. J. Wallace, and J. Knauer. Observation of a hydrodynamically driven, radiative-precursor shock. *Phys. Rev. Lett.*, 89:165003, Sep 2002.

[120] M. H. Key, M. D. Cable, T. E. Cowan, K. G. Estabrook, B. A. Hammel, S. P. Hatchett, E. A. Henry, D. E. Hinkel, J. D. Kilkenny, J. A. Koch, W. L. Kruer, A. B. Langdon, B. F. Lasinski, R. W. Lee, B. J. MacGowan, A. MacKinnon, J. D. Moody, M. J. Moran, A. A. Offenberger, D. M. Pennington, M. D. Perry, T. J. Phillips, T. C. Sangster, M. S. Singh, M. A. Stoyer, M. Tabak, G. L. Tietbohl, M. Tsukamoto, K. Wharton, and S. C. Wilks. Hot electron production and heating by hot electrons in fast ignitor research. *Phys. Plasmas*, 5(5):1966–1972, 1998.

[121] J. D. Kilkenny, S. G. Glendinning, S. W. Haan, B. A. Hammel, J. D. Lindl, D. Munro, B. A. Remington, S. V. Weber, J. P. Knauer, and C. P. Verdon. A review of the ablative stabilization of the Rayleigh–Taylor instability in regimes relevant to inertial confinement fusion. *Phys. Plasmas*, 1(5):1379–1389, 1994.

[122] M. Klapisch, A. Bar-Shalom, J. Oreg, and D. Colombant. Recent developments in atomic physics for the simulation of hot plasmas. *Phys. Plasmas*, 8(5):1817–1828, 2001.

[123] R. W. Klebesadel, I. B. Strong, and R. A. Olson. Observations of Gamma-Ray Bursts of Cosmic Origin. *Astrophys J. Lett*, 182:L85, June 1973.

[124] J. P. Knauer, R. Betti, D. K. Bradley, T. R. Boehly, T. J. B. Collins, V. N. Goncharov, P. W. McKenty, D. D. Meyerhofer, V. A. Smalyuk, C. P. Verdon, S. G. Glendinning, D. H. Kalantar, and R. G. Watt. Single-mode, Rayleigh-Taylor growth-rate measurements on the omega laser system. *Phys. Plasmas*, 7(1):338–345, 2000.

[125] S. Kneip, C. McGuffey, J. L. Martins, S. F. Martins, C. Bellei, V. Chvykov, F. Dollar, R. Fonseca, C. Huntington, G. Kalintchenko, A. Maksimchuk, S. P. D. Mangles, T. Matsuoka, S. R. Nagel, C. A. J. Palmer, J. Schreiber, K. Ta Phuoc, A. G. R. Thomas, V. Yanovsky, L. O. Silva, K. Krushelnick, and Z. Najmudin. Bright spatially coherent synchrotron x-rays from a table-top source. *Nat Phys*, 6(12):980–983, 12 2010.

[126] R. Kodama, K. Mima, K. A. Tanaka, Y. Kitagawa, H. Fujita, K. Takahashi, A. Sunahara, K. Fujita, H. Habara, T. Jitsuno, Y. Sentoku, T. Matsushita, T. Miyakoshi, N. Miyanaga, T. Norimatsu, H. Setoguchi, T. Sonomoto, M. Tanpo, Y. Toyama, and T. Yamanaka. Fast ignitor research at the institute of laser engineering, osaka university. *Phys. Plasmas*, 8(5):2268–2274, 2001.

[127] M Koenig, T Vinci, A Benuzzi-Mounaix, S Lepape, N Ozaki, S Bouquet, L Boireau, S Leygnac, C Michaut, C Stehle, JP Chieze, D Batani, T Hall, K Tanaka, and M Yoshida. Radiative shock experiments at LULI. *ASTROPHYSICS AND SPACE SCIENCE*, 298(1-2):69–74, JUN 2005. 5th International Conference on High Energy Density Laboratory Astrophysics, Tucson, AZ, Mar. 10-13, 2004.

[128] A. L. Kritcher, P. Neumayer, C. R. D. Brown, P. Davis, T. Döppner, R. W. Falcone, D. O. Gericke, G. Gregori, B. Holst, O. L. Landen, H. J. Lee, E. C. Morse, A. Pelka, R. Redmer, M. Roth, J. Vorberger, K. Wünsch, and S. H. Glenzer. Measurements of ionic structure in shock compressed lithium hydride from ultrafast x-ray Thomson scattering. *Phys. Rev. Lett.*, 103:245004, Dec. 2009.

[129] A.L. Kritcher, T. Döppner, C. Fortmann, O.L. Landen, R. Wallace, and S.H. Glenzer. Development of x-ray Thomson scattering for implosion target characterization. *High Energy Density Physics*, 7(4):271 – 276, 2011.

[130] A.L. Kritcher, P. Neumayer, M.K. Urry, H. Robey, C. Niemann, O.L. Landen, E. Morse, and S.H. Glenzer. K-alpha conversion efficiency measurements for x-ray scattering in inertial confinement fusion plasmas. *High Energy Density Phys.*, 3(1-2):156 – 162, 2007. Radiative Properties of Hot Dense Matter.

[131] N. L. Kugland, G. Gregori, S. Bandyopadhyay, C. M. Brenner, C. R. D. Brown, C. Constantin, S. H. Glenzer, F. Y. Khattak, A. L. Kritcher, C. Niemann, A. Otten, J. Pasley, A. Pelka, M. Roth, C. Spindloe, and D. Riley. Evolution of elastic x-ray scattering in laser-shocked warm dense lithium. *Phys. Rev. E*, 80:066406, Dec 2009.

[132] H. J. Kull and S. I. Anisimov. Ablative stabilization in the incompressible Rayleigh-Taylor instability. 29(7):2067–2075, 1986.

[133] C. Kuranz, H.-S. Park, B. Remington, R. Drake, A. Miles, H. Robey, J. Kilkenny, C. Keane, D. Kalantar, C. Huntington, C. Krauland, E. Harding, M. Grosskopf, D. Marion, F. Doss, E. Myra, B. Maddox, B. Young, J. Kline, G. Kyrala, T. Plewa, J. Wheeler, W. Arnett, R. Wallace, E. Giraldez, and A. Nikroo. Astrophysically relevant radiation hydrodynamics experiment at the national ignition facility. *Astrophysics and Space Science*, pp. 1–5, 2011. 10.1007/s10509-011-0679-9.

[134] C. C. Kuranz, B. E. Blue, R. P. Drake, H. F. Robey, J. F. Hansen, J. P. Knauer, M. J. Grosskopf, C. Krauland, and D. C. Marion. Dual, orthogonal, backlit pinhole radiography in omega experiments. *Rev. Sci. Instrum.*, 77(10):10E327, 2006.

[135] C. C. Kuranz, R. P. Drake, M. J. Grosskopf, A. Budde, C. Krauland, D. C. Marion, A. J. Visco, J. R. Ditmar, H. F. Robey, B. A. Remington, A. R. Miles, A. B. R. Cooper, C. Sorce, T. Plewa, N. C. Hearn, K. L. Killebrew, J. P. Knauer, D. Arnett, and T. Donajkowski. Three-dimensional blast-wave-driven Rayleigh-Taylor instability and the effects of long-wavelength modes. *Phys. Plasmas*, 16(5):056310, May 2009.

[136] C. C. Kuranz, R. P. Drake, E. C. Harding, M. J. Grosskopf, H. F. Robey, B. A. Remington, M. J. Edwards, A. R. Miles, T. S. Perry, B. E. Blue, T. Plewa, N. C. Hearn, J. P. Knauer, D. Arnett, , and D. R. Leibrandt. Two-dimensional blast-wave-driven Rayleigh-Taylor instability: Experiment and simulation. *The Astrophysical Journal*, 696(1):749–759, 2009.

[137] M. Lamoureux, L. Jacquet, and R. H. Pratt. Angular distribution and polarization of the continuum emission in anisotropic plasmas. *Phys. Rev. A*, 39:6323–6334, Jun 1989.

[138] O. L. Landen. High-resolution time- and two-dimensional space-resolved x-ray imaging of plasmas at NOVA. *Rev. Sci. Instrum.*, 63:5075–5078, Oct. 1992.

[139] O. L. Landen, D. R. Farley, S. G. Glendinning, L. M. Logory, P. M. Bell, J. A. Koch, F. D. Lee, D. K. Bradley, D. H. Kalantar, C. A. Back, and R. E. Turner. X-ray backlighting for the national ignition facility. *Rev. Sci. Instrum.*, 72(1):627–634, 2001.

[140] O. L. Landen, S. H. Glenzer, M. J. Edwards, R. W. Lee, G. W. Collins, R. C. Cauble, W. W. Hsing, and B. A. Hammel. Dense matter characterization by x-ray Thomson scattering. *Journal of Quantitative Spectroscopy and Radiative Transfer*, 71(2-6):465 – 478, 2001.

[141] H. J. Lee, P. Neumayer, J. Castor, T. Döppner, R. W. Falcone, C. Fortmann, B. A. Hammel, A. L. Kritcher, O. L. Landen, R. W. Lee, D. D. Meyerhofer, D. H. Munro, R. Redmer, S. P. Regan, S. Weber, and S. H. Glenzer. X-ray Thomson-scattering measurements of density and temperature in shock-compressed beryllium. *Physical Review Letters*, 102(11):115001, 2009.

[142] Edison Liang and Katherine Keilty. An analytic approximation to radiative blast wave evolution. *The Astrophysical Journal*, 533(2):890, 2000.

[143] J. D. Lindl. *Inertial Confinement Fusion.* AIP Press, Springer, New York, 1998.

[144] John Lindl. Development of the indirect-drive approach to inertial confinement fusion and the target physics basis for ignition and gain. *Phys. Plasmas*, 2(11):3933–4024, 1995.

[145] V. Lobatchev and R. Betti. Ablative stabilization of the deceleration phase Rayleigh-Taylor instability. *Phys. Rev. Lett.*, 85(21):4522–4525, Nov. 2000.

[146] W. Lu, M. Tzoufras, C. Joshi, F. S. Tsung, W. B. Mori, J. Vieira, R. A. Fonseca, and L. O. Silva. Generating multi-gev electron bunches using single stage laser wakefield acceleration in a 3d nonlinear regime. *Phys. Rev. ST Accel. Beams*, 10(6):061301, Jun 2007.

[147] B. Maddox. Characterization of image plate detectors for quantitative high energy density x-ray radiography experiments.

[148] S. P. D. Mangles, C. D. Murphy, Z. Najmudin, A. G. R. Thomas, J. L. Collier, A. E. Dangor, E. J. Divall, P. S. Foster, J. G. Gallacher, C. J. Hooker, D. A. Jaroszynski, A. J. Langley, W. B. Mori, P. A. Norreys, F. S. Tsung, R. Viskup, B. R. Walton, and K. Krushelnick. Monoenergetic beams of relativistic electrons from intense laser-plasma interactions. *Nature*, 431(7008):535–538, Sept. 2004.

[149] S. P. D. Mangles, A. G. R. Thomas, O. Lundh, F. Lindau, M. C. Kaluza, A. Persson, C.-G. Wahlström, K. Krushelnick, and Z. Najmudin. On the stability of laser wakefield electron accelerators in the monoenergetic regime. *Phys. Plasmas*, 14(5):056702, 2007.

[150] G. F. Marani, R. J. Nemiroff, J. Norris, and J. T. Bonnell. On Similarities among GRBs. In *American Astronomical Society Meeting Abstracts #190*, vol. 29 of *Bulletin of the American Astronomical Society*, p. 839, May 1997.

[151] M. M. Marinak, S. G. Glendinning, R. J. Wallace, B. A. Remington, K. S. Budil, S. W. Haan, R. E. Tipton, and J. D. Kilkenny. Nonlinear Rayleigh-Taylor evolution of a three-dimensional multimode perturbation. *Phys. Rev. Lett.*, 80(20):4426–4429, May 1998.

[152] M. M. Marinak, R. E. Tipton, O. L. Landen, T. J. Murphy, P. Amendt, S. W. Haan, S. P. Hatchett, C. J. Keane, R. McEachern, and R. Wallace. Three-dimensional simulations of nova high growth factor capsule implosion experiments. *Phys. Plasmas*, 3(5):2070–2076, 1996.

[153] R. G. McClarren, R. P. Drake, J. E. Morel, and J. P. Holloway. Theory of radiative shocks in the mixed, optically thick-thin case. *Phys. Plasmas*, 17(9):093301, 2010.

[154] M. V. Medvedev, D. Lazzati, B. C. Morsony, and J. C. Workman. Jitter radiation as a possible mechanism for gamma-ray burst afterglows: spectra and light curves. *Astrophys J.*, 666, 2007. JILA Pub. 8044.

[155] Mikhail V. Medvedev and Abraham Loeb. Generation of magnetic fields in the relativistic shock of gamma-ray burst sources. *The Astrophysical Journal*, 526(2):697, 1999.

[156] E. E. Meshkov. Instability of the interface of two gases accelerated by a shock wave. *Sovient Fluid Dynamics*, 4:101–104, 1969.

[157] P. Meszaros and M. J. Rees. Optical and Long-Wavelength Afterglow from Gamma-Ray Bursts. *Astrophys J.*, 476:232, Feb. 1997.

[158] R.M. More. Atomic physics in interial confinement fusion. Technical Report LLNL-Report UCRL-84991, Academic Press, Mar. 1981.

[159] J. Myatt, W. Theobald, J. A. Delettrez, C. Stoeckl, M. Storm, T. C. Sangster, A. V. Maximov, and R. W. Short. High-intensity laser interactions with mass-limited solid targets and implications for fast-ignition experiments on omega ep. *Phys. Plasmas*, 14(5):056301, 2007.

[160] P. Neumayer, B. Aurand, M. Basko, B. Ecker, P. Gibbon, D. C. Hochhaus, A. Karmakar, E. Kazakov, T. Kühl, C. Labaune, O. Rosmej, An. Tauschwitz, B. Zielbauer, and D. Zimmer. The role of hot electron refluxing in laser-generated k-alpha sources. *Phys. Plasmas*, 17(10):103103, 2010.

[161] P. Neumayer, H.J. Lee, D. Offerman, E. Shipton, A. Kemp, A.L. Kritcher, T. Dppner, C.A. Back, and S.H. Glenzer. Isochoric heating of reduced mass targets by ultra-intense laser produced relativistic electrons. *High Energy Density Physics*, 5(4):244 – 248, 2009.

[162] P. M. Nilson, W. Theobald, J. Myatt, C. Stoeckl, M. Storm, O. V. Gotchev, J. D. Zuegel, R. Betti, D. D. Meyerhofer, and T. C. Sangster. High-intensity

laser-plasma interactions in the refluxing limit. *Phys. Plasmas*, 15(5):056308, 2008.

[163] K.-I. Nishikawa, J. Niemiec, P. E. Hardee, M. Medvedev, H. Sol, Y. Mizuno, B. Zhang, M. Pohl, M. Oka, and D. H. Hartmann. Weibel instability and associated strong fields in a fully three-dimensional simulation of a relativistic shock. *The Astrophysical Journal Letters*, 698(1):L10, 2009.

[164] P. A. Norreys, R. Allott, R. J. Clarke, J. Collier, D. Neely, S. J. Rose, M. Zepf, M. Santala, A. R. Bell, K. Krushelnick, A. E. Dangor, N. C. Woolsey, R. G. Evans, H. Habara, T. Norimatsu, and R. Kodama. Experimental studies of the advanced fast ignitor scheme. *Phys. Plasmas*, 7(9):3721–3726, 2000.

[165] John Nuckolls, Lowell Wood, Albert Thiessen, and George Zimmerman. Laser compression of matter to super-high densities: Thermonuclear (ctr) applications. *Nature*, 239:139–142, Sept. 1972.

[166] T.K. Nymark, P. Chandra, and C. Fransson. Modeling the x-ray emission of sn 1993j. *Astronomy and Astrophysics*, 494:179–189, 2009.

[167] B. Paczynski and J. E. Rhoads. Radio Transients from Gamma-Ray Bursters. *Astrophys J. Lett*, 418:L5, Nov. 1993.

[168] H.-S. Park, D. M. Chambers, H.-K. Chung, R. J. Clarke, R. Eagleton, E. Giraldez, T. Goldsack, R. Heathcote, N. Izumi, M. H. Key, J. A. King, J. A. Koch, O. L. Landen, A. Nikroo, P. K. Patel, D. F. Price, B. A. Remington, H. F. Robey, R. A. Snavely, D. A. Steinman, R. B. Stephens, C. Stoeckl, M. Storm, M. Tabak, W. Theobald, R. P. J. Town, J. E. Wickersham, and B. B. Zhang. High-energy k alpha radiography using high-intensity, short-pulse lasers. *Phys. Plasmas*, 13(5):056309, 2006.

[169] H.-S. Park, B. R. Maddox, E. Giraldez, S. P. Hatchett, L. T. Hudson, N. Izumi, M. H. Key, S. Le Pape, A. J. MacKinnon, A. G. MacPhee, P. K. Patel, T. W. Phillips, B. A. Remington, J. F. Seely, R. Tommasini, R. Town, J. Workman, and E. Brambrink. High-resolution 17–75 kev backlighters for high energy density experiments. *Phys. Plasmas*, 15(7):072705, 2008.

[170] N. J. Peacock, D. C. Robinson, M. J. Forrest, P. D. Wilcock, and V. V. Sannikov. Measurement of the electron temperature by Thomson scattering in tokamak t3. *Nature*, 224:488–490, Nov 1969.

[171] François Perrot and M. W. C. Dharma-wardana. Spin-polarized electron liquid at arbitrary temperatures: exchange-correlation energies, electron-distribution functions, and the static response functions. *Phys. Rev. B*, 62:16536–16548, Dec. 2000.

[172] A. Pukhov and J. Meyer ter Vehn. Laser wake field acceleration: the highly non-linear broken-wave regime. *Applied Physics B: Lasers and Optics*, vol. 74(4-5):355–361, April, 2002.

[173] J.W. Rayleigh. *Investigation of the character of the equilibrium of an incompressible heavy fluid of variable density*, vol. 14. Proceedings of the London Mathematical Society, 1883.

[174] Francis Reddy. Nasa-new gamma-ray burst smashes cosmic distance record, April 28 2009.

[175] S. P. Regan, J. A. Delettrez, V. N. Goncharov, F. J. Marshall, J. M. Soures, V. A. Smalyuk, P. B. Radha, B. Yaakobi, R. Epstein, V. Yu. Glebov, P. A. Jaanimagi, D. D. Meyerhofer, T. C. Sangster, W. Seka, S. Skupsky, C. Stoeckl, D. A. Haynes, J. A. Frenje, C. K. Li, R. D. Petrasso, and F. H. Séguin. Dependence of shell mix on feedthrough in direct drive inertial confinement fusion. *Phys. Rev. Lett.*, 92:185002, May 2004.

[176] S P Regan, P B Radha, T R Boehly, T Doeppner, K Falk, S H Glenzer, V N Goncharov, G Gregori, O L Landen, R L McCrory, D D Meyerhofer, P Neumayer, T C Sangster, and V A Smalyuk. Inferring the electron temperature and density of shocked liquid deuterium using inelastic x-ray scattering. *Journal of Physics: Conference Series*, 244(4):042017, 2010.

[177] Sean P. Regan, John A. Marozas, R. Stephen Craxton, John H. Kelly, William R. Donaldson, Paul A. Jaanimagi, Douglas Jacobs-Perkins, Robert L. Keck, Terrance J. Kessler, David D. Meyerhofer, T. Craig Sangster, Wolf Seka, Vladimir A. Smalyuk, Stanley Skupsky, and Jonathan D. Zuegel. Performance of 1-thz-bandwidth, two-dimensional smoothing by spectral dispersion and polarization smoothing of high-power, solid-state laser beams. *J. Opt. Soc. Am. B*, 22(5):998–1002, May 2005.

[178] A. Reighard and R. Drake. The formation of a cooling layer in a partially optically thick shock. *Astrophysics and Space Science*, 307:121–125, 2007. 10.1007/s10509-006-9237-2.

[179] A. B. Reighard, R. P. Drake, K. K. Dannenberg, D. J. Kremer, M. Grosskopf, E. C. Harding, D. R. Leibrandt, S. G. Glendinning, T. S. Perry, B. A. Remington, J. Greenough, J. Knauer, T. Boehly, S. Bouquet, L. Boireau, M. Koenig, and T. Vinci. Observation of collapsing radiative shocks in laboratory experiments. *Phys. Plasmas*, 13(8):082901, 2006.

[180] A. B. Reighard, R. P. Drake, J. E. Mucino, J. P. Knauer, and M. Busquet. Planar radiative shock experiments and their comparison to simulations. *Phys. Plasmas*, 14(5):056504, 2007.

[181] Amy B. Reighard. *Collapsing Radiative Shock Experiments on the Omega Laser*. PhD thesis, University of Michigan, 2007.

[182] B. A. Remington, S. V. Weber, M. M. Marinak, S. W. Haar, J. D. Kilkenny, R. Wallace, and G. Dimonte. Multimode Rayleigh-Taylor experiments on nova. *Phys. Rev. Lett.*, 73(4):545–548, Jul 1994.

[183] Sarah J. Reynolds, Sriharsha Pothapragada, and Mikhail V. Medvedev. Angular dependence of jitter radiation spectra from small-scale magnetic turbulence. *The Astrophysical Journal*, 713(2):764, 2010.

[184] R. D. Richtmyer. Taylor instability in a shock acceleration of compressible fluids. *Communications on Pure and Applied Mathematics*, 13(2):297–319, 1960.

[185] E. Rutherford. The scattering of α and β particles by matter and the structure of the atom. *Philosophical Magazine*, 21:669–688, 1911.

[186] D. Ryutov, R. P. Drake, J. Kane, E. Liang, B. A. Remington, , and W. M. Wood-Vasey. Similarity criteria for the laboratory simulation of supernova hydrodynamics. *The Astrophysical Journal*, 518(2):821–832, 1999.

[187] D D Ryutov and B A Remington. Scaling astrophysical phenomena to high-energy-density laboratory experiments. *Plasma Physics and Controlled Fusion*, 44(12B):B407, 2002.

[188] D. Salzmann. *Atomic Physics in Hot Plasmas*. International Series of Monographs on Physics. Oxford University Press, 1998.

[189] J. Sanz. Self-consistent analytical model of the Rayleigh-Taylor instability in inertial confinement fusion. *Phys. Rev. Lett.*, 73(20):2700–2703, Nov. 1994.

[190] J. Sanz, J. Ramírez, R. Ramis, R. Betti, and R. P. J. Town. Nonlinear theory of the ablative Rayleigh-Taylor instability. *Phys. Rev. Lett.*, 89(19):195002, Oct. 2002.

[191] L.I. Sedov. Propagation of strong shock waves. *Journal of Applied Mathematics and Mechanics*, 10:241–250, 1946.

[192] J.F. Seely, C.A. Back, C. Constantin, R.W. Lee, H.-K. Chung, L.T. Hudson, C.I. Szabo, A. Henins, G.E. Holland, R. Atkin, and L. Marlin. Krypton k-shell x-ray spectra recorded by the henex spectrometer. *Journal of Quantitative Spectroscopy and Radiative Transfer*, 99(1-3):572 – 583, 2006.

[193] K. Shigemori, T. Ditmire, B. A. Remington, V. Yanovsky, D. Ryutov, K. G. Estabrook, M. J. Edwards, A. J. MacKinnon, A. M. Rubenchik, K. A. Keilty, and E. Liang. Developing a radiative shock experiment relevant to astrophysics. *The Astrophysical Journal Letters*, 533(2):L159, 2000.

[194] W. L. Slattery, G. D. Doolen, and H. E. DeWitt. Improved equation of state for the classical one-component plasma. *Phys. Rev. A*, 21:2087–2095, Jun 1980.

[195] V. A. Smalyuk, T. R. Boehly, D. K. Bradley, V. N. Goncharov, J. A. Delettrez, J. P. Knauer, D. D. Meyerhofer, D. Oron, and D. Shvarts. Saturation of the Rayleigh-Taylor growth of broad-bandwidth laser-imposed nonuniformities in planar targets. *Phys. Rev. Lett.*, 81:5342–5345, Dec. 1998.

[196] V. A. Smalyuk, S. X. Hu, V. N. Goncharov, D. D. Meyerhofer, T. C. Sangster, D. Shvarts, C. Stoeckl, B. Yaakobi, J. A. Frenje, and R. D. Petrasso. Rayleigh-taylor growth stabilization in direct-drive plastic targets at laser intensities of $\sim 1 \times 10^{15}$ w/cm^2. *Phys. Rev. Lett.*, 101(2):025002, Jul 2008.

[197] Chantal Stehle, Matthias Gonzlez, Michaela Kozlova, Bedrich Rus, Tomas Mocek, Ouali Acef, Jean Philippe Colombier, Thierry Lanz, Norbert Champion, Krzysztof Jakubczak, Jiri Polan, Patrice Barroso, Daniel Bauduin, Edouard Audit, Jan Dostal, and Michal Stupka. Experimental study of radiative shocks at pals facility. *Laser and Particle Beams*, 28(02):253–261, 2010.

[198] Donna Strickland and Gerard Mourou. Compression of amplified chirped optical pulses. *Optics Communications*, 55(6):447 – 449, 1985.

[199] J.J. Su, T. Katsouleas, J.M. Dawson, P. Chen, and M. M. Jones. Stability of the driving bunch in the plasma wakefield accelerator. *IEEE Transactions on Plasma Science*, 15:192–198, April 1987.

[200] T. Tajima and J. M. Dawson. Laser electron accelerator. *Phys. Rev. Lett.*, 43(4):267–270, Jul 1979.

[201] H. Takabe, K. Mima, L. Montierth, and R. L. Morse. Self-consistent growth rate of the Rayleigh–Taylor instability in an ablatively accelerating plasma. *Physics of Fluids*, 28(12):3676–3682, 1985.

[202] Albert Tarantola. *Inverse Problem Theory and Methods for Model Parameter Estimation*. 2004.

[203] R.C. Tautz and I. Lerche. Radiation from non-linear weibel plasma modes. *Physics Reports*, (0), 2012.

[204] Geoffrey Taylor. The formation of a blast wave by a very intense explosion. i. theoretical discussion. *Proceedings of the Royal Society of London. Series A, Mathematical and Physical Sciences*, 201(1065):pp. 159–174, 1950.

[205] Geoffrey Taylor. The formation of a blast wave by a very intense explosion. ii. the atomic explosion of 1945. *Proceedings of the Royal Society of London. Series A. Mathematical and Physical Sciences*, 201(1065):175–186, 1950.

[206] Geoffrey Taylor. *The Instability of Liquid Surfaces when Accelerated in a Direction Perpendicular to their Planes*, vol. 201. Proceedings of the Royal Society of London, Mar. 1950.

[207] W. Theobald, K. Akli, R. Clarke, J. A. Delettrez, R. R. Freeman, S. Glenzer, J. Green, G. Gregori, R. Heathcote, N. Izumi, J. A. King, J. A. Koch, J. Kuba, K. Lancaster, A. J. MacKinnon, M. Key, C. Mileham, J. Myatt, D. Neely, P. A. Norreys, H.-S. Park, J. Pasley, P. Patel, S. P. Regan, H. Sawada, R. Shepherd, R. Snavely, R. B. Stephens, C. Stoeckl, M. Storm, B. Zhang, and T. C. Sangster.

Hot surface ionic line emission and cold k-inner shell emission from petawatt-laser-irradiated cu foil targets. *Phys. Plasmas*, 13(4):043102, 2006.

[208] W. Theobald, A. A. Solodov, C. Stoeckl, K. S. Anderson, R. Betti, T. R. Boehly, R. S. Craxton, J. A. Delettrez, C. Dorrer, J. A. Frenje, V. Yu. Glebov, H. Habara, K. A. Tanaka, J. P. Knauer, R. Lauck, F. J. Marshall, K. L. Marshall, D. D. Meyerhofer, P. M. Nilson, P. K. Patel, H. Chen, T. C. Sangster, W. Seka, N. Sinenian, T. Ma, F. N. Beg, E. Giraldez, and R. B. Stephens. Initial cone-in-shell fast-ignition experiments on omega. *Phys. Plasmas*, 18(5):056305, 2011.

[209] R. Tommasini, S. P. Hatchett, D. S. Hey, C. Iglesias, N. Izumi, J. A. Koch, O. L. Landen, A. J. MacKinnon, C. Sorce, J. A. Delettrez, V. Yu. Glebov, T. C. Sangster, and C. Stoeckl. Development of compton radiography of inertial confinement fusion implosions. *Phys. Plasmas*, 18(5):056309, 2011.

[210] F. S. Tsung, W. Lu, M. Tzoufras, W. B. Mori, C. Joshi, J. M. Vieira, L. O. Silva, and R. A. Fonseca. Simulation of monoenergetic electron generation via laser wakefield accelerators for 5–25 tw lasers. *Phys. Plasmas*, 13(5):056708, 2006.

[211] Léon Van Hove. Correlations in space and time and born approximation scattering in systems of interacting particles. *Phys. Rev.*, 95:249–262, Jul 1954.

[212] Pascal Viot. *Simulation numérique en physique statistique Cours commun aux Parcours "Physique des Liquide" et "Modélisation Statistique et Algorithmique des systèmes hors d'équilibre"*. Laboratory de Physique Théorique de la Matière Condensée, 4, Place Jussieu, 75252 Paris Cedex 05, Dec. 2011.

[213] A. J. Visco, R. P. Drake, S. H. Glenzer, T. Döppner, G. Gregori, D. H. Froula, and M. J. Grosskopf. Measurement of radiative shock properties by x-ray Thomson scattering. *Phys. Rev. Lett.*, 108:145001, Apr 2012.

[214] Erich S. Weibel. Spontaneously growing transverse waves in a plasma due to an anisotropic velocity distribution. *Phys. Rev. Lett.*, 2:83–84, Feb. 1959.

[215] K. B. Wharton, S. P. Hatchett, S. C. Wilks, M. H. Key, J. D. Moody, V. Yanovsky, A. A. Offenberger, B. A. Hammel, M. D. Perry, and C. Joshi. Experimental measurements of hot electrons generated by ultraintense (10^{19}W/cm^2) laser-plasma interactions on solid-density targets. *Phys. Rev. Lett.*, 81:822–825, Jul 1998.

[216] J. Workman, J. R. Fincke, G. A. Kyrala, and T. Pierce. Uniform large-area x-ray imaging at 9 keV using a backlit pinhole. *Appl. Opt.*, 44(6):859–865, 2005.

[217] Jonathan Workman and George A. Kyrala. Scaling of x-ray k-shell sources from laser-solid interactions. vol. 4504, pp. 168–179. SPIE, 2001.

[218] J. G. Wouchuk and A. R. Piriz. Growth rate reduction of the Rayleigh–Taylor instability by ablative convection. *Phys. Plasmas*, 2(2):493–500, 1995.

[219] K. Wünsch, P. Hilse, M. Schlanges, and D. O. Gericke. Structure of strongly coupled multicomponent plasmas. *Phys. Rev. E*, 77:056404, May 2008.

[220] B. Yaakobi, T. R. Boehly, T. C. Sangster, D. D. Meyerhofer, B. A. Remington, P. G. Allen, S. M. Pollaine, H. E. Lorenzana, K. T. Lorenz, and J. A. Hawreliak. Extended x-ray absorption fine structure measurements of quasi-isentropically compressed vanadium targets on the omega laser. *Phys. Plasmas*, 15(6):062703, 2008.

[221] V. Yanovsky, V. Chvykov, G. Kalinchenko, P. Rousseau, T. Planchon, T. Matsuoka, A. Maksimchuk, J. Nees, G. Cheriaux, G. Mourou, and K. Krushelnick. Ultra-high intensity- 300-TW laser at 0.1 Hz repetition rate. *Opt. Express*, 16(3):2109–2114, 2008.

[222] K. Yasuike, M. H. Key, S. P. Hatchett, R. A. Snavely, and K. B. Wharton. Hot electron diagnostic in a solid laser target by K-shell lines measurement from ultraintense laser–plasma interactions (3 x 10^{20} W/cm^2 $\leq$ 400 J). *Review of Scientific Instruments*, 72(1):1236–1240, 2001.

[223] Stéphane Zaleski and Philippe Julien. Numerical simulation of Rayleigh-Taylor instability for single and multiple salt diapirs. *Tectonophysics*, 206:55 – 69, 1992.

[224] Ya. B. Zel'dovich and Yu P. Raizer. *Physics Of Shock Waves And High-Temperature Hydrodynamic Phenomena*. Dover, Mar. 2002.